



FACULTY OF PHYSICS AND ASTRONOMY

NANOBIOMEDICAL CENTRE

ADAM MICKIEWICZ UNIVERSITY IN POZNAŃ

**Plasmonic properties of anisotropic, ultra-thin Au films and its
resulting dichroic Raman effect towards the development of
surface enhanced Raman spectroscopy**

by

EPHRAIM T. MATHEW

Supervisor: Prof. AMU Dr. hab Maciej Wiesner

Auxiliary supervisor: Dr. Jacek Jencyk

This dissertation is submitted for the degree of

DOCTOR OF PHILOSOPHY IN PHYSICS

Poznań, December 2025

This work was financially supported by the LaSensA project carried out under the M-ERA.NET 2 scheme (European Union's Horizon 2020 research and innovation programme, grant No. 685451) and co-funded by the Research Council of Lithuania (LMTLT), agreement No. S-M-ERA.NET-21-2, the National Science Centre of Poland, project No. 2020/02/Y/ST5/00086, and the Saxon State Ministry for Science, Culture and Tourism (Germany), grant No. 100577922, as well as from the tax funds on the basis of the budget passed by the Saxon state parliament.



This work is dedicated to my family, teachers and friends who supported, inspired and motivated me to pursue scientific research.

Declaration

Declaration of the candidate

I hereby declare that the content of this dissertation is original research. It has been composed by me and has not been submitted for any previous degree or professional qualification. The whole experimental work was carried out by me, the members of the research group I was working in and our external collaborators, during my contract period within the LaSensA project carried out under the M-ERA.NET 2 scheme (European Union's Horizon 2020 research and innovation programme, grant No. 685451) under the supervision of Prof. Dr. hab Maciej Wiesner and Dr. Jacek Jencyk. The contributions from respective Authors are provided in their Contribution Statements. The purpose of submission of this dissertation is to obtain the degree of Doctor of Philosophy in Physics at the Faculty of Physics of Adam Mickiewicz University in Poznań, Poland.



.....
M.Sc. Ephraim Mathew

Declaration of the supervisor

The declaration made by the candidate is, to the best of my knowledge, accurate. The dissertation is ready to be reviewed.



.....
Prof. Dr. hab Maciej Wiesner

Acknowledgment

I am grateful to everyone who motivated, supported and constantly encouraged me throughout the course of my doctoral studies in bringing this experimental PhD research into fruition. This research experience significantly developed my ability to professionally-plan, construct and execute comprehensive scientific tasks and experiments.

I reminisce and express my profound gratitude to late *Prof. Stefan Jurga*, first of all for believing and hiring me in this project. For inspiring me to perform plasmonics based research, and for the motivation and support during the course on my enrollment in doctoral studies. I would like to thank my supervisor *Prof. AMU dr. hab Maciej Wiesner* for guiding me, for the scientific discussions, providing alternative suggestions, experimental resources and getting me started on Raman spectroscopy, AFM and SEM techniques which were of the foremost importance for the completion of this thesis. Further, I express my sincere gratitude to *Dr. Jacek Jenczyk* my auxiliary supervisor for constantly encouraging and providing valuable suggestions in fabrication, characterization and in analysis of results. Thank you very much for the discussions we had regarding my research plan. Especially for the important suggestion of choosing the thiophenol as an analyte which was a turning point in this study and for providing the corrugated templates which proved to be the backbone in inducing anisotropy to the plasmonic systems. I express my deep sense of gratitude to *Prof. AMU dr. hab Mikołaj Lewandowski* the principal investigator of my research project for the constant support, motivation and encouragement throughout my PhD research, for providing the necessary resources for half a dozen scientific trips such as internships and international conferences. For providing suggestions on UHV annealing and deposition methodology, and especially for the valuable advice on career development and future research endeavors. I am obliged to thank with gratitude to *Prof. Igor Iatsunskyi* for his collaboration in providing important ellipsometry based polarized measurements which was the most essential optical characterization requirement for plasmonics based researches. I am also obliged to thank *Prof. AMU dr. hab Andriy Serebryannikov* from the faculty of physics and *Dr. Joel Henzie* (NIMS, Japan) for providing the necessary EM simulations which were used to corroborate and theoretically validate the experimental results. Further, I thank all my friends, colleagues, scientific and non-scientific staff of Nano-Biomedical Centre, Poznań especially my co-authors from surface science group: *Dr. Weronika Andrzejewska*, *Dr. Zygmunt Miłosz*, *Dr. Mariya Dobrotvorska* and *mgr. Szymon Murawka* for their support, collaboration and friendship during these years. I am grateful to *Dr. Alicja Jorasz* for her untiring help and support in administrative tasks from the day of my enrollment in the university. My sincere thanks to *Dr. Patryk Florczak* for his continuous help, discussion and support in chemical procedures performed towards analyte deposition for this study. I would also like to thank and acknowledge *Dr. Domantas Peckus* from (Kaunas Institute of Technology, Lithuania) for his help in performing polarized-transient absorption measurements for this study. Further, I thank *Prof. Andreas Fery* and *Dr. Ziwei Zhou* from the (Leibniz-Institut für Polymerforschung Dresden, Germany) for giving me an opportunity to pursue an internship with their group and providing me with a fellowship to further expand my exposure in plasmonics research during my PhD studies.

I thank the Faculty of Physics, Adam Mickiewicz University in Poznań, The office of the Doctoral school of Exact Sciences especially of *Ms. Agnieszka Kurzajak* and *Mr. Robert Lipiński*. The office of the Dean of the doctoral school and research, Research University – Excellence Initiative (IDUB) of Adam Mickiewicz University, The National Science Center of Poland - Warsaw, and the consortiums of the M ERANET research project titled “Ordered 2Dimensional arrays in lasing and sensing applications” and the institutions of their respective source of fundings.

I am obliged whole heartedly to thank with fond reminiscence, the *Knysz family* and the *Zimmer family* for hosting me in Poznań these years. For their care and support during my stay with them. I also thank the 4th community of NCW, *Sw. Wojciech*, Poznań for their care, support and love all these years.

Finally, yet foremost, I am grateful to God for the gift of my parents, grandparents and family for their continuous care, love and encouragement all these years, especially to my father for encouraging and supporting me to pursue higher education even amidst unexpected calamities. I would like to thank all my teachers who inspired and moulded me all through these years. My friends, especially *Ms. Indhu* for her help and support during my Masters studies in the University of Madras. I would like to thank *Rev. Robin Doss* for his guidance and direction, and in helping me to discern, and to arrive in Poznań, Poland.

Abstract

Metal structures that possess dimensional or periodic features ideally from 5nm to 1000nm range, exhibit unique optical properties due to the excitation of “plasmon polaritons” in metal\dielectric interface under certain resonance conditions. Such excited plasmons with polaritonic nature, enhances the electromagnetic (EM) near-field incident onto metals surfaces, making them suitable for applications in surface enhanced spectroscopies. This phenomenon can be truly regarded as an effect due to light-matter interaction at the nanoscale.

This thesis focuses on the study of plasmonic properties of ultrathin Au metal films deposited on corrugated Al₂O₃ dielectric templates, particularly in utilizing it as an application for surface enhanced Raman spectroscopy substrate, and studying its Raman scattering amplification processes. These anisotropic plasmonic substrates were fabricated by depositing ultrathin Au films onto surface-reconstructed corrugated Al₂O₃ templates by an electron beam evaporation technique operating in ultra-high vacuum (UHV) condition ($\sim 10^{-10}$ mbar). The in-plane structural anisotropy of the deposited metal films, which is induced by the corrugated Al₂O₃ template were characterized by atomic force microscopy (AFM). Its resulting anisotropic plasmonic effect was studied by optimizing excitation light attributes, such as polarization and wavelength in steady state and transient absorption spectroscopy (TAS). Experimental results revealed that the deposited ultrathin Au metal films with thickness (t) below the percolation threshold exhibiting ordered 2D metal nanoparticle (MNP) arrays nucleated onto the corrugated templates with period $P \cong d$, where d = diameter of the nucleating MNP. Excitation of localized surface plasmon polariton (LSPP) modes hybridized as collective plasmon modes was observed due to the strong coupling between the MNPs in these arrays with inter-particle gap $S \leq r$, where r = radius of the MNP. This was further confirmed by corroborating the experimental results with EM simulations and nearfield distributions. Further, polarized-TAS measurements performed on these samples were compared with the steady state measurements, these results revealed the relaxation dynamics of the generated non-radiative charge carriers on these samples and subsequent hot charge carriers induced permittivity modulations of the non-percolated ultrathin film. In contrast, propagating hybrid surface plasmon polariton (SPP) modes were excited on connected percolated Au films (exhibiting Drude metal characteristics) deposited on the corrugated templates. Precisely optimized pre and post deposition annealing processes were performed to improve the film percolation of $t \sim 10$ nm ultrathin Au film. This facilitated in the excitation of hybrid SPP modes in the near-infrared (NIR) range. Finally, the experimental observations were further supported and corroborated with simulated reflectance spectra and EM nearfield spatial distributions.

As a result of the enhanced EM near-fields on these plasmonic sample surfaces due to the polaritons, these anisotropic samples were tested for SERS sensing in polarized and wavelength scanned Raman measurements. Enhanced, dichroic SERS response of thio-phenol analytes was observed from the fabricated anisotropic, ultrathin Au films. These dichroic SERS effects allowed to directly compare their intensities and anisotropies of different Raman vibration modes of an analyte and provided a clearer depiction of the SERS anisotropies on these samples.

Utilizing this methodology:

- 1, The SERS dichroism of probe analyte's Raman vibration peaks of different Stokes shifted frequency was analyzed and interpreted to verify the EM nearfield mechanism of SERS enhancement.

and

2, The SERS dichroism of probe analyte's Raman vibration modes of different polarizability tensor was analyzed and interpreted to the study surface selection rules on these samples and their relative Raman peak intensity enhancements.

The work also investigated and reports the absolute SERS enhancements resulting from both localized and delocalized plasmon polariton modes in ultrathin Au films. And thus, provides an understanding for the design of plasmonic SERS substrates based on these ultrathin Au metal nanostructures. The fabricated anisotropic plasmonic samples discussed in the thesis exhibited enhanced SERS with a distributed hotspot and wider Stokes shifted spectral region fulfilling most of the seminal requirement for efficient and robust large-area SERS sensing.

Streszczenie

Struktury metaliczne posiadające cechy wymiarowe lub periodyczne w zakresie od około 5 nm do 1000 nm wykazują unikalne właściwości optyczne, wynikające ze wzbudzenia plazmonów–polarytonów na granicy metal–dielektryk w określonych warunkach rezonansowych. Tak wzbudzone plazmony o charakterze polarytonowym prowadzą do silnego wzmocnienia elektromagnetycznych pól bliskiego zasięgu padających na powierzchnie metaliczne, co czyni tego typu struktury szczególnie przydatnymi w zastosowaniach powierzchniowo wzmocnionych technik spektroskopowych. Zjawisko to można jednoznacznie uznać za efekt oddziaływania światła z materią w nanoskali.

Niniejsza praca koncentruje się na badaniu właściwości plazmonicznych ultracienkich warstw metalicznych złota (Au) osadzonych na pofałdowanych dielektrycznych szablonach Al_2O_3 , ze szczególnym uwzględnieniem ich zastosowania jako podłoża do powierzchniowo wzmocnionej spektroskopii Ramana oraz analizy procesów wzmocnienia rozpraszania ramanowskiego. Anizotropowe podłoża plazmoniczne wytwarzano poprzez osadzanie ultracienkich warstw Au na powierzchniowo zrekonstruowanych, pofałdowanych szablonach Al_2O_3 metodą odparowania wiązką elektronów, prowadzonego w warunkach ultrawysokiej próżni (UHV~ 10^{-10} mbar). Anizotropia strukturalna w płaszczyźnie osadzonych warstw metalicznych, indukowana przez pofałdowaną powierzchnię Al_2O_3 , została scharakteryzowana za pomocą mikroskopii sił atomowych (AFM).

Wynikające z tej anizotropii efekty plazmoniczne badano poprzez optymalizację parametrów światła wzbudzającego, takich jak polaryzacja oraz długość fali, zarówno w pomiarach stanu ustalonego, jak i w przejściowej spektroskopii absorpcyjnej (TAS). Wyniki eksperymentalne wykazały, że osadzone ultracienkie warstwy Au o grubości t poniżej progu perkolacji tworzą uporządkowane dwuwymiarowe układy nanocząstek metalicznych, nukleujące na pofałdowanych szablonach z okresem $P \cong d$, gdzie d oznacza średnicę nukleujących nanocząstek. W takich strukturach zaobserwowano wzbudzenie zlokalizowanych powierzchniowych modów plazmonów–polarytonów, które na skutek silnego sprzężenia pomiędzy nanocząstkami ulegają hybrydyzacji w kolektywne mody plazmoniczne, przy odległościach międzycząsteczkowych $S \leq r$, gdzie r jest promieniem nanocząstki.

Powyższe obserwacje zostały potwierdzone poprzez porównanie wyników eksperymentalnych z symulacjami pola elektromagnetycznego oraz analizą rozkładów pól bliskiego zasięgu. Ponadto, pomiary przejściowej spektroskopii absorpcyjnej z kontrolowaną polaryzacją porównano z pomiarami stanu ustalonego. Uzyskane wyniki ujawniły dynamikę relaksacji generowanych nieradiacyjnych nośników ładunku oraz indukowane przez gorące nośniki modulacje przenikalności elektrycznej w nieperkolowanych ultracienkich warstwach Au.

Dla porównania, w przypadku połączonych, perkolowanych warstw Au, wykazujących metaliczny charakter opisany modelem Drude'a, wzbudzane były propagujące hybrydowe mody powierzchniowe plazmon–polaryton. Precyzyjnie zoptymalizowane procesy wygrzewania przed i po osadzeniu umożliwiły poprawę perkolacji ultracienkich warstw Au o grubości około 10 nm, co sprzyjało wzbudzaniu hybrydowych modów plazmon–polaryton w zakresie bliskiej podczerwieni. Obserwacje eksperymentalne zostały dodatkowo potwierdzone poprzez symulowane widma spektroskopii odbiciowej oraz przestrzenne rozkłady pól elektromagnetycznych bliskiego zasięgu.

W wyniku silnego wzmocnienia elektromagnetycznych pól bliskiego zasięgu na powierzchniach badanych struktur plazmonicznych zaobserwowano silny sygnał ramanowski.

Przygotowane, anizotropowe próbki zostały poddane testom jako podłoża do detekcji SERS w pomiarach ramanowskich z kontrolowaną polaryzacją oraz różną długością fali światła

wzbudzającego. Zaobserwowano wzmocnioną, dichroiczną odpowiedź SERS dla cząsteczek tiofenolu na wytworzonych anizotropowych ultracienkich warstwach Au. Efekty dichroizmu SERS umożliwiły bezpośrednie porównanie intensywności oraz anizotropii różnych modów drgań ramanowskich badanego materiału, dostarczając informacji o anizotropii wzmocnienia SERS w tym materiale.

W szczególności:

1. Uzyskano, przeanalizowano i zinterpretowano dichroizm pasm drgań ramanowskich badanego materiału o różnych przesunięciach Stokesa, co umożliwiło weryfikację elektromagnetycznego mechanizmu wzmocnienia SERS.

2. Uzyskano, przeanalizowano i zinterpretowano dichroizm modów drgań ramanowskich charakteryzujących się różnymi składowymi tensora polaryzowalności, co pozwoliło na analizę reguł wyboru powierzchniowego w SERS oraz względnych wzmocnień intensywności poszczególnych pasm.

Praca obejmuje również analizę bezwzględnych współczynników wzmocnienia SERS, wynikających zarówno ze zlokalizowanych, jak i zdelokalizowanych modów plazmon–polariton w ultracienkich warstwach Au. Uzyskane wyniki dostarczają podstaw do projektowania plazmonicznych podłoży SERS opartych na ultracienkich nanostrukturach metalicznych. Wytworzone anizotropowe próbki plazmoniczne charakteryzują się silnym wzmocnieniem sygnału SERS, rozproszoną siecią obszarów silnej lokalizacji pola oraz szerokim zakresem przesunięć Stokesa, spełniając kluczowe wymagania dla wydajnych i stabilnych, wielkoobszarowych sensorów SERS.

Contents

Declaration.....	3
Acknowledgment.....	4
Abstract.....	6
Streszczenie	8
Contents	10
List of abbreviations	12
List of important symbols	13
1. Introduction.....	14
1.1. Significance and scope of the studies	17
1.2. Thesis outline.....	21
1.3. Structure formation of ultrathin metal films – Theory	22
1.3.1. Non-percolated ultrathin Au films.....	25
1.3.2. Percolated ultrathin Au films.....	25
1.3.3. De-wetting pathways of ultrathin metal films	26
1.4. Optical properties of ultrathin metal films – Theory	27
1.4.1. Maxwells equations of EM waves and Drude-Lorentz model of free electron gas in Metals	28
1.4.2. Permittivity of ultra-thin metal films at plasmon polaritons excitation	32
1.4.5. Plasmonic hybridization on ultrathin metal films.....	37
1.4.6. Ultrafast plasmon relaxation dynamics	40
1.5. Surface enhanced Raman scattering (SERS) sensing – Theory	42
1.5.1. Raman scattering effect	42
1.5.2. Polarizability tensor.....	44
1.5.3. Electromagnetic (EM) near-field enhancement.....	45
2. Experimental methods	48
2.1. Fabrication of anisotropic ultrathin Au films.....	48
2.1.1. Surface reconstruction of Al ₂ O ₃ templates	48
2.1.2. Ultrathin Au metal deposition	51
2.1.3. Analyte molecules chemisorption.....	54
2.2. Characterization, measurement and simulation techniques	54
2.2.1. Atomic force microscopy (AFM).....	54
2.2.2. Ultraviolet-visible spectroscopy (UV-vis).....	55
2.2.3. Ellipsometry	56
2.2.4. Transient absorption spectroscopy (TAS)	57
2.2.5. Raman spectroscopy	58
2.2.6. Simulation techniques	59
3. Plasmonic properties of non-percolated, anisotropic Au metal films	61
3.1. Formation and structure of non-percolated, anisotropic Au metal films.....	61
3.2. Optical response of non-percolated, anisotropic Au metal films	65
3.3. Plasmonic hybridization on 2D-MNP arrays	70

3.4. Plasmonic anisotropy of non-percolated Au metal films on corrugated sapphire templates under steady state spectroscopy	74
3.5. Plasmonic anisotropy of non-percolated Au metal films on corrugated sapphire templates under ... transient optical spectroscopy	74
4. Plasmonic properties of percolated, anisotropic Au metal films.....	79
4.1. Formation and structure of percolated Au metal films	79
4.2. Optical response of percolated, anisotropic Au metal films	81
4.3. Excitation of propagating surface plasmon polariton (SPP) mode	83
4.4. Plasmonic anisotropy of percolated Au metal films on corrugated sapphire templates.....	85
5. Dichroic SERS effect on anisotropic, ultra-thin Au metal films	86
5.1. Anisotropic SERS effect on non-percolated Au metal films on corrugated sapphire	86
templates	86
5.1.1. Super and sub-radiant SERS.....	86
5.1.2. Non-linear Raman scattering process and verification of EM near-field mechanism.....	91
of SERS.	91
5.2. Anisotropic SERS effect on percolated Au films on corrugated sapphire templates.....	101
5.2.1 Near-Infrared NIR-SERS sensing on percolated, anisotropic Au metal films.....	101
5.2.2. SERS surface selection rules for non-isotropic molecules on percolated corrugated.....	103
Au metal films	103
6. Summary and outlook.....	107
Bibliography	110
List of journal publications (related to the PhD Thesis)	122
List of conference presentations (related to the PhD Thesis).....	122
List of internships and foreign research visits (related to the PhD Studies)	123
List of awards in competitions (during the PhD Studies)	124
Other scientific activities (during the PhD Studies)	124
Contribution statements (for publications related to the PhD Thesis)	125
Permissions to use figures from articles in the theoretical chapter 1 of the Thesis.....	143

List of abbreviation in the thesis

EM - Electromagnetic	TAS – Transient absorption spectroscopy
SERS – Surface enhanced Raman scattering	LRSP - Long range surface plasmon polariton
CCD – Charge coupled-device	SRSPP - Short range surface plasmon polariton
AFM – Atomic force microscope	2D-MNP – 2-Dimensional Metal nanoparticle
SM-SERS – Single molecule SERS	NIR - near infrared
UHV - Ultrahigh vacuum	AI – Artificial intelligence
MNP – Metal nanoparticle	LED – Light emitting diode
FDTD - Finite difference time domain	SEM – Scanning electron microscope
UV – Ultraviolet	SLR – Surface lattice resonance
NIR – Near infrared	FWHM – Full width half maximum
SPP – Surface plasmon polariton	EF – Enhancement factor
LSPR – Localized surface plasmon resonance	SAM – Self assembled monolayer
PT - Phenyl thiolate	SRS – Stimulated Raman scattering
SNOM – Scanning nearfield microscopy	

List of important symbols in the thesis

Al_2O_3 - Aluminum oxide	β_d – Collision less Landau damping factor
$h\nu$ – Photon energy	γ – Collision based damping factor
\hbar – Reduced planks constant	α_{np} – Polarizability of MNP
ω_p – Plasmon frequency	Ψ_{LSPR} – Representation of the LSPR mode of MNP - in molecular hybridization theory
$\tilde{\omega}_p$ – Plasmon frequency including bound electrons contribution	g – Dipole enhancement factor
P – Period of corrugation	g^s – Enhancement factor at stokes frequency
P_{ind} – Induced polarization in the medium	g' – Enhancement factor due to collective plasmon mode
σ_p – Induced polarization in an MNP	E_o – Incident electric field
S – Inter-particle spacing	E_p – Enhanced electric field due to plasmon resonance
S_s – Supersaturation	$E_{p'}$ – Enhanced electric field due to collective plasmon resonance
s – Radial position of the molecule	k_x diffracted – Wavevector of diffracted field
p_v – Vapour pressure	k_x spatial corrugation – Spatial corrugation vector
p_s – Substrate pressure	λ_{TEp} – Plasmon resonance excited at TE incident polarization
R – Au deposition rate	λ_{TMp} – Plasmon resonance excited at TM incident polarization
r_p – Position vector	$\lambda_{p3,5}$ – Higher order super-radiant plasmon modes
r – Radius of MNP	$\lambda_{p2,4}$ – Higher order sub-radiant plasmon modes
K – Boltzmann constant	$\lambda_{pump\ exc}$ – Excitation wavelength of pump pulse
κ – Imaginary part of refractive index	Γ – Plasmon bandwidth
f_c – Percolation threshold	λ_{exc} – Excitation wavelength in steady state spectroscopy
f – Surface coverage of Au	
\tilde{n} – Complex refractive index	
N_{np} – Number of MNPs in the array	
α_m – Attenuation constant	
β – Propagation constant	

1.Introduction

Spectroscopy:

Light –matter interactions are standard, everyday phenomena which allow us to measure and observe our surroundings. Such as vision which enables us the power of sensing with our eyes. Sir Isaac Newton coined the term “spectrum” which in Latin means “image” in order to describe the band of colors dispersed using a prism¹. The study and analysis of spectra is known as the field of spectroscopy.

Various spectroscopic techniques are continuously developed to identify and investigate: the properties of elements, atomic and molecular structures, their interactions and reactions even from the farthest galaxies to inherent proteins and DNA molecules in terrestrial organisms^{2,3}. Thus, serving as an important tool in the fields of medicine, chemistry, physics and astronomy^{2,4}.

It was James Clerk Maxwell who formulated the equations unifying electricity and magnetism describing how electromagnetic (EM) waves propagate and interact with matter⁵. Meanwhile, the discovery of discrete spectral lines obtained from the hydrogen atom and the dependence of wavelength of radiation on the temperature of a black body paved way for the basis of quantum mechanics⁶. It also proved that the light-matter interactions involved quantized energy transfer, where the electrons bound to an atom absorb or emit photons with specific energies^{7,8}. This analysis of light-matter interactions (spectroscopy) was the foremost reason which paved way for the concept of wave-particle duality of elementary particles such as photons and electrons^{9,10}. These concepts were crucial in understanding optical phenomena such as absorption, emission, scattering, reflection, refraction, interference, diffraction and transmission which are governed and explained either by the electromagnetic theory or quantum mechanics based on the investigated system^{11,12}. As a result of these advancements in the analysis of light-matter interaction^{13,14}, further led to the development of other applications apart from spectroscopy and sensing, such as: *photovoltaics*¹⁵⁻¹⁷, *antennas*^{18,19}, *optical tweezers*²⁰⁻²¹, *optical modulators*²², *lasers*^{23,24}, *light emitting devices*^{25,26} and *optical fibers*²⁷.

Particularly, with the invention of lasers in 1960²⁸, where the properties of light could be manipulated to a greater extent facilitated in the realization of more sophisticated advancement and development in the field of photonics and optical components: such as advanced *confocal microscopy*²⁹, *spectroscopic imaging*³⁰, *diagnostics*³¹, *display*³² and in *communication technology*^{33,34}. These photonics-based devices even dominated the field of electronics which had a hegemony in the previous 20th century. This century has been termed rightly as the "century of light" as photonics and optics-based devices drive innovation, communication and technology today³⁵.

Raman spectroscopy.

Importantly, after the advent of lasers a dwindling scattering spectroscopy known as “Raman spectroscopy” which had no relevance for commercial application until then, was revived³⁶. The Raman scattering effect was discovered by Sir. Chandrasekhara Venkata Raman who demonstrated this ground breaking phenomena of inelastic scattering of matter³⁷. It is

recognized as a significant technique to analyze the composition of liquids, gases, and solids and to differentiate molecular structure^{38,39}. Thus designated as a National Historic Chemical Landmark by the American Chemical Society in 1998⁴⁰. Even though, the first commercial Raman instrument equipped with a dispersive grating and a laser source, was only introduced in the early 1966 by Coderg and Spex companies^{41,42}. As a result of the focused and intense laser excitation the application of Raman spectroscopy widened.

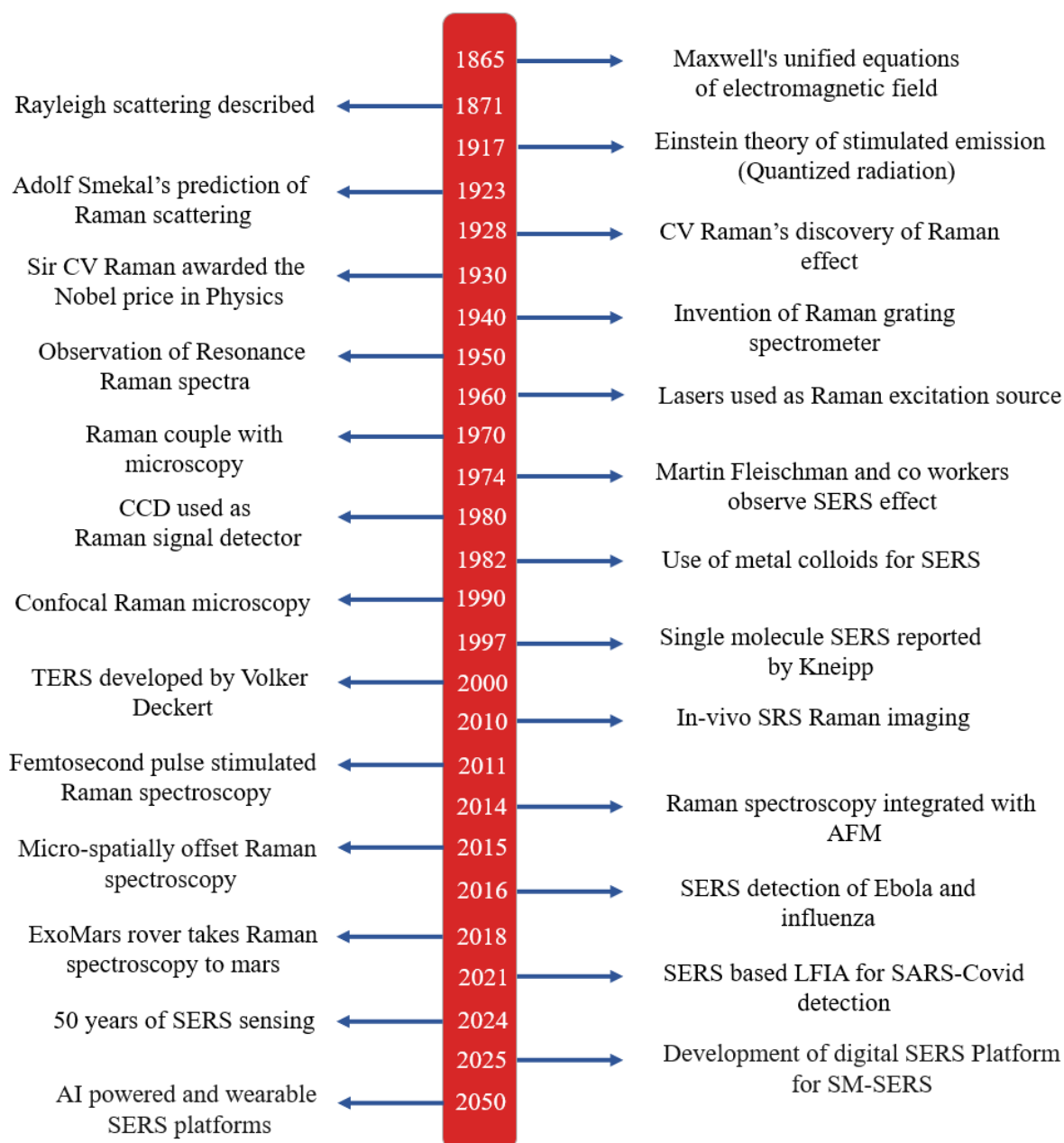


Figure 1.1. Timeline depicting the development of the Raman and surface enhance Raman scattering effect into a modern analytical spectroscopic technique^{41,42}.

Raman spectroscopy acquired a greater impact on chemical analysis and particularly in studying chemical and molecular bonds as Raman peak frequencies are specific to each molecular bond vibrations and their symmetry³⁹. This allowed to acquire the fingerprint Raman spectra of molecules in bio-chemical analysis⁴³. However, with the further development of infrared

absorption spectroscopy by Fourier transform which also provides characteristic vibrational peaks of molecules, the difficult and time-consuming Raman spectroscopy was often less used^{44,45}. Until further advancement in optical components and photonic technologies around the 80s, such as the integration of a microscope and a charge coupled device (CCD detector) to the Raman instrument made it a regular analytical device among researchers from different fields^{46,47}.

After decades of its discovery the Raman scattering effect can be conclusively affirmed to have developed into a *quick*⁴⁸, *one-step*⁴³, *label free*⁴⁹, *non-destructive*⁴⁶ analytical spectroscopic method. Material information and precise details such as breaking or formation of *chemical bonds*^{50,51}, *phase transitions*⁵², *residual strain/stress*⁵³, or the *presence of lattice defects*⁵³ are quickly measured on samples utilizing it. It also excelled in its advantage over IR absorption spectroscopy requiring *minimal sample preparation*⁴⁶, *its sensing capability of aqueous solutions with better selectivity*⁵⁴, *depolarization studies*⁵⁵, and *in detecting IR-inactive vibrational modes*⁵⁶. Continuously there is still an ongoing development of Raman spectroscopic technique on its integration with other optical techniques such as: *coherent Raman scattering microscopy*⁵⁷, *resonance Raman scattering*⁵⁸, *confocal Raman scattering imaging*⁵⁹ and *stimulated Raman scattering microscopy*⁶⁰ being realized. The timeline for the development of the Raman scattering effect into the different types of modern ubiquitous spectroscopic and microscopic methods are portrayed in Figure 1.1.

Although these techniques effectively increased its sensitivity, selectivity and range. Analysis of ultra-low analyte concentrations and single molecule sensing was non-effective and are still commercially unachievable for large-scale robust sensing with these aforementioned Raman spectroscopy developments⁶¹. This is due to the nature of this phenomena as roughly only one in a million photons are in-elastically scattered⁶², with further limitations due fluorescence interference and complex sample preparation processes.

Surface enhanced Raman spectroscopy.

In 1973, Martin Fleischmann and his co-workers in the University of Southampton observed an enormous Raman scattering enhancement of pyridine molecules adsorbed on electrochemically roughened silver surface⁶³. This effect would be later termed as Surface enhanced Raman scattering (SERS) effect and would be conferred with the award of National Chemical Landmark by the Royal Society of Chemistry to the University of Southampton in the 40th anniversary of this important discovery⁶⁴. This technique amplified the scattering signals of the inherently weak but structurally rich Raman scattering of analytes of low concentration⁶⁵. One of the primary reasons for the enhancement of the Raman scattering of molecules on these metal surfaces are the “enhanced EM nearfield” due to the excitation of plasmon⁶⁶. The mechanism of this enhancement involving the excitation of surface plasmons was suggested and proposed by Albrecht, Creighton^{66,67}. and Philpott⁶⁶. Importantly, the dependence of SERS intensity based on the enhanced EM near-field due to localized surface plasmon excitations was reported by Moskovits⁶⁸. This thesis is primarily focused in understanding the optical properties of percolated and non-percolated ultra-thin Au metal films ($t \leq 10$ nm) deposited on corrugated sapphire templates solely towards utilizing it for surface enhanced Raman spectroscopy application.

Particularly two types of light-matter interactions:

1. Photon (quantized electromagnetic field $h\nu$) and its interaction with plasma (free electron gas) on the surface of the ultra-thin percolated and non-percolated Au metal films (*which results in quantized plasmon resonances*).

and

2. Photon (quantized electromagnetic field $h\nu$) and its interaction with the vibrational modes (optical phonons) of a molecule's bonds (*which re-radiates weak inelastic Raman scattering*).

are analyzed and studied in depth to understand the enhancement of in-elastic Raman signals on these plasmonic samples so as to design effective and robust ultrathin film-based SERS substrates. Here, the weak inelastic light scattering from vibrational modes is strongly enhanced for molecules present on metals surface, this is due to the unique excitation of polaritons (hybrid quasiparticles) comprising enhanced photon density (EM near-field) in the metal/dielectric interface as mentioned above^{68,69}. These excited plasmon-polaritons with quantized collective oscillation of free electrons ($\hbar\omega_p$) are excited when photons transfer their energy to the free electron oscillations in the metal surface resulting in a polaritonic coupling as a result of resonance^{69,70}.

In this work the intensity of the enhanced Raman vibrational modes is corroborated with the wavelength, spatial and temporal features of the excited plasmon-polariton modes, as different types of plasmon-polariton modes are excited depending on the geometrical shape, morphology and periodic surface topography of the deposited ultrathin Au films^{71,72}. The type of plasmon-polariton mode that is supported on these samples can be essentially known by solving the Maxwell's equation for EM waves onto geometric mediums possessing boundary conditions and optical properties reflecting both percolated and non-percolated metal/ dielectric interfaces, as structural modulations induced on metals surface reorder the collective oscillation of free electrons ω_p in it influencing photon-plasma interaction⁷⁰. Numerical methods based on finite-difference time-domain (FDTD) and finite integration methods are utilized to solve Maxwell's equations on plasmonic nanostructures with complex geometries⁷³. These simulations also allow researchers to design and optimize plasmonic devices for various applications, such as *biosensing*⁷⁴, *optical antennas*¹⁸, and *metamaterials*⁷⁵. Finally, polarized and wavelength scanned Raman analysis was performed for a selected non-isotropic thiophenol molecule on these fabricated samples which enabled to validate the EM nearfield mechanism of SERS and study its surface selection rules. The significance and scope of this original experimental thesis is discussed in the upcoming section 1.1.

1.1. Significance and scope of the thesis.

Utilization of sensors has acquired paramount importance in the field of biomedicine, food safety, and environmental monitoring^{76,77}. Importantly, accurate and quick detection of biochemical markers is a vital necessity for *forensics*⁷⁸, *early disease diagnosis*⁷⁹ and *pollution control*⁸⁰. Hence the demand for a real-time sensing probe is growing rapidly⁸¹. The detection of low-concentration analytes and markers are difficult with traditional diagnostic and spectroscopic probes^{82,83}. As they rely heavily on specialist and doctors for authorized

verification and diagnosis. Additionally, they are time consuming, with poor resolution and provide limited information especially on the biochemistry underlying the contamination or infection. Thus, the ability to detect low concentration chemical and biological molecules in a quick, sensitive and reliable manner is of high importance in this industrialized world^{84,85}.

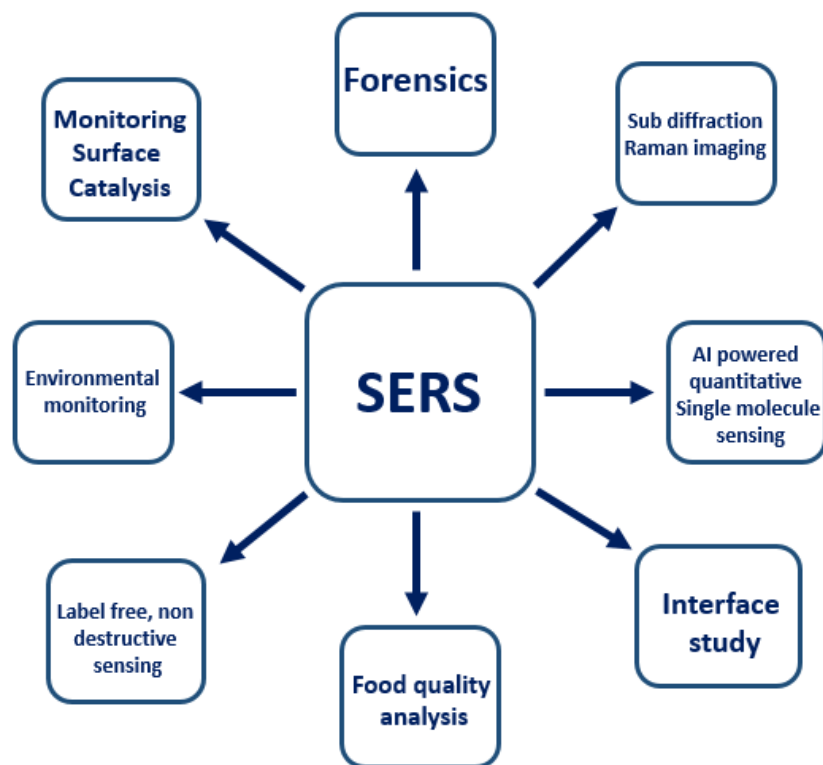


Figure 1.2. Scope and applicative relevance of surface enhanced Raman scattering effect.

Surface-enhanced Raman spectroscopy (SERS) is an already common versatile technique providing both qualitative and quantitative information of the probe analytes, as it measures both the intensity and frequency of the in-elastically scattered light by matter. Figure 1.2 shows the chart illustrating the scope and various other applicative relevance of SERS effect. It has rapidly advanced for its significant signal enhancement, fingerprinting ability to identify low concentration molecules in a one-step process^{86,87}. Recent developments in AI powered SERS platforms shows promising scope in revolutionizing quick and accurate quantitative analyte sensing^{88,89}. The key characteristic of a SERS-active substrate is the enhanced EM nearfield which amplifies the Raman scattering signal of an analyte present in its vicinity. Where the EM nearfields frequency, spatial distribution and intensity can be optimized by changing the size, shape, orientation and periodicity of the metal nanostructure^{71,90}. However, SERS substrates exhibiting plasmon resonance in the UV–visible range induces photochemical reactions^{91,92} and disadvantages such as *photo-bleaching*⁹³, *photo-degradation*⁹⁴, and *interference effects*⁹⁵ due to fluorescence resulting from both analyte and metal surface. For this reason, Raman excitation laser in the near- infrared (*NIR*) wavelength range is utilized for reducing the energy transferred to the system, minimizing photo-induced effects on the probe analytes and sample degradation^{95,96}.

In this PhD research, I utilized a well-established temperature-induced surface reconstruction of (α - Al_2O_3) technique⁹⁷, which was used to fabricate large-area (2x2cm) corrugated templates of different corrugation periods for ultra-thin plasmonic Au film deposition. Percolated and non-percolated Au films were deposited on these templates under ultrahigh vacuum (*UHV*) conditions to study their optical properties and investigate them for SERS application. As, non-percolated and near-percolating ultrathin films supporting both localized and delocalized plasmon modes have been reported to exhibit unique plasmonic properties with enhanced scattering cross-sections suitable for SERS application⁹⁸⁻¹⁰⁰. Figure 1.3 shows the illustration of the properties and advantages of the Al_2O_3/Au plasmonic system fabricated and studied in this thesis. Here, the Au films self-assemble into *2D-MNP* arrays with in-plane anisotropic ordering on these corrugated sapphire templates at thickness below the metal percolation threshold under optimal deposition conditions. This approach performed in this study eliminates the requirement for complex glancing-angle deposition techniques as reported in other studies¹⁰¹⁻¹⁰³. These substrates decorated with metal nanoparticles *MNPs* exhibit tunable localized plasmon polariton modes dependent on the excitation polarization confining the illuminated light into sub-diffraction volumes^{104,105}.

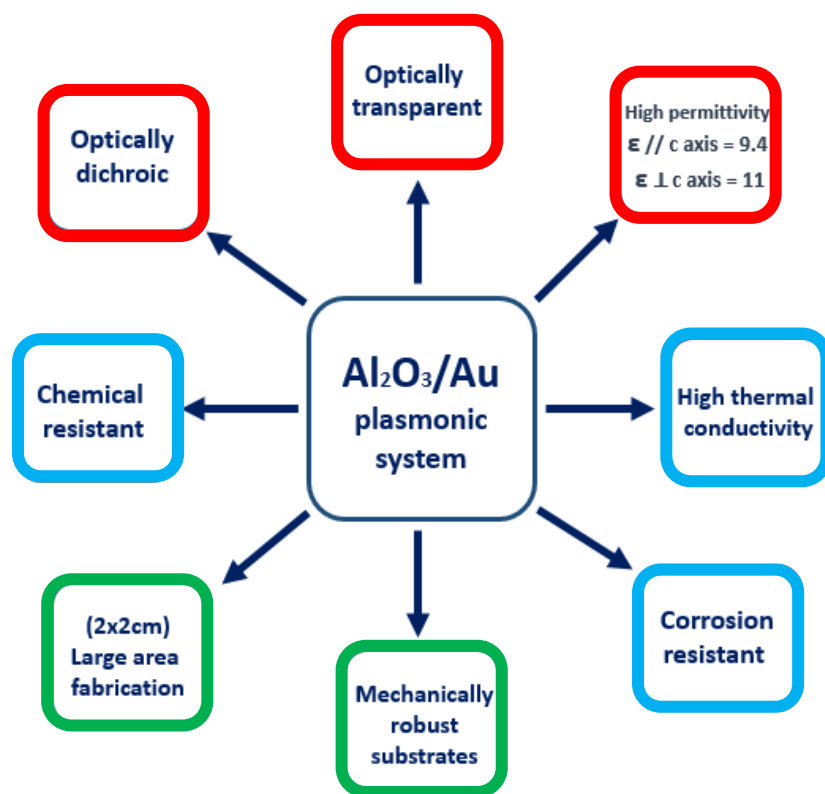


Figure 1.3. Properties and advantages of Al_2O_3/Au (dielectric/metal) based plasmonic system which is fabricated and studied in this original experimental thesis.

This confinement of light with high order of near-field enhancement ($\sim 10^{10}$) breaks the classical diffraction limit for sensing in sub-nano-metric areas¹⁰⁵. Although, the fabrication of these ordered *MNP* arrays with dimensions and period below 20 nm are difficult to achieve by conventional photo- and e-beam lithographic techniques¹⁰⁶. Wet chemistry¹⁰⁷ and colloidal suspension techniques¹⁰⁸ also result in poor reproducibility due to agglomeration and particle

overlaps leading to non-uniform *MNP* inter-particle gaps. The resulting spatially non-uniform plasmonic modes excited in these non-ordered gaps, with different EM near-field strength and frequency limits the feasibility of utilizing these samples for reliable, robust, large-area SERS sensing as well as studying non-linear Raman scattering processes and SERS surface selection rules. Giant EM-nearfield enhancement was observed on these fabricated samples, as the excited collective plasmon-polariton modes “hybridize” due to interaction between the *MNP* arrays with inter-particle spacing $S < r$, where r is the radius of the *MNP*. The anisotropically ordered arrays were highly specific to light attributes such as polarization and wavelength and exhibited an anisotropic plasmonic effect. Polarized and wavelength scanned SERS measurements performed on it revealed a dichroic SERS anisotropy. These distinct dichroic anisotropies were compared and studied for SERS excitation at both super and sub-radiant collective plasmon mode frequencies. This analysis on ordered *MNP* arrays with ultra-small inter-particle gaps $S < r$ highlighted the roles of S and *MNP ordering* in the SERS enhancement of an investigated analyte. The performed experimental studies are pivotal for designing SERS substrates with very small inter-particle gaps, as they generate a large number of intense and well-distributed SERS hotspots in real space.

However, for metal deposited above the percolation threshold thickness, laterally continuous periodic metal films which can support “propagating” surface plasmon polariton (SPPs) modes are formed. These structures supporting delocalized SPP modes also have a diverse range of applications such as *on-chip communications*¹⁰⁹, *waveguides*¹¹⁰, *THz devices*¹¹¹ and in increasing the spatial resolution of *scanning near field microscopy (SNOM)*¹¹² apart from SERS sensing. For non-isotropic analytes such as phenyl-thiolates (*PT*) adsorbed on metal surfaces as used in this study, the polarization and strength of the enhanced electric field components on the surface influences its relative Raman peak intensities based on the molecule’s Raman polarizability tensor (α)⁶⁷. “Surface selection rules” based on varying Raman peak intensities in SERS for probe molecules adsorbed on surface of metal was proposed in Refs^{113,114}. Polarized SERS performed on these SPP supporting samples and the analysis of their ratio of relative Raman intensities was utilized to predict the orientation of adsorbed *PT* molecules on the surface. These percolated anisotropic samples supported propagating near-infrared SPPs with the generation of large electric field components parallel and perpendicular to the surface based on their spatial corrugation vector k_x spatial corrugation. Further, the corrugation-induced plasmonic anisotropy and adsorbed molecular vibration – polariton interaction was investigated. SPPs excited in these percolated films have near-field in NIR ranges which exerts a large molecule dipole oscillator strength with reduced photo-induced disadvantages¹¹⁵ such as charge transfer and interference background signal in spectra. This makes these substrates suitable for the study of molecular vibrations – polariton interaction¹¹⁵⁻¹¹⁷. Further, molecular emitters on the surface of periodic metal nanostructures couple to the nearfield SPP mode and re-radiate their energy as Bragg scattered light, this has a promising scope due to its applicative relevance in developing molecule based emissive devices such as *OLED (Organic Light Emitting Diode)*¹¹⁸ and *molecular dye laser*¹¹⁹. Finally, this study sheds light on the dependence of propagating SPP modes surface field orientations in the enhancement of Raman vibration scattering of both diagonal and non-diagonal components of α of a molecule adsorbed on corrugated plasmonic surface.

These studies on percolated and non-percolated Au metal films validated the EM nearfield mechanism of SERS and also provided understanding for optimizing excitation light attributes such as polarization and wavelength in SERS sensing. Finally, the positives and drawbacks of the fabricated samples in SERS application are discussed.

1.2. Thesis outline

The structure of this thesis is as follows:

Chapter 1 introduces the main theoretical concepts and fundamentals required for the experimental methods and discussions presented in the thesis. First, I will state the definition and structural differentiation of percolated and non-percolated ultrathin metal films. Then, I will introduce the fundamental Maxwell's equations of EM waves to understand the behavior of light in plasmonic systems. The Drude model of a free-electron gas in a metal is derived to model the behavior of plasmas in metals and conditions for the formation of plasmon polaritons during light-matter interaction in ultrathin Au metal films are explored. Further, the interaction and hybridization between two plasmonic modes their spatial and temporal properties and an anisotropic plasmonic effect resulting due to it are presented. The theory of non-radiative decay of plasmons through the excitation of charge carriers and their relaxation is presented and introduced. Finally, the theoretical background of Raman scattering effect and the mechanism of surface enhanced Raman scattering (SERS) are discussed.

Chapter 2 describes the experimental techniques used throughout this thesis. The fundamentals, instrumentation, operation and parameters of the fabrication techniques used in the thesis are presented. Characterization instruments such as atomic force microscope, UV vis spectrometer, ellipsometer, transient absorption spectrometer and Raman spectrometer their working and principle are described. Including the instrumentation setup and parameters used in polarized and wavelength scanned optical measurements. Next, some of the theoretical simulation methods such as finite integration method and finite-difference time-domain (FDTD) methods which were used in the studies are presented and discussed.

Chapter 3 This chapter presents and discusses the plasmonic properties of the fabricated non-percolated, anisotropic metal films on corrugated sapphire templates. The structure of the fabricated non-percolated Au film on corrugated sapphire substrates is analyzed and discussed. Polarized steady state and transient absorption spectra are compared and interpreted, the excitation of collective plasmon modes through hybridization is discussed. The reason for the anisotropic plasmonic effect in these samples is interpreted and explored. Their spatial and temporal features are studied and discussed by EM simulations.

Chapter 4 This chapter presents and discusses the plasmonic properties of the percolated, anisotropic Au films deposited on corrugated sapphire templates. The structure of the fabricated percolated Au film on corrugated sapphire substrates especially their post and pre deposition annealing process is analyzed and discussed in detailed. The polarized spectroscopic results are interpreted. The conditions for exciting propagating surface plasmon polaritons are studied through plotting dispersion curves and modelling EM nearfield distributions. Finally, the reason for the anisotropic plasmonic effect in these samples are interpreted and explored.

Chapter 5 This chapter discusses the Raman spectroscopy measurements performed on the ultrathin Au films deposited on corrugated sapphire templates. Through polarized and wavelength scanned Raman measurements SERS resulting from both the super and sub-radiant collective plasmon modes on non-percolated ultrathin Au films are presented. The dependence of inter-particle spacing and metal nanoparticle ordering in the SERS enhancement of phenyl thiolate probe analytes are discussed and presented. Further, the SERS enhancements due to propagating surface plasmon polariton modes excited on percolated ultrathin films are presented. A resulting dichroic SERS intensities of Raman vibrational modes of different Raman polarizability tensors are investigated and reported. The polarized and wavelength scanned Raman results are utilized to validate the EM nearfield mechanism SERS.

Chapter 6 the experimental findings and conclusions of the previous chapters are summarized and future outlooks of the thesis are presented. Possible applications and drawbacks of the fabricated samples are discussed.

Theory and fundamentals

1.3. Structure formation of ultrathin metal films - Theory

Real structure of a deposited metal layer is an important parameter which determines the physical, optical, and electronic properties of an ultrathin metal film. It is necessary to understand the fundamentals of ultrathin film structure formation, as engineering and reproducing optical properties of an ultrathin film becomes a severe constrain during deposition processes. In nature, a solid structure most certainly has defects both intrinsic and extrinsic. Deposition of ultrathin metal films by electron beam evaporation process is a non-equilibrium process with impurity atoms of residual gas molecules in the deposition chamber contributing to extrinsic defects¹²⁰. These defects play an important role in the structure formation of ultrathin films during deposition processes and thus ultimately influencing its physical properties, interaction with light and its subsequent optoelectronic properties^{120,121}.

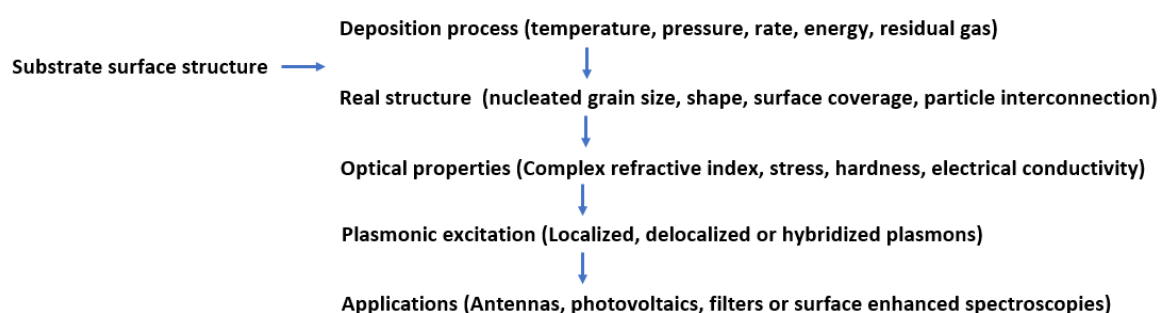


Figure 1.4 Qualitative illustration of factors that control ultrathin film structure formation and their resulting properties and application.

This comparatively makes the number of defects in ultrathin films fabricated by electron beam evaporation process ~ 5 orders of magnitude larger than bulk metal films¹²⁰. As a result, ultrathin metal films with $t \leq 10\text{nm}$ fabricated for optical grade applications through electron beam evaporation are usually porous with interconnected networks or polycrystalline in structure. These ultrathin films exhibit distinct optical and electronic properties from their bulk

counterparts¹²¹. During deposition ultrathin films have a metastable non-equilibrium structural phase where their real structure tends to change whenever the energy in the deposition system changes. Thus, real structure formation is linked by both the deposition parameters and the type of ultrathin metals. In order to tune the optical properties of ultrathin films dependent on its real structure, the mechanism of thin film structure formations based on diffusion and adsorption processes such as: nucleation, coalescence and ensuing thickness growth should be studied and understood by optimizing deposition parameters^{120,122}. Figure 1.4 shows the qualitative illustration of factors that control ultrathin film structure formation, their resulting properties and application that can be realized by optimizing the deposition parameters.

Growth mechanism.

(A) Nucleation

The initial formation of ultrathin metal films undergoes heterogeneous nucleation when deposited by electron beam evaporation. Both the atoms of the evaporated metal as vapor and the atoms on the substrate different that of the vapor contribute to the condensation of metal adatoms on the surface¹²⁰. The vapor pressure of the evaporated metal from a target source with temperature T can be assigned as p_v , and the equilibrium vapor pressure on the substrate with temperature T_s as p_s .

Subsequent nucleation takes place at usually high supersaturations S_s

$$\text{Where, } S_s = \frac{p_v}{p_s} \quad (1)$$

The electron beam deposition rate R can be related to p_v as

$$R = \frac{p_v}{(2\pi m_m KT)^{1/2}} \quad (2)$$

m_m = atomic mass of the deposited metal atom, K = Boltzmann constant and T = temperature of the evaporation source.

Apart from the pressure dependent supersaturations S_s which initiates the nucleation, the surface energies of the ultrathin metal film ϑ_{ut} and the substrate ϑ_{st} together with their interaction energy ϑ_* also influences the further growth mechanism of the ultrathin film based on the Young's equation 2.1¹²⁰.

$$\vartheta_{st} = \vartheta_* + \vartheta_{ut} \cos \varphi \quad (2.1)$$

where the wetting angle φ of the condensating nuclei on the substrate is described by the Young's equation 2.1.

- (i) Layer by layer method - where the ultrathin metal nuclei grow on top of the other as a 2-Dimensional layer. Here the interaction between the ultrathin film atoms and the substrate atoms is greater when compared to the interaction between their adjacent metal atoms, as $\vartheta_{st} > \vartheta_* + \vartheta_{ut}$ and subsequently ($\varphi = 0$).
- (ii) Metal islands – where the ultrathin metal nuclei's grow as 3-Dimensional islands. Here the interaction between the ultrathin films with their adjacent metal nuclei's is

more efficient than the interaction with the substrate atoms, as $\vartheta_{st} < \vartheta_* + \vartheta_{ut}$ and subsequently ($\varphi > 0$).

- (iii) Whereas, initial monolayer layer growth and subsequent island growth occurs when ϑ_* increases as films thickness t grows^{120,122}.

(B) Coalescence

Coalescence is the process of increase in surface coverage f of the metal nuclei, until adjacent metal grains interconnect to form a connected metal network¹²³. Whereas separated crystal grains in a 2-dimensional polycrystalline film can also coalesce to form connected crystal network with reduced grain boundaries in the 2D polycrystalline film. In this study a structural coalescence process (fusion of individual metal islands) for increasing deposition thickness t influenced by both the factors of supersaturation and surface energies determines the diffusion of the islands, transporting them to open gaps to form connected metal networks^{122,124}.

The thickness t at which these islands form a continuous network of metal is known as the percolation threshold f_c . To percolate means to pass or to cause to pass through a porous material where connective paths appear to facilitate charge delocalization. Figure 1.5 shows the schematics of the temporal coalescence of metal nuclei to achieve structural percolation. This transition plays an important role in determining the optical and electrical properties of ultrathin films as the films transforms from an insulative to a conductive phase^{122,125}.

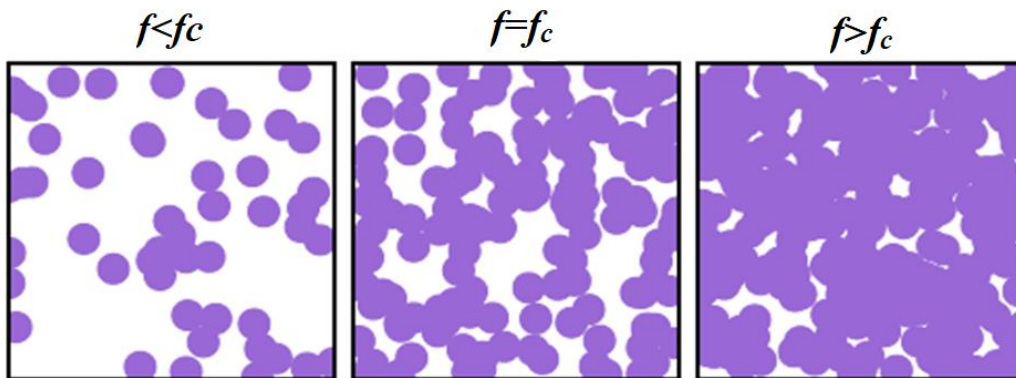


Figure 1.5. Illustration of a model showing the temporal coalescence of metal nuclei towards percolation (Adapted with permission¹²²).

(C) Thickness growth

The mean percolation threshold thickness t for Au ranges from 4 to 12nm depending upon the film substrate, chamber pressure and other deposition parameters. However considerable percentage of light in the visible region is reflected by the percolated metals only at very large film thickness $t \gg 50\text{nm}$ transitioning as mirrors¹²¹. Further, the structure formation of Au ultrathin films for increasing thickness $t \gg 12\text{nm}$ are further determined by the substrate temperature T_s and melting point of metal T_m . Thus, different structure formation processes can occur based on T_s/T_m on increasing metal thickness well above percolation threshold and is beyond the scope of the experiments performed in this thesis^{120,126}.

These growth models of ultrathin metal films discussed above show that fabrication of ultrathin metal films by electron beam evaporation, is a process influenced by a considerable amount of residual gas molecules in the deposition chamber influencing adatom diffusion processes, and is a poor technique to acquire homogeneous phase ultrathin metal films. Due to this reason electron beam evaporation operating in ultra-high vacuum conditions ($\sim 10^{-10}$ mbar) was utilized to deposit ultrathin films for plasmonic applications to improve optical grade quality and reproducibility.

1.3.1. Non-percolated ultrathin Au films

Noble metal such as Au ultrathin films deposited on dielectric substrates follow the Volmer-Webber growth mechanism (as metal islands) due to $\vartheta_{st} < \vartheta_* + \vartheta_{ut}$ ^{127,120}. They nucleate as isolated islands at metal thickness t well below the percolation threshold at low deposition rates. This is due the poor wettability of metals evaporated on miscut sapphire substrates. These deposited ultrathin films are in an insulating phase as a result of the very low metal surface coverage f ^{120,122}. At Au thickness t below and near the metal percolation threshold these films exhibit anomalous optical constants when compared to the bulk metal¹²⁸. The reason for this, is the real structure of the non-percolated ultrathin metal films as metal islands, as discussed. Figure 1.6 shows the SEM images of a ~ 6 nm thick of non-percolated Au film deposited on corrugated sapphire template with template period $P \approx d$ and $P > d$, where d is the diameter of the nucleating metal grain. The interaction of these particles with light are governed by their surface plasmon resonances, exciting a localized plasmon polariton mode. This phenomenon due to the non-percolated island films will be discussed in detail in section 1.4.2.

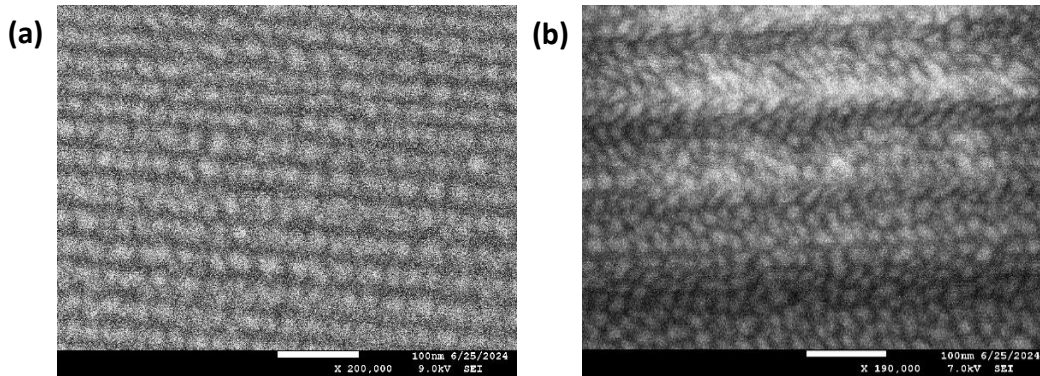


Figure 1.6. SEM images of a ~ 6 nm thick non-percolated Au film deposited on corrugated sapphire template with (a). $P \approx d$ and (b). $P \geq d$. The SEM images have low resolution and contrast²¹⁸. This is because the sapphire is a highly insulating material with a large dielectric constant. *Its poor electrical conductivity led to significant charging effects during SEM imaging, limiting the feasibility of obtaining high-quality images* (the white scale bar in the images represents 100nm).

1.3.2. Percolated ultrathin Au films

Ultrathin films with thickness at the percolation threshold f_c exhibit a structure of connected networks. The percolation threshold in metal films is more precisely defined as the

concentration of metal islands surface coverage f where current can flow from one edge of the sample to the other^{120,122}. Figure 1.7. shows the SEM image of $\sim 10\text{nm}$ thick Au deposited on corrugated sapphire templates exhibiting connected network of percolated ultrathin film structure. It can be observed that the resolution and contrast of the SEM image in Figure 1.7. improves when compared to Figure 1.6. due to the increased film connectivity facilitating electric conductance across the percolated Au layer. This resulted in a reduced charging effect in the sample when compared to non-percolated films deposited on sapphire which limited the resolution and contrast of SEM image during measurement. The threshold transition of this insulative to conductive phase is similar to phase transitions due to temperature, where at a critical temperature the system changes from insulator to polycrystalline or crystalline material.

Whereas, here the phase transition is due to the geometrical feature-based transition to a conductive phase¹²⁵ due to their interconnection as metal networks. After this transition the ultrathin film undergoes a process known as hole filling for increasing deposition t till the channels in the percolated network are completely filled and the surface coverage can be considered as $f = 1$ acting as an effective mirror¹²⁰.

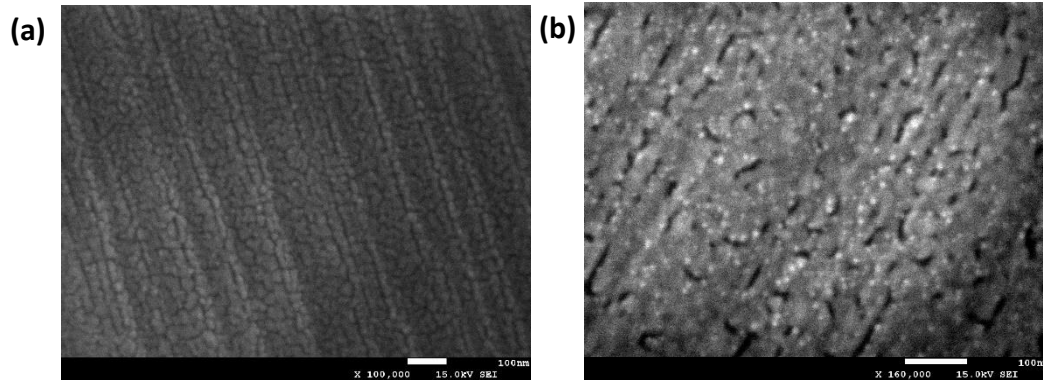


Figure 1.7 (a), (b). SEM image of a $\sim 10\text{nm}$ thick of percolated Au film deposited on corrugated sapphire templates with period $P \geq d$. (the white scale bar in the images represents 100nm)²¹⁸.

1.3.3. De-wetting pathway of ultrathin metal films

The real structure of ultrathin films such as size, distribution of metal islands, voids and metal interconnection networks can be also optimized by thermal annealing process¹²⁹. Post deposition annealing processes are usually carried out to tune the properties of the fabricated ultrathin metal films. The temperature induced de-wetting process depends on the morphology of the ultrathin films, and proceeds as formation of pinhole like voids, their broadening and expansions. These de-wetting pathways take diverse routes depending on the mass of the deposited just percolated film¹³⁰⁻¹³². For films with $t \leq 12\text{nm}$ faster de-wetting than in-plane grain growth is observed as large number of voids are present at both the metal/ambient interface and the metal/substrate interface, whereas for films with thickness $t \geq 12\text{nm}$ the voids at metal/substrate interface are closed and do not protrude throughout the film, here a faster kinetics of in-plane grain growth driven by the reduction in grain boundary energy is observed when compared to film de-wetting. Figure 1.8. shows the schematics of in-situ time dependent transmission measurements for a nominal Au film of $t \sim 10\text{ nm}$ deposited on glass slides and

annealed at a high temperature of $T \sim 550^\circ\text{C}$ ¹²⁹, it shows the trend of time dependent kinetics of structure formation during high temperature annealing.

Subsequently, for just percolated Au films of $10\text{ nm} < t < 12\text{ nm}$ deposited on sapphire dielectrics under UHV conditions as used in this thesis, a low temperature annealing $T \leq 300^\circ\text{C}$ can improve the metal networks film connectivity before the film de-percolates at longer annealing time¹³⁰. As for higher temperature post deposition annealing process $T \geq 600^\circ\text{C}$ at a longer time results in the formation of large isolated metal island depending of the thickness of the deposited metal and the corrugated template periods. The thermal and wetting properties of the underlying template influence the kinetics of the thermal de-wetting processes considerably. Robust dielectric substrates like sapphire with high melting point are beneficial to study thermally controlled plasmonic metal nanostructures for optoelectronic applications¹³²

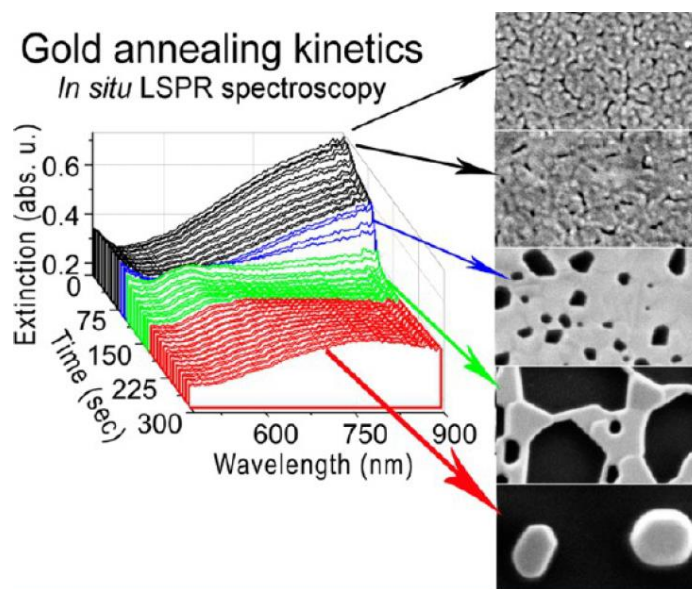


Figure 1.8. Schematics of in-situ transmission measurements exhibiting the trend of time dependent kinetics of structure formation for nominal Au $t \sim 10\text{ nm}$ deposited on glass slides and annealed at high temperature $T \sim 550^\circ\text{C}$. (Adapted with permission¹²⁹).

1.4 Optical properties of ultrathin metal films - Theory

The optical properties of ultrathin films are different than that of their bulk form, as ultrathin metal films in the dimension of nanoscale are governed by quantum effects and exhibit peculiar complex optical constants^{128,133}. Investigating optical properties of ultrathin metals is the analysis of light-metal interactions, and studying its subsequent responses such as reflection, transmission, absorption, scattering, refraction or diffraction spectra. The fundamentals and theoretical concepts to understand light-metal interactions on percolated and non-percolated metal films, the types of plasmon polariton modes excited on them, their hybridization and relaxation processes are presented.

1.4.1. Maxwell's equation of EM waves and Drude-Lorentz model of free electron gas in metals

Maxwell's equations describe the behavior of electric and magnetic fields (light) and their response when they interact with polarizable media (matter)⁵.

$$\nabla \cdot \mathbf{D} = \rho_f, \text{ where } \mathbf{D} = \epsilon \mathbf{E} \text{ - Gauss law for electricity} \quad (3)$$

$$\nabla \cdot \mathbf{B} = 0 \text{ - Gauss law for magnetism} \quad (4)$$

$$\nabla \times \mathbf{E} = - \frac{\partial \mathbf{B}}{\partial t} \text{ - Faradays law of induction} \quad (5)$$

$$\nabla \times \mathbf{H} = \mathbf{J} + \frac{\partial \mathbf{D}}{\partial t} \text{ - Amperes law} \quad (6)$$

\mathbf{D} = Electric flux density, \mathbf{E} = Electric field vector, ρ = charge density

\mathbf{B} = Electric flux density \mathbf{M} = Magnetic field vector, \mathbf{J} = current density

“From a long view of the history of mankind, seen from, say, ten thousand years from now, there can be little doubt that the most significant event of the 19th century will be judged as Maxwell's discovery of the laws of electrodynamics. The American Civil War will pale into provincial insignificance in comparison with this important scientific event of the same decade.”

- Richard Feynman

Solving the Maxwell's equations in different metallic medium portraying percolated and non-percolated ultrathin film structures is performed in order to model their optical responses. From the curl equations 5 and 6, the wave equation of an electric field's response when it interacts with polarizable medium is obtained as:

$$\nabla^2 E(r_p, t) = \frac{n^2}{c^2} \frac{\partial^2 E(r_p, t)}{\partial t^2} + \frac{\partial^2 P_{ind}(r_p, t)}{\partial t^2} + \frac{\partial J(r_p, t)}{\partial t} \quad (7)$$

Where P_{ind} = Polarization of the medium, n = refractive index and c = speed of light, r_p = position vector.

The polarization or current density terms in the equation 7 can be neglected or included based on the type of medium with which the incident electric field interacts¹³⁴⁻¹³⁶. Whereas, wave equation for magnetic field is not solved and presented here as the magnetization is negligible for noble metals such as Au at optical frequencies as used in the experiments in this thesis. The wave equation associated with the electric field in a one-dimension case and its solution in exponential form using Euler's formula is:

$$\frac{\partial^2 E}{\partial x^2} = \frac{n^2}{c^2} \frac{\partial^2 E}{\partial t^2} \quad (8)$$

$$E_{(x,t)} = E_0 \exp(ikx - i\omega t) \quad (9)$$

Subsequently its frequency depended dispersion relation describing the wavevector k in a medium can be solved from equation 8 and 9 as:

$k_o = \pm \frac{\omega}{c}$, $k = \pm \frac{\omega}{c} \tilde{n}$, where \tilde{n} is complex refractive index for absorbing materials such as metals

$$k = \pm \frac{\omega}{c} (n' + in'') = \pm (\beta + i \frac{\alpha_m}{2}) \quad (10)$$

where, $\beta = k_o n'$ = propagation constant and $\alpha_m = 2k_o n''$ = attenuation constant¹³⁵.

Subsequently, the complex refractive index of metals can be related to its complex permittivity as:

$$\tilde{n} = (n' + in'') = (n + i\kappa) \quad (10.1)$$

$$\epsilon_1 = n^2 - \kappa^2 \text{ and } \epsilon_2 = 2n\kappa \quad (10.2)$$

Now, assuming that the free electron with a mass m_o and charge e behaves as a harmonic oscillator coupled to the ions and driven by the incident electric field as in Figure 1.9. in order to model the ϵ of metals.

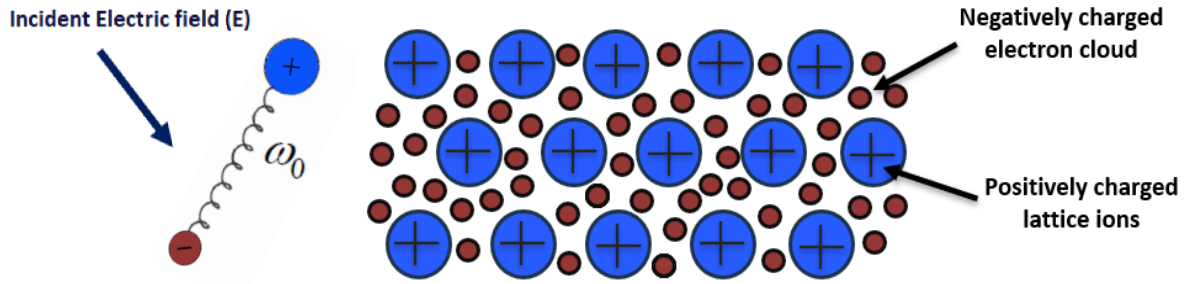


Figure 1.9. Schematics exhibiting the Drude-Lorentz model of free electron gas in metals with positively charged ions contributing to restoring force.

The response of metals to their interaction with light can be modelled by solving the equation of motion for the oscillating electrons in a free electron gas model with ionic cores, as in equation 11: *note: In this section 1.4.1. the symbol t is designated as time.*

$$m_o \frac{\partial^2 x}{\partial t^2} + m_o \gamma \frac{\partial x}{\partial t} + m_o \omega_o x = - eE \quad (11)$$

Where γ is the damping factor. The displacement x of the electron is given as $x(t) = x_o \exp(-i\omega t)$ when the driving force related to the incident electric field E_o is given by $E(t) = E_o \exp(-i\omega t)$.

$x_o = \frac{-eE_o/m_o}{\omega_o^2 - \omega^2 - i\gamma\omega}$ can be substituted to obtain the value of displacement x of the oscillating electron^{135,136}. Subsequently, the polarization P_{ind} (macroscopic dipole moment) for a N number of oscillating electrons in the metal can be given as:

$$P_{ind} = - N e x(t) = \frac{Ne^2 E/m}{\omega_o^2 - \omega^2 - i\gamma\omega} \quad (12)$$

The electric field displacement D resulting due to this macroscopic polarization P_{ind} can be written as $D = \epsilon_o E + P_{ind} = \epsilon_o \epsilon_r E$, where, $\epsilon_r(\omega) = (1 + \chi)$.

This gives the relative permittivity ϵ_r of the metals as:

$$\epsilon_r(\omega) = (1 + \chi) + \left(\frac{\omega_p^2}{\omega_o^2 - \omega^2 - i\gamma\omega} \right) \quad (12.1)$$

$\omega_p = \sqrt{\frac{Ne^2}{m \epsilon_o}}$, where ω_p is the electrons bulk plasma oscillation frequency in metals^{135,137,138}, and χ is the electric susceptibility.

Here, the first term in equation 12.1. is related to the background permittivity intrinsic to the properties of the type of metal and the second term to the plasmon resonance. For ($\omega \ll \omega_p$) in the infrared ranges, the restoring force $\omega_o = 0$ as the free electrons in metals follow the applied incident field and its permittivity can be approximated as:

$$\epsilon_{\text{free electrons}}(\omega) = 1 - \frac{\omega_p^2}{\omega^2 + i\gamma\omega} \quad (12.2), \text{ at } \epsilon(\infty) \text{ when the term related to the background permittivity is considered as 1.}$$

And, subsequently the real and imaginary term of the permittivity^{135,139} can be written as:

$$\epsilon_{\text{free electrons}}(\omega) = \text{Re} \left(\epsilon(\infty) - \frac{\omega_p^2}{\omega^2 + \gamma^2} \right) + \text{Im} \left(\frac{i\omega_p^2 \gamma}{\omega(\omega^2 + \gamma^2)} \right) \quad (13)$$

Figure 1.10. shows the graph plotted from the calculated real and imaginary part of the permittivity ϵ for gold based on equation 13. according to the free electron model, for Au metal constants: ($\omega_p = 13.8 \cdot 10^{15} \text{ s}^{-1}$, $\gamma = 1.075 \cdot 10^{14} \text{ s}^{-1}$ and $\omega_o = 0$).

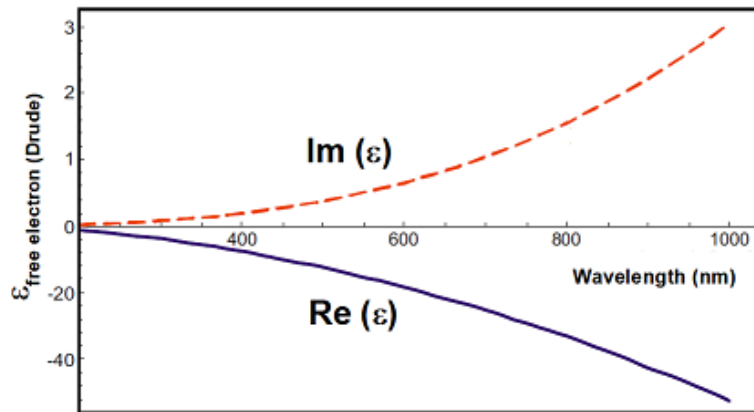


Figure 1.10. Graph plotted from the calculated real and imaginary part of the permittivity ϵ for gold according to equation 13 based on the free electron model with Au metal constants ($\omega_p = 13.8 \cdot 10^{15} \text{ s}^{-1}$, $\gamma = 1.075 \cdot 10^{14} \text{ s}^{-1}$ and $\omega_o = 0$)¹⁴⁰. The blue solid line represents the real part of $\epsilon_{\text{free electrons}}$, the red, dashed line represents the imaginary part of $\epsilon_{\text{free electrons}}$. (Adapted with permission¹⁴⁰).

Subsequently, for UV-vis frequencies the higher energy of the incident field can excite the inter-band lying bound electrons in the metal which includes additional terms related to the binding force, here the restoring force becomes $\omega_o \neq 0$ subsequently altering and contributing to the permittivity^{135,140} as:

$$\epsilon_{\text{bound}}(\omega) = \epsilon_r'(\omega) + i\epsilon_r''(\omega) = \epsilon(\infty) + \frac{\tilde{\omega}_p^2}{\omega_o^2 - \omega^2 - i\gamma\omega} \quad (13.1)$$

Where, $\tilde{\omega}_p = \sqrt{\frac{N e^2}{m \epsilon_0}}$ with N being density of bound electrons and $\omega_o = \sqrt{\frac{l}{m_e}}$, l = spring constant due to electrons bound to the ionic core.

The real and imaginary term^{135,140} of the $\epsilon_{bound}(\omega)$ can be written as

$$\epsilon_{bound}(\omega) = \text{Re}(\epsilon(\omega)) + \frac{\tilde{\omega}_p^2(\omega_o^2 + \omega^2)}{(\omega_o^2 + \omega^2)^2 + \gamma^2 \omega^2} + \text{Im}\left(\frac{i \tilde{\omega}_p^2 \gamma}{(\omega_o^2 + \omega^2)^2 + \gamma^2 \omega^2}\right) \quad (14)$$

Figure 1.11. shows the graph plotted from the calculated real and imaginary part of the permittivity ϵ for gold according to equation 14. based on the Lorentz model for Au metal constants ($\omega_p = 45.10 \cdot 10^{14} \text{ s}^{-1}$, $\gamma = 8.35 \cdot 10^{16} \text{ s}^{-1}$ and $\omega_o = 2\pi c/\lambda$, $\lambda = 450 \text{ nm}$)¹⁴⁰. The permittivity of Au metal in the spectral region of above $\sim 500 \text{ nm}$ wavelength can be approximated moreover by considering the sum of both the $\epsilon_{free \text{ electrons}}$ and ϵ_{bound} .

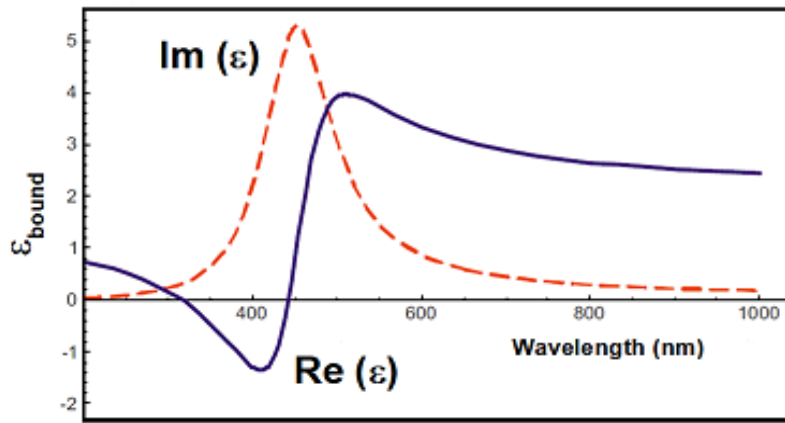


Figure 1.11. Graph plotted from the calculated Real and imaginary part of the permittivity ϵ for gold according to equation 14. based on the Lorentz model with Au metal constants ($\omega_p = 45.10 \cdot 10^{14} \text{ s}^{-1}$, $\gamma = 8.35 \cdot 10^{16} \text{ s}^{-1}$ and $\omega_o = 2\pi c/\lambda$, $\lambda = 450 \text{ nm}$)¹⁴⁰. The blue solid line represents the real part of ϵ_{bound} , the red dashed line represents the imaginary part of ϵ_{bound} (Adapted with permission¹⁴⁰).

Figure 1.12a shows the graph plotted with experimental real and imaginary part of the permittivity ϵ for bulk Au film measured by Johnson and Christy et al¹⁴¹. It can be seen that for wavelength below $\sim 500 \text{ nm}$ the experimental value of imaginary part of the permittivity – (red line in the Figure 1.12a) deviates significantly from the trend of the calculated permittivity curve of Au in Figure 1.12c based on Drude-Lorentz model combining both the equations 13 and 14. This is due to the contribution of further higher inter-band electron transitions which are not considered in the discussed models.

Although the experimental values of their permittivity can be modelled by adding a constant offset which accounts for the additional contribution from these other higher energy transitions for yielding the full metal permittivity^{135,136}. Analysis of the optical properties of

ultrathin films in this thesis can be approximated combining the discussed Drude free electron and Lorentz models based on equation 13. and 14. as the investigation of plasmon excitation and utilization of Raman excitation wavelengths being in the spectral region above 500nm.

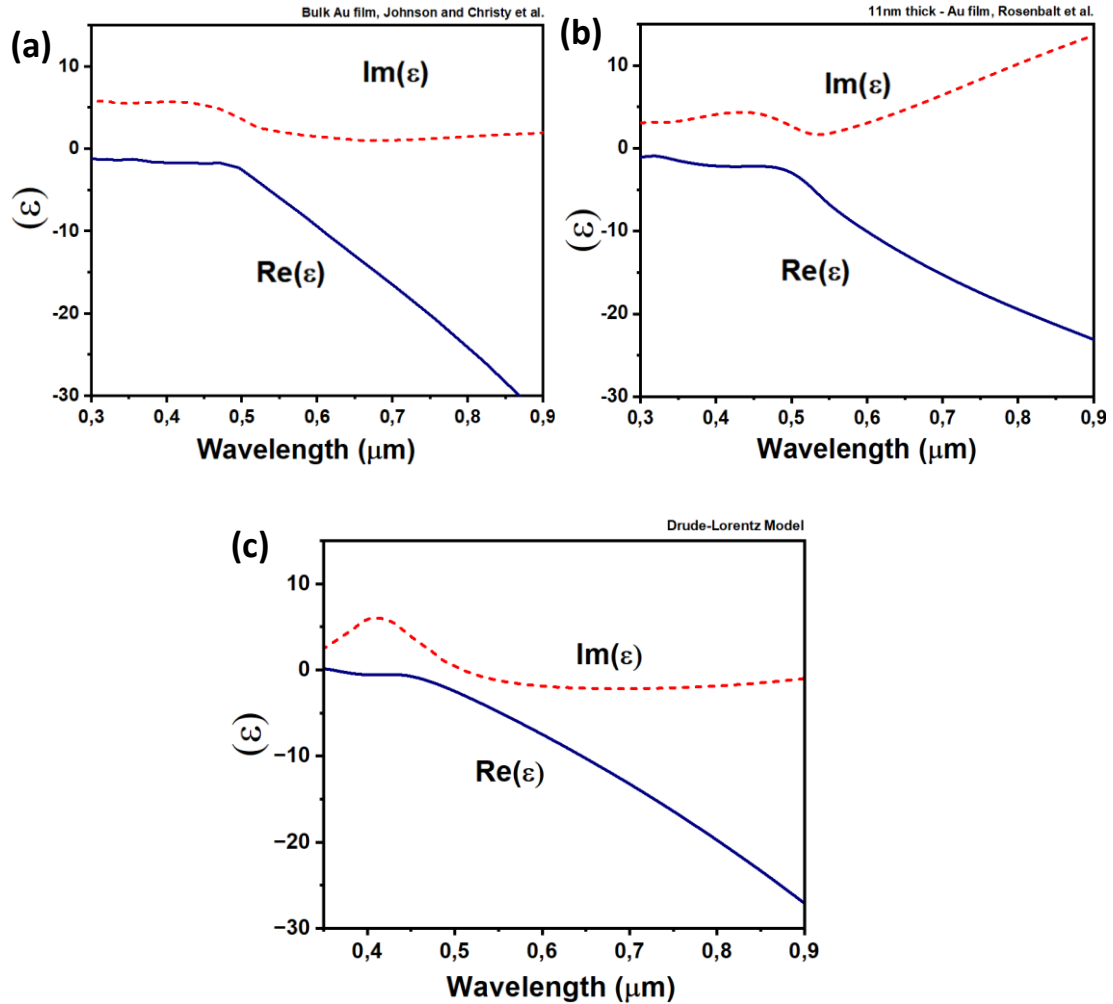


Figure 1.12. (a), Shows the graph plotted with real and imaginary part of the permittivity ϵ of Au metal based on the Drude-Lorentz model combining equation 13 and 14. (b), Shows the graph plotted with experimentally measured real and imaginary part of the permittivity ϵ for bulk Au film by Johnson and Christy et al¹⁴¹. (c), Shows the real and imaginary part of the permittivity ϵ experimentally measured for a 11nm thick Au film by Rosenblatt et al¹⁴². The blue solid line represents the real part of ϵ and the red dashed line represents the imaginary part of ϵ .

1.4.2. Permittivity of ultra-thin metal films at plasmon polariton excitation.

Figure 1.12b. shows the real and imaginary part of the permittivity ϵ experimentally measured by Rosenblatt et al. for a 11nm thick ultrathin Au film, it exhibits permittivity modulation in the optical frequencies when compared to the bulk metal ϵ measured by Johnson and Christy et al.¹⁴¹ in Figure 1.12a. This is due to the excitation of surface plasmon resonances during light matter interaction onto the just percolated Au film of $t \sim 11$ nm with rough interconnected real structure when compared to the bulk metal film, this modulates the effective dielectric function

of the material medium exhibiting modified optical constants when compared to their bulk form¹²⁸. Subsequently for ultra-thin metal films with thickness t below the percolation threshold the film exhibit Au metal island like real structure as discussed in the section 1.3.1. The nucleating Au grains in non-percolated metal films resembles disconnected network of nanoparticles with diameter $d \ll \lambda$ (λ the wavelength of the incident light). The incident field is assumed to be uniform around the metal grain so as the EM phase remains constant over it without any retardation effects, whereas *MNPs* with larger diameters excite higher order plasmon modes due to the retardation effects¹⁴³. So, the polarizability α_{np} of these *MNPs* with $d \ll \lambda$ can be derived based on the quasi-static approximation as electrodynamic calculations are replaced with Laplace electrostatic equations as^{135,139}:

$$\alpha_{np} = 4\pi\epsilon_0^3 \left(\frac{\epsilon_m - \epsilon_d}{\epsilon_m + 2\epsilon_d} \right) \quad (15)$$

where ϵ_m = permittivity of metal and ϵ_d = permittivity of the surrounding dielectric medium

when the denominator in the equation 15 becomes minimum at certain frequencies, the polarizability becomes large so as to give rise to a strong resonance between the collective electron oscillation and the incident EM wave known as localized surface plasmon resonance (LSPR) mode as in Figure 1.13a. For metal nanoparticles with $d \ll \lambda$ as studied in this thesis the induced polarization in the nanoparticle σ_{np} forms a dipolar LSPR mode^{135,140} as in Figure 1.13b. based on the equation 16.

$$\sigma_{np} = 3\epsilon_d \left(\frac{\epsilon_m - \epsilon_d}{\epsilon_m + 2\epsilon_d} \right) E_o \cos \theta_p \quad (16)$$

where θ_p is the polar angle between the incident field and the position vector, E_o is the incident electric field.

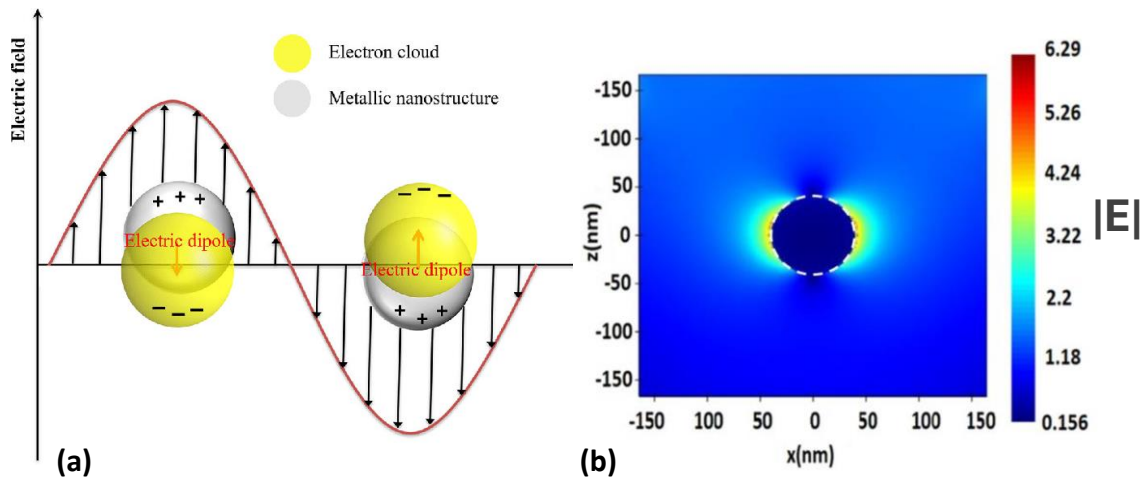


Figure 1.13 (a), Schematic illustration of dipolar LSPR mode for a plasmonic nanosphere with $d \ll \lambda$. (Adapted with permission¹⁴⁴). **(b)** FDTD Simulations exhibiting enhanced electromagnetic nearfield due to the excitation of dipole localized plasmon polariton mode on a 40nm diameter Ag sphere. (Adapted with permission¹⁴⁵).

The localized plasmon mode excitation is a result of the *MNPs* geometrical structure-based modification of effective permittivity apart from the intrinsic-background permittivity of the Au metal, resulting in an induced polarization σ_{np} in the *MNP* when the denominator term in the equation 16. depending on the primitivities of the metal and dielectric becomes minimum at certain frequencies.

From equation 13 substituting the permittivity value of a Drude metal as $\epsilon_m = 1 - \left(\frac{\omega_p^2}{\omega^2}\right)$ when ignoring the term γ due to losses in it to model an ideal Drude metal with ($\gamma \ll \omega$), and the permittivity of surrounding dielectric medium as $\epsilon_d = 1$, the frequency where the denominator term ($\epsilon_m + 2\epsilon_d$) in equation 16 achieves a minimum value of zero can be solved as:

$$\epsilon_m + 2\epsilon_d \rightarrow 1 - \left(\frac{\omega_p^2}{\omega^2}\right) + 2(1) = 0 \quad (16.1)$$

$$\omega^2 = \frac{\omega_p^2}{3} \quad (16.2)$$

As a result, the permittivity ϵ_m dependent maximum induced polarization (frequency of the LSPR modes excitation) in the metal nanoparticle when $\epsilon_d = 1$ can be calculated to be in the frequency range determined by equation 17:

$$\omega_{LSPR} = \frac{\omega_p}{\sqrt{3}} \quad (17)$$

This explains the anomalous optical constants of non-percolated ultrathin metal films governed by the excitation of localized plasmon polaritons. Subsequently, for ultrathin film with thickness above the percolation threshold, the metal layer acts as a connected network of Au grains exhibiting Drude metal characteristics of delocalized free electron gas, in this case the incident light gets reflected (or extincted) due to the trend of its imaginary permittivity at frequencies of $\omega \ll \omega_p$ ($\omega_p \sim 8.5$ eV for Au) as in Figure 1.12b. Although, propagating surface plasmon polariton (SPP) modes can be excited on the metal/dielectric interface^{135,137,140}. This is as a result of the polarized charges induced at the metal/dielectric interface due to the incident electric fields discontinuity along the direction perpendicular to the metal/dielectric mediums with different permittivity's^{140,137}. To derive the conditions for supporting these propagating SPP modes, Maxwells equations are solved for the medium reflecting completely percolated-metal/dielectric interface. The components of EM fields wavevector in a metal k_m and dielectric medium k_d when a field incident on a metal/dielectric interface along the z direction as in Figure 1.14a. is given as:

$$\mathbf{k}_d = (k_{dx}, 0, -k_{dz}) \quad (18)$$

$$\mathbf{k}_m = (k_{mx}, 0, -k_{mz}) \quad (19)$$

From the dispersion relation in equation 10. The sum of the vector components in equation 19. can be written as:

$$k_x^2 + k_{mz}^2 = (n^2 \frac{\omega^2}{c^2}) = \epsilon_m k_o^2$$

$$k_{mz}^2 = \epsilon_m k_o^2 - k_x^2 \quad (20)$$

Equation 20. shows that when the permittivity of metal ϵ_m is negative at certain frequencies, the incident wavevector component k_{mz}^2 in the percolated metal film become imaginary and the wave attenuates inside the metal when assuming that the wave is propagating in the k_x^2

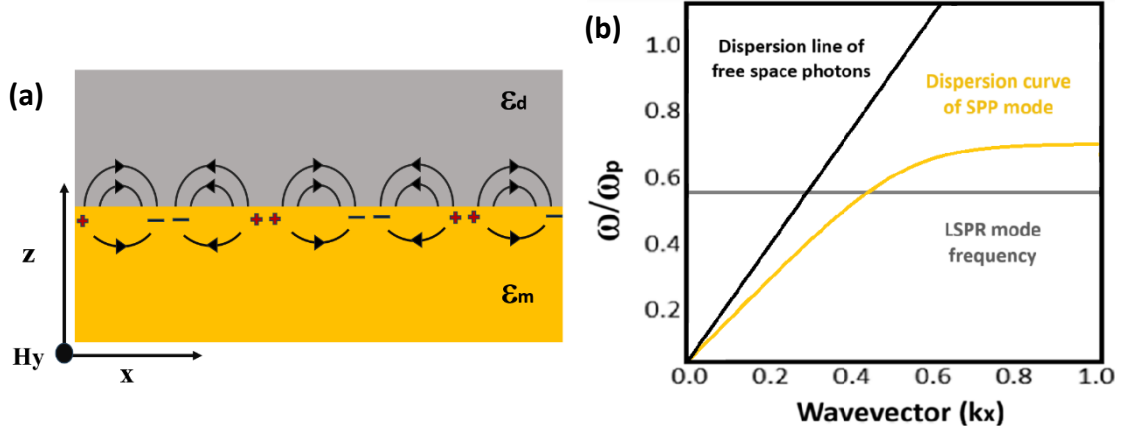


Figure 1.14 (a), Schematic illustration of propagating SPP mode on a metal/dielectric interface with propagation direction along the x direction, the black curved lines with arrows represent the electric field lines and the plus and minus signs represent the charge oscillation at the interface. The permittivity of adjacent regions marked by ϵ_d (dielectric) and ϵ_m (metal). **(b)** Dispersion relation for both an SPP (solid yellow line) and an LSPR (solid grey line) in comparison to the ‘light line’ (solid black line) for photons in free space, with their corresponding equations.

direction^{135,137,140}. Now solving the Maxwell’s equation for the propagation of a wave along the x direction in a metal/dielectric interface using the curl equation 6.^{135,140} : $\nabla \times \mathbf{H} = \mathbf{J} + \frac{\partial \mathbf{D}}{\partial t}$, Since, there are no free flow of charges in the interface, the term current density \mathbf{J} is omitted as:

$$\nabla \times \mathbf{H} = \frac{\partial \mathbf{D}}{\partial t} = -i\omega\epsilon\mathbf{E}$$

For a transverse magnetic (TM) electric field incident on the metal/dielectric interface, the incident TM fields magnetic component $H_y \hat{y}$ in the dielectric as H_{dy} and metal medium as H_{my} can be expressed as:

$$H_{dy} = h_m e^{i k_{dx} x} \cdot e^{-k_{dz} z} \quad (21)$$

$$H_{my} = h_m e^{i k_{mx} x} \cdot e^{-k_{mz} z} \quad (22)$$

Solving the curl equation ($\nabla \times \mathbf{H}$) on the dielectric medium based on equation 21.

$$(\nabla \times \mathbf{H}) = \begin{vmatrix} \hat{x} & \hat{y} & \hat{z} \\ \frac{\partial}{\partial x} & \frac{\partial}{\partial y} & \frac{\partial}{\partial z} \\ 0 & H_y & 0 \end{vmatrix} = -i\omega\epsilon_d \mathbf{E}$$

$$= -\frac{\partial H_y}{\partial z} \hat{x} + \frac{\partial H_y}{\partial x} \hat{z} = -i\omega \varepsilon_d E$$

$$\omega \varepsilon_d E = +ik_{dz} H_{dy} \hat{x} - k_{dx} H_{dy} \hat{z} \quad (23)$$

So, from equation 23 the electric field component in the dielectric E_d can be derived as

$$E_d = \frac{H_{dy}}{\varepsilon_d \omega} (k_{dz} \hat{x} - k_x \hat{z}) \quad (24)$$

And subsequently the electric field component in the metal medium E_m can also be derived from equation 24. based on the field continuity law as¹³⁴.

$$E_m = \frac{H_{dy}}{\varepsilon_m \omega} (-k_{mz} \hat{x} - k_x \hat{z}) \quad (25)$$

This shows that the electric fields components for a surface plasmon polariton are along the x and z directions on the interface as in Figure 1.14a. Based on the complex optical constants and dielectric functions determined in the equations 24 and 25 the below relation in equation 26 should be satisfied at certain frequencies for SPP waves to be excited and to propagate along the x direction^{135,140}.

$$\frac{k_{dz}}{k_{mz}} = \frac{-\varepsilon_d}{\varepsilon_m} \quad (26)$$

The propagation constant $\beta = k_x$ of a SPP excited in the interface and propagates along the x direction can be derived from the equation 26 as:

$$k_x^2 = \left(\frac{\varepsilon_m \varepsilon_d}{\varepsilon_m + \varepsilon_d} \right) k_o^2 \quad (26.1.)$$

A range of propagation constants for possible SPP modes excited on a metal/dielectric interface can be plotted depending on the dispersive permittivity's of the metal/dielectric interface medium to give the SPP dispersion curve as in Figure 1.14b (solid yellow line). Collective electron oscillation of SPP modes (with maximum induced polarization) can be excited at frequencies where the denominator in the dispersion relation ($\varepsilon_m + \varepsilon_d$) in equation 26.1. achieves a minimum value^{135,140,146}.

Similarly, substituting $\varepsilon_m = 1 - \left(\frac{\omega_p^2}{\omega^2} \right)$ and $\varepsilon_d = 1$ in the denominator term ($\varepsilon_m + \varepsilon_d$) of equation 26.1 the frequency where the denominator term ($\varepsilon_m + \varepsilon_d$) in equation 16. achieves a minimum value of zero can be solved as:

$$\varepsilon_m + \varepsilon_d = 0, \rightarrow 1 - \left(\frac{\omega_p^2}{\omega^2} \right) + 1 = 0$$

$$\omega^2 = \frac{\omega_p^2}{2}$$

The frequency of SPP ω_{SPP} when $\varepsilon_m = 1 - \left(\frac{\omega_p^2}{\omega^2} \right)$ and $\varepsilon_d = 1$ can be calculated to be in the

$$\text{range of } \omega_{SPP} = \frac{\omega_p}{\sqrt{2}} \quad (27)$$

Further, the equation expressing the wavevector of the excited SPP mode extending in both the metal and dielectric medium due to its polaritonic nature can also be derived from equation 26. as:

$$k_{mz}^2 = \left(\frac{\varepsilon_m}{\varepsilon_m + \varepsilon_d} \right) k_o^2 \quad (28)$$

$$k_{dz}^2 = \left(\frac{\varepsilon_d}{\varepsilon_m + \varepsilon_d} \right) k_o^2 \quad (29)$$

Since, ε_m is complex for absorbing media such as metals, its wavevectors should be expressed in complex form, where $\beta = k'$ is the real part denoting the propagation constant and $\alpha_m = k''$ which denotes the damping of the SPP due propagation in the interface as already discussed in section 1.4.1.

Here, when $\varepsilon_m + \varepsilon_d$ becomes minimum, the wavevector k_{mz} and k_{dz} in the metal and dielectric medium becomes imaginary as a result of the damping effects in metals based on both collision and non-collision of charges (due to material properties, when including the term γ related to the damping losses in the permittivity of the metals ε_m as in equation 12.2 and 13.1). Further, substituting $\delta = \frac{2\pi}{k}$ in equation 28 and 29., we obtain the penetration depth δ of the respective fields which are evanescent in the metal and dielectric mediums due to the damping losses as^{135,140,146}:

$$\delta_{dz} = \lambda_o \text{Im} \left| \frac{\varepsilon_m + \varepsilon_d}{\varepsilon_d^2} \right|^{1/2} \quad (30) \quad \delta_{mz} = \lambda_o \text{Im} \left| \frac{\varepsilon_m + \varepsilon_d}{\varepsilon_m^2} \right|^{1/2} \quad (31)$$

1.3.5. Plasmon hybridization on ultrathin metal films.

For percolated ultrathin metal films with thickness $t \sim 10\text{nm}$ as studied in this thesis the evanescent field with a penetration depth δ_{mz} of the excited SPP mode in the metal medium can stretch over to the Au metal/template interface to form hybridized symmetric and asymmetric SPP modes known as long range surface plasmon polariton (LRSPP) and short-range surface plasmon polariton (SRSPP)^{146,147} as in Figure 1.15a. For metal thin films with thickness t larger than the penetration depth of the field δ_{mz} in the metal. The SPP excited in the metal/air and metal/substrate interface do not interact however for thinner films with t lesser than δ_{mz} the SPP plasmon modes in the two interfaces hybridize.

The dispersion relation for coupled SPPs excited in an ultrathin metal layer with $t < \delta_{mz}$ and two dielectric interfaces^{146,140} is given as:

$$e^{-2k_{mz}t} = \frac{\left(\frac{k_{zd1}}{\varepsilon_{d1}} + \frac{k_{zm}}{\varepsilon_m} \right) \left(\frac{k_{zd2}}{\varepsilon_{d2}} + \frac{k_{zm}}{\varepsilon_m} \right)}{\left(\frac{k_{zd1}}{\varepsilon_{d1}} - \frac{k_{zm}}{\varepsilon_m} \right) \left(\frac{k_{zd2}}{\varepsilon_{d2}} - \frac{k_{zm}}{\varepsilon_m} \right)} \quad (32), \text{ where } t \text{ is the thickness of the metal thin film.}$$

When t becomes larger than δ_{mz} the exponential term $e^{-2k_{mz}t}$ becomes negligible and the equation reduces to the dispersion relation for SPP in a single interface in equation 26. In case of symmetrical dielectric ε_d layer on both the sides of the metal layer as $\varepsilon_{d2} = \varepsilon_{d1} = \varepsilon_d$. The dispersion relation simplifies as equation 33.

$$e^{-2k_{mz}t} = \left(\frac{\frac{k_{zd} + k_{zm}}{\epsilon_d} + \frac{k_{zm}}{\epsilon_m}}{\frac{k_{zd} - k_{zm}}{\epsilon_d} - \frac{k_{zm}}{\epsilon_m}} \right)^2 \text{ This equation has 2 roots as } \rightarrow e^{-k_{mz}t} = \pm \frac{\left(\frac{k_{zd} + k_{zm}}{\epsilon_d} + \frac{k_{zm}}{\epsilon_m} \right)}{\left(\frac{k_{zd} - k_{zm}}{\epsilon_d} - \frac{k_{zm}}{\epsilon_m} \right)} \quad (33)$$

By rearranging the equation, the dispersion relation can be split into a pair of equations simplified^{146,140,135} as:

$$k_{zd} + \epsilon_d / k_{zm} + \epsilon_m = - \frac{e^{-k_{zm}t} \pm 1}{e^{-k_{zm}t} \pm 1} = \begin{cases} - \frac{\frac{e^{-k_{zm}t}}{2} + \frac{e^{-k_{zm}t}}{2}}{\frac{e^{-k_{zm}t}}{2} - \frac{e^{-k_{zm}t}}{2}} = \coth\left(\frac{k_{zm}t}{2}\right) \\ - \frac{\frac{e^{-k_{zm}t}}{2} - \frac{e^{-k_{zm}t}}{2}}{\frac{e^{-k_{zm}t}}{2} + \frac{e^{-k_{zm}t}}{2}} = \tanh\left(\frac{k_{zm}t}{2}\right) \end{cases}$$

$$\frac{\frac{k_{zd}}{\epsilon_d}}{\frac{k_{zm}}{\epsilon_m}} = \coth\left(\frac{k_{zm}t}{2}\right) \quad (34)$$

$$\frac{\frac{k_{zd}}{\epsilon_d}}{\frac{k_{zm}}{\epsilon_m}} = \tanh\left(\frac{k_{zm}t}{2}\right) \quad (35)$$

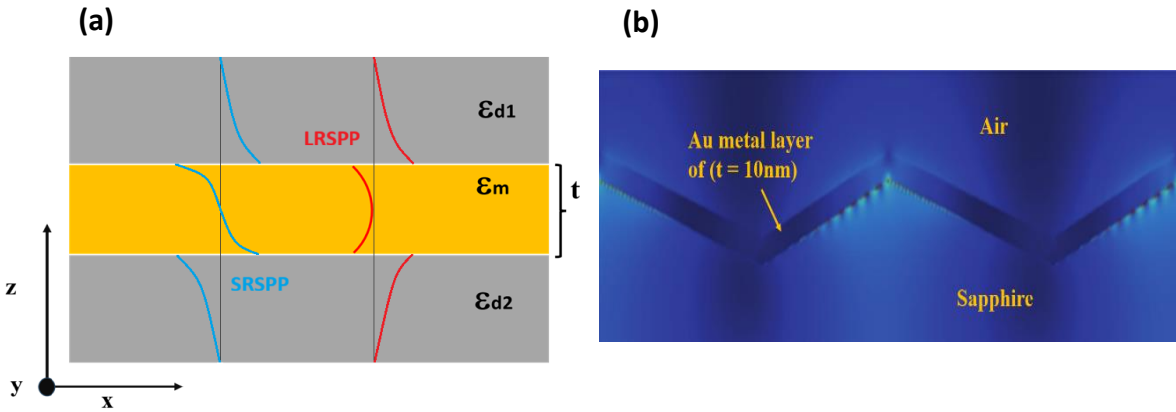


Figure 1.15 (a), Schematic illustrating a symmetric cladding dielectric/metal/dielectric system for metal thickness $t < \delta_{mz}$, the interaction of SPP modes on both the interfaces resulting in a hybridized symmetric and asymmetric modes designated as LRSP (red lines representing the symmetric electric field components along the z and x direction) and SRSP modes (blue lines representing the asymmetric electric field components along the z and x direction). **(b)** FDTD simulations showing the enhanced EM near field on both the interfaces of an asymmetric (air) dielectric/(Au) metal/ (sapphire) dielectric system coupling to form hybridized SPP modes due to $t < \delta_{mz}$.

As the metal thickness t decreases below δ_{mz} the exponential term $e^{-2k_{mz}t}$ in equation 33 is taken into account and the SPP on both the interfaces couple to form hybridized higher frequency symmetric and lower frequency asymmetric modes based on the equation 34 and 35^{146,138,135}.

Subsequently, when analyzing the real structure of non-percolated ultrathin metal films which exhibits heterogeneous Au grain nucleation as 2D arrays. The inter-particle spacing S between the arrays decreases for increasing metal thickness t near to the percolation threshold f_c . This causes the LSPR modes of individual particles to couple and hybridize^{148,149}. These LSPR resonances modes of metal nano-grains and their interaction can be understood based on the theory of molecular hybridization^{150,151}. These plasmon hybridization in metal nanoparticle arrays occur only when the inter-particle spacing $S \leq r$. Subsequently, for $S \geq \lambda_{LSPR}$ where λ_{LSPR} is the localized plasmon wavelength, their localized near field couple through diffraction to form hybridized plasmonic-photonic mode known as surface lattice resonance (SLR)¹⁵². The dependence of collective plasmonic resonance due to hybridization on the interparticle spacing S can be well understood from the Figure 1.16a¹⁵³⁻¹⁵⁵, showcasing the modification of absorption cross-section of *MNP* cluster for incremental increase of S .

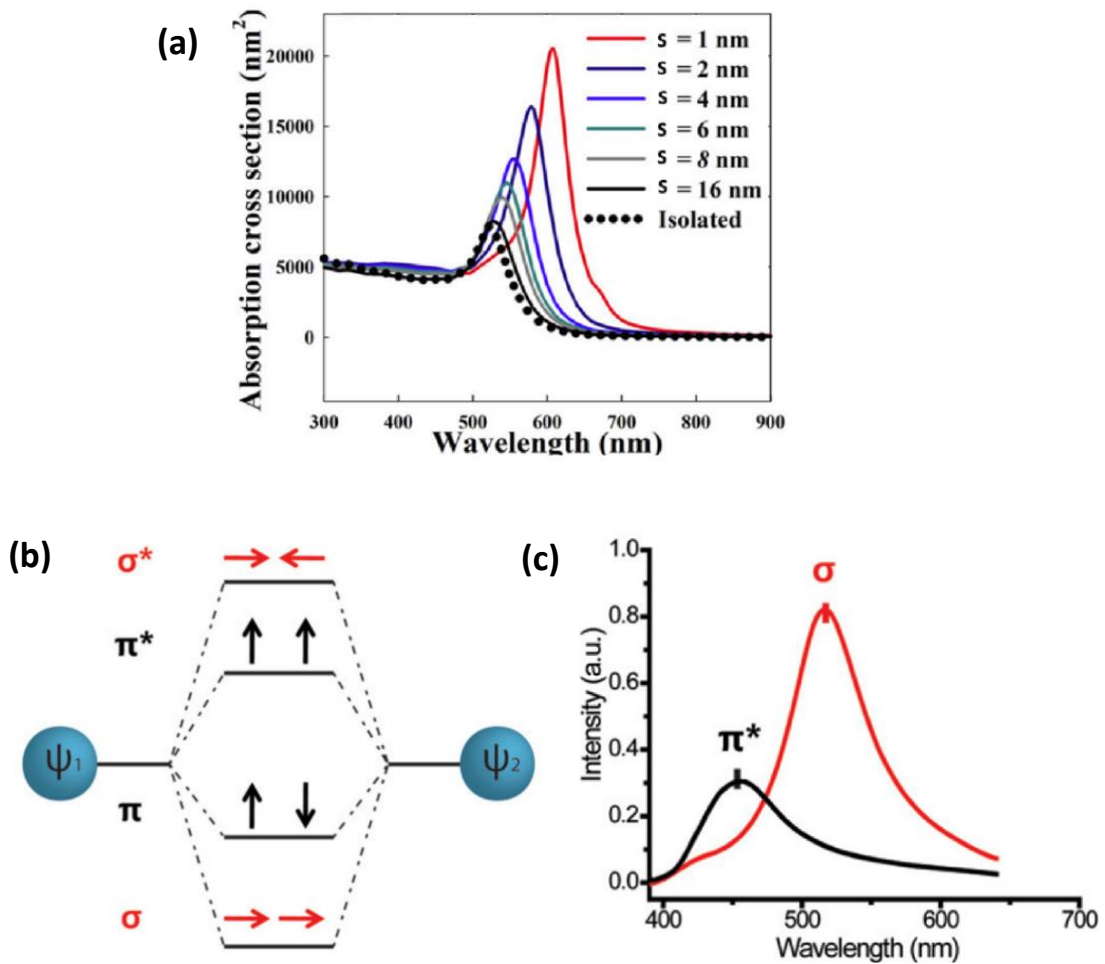


Figure 1.16 (a), Absorption cross-section spectra of a nanoparticle cluster with $N= 19$ for increasing interparticle distance S , the diameter of individual MNP is 20 nm. (Adapted with permission¹⁵³). **(b)**, Hybridization model¹⁴⁸ to explain the coupling of dipole modes in MNP dimer with $d \ll \lambda$, where λ is the incident field wavelength. (Adapted with permission¹⁴⁸). **(c)**, Polarization dependent scattering spectra of the dimer MNP discussed in Figure 1.6b. The red spectra depict the in-phase bonding mode (σ) at longitudinal polarization parallel to the dimer axis and black spectra represents the antibonding mode (π^*) for transverse polarization perpendicular to the dimer axis. (Adapted with permission¹⁴⁸).

The exhibited trend of red shifting and intense absorption cross-section for decreasing S between the particles in the cluster is due to the interaction between the nearfields of the individual $MNPs$ reducing their coulombic restoring force and shifts their resonance to lower frequencies. Whereas, the hybridization in ordered nanoparticle arrays can be understood through the molecular hybridization theory^{148,150}, modelled on a simple symmetric nanoparticle pair (a dimer) under linearly polarized excitation as in Figure 1.16b. The LSPR modes (represented in this current section as $\Psi_{LSPR 1}$ and $\Psi_{LSPR 2}$) of the respective individual nanoparticles in the dimer model in Figure 1.16b., can form in-phase ($\Psi_{LSPR 1} + \Psi_{LSPR 2}$) or out-of-phase ($\Psi_{LSPR 1} - \Psi_{LSPR 2}$) modes during hybridization based on the angle between linearly polarized excitation and dimer axis. For excitation polarization perpendicular to the dimer axis the out-of-phase combination reflects a bonding mode (π) and the in-phase combination an antibonding mode (π^*) are excited. Whereas, for polarization parallel to the dimer axis the out-of-phase combination reflects an antibonding mode (σ^*) and the in-phase combination a bonding mode (σ). as in Figure.1.16b. Only the in-phase bonding mode (σ) at longitudinal polarization and the antibonding mode (π^*) are optically excited and manifested in spectroscopic analysis as in Figure. 1.16c. This is due to the cancellation of oppositely oriented dipoles in the out-of-phase modes on symmetric nanoparticle dimer^{148,150}.

Subsequently, when the number of nanoparticles N_{np} increases along a uni-direction as a one-dimensional array, the plasmon modes excited for polarizations parallel to the array axis is red shifted from the dimer resonance as a result of further reduced coulombic restoring force due to increase in interactions and coupling between the N_{np} number of localized near-fields in the MNP array^{151,154}. The plasmon resonance mode blue shifts for polarizations perpendicular to the 1-dimensional array axis due to the subsequent increase in the coulombic restoring force between the hybridizing nearfields of particles with a larger interparticle spacing S ¹⁵⁶. Whereas, in ultra-thin films deposited on flat sapphire substrates exhibiting disorder due to the random heterogeneous nucleation of Au grains, an isotropic plasmonic effect is observed. These collective plasmon modes excited due to the coupling of LSPR dipole modes between adjacent $MNPs$, have enhanced near field enhancement and ultras-small modal volumes, typically in the order based on the term $\sqrt{rS^3}$, when compared to single nanoparticle λ_{LSPR} modal volume¹⁵⁷. Subsequently, hybridization and their manifestation of higher order modes for increase number of $MNPs$ in the array will be discussed in detailed when interpreting the optical properties on non-percolated metal films deposited on corrugated sapphire exhibiting nucleation of ordered 2-dimensional arrays in chapter 3.

1.4. Ultrafast plasmon relaxation dynamics

The excited plasmon modes on these ultrathin films with confined near-field $E_p(\lambda_p)$ due to the polaritons can also be considered as a nano-optical resonator with the frequency of $\lambda_p = \hbar\omega_p$ of the quantized collective oscillation of electrons, where the intensity in the optical resonator can be expressed by the parameter Q/V , Q is related to the lifetime of the plasmon (quality factor) and V the excited modal volume. For plasmon resonances excited on metals with permittivity $\varepsilon(\omega)$ described as:

$$\varepsilon(\omega) = \varepsilon_r'(\omega) + i\varepsilon_r''(\omega) = 1 - \frac{\omega_p^2}{\omega^2 + i\gamma\omega - \beta_d k^2} \quad (36)$$

where, $i\gamma\omega$ expresses the damping term where $\gamma = \frac{2\pi}{\tau}$, and τ is the initial radiative relaxation time due to charge oscillations and the relaxation time of the non-radiative charge scattering.

The group velocity $v_g = \frac{\partial\omega}{\partial k}$ of the excited collective plasmons and phase velocity $v_p = \frac{\omega}{k}$ of the individual electron (wave) component differs significantly. So additionally, a damping term $\beta_d k^2$ in equation 36. related to the collision-less Landau damping effect is included to consider the losses energy transfer between a single electron and collective electron oscillations (plasmon)¹⁵⁸. This is known as plasmon dephasing due to the phase-velocity mismatch between the single electron and collective oscillation of plasmonic resonance in metals¹⁵⁹. Apart from frequency dependent initial radiative damping on Au nanoparticle which decays quickly after irradiation and subsequent plasmon excitation, non-radiative damping mechanisms such as the above discussed Landau damping within the electron oscillations and its resulting cascade of collision-based electron-electron, electron-phonon and phonon-phonon scattering decays is also a cause for the broadening of the plasmon bandwidth $\Gamma \geq 100nm$ resulting in the decrease of radiative plasmon life time.

The plasmon quality factor $Q = \frac{\omega_{resonance}}{\Gamma}$, in energy units $\Gamma = \frac{2\hbar}{T_{dp}}$

where T_{dp} is the plasmon dephasing time¹³⁵.

The different times scales of these phenomena of the excited plasmon's decay, dephasing and its generated charge carrier's relaxation dynamics are presented in Figure 1.17. It proceeds as initial photon absorption, where the driven oscillation of collective electrons quickly decays through radiative or Landau dephasing within a period ~ 10 femtoseconds (fs). This dephasing results in a generation of hot electrons initially described by a non-thermal distribution below the Fermi level. Subsequently after $\sim 100-500 fs$ through non-radiative relaxation processes such as electron-electron scattering, the occupation thermalizes to a hot Fermi distribution. Further, after $\sim 500 fs$ of laser irradiation the effective dielectric function of the metal/dielectric medium also corresponds to the hot Fermi distribution together with the real structure of the ultrathin film. Studies have reported simulations and calculation to determine the dielectric of the film by calculating the smearing at the Fermi edge^{160,158}.

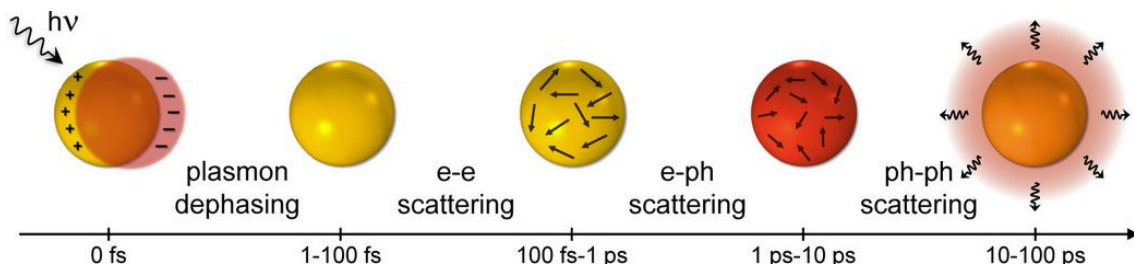


Figure. 1.17. Ultrafast pulse photoexcitation and relaxation dynamics of MNP, showcasing the incidence of light pulses and photoexcitation of plasmon resonance, Landau damping based plasmon dephasing, collision-based electron-electron scattering, electron phonon interaction, phonon vibration and thermal dissipation of energy to the surroundings ($ps =$ picosecond), (Adapted with permission¹⁶⁰).

Within the next few picoseconds (*ps*) the generated thermalized electron distribution peaked around the Fermi level dissipates its thermal energy to the lattice via electron-phonon interactions to attain equilibrium. Finally, the confined region in the vicinity of the metal surface acquires an increase in local temperature due to the phonon-phonon scattering processes. Here importantly, the temporal dynamics of the radiative decay of the excited plasmon modes on the ultrathin films, should be particularly investigated for designing the real structure of the ultrathin films for improving “surface enhanced spectroscopy” applications. Transient absorption spectroscopy (TAS) based on pump-probe configuration can provide complementary information on both the radiative and non-radiative plasmon mode decay dynamics. However, given the picosecond temporal resolution of the optical pulse delay system used in this study. The measurements are limited to picosecond time delays. Therefore, time resolved absorption experiments in this study are performed to investigate the temporally delayed non-radiative decay of the excited charge carriers in the picosecond regimes.

1.4. Surface enhanced Raman scattering (SERS) sensing

Surface enhanced Raman scattering is the phenomena which enhances the weakly scattered in-elastic Raman signals of analytes on metals surfaces. As discussed in the previous sections the excitation of plasmon polaritons with enhanced EM nearfield enhances the scattering of molecules present within the vicinity of the enhanced near-field. The theoretical concepts for understanding the phenomena of Raman scattering and SERS is discussed and presented.

1.4.1. Raman scattering effect

Raman effect is a non-linear scattering phenomenon which allows to observe vibrational states of matter. It involves in the excitation of optical phonons, when the incident light is absorbed initially this creates a virtual electronic state (polarizing electrons) - which subsequently interacts with elementary phononic vibrations in the investigated material. As these excited vibrational modes are quantized, they emit a scattered photon during its relaxation with spectral lines of discrete energy¹⁶¹. These Raman scattered photons differ in energy from the incident photon, as the excited vibrational state relaxes to a lower or higher vibrational state than its original state. This change in the energy corresponds to the intrinsic frequency of the investigated materials phononic vibrations, and serves as an important tool in the field of spectroscopy and in analytical chemistry^{161,162}. Apart from the fraction of light scattered from matter when compared to absorption and reflection, only 1 in 1 million photons are in-elastically scattered⁶². Scattering processes are dominated by elastically scattered photons know as Rayleigh scattering which is $\sim 10^7$ times more intense when compared to the in-elastic Raman scattering effect. Figure 1.18a. shows the energy level Jablonski diagram depicting the energy changes involved in the Rayleigh and Raman scattering process. Raman scattered photons are known as stokes shifted photons when the excited vibrational state relaxes down to a higher energy vibrational state than its original state as depicted in Figure 1.18b. Subsequently, when an excited vibrational state in a higher energy state relaxes to a lower energy state than its original state the photon scattering with an increased energy are known as anti-stokes scattering¹⁶³. The Stokes scattering phenomena is the commonly observed method to analyze the fingerprint vibration of investigated material as they are dominant in room temperature measurements suitable for bio-chemical analysis. This also serves as a

complimentary to IR spectroscopy due to its ability to analyze diluted solutions and IR inactive vibrational modes.

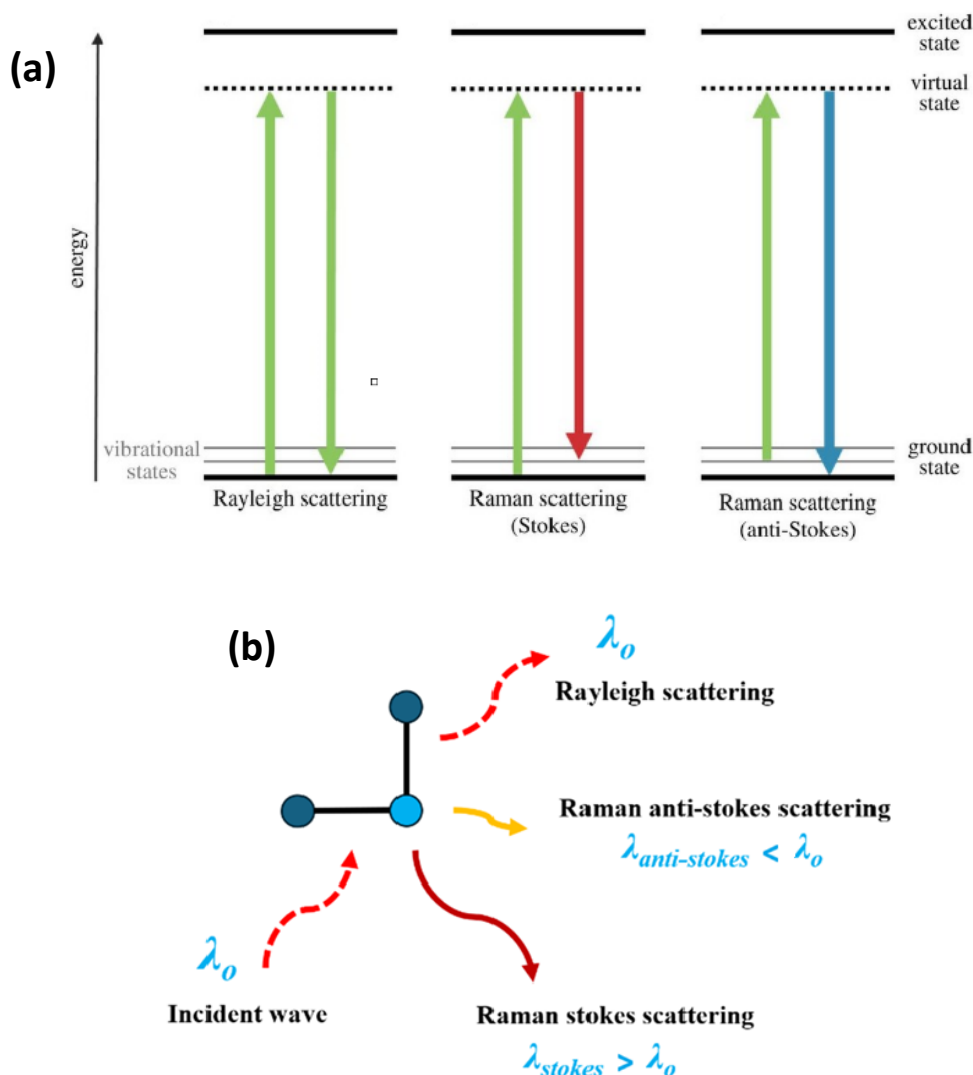


Figure. 1.18.(a) Jablonski energy level diagrams for the phenomena's during light-molecule interaction such as absorption, Rayleigh scattering, stokes and anti-stokes Raman scattering processes (Adapted with permission¹⁶³). (b) shows the simple schematics of the Raman and Rayleigh scattering processes.

In contrary to absorption-based IR spectroscopy, the weak Raman scattering is based on certain surface selection rules. Here, I present the theoretical background for the condition for Raman scattering process in a molecule to occur. Under Raman laser excitation the electron cloud and the nuclei in the molecules are polarized and a dipole moment is induced in the molecule to excite it to a virtual state. The size of the induced moment p by the incident field is dependent on the polarizability tensor α of the molecule as in equation 37¹⁶¹.

$$p = \alpha E \quad (37)$$

where α is the molecule's polarizability

The incident electric field magnitude can be given as:

$$E = E_{exc} \cos(2\pi\nu_0 t_i) \quad (38)$$

where t_i is time in this section

$$\text{So, } p = \alpha E_{exc} \cos(2\pi\nu_0 t_i) \quad (39)$$

Thus, the polarizability α of the molecule changes as the induced dipole moment p oscillates in phase based on the incident field E and subsequently influencing the geometry of the molecule. Further, expanding the polarizability α in equation 40 as a Taylor series in a coordinate r_p about its initial equilibrium coordinate (r_o):

$$\alpha = \alpha_o \left(\frac{\partial \alpha}{\partial r_p} \right)_{r_o} (r_p - r_o) + \quad (40)$$

Now, α can be expanded in terms of the vibrational displacement coordinate of the i^{th} normal mode. which is

$$q_i = q_i^o \cos(2\pi\nu_i t_i) \quad (41)$$

where, ν_i is the frequency of the normal mode i

$$p(t_i) = \alpha E_{exc} \cos(2\pi\nu_0 t_i) + \frac{1}{2} \left(\frac{\partial \alpha}{\partial q_i} \right) E_{exc} q_i^o [\cos(2\pi(\nu_0 - \nu_i) t_i) + \cos(2\pi(\nu_0 + \nu_i) t_i)] \quad (42)$$

The first term in this equation 42. is related to the Raleigh scattering, the second and third term represents the anti-stokes and stokes frequencies^{161,162}. Further, the scattered intensity of the Raman signal is proportional to the derivative of the polarizability squared as:

$$I_{Raman \text{ stokes scattering}} \propto |P \cdot E_{exc}|^2 = \left| \left(\frac{\partial \alpha}{\partial q_i} \right)_o \right|^2 I_{exc}^2 \quad (43)$$

Thus, as the polarizability tensor α changes for any of the excited vibrational or rotational state, then Raman scattering occurs and the vibrational mode is set to be Raman active^{161,164}.

1.4.2. Polarizability tensor

Although for non-isotropic molecules like thiophenol as used in this thesis, the polarizability tensor α is not scalar and can be written as a second rank tensor matrix^{67,114} as in equation 44.

$$\begin{pmatrix} p_x \\ p_y \\ p_z \end{pmatrix} = \begin{pmatrix} \alpha_{xx} & \alpha_{xy} & \alpha_{xz} \\ \alpha_{yx} & \alpha_{yy} & \alpha_{yz} \\ \alpha_{zx} & \alpha_{zy} & \alpha_{zz} \end{pmatrix} \begin{pmatrix} E_x \\ E_y \\ E_z \end{pmatrix} \quad (44)$$

As α_{xy} represents the polarizability of the molecule, where the dipole moment is induced in the x direction due to the incident electric field polarized along the y direction. These nine coefficients in equation 44. are the components of the polarizability tensor α and they become $\alpha_{xy} = \alpha_{yx}$, $\alpha_{zx} = \alpha_{xz}$, $\alpha_{yz} = \alpha_{zy}$ into six independent coefficients which define an ellipsoid^{165,166} as in equation 45.

$$\alpha_{xy}x^2 + \alpha_{yy}y^2 + \alpha_{zz}z^2 + 2\alpha_{xy}xy + 2\alpha_{yz}yz + 2\alpha_{zx}zx = 1 \quad (45)$$

1.4.3. Electromagnetic (EM) near-field mechanism of SERS

Here, the theoretical background for the Raman enhancement occurring due to the enhanced EM nearfield in metal surfaces is presented. The case of a spherical nanoparticle with $d \ll \lambda$ is used to derive the relationship between its enhanced near-field and the subsequent Raman enhancement for molecules present in the vicinity of this field. The Laplace electrostatic equations replace the electrodynamics calculations in the quasi-static approach as $d \ll \lambda$.

From equation 16. the polarization induced electric field in the surface of the nanoparticle with $d \ll \lambda$ is given by:

$$\sigma_p = 3\epsilon_0 g E_{exc} \cos \theta \quad (46)$$

where the collective resonance-based dipole enhancement factor $g = \frac{\epsilon_m - \epsilon_d}{\epsilon_m + 2\epsilon_d}$.

The maximum enhancement of LSPR resonance occurs when g becomes large as discussed in section 1.4.2. The intensity of the nearfield E_p^2 at the surface of metal is very large, when the value of the factor g from equation 46. becomes very large exciting a plasmon mode^{71,164}. It can be expressed as in the equation 47.

$$E_p^2 = E_{exc}^2 |g|^2 (1+3\cos^2\theta) \quad (47)$$

where θ is the angle between the incident electric field and the vector s denoting the position of the molecule located on the sphere surface.

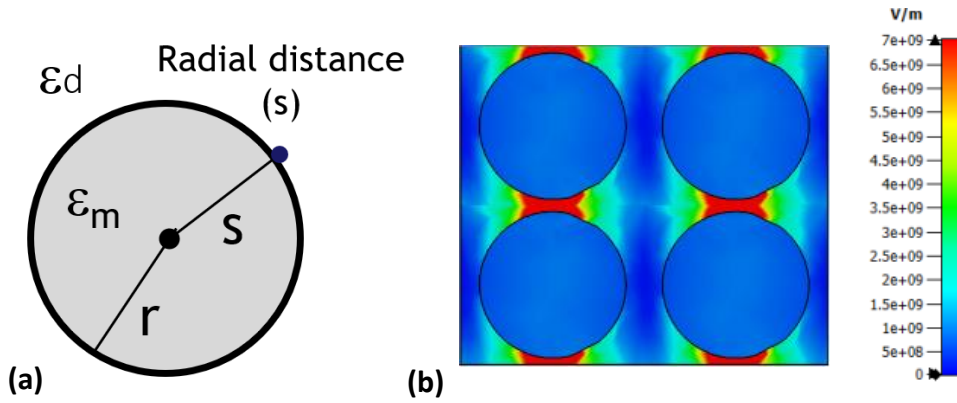


Figure.1.19 (a) Schematic depicting the position of analyte on the MNP surface, s is the radial distance of the molecule and r is the radius of the MNP⁷¹. (b) FDTD simulations exhibiting the EM nearfield interaction and hybridization in Au grains arrays system with $S \leq r$ reflecting the real structure of the fabricated non-percolated ultrathin Au film on corrugated sapphire templates. The EM nearfield represents the excited collective plasmon polariton mode with a distributed plasmonic hotspots.

Based on the equation 47 the largest field intensity is enhanced for $\theta = 0^\circ$ and 180° . Subsequently, the incident electric field $E_{exc}(\lambda_{exc})$ is enhanced maximum by the factor g as $E_p(\lambda_{exc})$ as in equation 48, *note: maximum enhancement occurs when $\lambda_{exc} = \lambda_p$.*

$$E_p(\lambda_{exc}) = g E_{exc}(\lambda_{exc}) \quad (48)$$

For a Raman analyte molecule present at the surface of the nanoparticle with a radial distance $s \approx r$, where, r is the radius of the nanoparticle as in Figure.1.19a. the enhanced field $E_p(\lambda_{exc})$ on the surface polarizes the molecule and it emits a Raman scattered photon $E_{stokes}(\lambda_{stokes})$ at a different wavelength^{66,68} based on equation 49.

$$E_{stokes}(\lambda_{stokes}) \propto \alpha E_p(\lambda_{exc}) \propto \alpha g E_{exc}(\lambda_{exc}) \quad (49)$$

This scattered field $E_{stokes}(\lambda_{stokes})$ can be again enhanced by the EM near-field $E_p(\lambda_{stokes})$ with a different magnification factor g^s within the surface of the nanoparticle and will differ from the factor g based on the FWHM of the excited plasmon mode λ_p .

This gives the total Raman stokes enhancement of a molecule present in the vicinity of the enhanced EM nearfield⁶⁸ as:

$$I_{Raman\ stokes} \propto |\alpha|^2 / g^s g^s I_{exc}(\lambda_{exc}) \quad (50)$$

And can also be written as:

$$I_{Raman\ stokes} = \frac{|E_{stokes}(\lambda_{stokes})|^2 |E_p(\lambda_{exc})|^2}{|E_p(\lambda_{stokes})|^2 |E_{exc}(\lambda_{exc})|^2}, \quad (51)$$

This is known as the $|E|^4$ model of SERS enhancement^{71,167}

So, SERS scattering process will depend on both: the near-fields enhanced at $E_p(\lambda_{exc})$, which polarizes and excites the Raman vibrations, and $E_p(\lambda_{Stokes})$, which simultaneously enhances its Stokes-shifted radiation.

Similarly, in the case of analyzing the real structure of non-percolated Au films exhibiting $2d$ -MNP arrays with interparticle separation $S \leq r$. The excited plasmon modes become hybridized into collective near-fields. These collective modes are more suitable for SERS when compared to single particle LSPR modes, as the near-field couplings between the neighboring particles dominate and scale with the characteristic S^{-3} dependence¹⁵⁷. When the interparticle gaps become as small as $S \leq r$, each MNP has a neighboring particle which can support a comparable near-field $E_p(\lambda_p)$. The region where the confined near-fields of the two particles overlap produces an enormous near-field amplification known as a ‘‘plasmonic hotspot’’ - as illustrated in Figure 1.19b. These plasmonic hotspots (collective plasmon-polariton modes with modified near field as $E_p(\lambda_{p'})$) can facilitate higher absolute SERS enhancement as compared to a single-particle LSPR mode with $E_p(\lambda_p)$ while also exhibiting a broader resonance peak^{66,71}. This may improve the feasibility of SERS sensing of analytes belonging to the same chemical group^{168,169}, as they emit very similar λ_{Stokes} positions for most of their Raman vibration modes. So in this case, the fields $E_p(\lambda_p)$ and $E_{Stokes}(\lambda_{Stokes})$ are further enhanced by a factor g' and g'' becoming $E_p(\lambda_{p'})$ and $E_{Stokes}(\lambda_{Stokes})$ as in equation 52.

$$E_{Stokes}(\lambda_{Stokes}) \propto \alpha E_p(\lambda_{p'}) \quad (52)$$

Note: when performing SERS measurement on non-percolated metal films exhibiting Au grain arrays as in equation 52. Here, the λ_p position of the individual MNPs plasmon resonance can change to another position as $\lambda_{p'}$ of the collective plasmon resonance.

The performed experimental measurements investigate and study the dependence of both the field enhancements E_p at λ_{exc} and E_p at λ_{Stokes} , their spatial and temporal influences on the SERS response thus validating the EM nearfield mechanism of SERS. Further the absolute enhancements due to both localized and delocalized plasmon modes excited on these ultrathin Au films are also reported

2. Experimental methods

In following section experimental sample fabrication and characterization techniques used in this thesis will be discussed. Apart from short theoretical descriptions, information about the experimental details and characterization parameters will be presented.

Template assisted deposition of ultrathin metal films were utilized to fabricate self-assembling anisotropic plasmonic structures in this work. Fabrication of these anisotropic structures as percolated and non-percolated Au films, and its characterization by 1. *Atomic force microscope (AFM)*, 2. *Ellipsometer*, 3. *UV-vis spectrometer*, and 4. *micro-Raman measurements* were conducted in the research facilities provided in the Nano-Biomedical center of Adam Mickiewicz University in Poznan, Poland. 5. *Transient optical spectroscopy* measurements were conducted in the Institute of material science, Kaunas University of Technology, Lithuania. EM simulation was performed together with the M-ERANET project partners and co-authors from the Faculty of Physics, Adam Mickiewicz University.

2.1. Fabrication of anisotropic ultrathin Au films

2.1.1. Surface reconstruction of Al_2O_3 templates

Spontaneous reconstruction of unstable single crystal surfaces is a technique that can be used to fabricate anisotropic templates for ultrathin film deposition. This is due to single crystal surfaces with a miscut along its equilibrium plane becomes intrinsically unstable as a result of its crystallographic anisotropy⁹⁷ see Figure 2.1a.

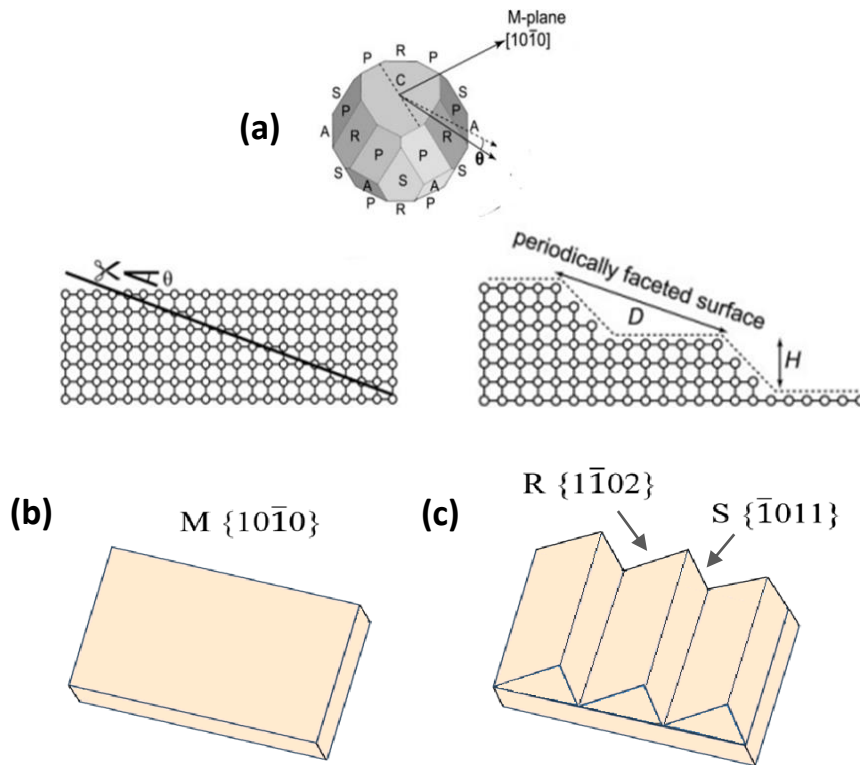


Figure 2.1 (a) Different facets of equilibrium α -sapphire in the order of increasing surface energy C {0001}, R {1 $\bar{1}$ 02}, S { $\bar{1}$ 011}, P {1123}, A {1120}, and M {10 $\bar{1}$ 0}, where the M plane is unstable to be observed (Adapted with permission⁹⁷). (b) Atomic surface depiction of the miscut along the M-plane of

the α sapphire. (c) Atomic surface depiction of the decomposition of the unstable M-Plane into stable corrugated facets of R and S plane.

Thus, when annealed in high temperature the unstable M plane surface as in Figure 2.1b. decomposes, by rearranging into stable facets in order to minimize its total surface energy^{97,170} see Figure 2.1c. In this study, polished sapphire ($\alpha\text{-Al}_2\text{O}_3$) single crystals with a $< 0,1^\circ$ miscut along the M-plane $[10\bar{1}0]$ were commercially purchased from CrysTec GmbH and utilized as templates. These surfaces with an extremely unstable singular surface as they are cut along a low index plane see (Figure 2.1a.) results in S\R faceted planes with V grooves upon high temperature annealing^{170,171}. A carbolite high-temperature chamber furnace was used to treat the substrates at operating temperatures up to 1700°C . Depending on the annealing time (between 12 and 24h) and temperature (1450 to 1550°C), the period of naturally forming corrugations varied as in Table 2.1

Table 2.1. Structural dimensions of the fabricated corrugated templates.

Template name	T1	T2	T3	T4	T5	T6	T7	T8	T9
Corrugation period	Flat	30 ± 5 nm	70 ± 8 nm	150 ± 25 nm	170 ± 25 nm	240 ± 25 nm	270 ± 25 nm	290 ± 25 nm	450 ± 30 nm
Corrugation height	Flat	2 ± 1 nm	8 ± 2 nm	18 ± 5 nm	19 ± 5 nm	25 ± 5 nm	25 ± 5 nm	30 ± 5 nm	35 ± 10 nm

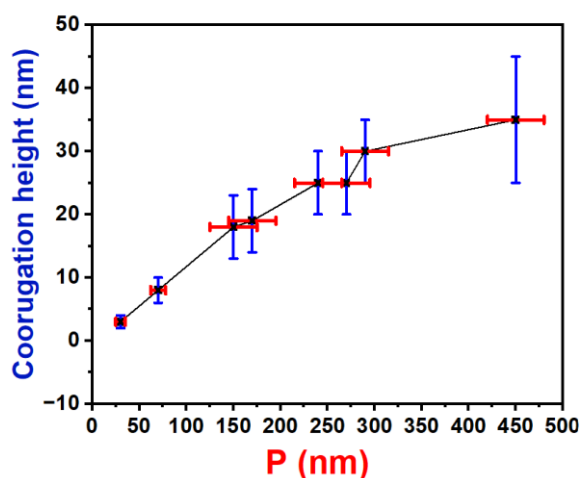


Figure 2.2. Graph illustrating the range of corrugation periods with their respective heights fabricated by utilizing the method of surface reconstruction of M-plane sapphire wafers. (blue error bars indicate the range of distribution of heights) and (red error bars indicate the range of distribution of corrugation periods P).

Such periodic surface facets extending all over the (2x2cm) commercially purchased wafer can be viewed as sophisticated optical surfaces which are difficult to fabricate in a mechanically hard substrate such as sapphire. The evolution of this surface reconstruction phases proceeds as: (a) surface smoothing, (b) nucleation of individual facets, (c) interaction between facets to form facet domains, (d) coalescence of facet domains and (e) facet coarsening as reported by Gabai et al⁹⁷ and Erb et al¹⁷¹. In this study, particularly the spontaneous reconstruction process

in the phase of coarsening was optimized to fabricate corrugated templates with different periods as shown in Figure 2.3.

The uniformity of corrugated structures decreased for larger value of corrugation period as in Figure 2.2 due to the high degree of node misalignment during facet merging to form larger corrugation periods, as a result of this the shorter corrugation periods formed at a short annealing time and a constant temperature exhibited the most uniformly corrugated structures¹⁷⁰.

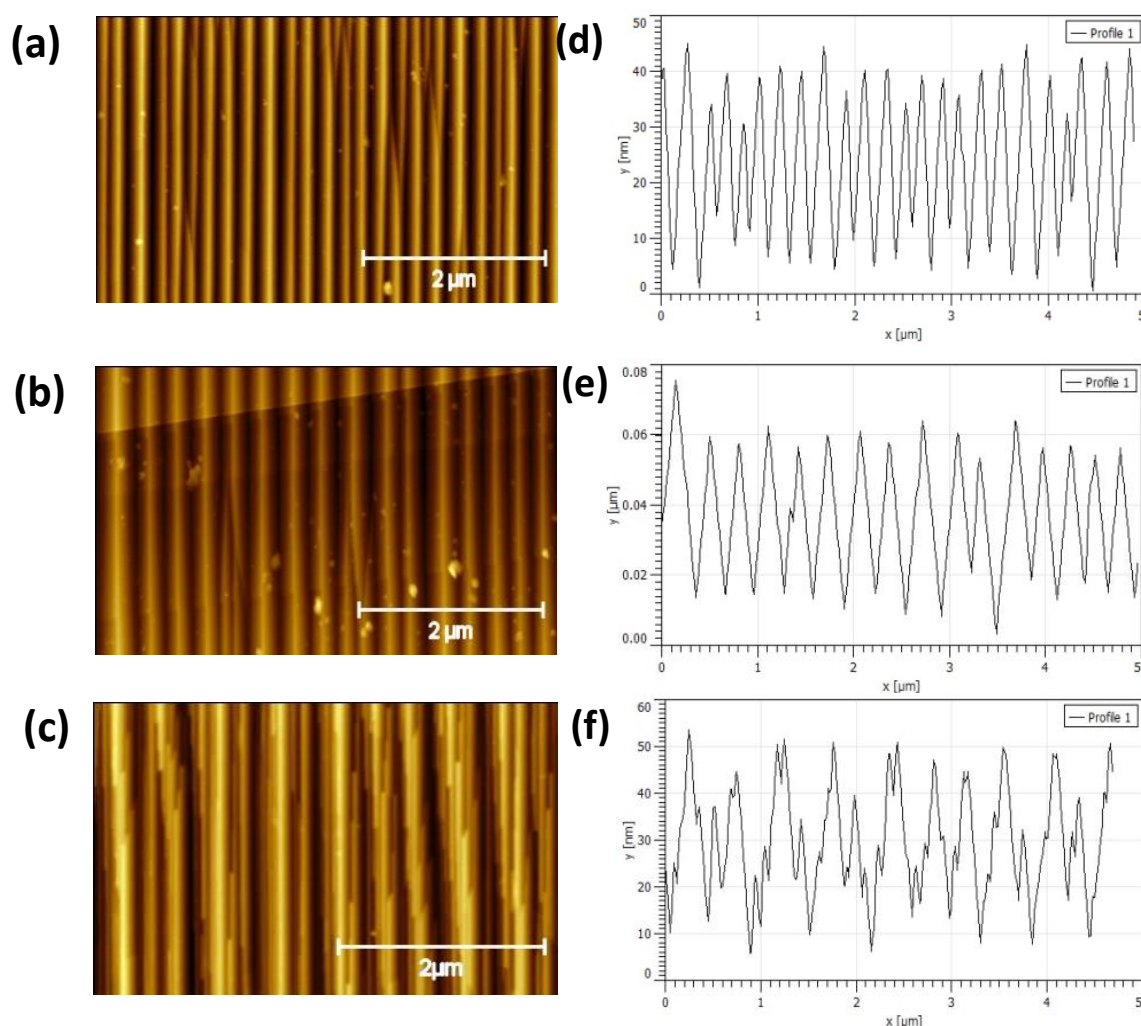


Figure 2.3. AFM topography of: (a) surface reconstruction of M-plane sapphire during the phase of coarsening, with a period of $P \sim 170$ nm, (b) Template with an increase in corrugation period to $P \sim 290$ nm as a result of the motion and elimination of facet junctions in smaller corrugation period, (c) Templates at longer annealing time resulting in an increase in the value of standard deviation δ of an averaged corrugation period P , (d, e, f). exhibiting their respective AFM line profiles (x) axis = width and (y) axis = height²¹⁷.

Further, surface corrugations with periods as small as ~ 130 nm were fabricated by this method. When utilizing double side polished sapphire wafers and subjecting it to high temperature annealing process, the corrugated surface reconstructions formed on both sides of the M-plane $[10\bar{1}0]$ wafer surface. On one side of the double-side-polished templates corrugation period of value $P \cong 30$ nm was observed as its wafer surface was exposed towards the air, while larger

corrugation periods with $P \cong 150$ nm were observed on the opposite side of the wafer lying on the Carbolite oven sample stage (see Figure 2.4.). These formation of corrugations with different periods is presumably due to the temperature gradient between both the surface of the double side polished sapphire wafers facing the sample stage and ambient atmosphere. Finally, the fabricated corrugated substrates with different periods were used as templates for plasmonic metal deposition.

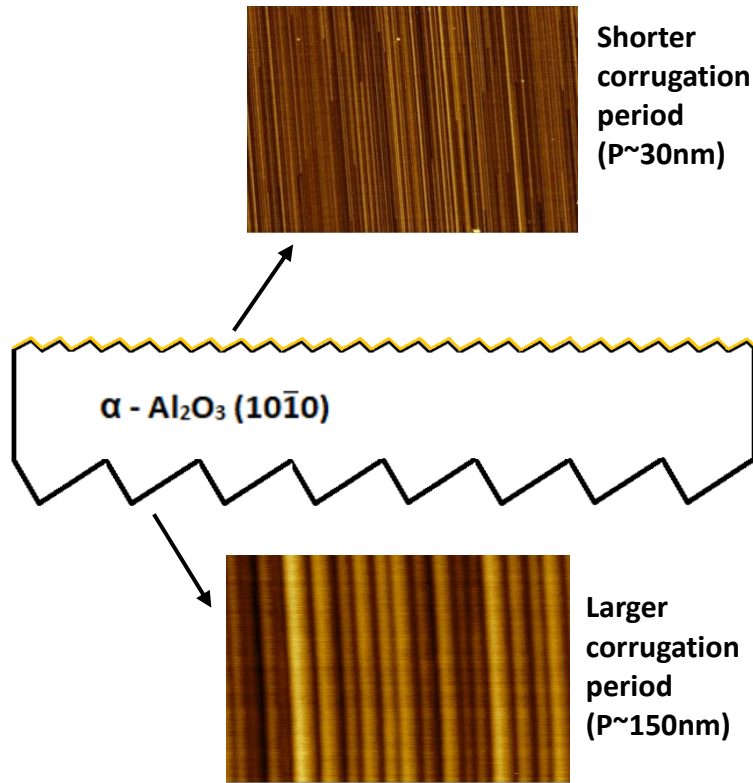


Figure 2.4. Schematic in the center depicting the formation of corrugations with different periods on both sides of the double side polished M-plane $[10\bar{1}0]$ wafers. (AFM images of the corresponding reconstructed templates with periods $P \sim 30$ nm on the side lying on the Carbolite oven sample stage and the exposed side with $P \sim 150$ nm)²¹⁸.

2.1.2. Ultrathin Au metal deposition

The electron beam evaporation method operating at ultrahigh vacuum condition $\sim 10^{-10}$ mbar was chosen in this study, particularly due to its low external contamination rate during metal depositions as required for optical grade plasmonic applications, as well as reliability in controlling the deposition rate, which influences the structural morphology of the deposited ultrathin film. In principle, an electron beam generated by thermionic emission is focused on to a crucible containing the target Au metal. Subsequently, the Au metal atoms in the target is transformed through evaporation into a vapour phase and precipitate on to the templates to form ultrathin metal films. The rate of deposition is precisely determined by the type of target material and the electron beam power. This is due to the conversion of the electron beams high kinetic energy into thermal energy during its bombardment and contact with Au surface atoms on the target, this subsequently dissipates the Au atoms to evaporate and deposit onto the sample (see Figure 2.5a).

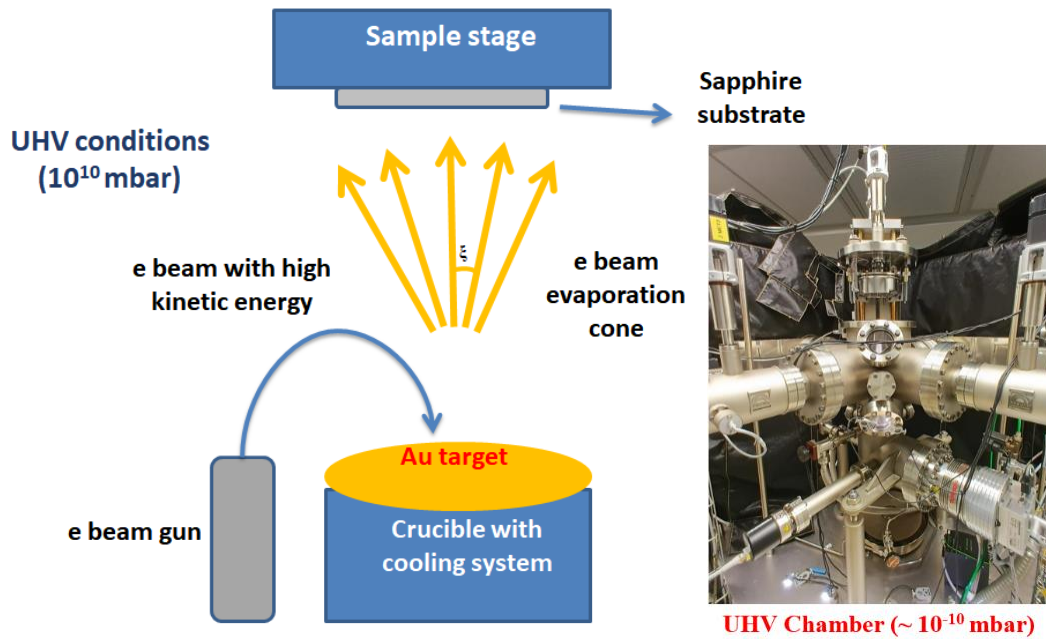


Figure 2.5. (a) Schematics depicting of an electron beam evaporation system operating under ultrahigh vacuum condition, the electron beam is focused by a magnetic coil onto the Au target (ξ is the oblique angle due to the electron beam cone). (b) Photographic image portraying the electron beam evaporation system operating under UHV in the Nano-Biomedical Centre in UAM, Poznan.

In this study a (Telemark/PREVAC) system operating under ultra-high vacuum (UHV) conditions ($\sim 10^{-10}$ mbar) was used to deposit Au layers of different thickness ($t = 2, 4, 6, 7, 8, 9$ and 10 nm) from a sapphire crucible containing Au target material. The samples were deposited in a very low deposition rates of $10 \text{ \AA} / \text{hour}$ and $79 \text{ \AA} / \text{hour}$ onto the flat and reconstructed templates as in (Table 2.2) for non-percolated and near-percolating films, and in (Table 2.3) for percolated Au films.

Table 2.2 Structural parameters of the fabricated plasmonic samples after deposition of non-percolated and near percolated Au films

Sample name	Sa1	Sa2	Sa3	Sa4	Sa5	Sa6	Sa7	Sa8	Sa9	Sa10	Sa11	Sa12	Sa13	Sa14	Sa15	Sa16	Sa17	Sa18
(P) corrugation period [nm]	flat	30 ± 5	30 ± 5	70 ± 8	150 ± 25	150 ± 25	150 ± 25	240 ± 25	240 ± 25	290 ± 25	290 ± 25	290 ± 25	290 ± 25	290 ± 25	290 ± 25	290 ± 25	290 ± 25	70 ± 25
(h) Corrugation height [nm]	flat	2 ± 1	2 ± 1	8 ± 2	18 ± 5	18 ± 5	18 ± 5	25 ± 5	25 ± 5	30 ± 5	30 ± 5	30 ± 5	30 ± 5	30 ± 5	30 ± 5	30 ± 5	30 ± 5	8 ± 2
(t) Au thickness [nm]	~ 6	~ 6	~ 7	~ 8	~ 6	~ 8	~ 10	~ 10	~ 8	~ 10	~ 2	~ 4	~ 6	~ 7	~ 8	~ 9	~ 10	~ 7
(d) Au grain Diameter (nm)	27 ± 2	27 ± 2	Elliptical grain 33 ± 2 nm in y axis, 24 ± 2 nm in x axis.	60 ± 5	27 ± 2	65 ± 5	-	-	65 ± 5	-	25 ± 5	25 ± 5	27 ± 5	30 ± 5	-	-	-	30 ± 5
Au deposition rate ($\text{\AA} / \text{hour}$)	10	10	10 (\AA / hour) slightly off-normal deposition	79	10	79	10	10	79	10	10	10	10	10	10	10	10	10

Table 2.3 Structural parameters of the fabricated plasmonic samples after deposition of percolated Au

Sample name	(SaP1)	(SaP2)	(SaP3)	(SaP4)
(P) corrugation period [nm]	flat	170 ± 25 nm	290 ± 25 nm	450 ± 30 nm
(h) Corrugation height [nm]	flat	19 ± 5 nm	30 ± 5 nm	35 ± 10 nm
(t) Au thickness [nm]	10 nm Au	10 nm Au	10 nm Au	10 nm Au
Au deposition rate (Å / hour)	79	79	79	79

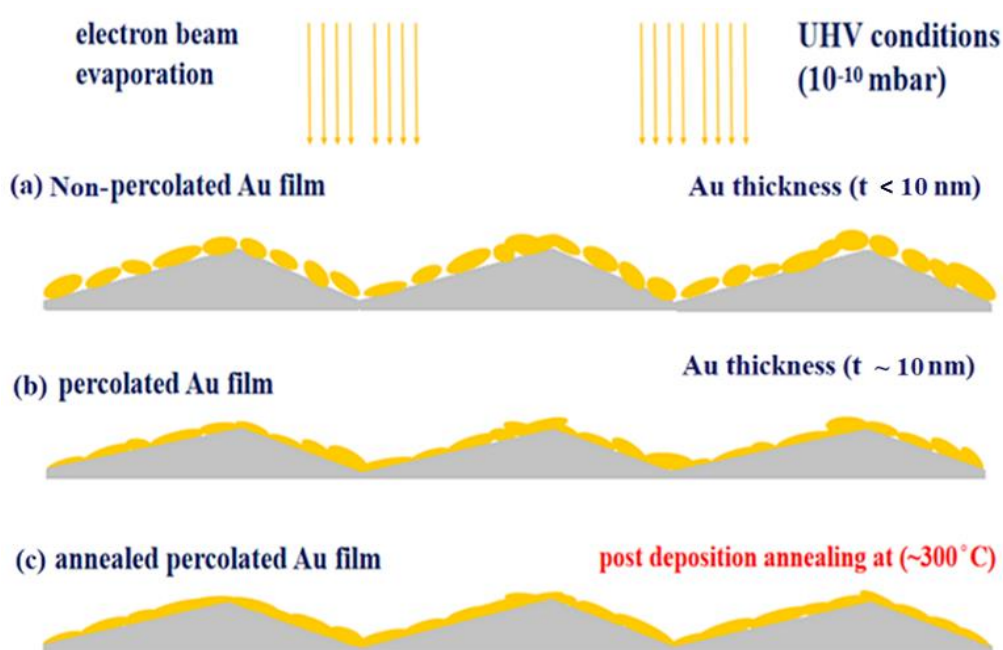


Figure 2.6. Simple schematics depicting formation of (a) non-percolated (for $t < 10\text{nm}$) and (b) percolated (for $t \sim 10\text{nm}$) Au films on corrugated sapphire templates at ultra-high vacuum conditions ($\sim 10^{10}$ mbar), (c) Depicts the post annealing process for improving the film connectivity of the deposited percolated ultrathin film.

Further, during the deposition of percolated ultrathin Au films onto the templates for samples SaP1,2,3 and 4. in Table 2.3. before the Au deposition process, all samples were outgassed at a temperature of 550°C for 1 hour. And subsequently, after the deposition, the samples were annealed again at 300°C for 20 min. The degassing, deposition and annealing were performed to facilitate percolation and improve the interparticle connectivity of the deposited ultrathin film at the deposition rate of (79 Å/hour) see Figure 2.6. (This method is discussed in detailed

in Chapter 4.1). The non-percolated Au films were obtained when depositing Au films with thickness below 10 nm as for the samples in Table 2.2.

2.1.3. Analyte molecules chemisorption

A simple organic molecule (thio-phenol) was chosen as the analyte in this study. The thio-phenol molecules chemisorb onto the Au surface forming a layer of phenyl thioliates across the sample due to the formation of Sulphur *S* - Au bonds¹⁷² as in Figure 2.7b. Thus, providing a feasibility to study the long-ranged SERS sensing capability of the substrates through SERS mapping measurements. Moreover, these non-isotropic molecules such as phenyl-thioliates with a C_{2V} symmetry^{67,113} on a substrate exhibit Raman spectra with relative peak intensities dependent on its Raman polarizability tensor α . This is advantageous for the experimental objective to study specific molecular vibrations –polariton interactions and verify the EM near-field mechanism of SERS enhancement. The performed experimental analysis was used to predict the orientation of the chemisorbed molecules on these plasmonic surfaces as these organo-thiols has promising applicative relevance in chemical sensing, and as lubricating and capping agents. The fabricated samples were immersed in a solution of 99.8 % thiophenol (purchased from Alfa Aesar) and dissolved in 99.8 % ethanol (POCH) (1:50 vol). After 10 min at room temperature the samples were removed from the solution and immersed in pure ethanol to remove un-bonded thio-phenol molecules. The whole process was repeated multiple times to form a layer of phenyl-thiolate molecules bonded to the Au surface.

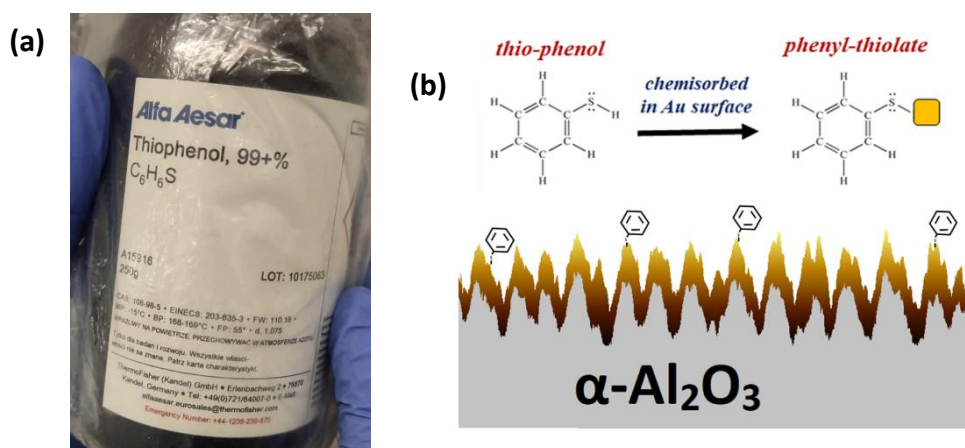


Figure 2.7. (a), Image of 99% thio-phenol solution commercially purchased from Alfa Aesar (b), Schematic depicting the chemisorption of thiophenol molecule onto the Au surface forming a layer of phenyl thiolate analyte layer suitable to characterize long ranged surface sensing capabilities of the fabricated plasmonic substrates.

2.2. Characterization, measurement and simulation techniques

2.1.1. Atomic force microscopy (AFM)

Atomic force microscopy (AFM) is a commonly used microscopic technique with demonstrated resolution on the order of fractions of a nanometre, Which makes this characterization technique better in resolution than tradition optical microscopy. It is used in this study to analyse the topography of the fabricated subwavelength plasmonic nanostructures.

AFMs use a laser beam deflection system where the illuminated laser beam is reflected from an AFM cantilever with a tip. As the tip in the cantilever oscillates due to the tip–sample’s attractive and repulsive interactions the modulations in the reflected beam are detected by a position-sensitive detector as exhibited in Figure 2.8a. The sharp tip is raster-scanned over the subwavelength plasmonic surface which measures the constant interaction forces using a feedback loop maintaining the constancy of the AFM lever deflection. By adjusting the parameters of the feedback loop the AFM can effectively track the tip–sample interaction, allowing the surface topography to be imaged accurately. A Bruker Dimension Icon atomic force microscope (AFM) as portrayed in Figure 2.8b. operating in soft tapping mode was used in this study. A micro fabricated SiN₃ tip model: FESP with parameters as shown in the image in Figure 2.8c. was particularly suitable and used to analyse these fabricated ultrathin films, where 10 × 10 μm² scans were performed at different locations onto the sample.

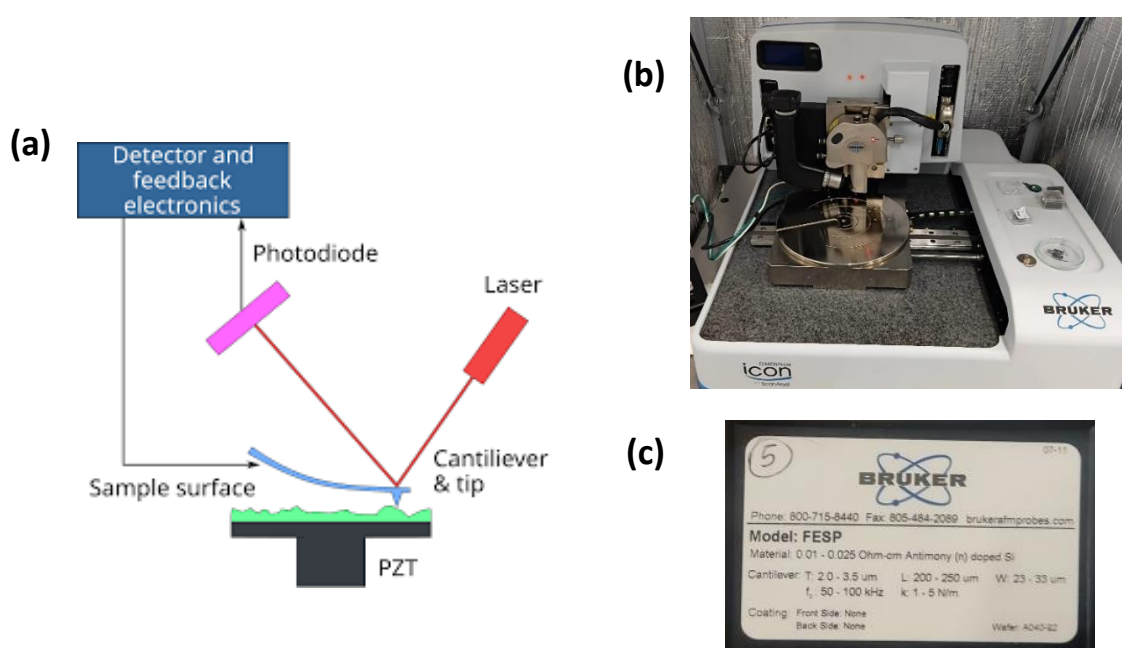


Figure 2.8. (a) Schematic illustration of working of an atomic force microscope (Adapted with permission²¹⁶) (b) Photographic image of a FESP tip container (with tip parameters) which was suitable and particularly used to image the topography of the non-percolated and percolated Au films. (c) Photographic image of the Bruker Dimension Icon atomic force microscope AFM utilized for the topographical analysis.

2.1.3. Ultraviolet-visible (UV-vis) spectroscopy

The Ultraviolet-visible-near-infrared spectroscopy (UV-Vis-NIR) refers to absorption or transmission spectroscopy performed within the ultraviolet-visible -NIR spectral region. This is the primary spectroscopic method to characterize the plasmon polariton modes excited in noble metals such as Au, Ag and Pt. Polarized transmission spectroscopy were particularly performed at normal incidence angle using a Perkin Elmer UV-visible spectrometer onto the fabricated anisotropic plasmonic samples. The examined samples were rotated to adjust the azimuthal angles as $\sigma = 0^\circ, 45^\circ$ and 90° (σ - an azimuthal angle between excitation polarization

and the corrugation vector). A rotating polarizer was used to optimize the polarization of the incident light onto the samples as in the Figure 2.9.

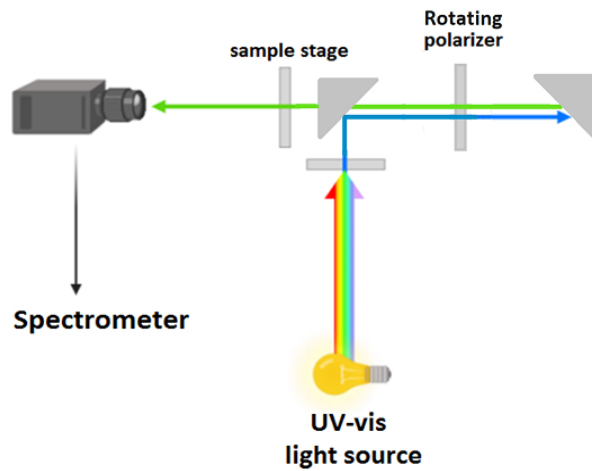


Figure 2.9. Schematic of construction of a UV- visible spectrophotometer. A rotating polarizer was integrated with the spectrometer to measure polarized transmission spectra.

2.1.4. Ellipsometry

Ellipsometry is a technique particularly used to characterize the dielectric properties of thin films including metals and semiconductors. In this study it is used to measure *p* and *s* polarized components of reflected light from the examined anisotropic plasmonic samples.

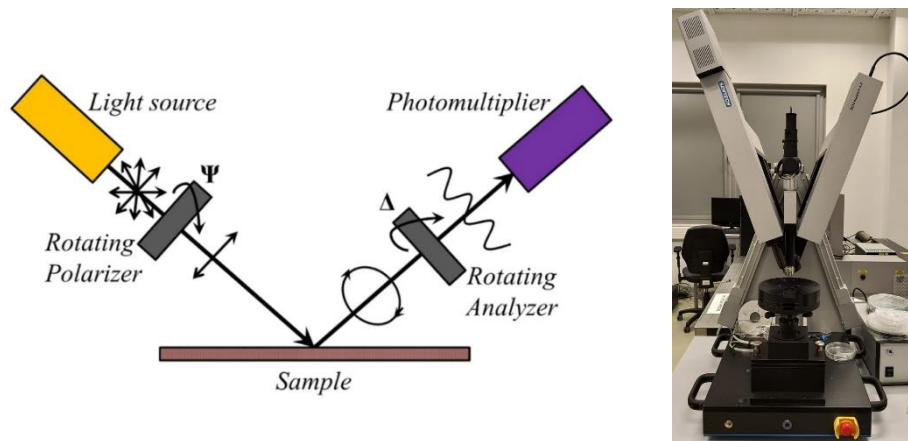


Figure 2.10a, Schematic of construction of an ellipsometer used for measuring the *s*-plane and *p*-plane polarization components from the anisotropic samples. (Adapted with permission¹⁷³). **b,** Photographic image of the SENTECH SER800 Ellipsometer in the Nano-Biomedical Centre, UAM.

A *SENTECH GmbH SER800* Ellipsometer operating at an oblique incidence angle $\theta=50^\circ$ was used to collect the ratio of complex amplitude and phase shift of *s*-plane and *p*-plane polarized components, of the reflected light. The complex reflectance ratio^{174,175} is based on the equation 53. as:

$$\rho = \frac{r^s}{r^p} = \tan \psi e^{i\Delta} \quad (53)$$

The schematics of the instrumentation of an ellipsometer is presented in Figure 2.10. Where, r_s and r_p are the ratios of the complex amplitude of s and p polarized components before and after reflection on the sample. Similarly, $\tan\Psi$ is the ratio of amplitude and Δ represents the phase shift of the reflected light with respect to the incident light in this section¹⁷⁴. All spectra were normalized to a reference signal collected from a 99.99% reflecting mirror. The samples were rotated for every $\sigma = 20^\circ$ (σ - an azimuthal angle between excitation polarization and the spatial corrugation vector k_x spatial corrugation) over the spectral regime of 400–1050 nm with a scanning interval of 1 nm.

2.1.5. Transient absorption spectroscopy

Transient absorption spectroscopy (TAS) is a pump probe setup-based spectroscopy, which can be used to analyze the relaxation processes of a short photo pulse induced excited states of a system.

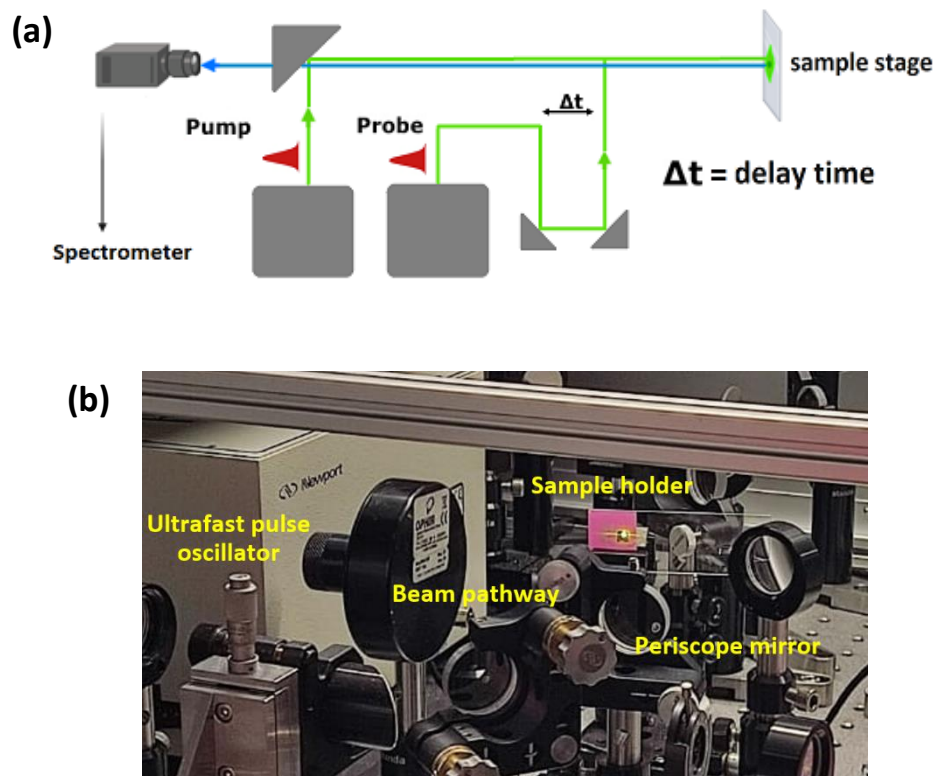


Figure 2.11a, Schematic of the optical alignment in a transient absorption spectrometer based on pump-probe measurements and **b**, Photographic image of the of the pump-probe setup assembled to measure transient absorption measurements in reflectance configuration.

In contrast to steady state optical measurements which measures the average optical response of the investigated system over time, TAS measures the optical spectra of the excited state as a function of ultrashort time delay capturing the dynamic processes of short-lived excited states. An ultra-short pump pulse at a desired wavelength is illuminated on the sample exciting photo

generated excited states in the system. Subsequently a probe pulse usually as a white light continuum is illuminated at very short delay time (pico-seconds) to probe the excited state^{176,177} as depicted in the Figure.2.11a.

Here, polarized-TAS measurements were performed on the fabricated ultrathin anisotropic plasmonic samples to investigate the life time and relaxation processes of the excited non-radiative modes and their anisotropic response. The performed polarized-TAS analysis combined with steady state absorption and scattering spectra can provide understanding on deconvolution of radiative and non-radiative plasmon damping pathways on plasmonic structures. Although temporally delayed non-radiative decay pathways in the picosecond regime is examined here on the fabricated samples, attosecond -femtosecond pulse and delay configurations can facilitate to investigate-ways to prolong radiative decay processes and increase the plasmon life time for efficient SERS. A Transient absorption spectrometer HARPIA (Light Conversion, LT) system was utilized to excite a pump pulse with a life time of 290 femto-seconds and 1030 nm in wavelength. The wavelength of the pump pulse was optimized and tuned as 450,650 and 800nm utilizing a collinear optical parametric generator Orpheus and harmonic generator Lyra (Light Conversion, LT). Subsequently a white light super continuum probe pulse was generated when the fundamental 1030nm laser was illuminated onto a 2 mm thickness sapphire plate. Both the supercontinuum pulse and the detection range of the absorption spectrometer dynamics was from 476 to 782nm in wavelength. The delay time between the pump and probe beam was optimized from 1 pico-second to 100 pico-seconds. The measured spectral absorbance varies temporally and is measured at different delays between the pump and the probe pulse. The measured transmitted intensity for the probe pulse through the sample is given as $I_1(\lambda, t_d)$, where t_d is the delay time.

$$I_1(\lambda, t_d) = I_o(\lambda) * 10^{-A(\lambda, t_d)} \quad (53.1)$$

$I_o(\lambda)$ is the intensity of the probe pulse initially and $A(\lambda, t_d)$ is the absorbance spectra of the sample at the respective temporal delays. The measured transient measurements can be expressed in unit of optical density (OD).

$$\Delta OD(\lambda, t_d) = A(\lambda, t_d) - A(\lambda, t_o) = \log_{10} \frac{I_1(\lambda, t_o)}{I_1(\lambda, t_d)} \quad (53.2)$$

Further, the samples were rotated for $\sigma = 0^\circ$ and 90° (σ - an azimuthal angle between excitation pump polarization and the spatial corrugation vector of the template), subsequently the polarization of the probe pulse onto the sample was adjusted parallel to the polarization of the pump pulse during measurements.

2.1.6. Raman spectroscopy

The non-linear Raman scattering spectroscopy as discussed in the introduction were performed using a commercial Renishaw in-Via micro-Raman system operating at excitation wavelengths $\lambda_{exc} = 633$ and 785 nm plane-polarized laser. Both polarized and wavelength scanned micro-

Raman spectra were collected through a 0.7 *N.A* microscopic objective within an aperture angle of 50° as shown in Figure 2.12a. At $\lambda_{exc}=785$ nm the laser power was 21 *mW*, 4 accumulations with 1 *s* exposure time scans were collected. Subsequently, at $\lambda_{exc} = 633$ nm the laser power was 1.6 *mW*, where 6 accumulations with 4s exposure time scans were collected.

A spectral resolution of about 1 cm^{-1} was achieved using a 1200 and 1800 l/mm grating for the respective laser wavelengths. A STANDA 050097 rotational step motor stage was used to perform polarized SERS measurement as in photographic image presented in Figure 2.12b. for an azimuthal angle σ determined between the laser polarization and the corrugation vector as depicted in Figure 2.12c. with a step of either $\Delta\sigma = 2.5^\circ$, $\Delta\sigma = 5^\circ$ or 20° , from $\sigma = 0^\circ$ to 180° based on the type of the examined plasmonic sample. SERS mapping spectra were collected at $\lambda_{exc} = 633$ and 785 nm by scanning the laser spot for a step of every 1 and 3 μm to check the large-scale uniformity of SERS signal on the fabricated plasmonic samples.

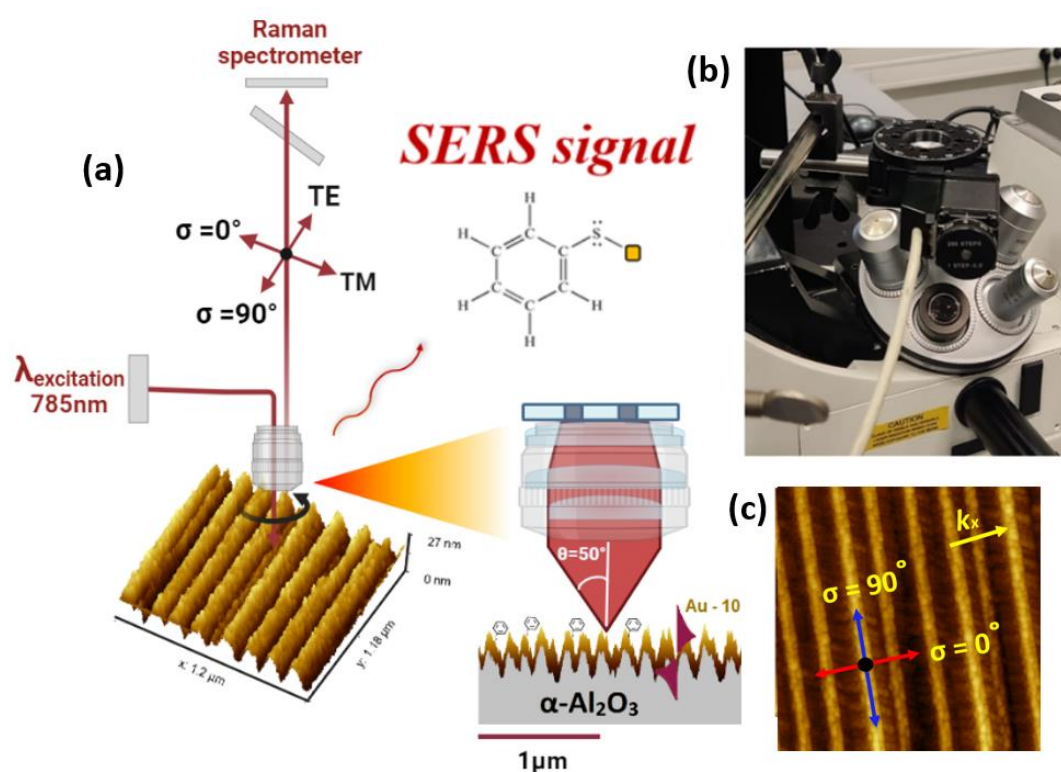


Figure 2.12a, Illustration of the performed polarized SERS measurement for the azimuthal angles σ , inset image depicting the aperture angle of 50° incidence due to the high numerical aperture $N.A = 0.7$ of the microscopic-objective utilized in the study. **b**, Photographic image portraying the rotational stage fixed to collect the backscattered Raman scattering signals from the sample. **c**, Schematics the azimuthal angle σ determined between the laser polarization and the spatial corrugation vector.

2.1.7. Simulations techniques

To model the optical properties of percolated Au on to the corrugated samples, we used the optical constants described by Rosenblatt et al¹⁴² for an 11-nm thick Au film. The optical constants of sapphire described by Palik^{178,179} were used to model the corrugated

sapphire template. The Au/Al₂O₃ corrugated plasmonic structure was drawn in an EM solver (Lumerical Solutions), subsequently a conformal 10 nm thick Au film was placed isotropically onto the corrugated sapphire surface. The simulations were conducted utilizing the periodic boundary conditions that the sample was excited with a TM polarized plane wave (PW) at angle of incidence $\theta = 0^\circ$ and 50° . The plane wave source exhibited a bandwidth (FWHM = 0.5 nm) to collect spectra with precision calculation and minimal substrate dispersion effects. The electric field intensity ($|E|^2$) was obtained by taking the square magnitude of the electric field vector in 3D space (i.e. $|E_x|^2 + |E_y|^2 + |E_z|^2$) along the plane of the corrugation. The spatial distribution of the charges due to the excited plasmon mode was presented by plotting the divergence of the electric field (∇E) along the plane of the surface corrugation.

Further to model the optical properties of the non-percolated Au on to these corrugated substrates, CST Studio Suite, a software based on finite integration method, was used for the theoretical simulations. As it requires relatively low costs and provides controllable convergence and accuracy, appropriate for the studies of photonic and plasmonic grade periodic structures particularly for structures with unit cells of rather arbitrary geometry. The simulated spectra's and near-field distributions have been obtained utilizing the frequency-domain solver with Floquet–Bloch boundary conditions and a tetrahedral mesh. Simulated non-percolated Au grains were drawn by an EM solver and were homogenized as a perfectly aligned Au array system onto the corrugated templates. Optical constants of a 6 nm thick Au film provided by Yakubovsky et al¹⁸⁰. were used in the EM simulations. The near-field distribution simulations were obtained along both $\sigma = 0$ and 90° polarization for a unit cell of infinite periodic arrays with different inter-particle distances along and across the corrugation direction. The power of the EM wave is assumed to be 1 W per unit cell. And the obtained 2D field distributions were obtained at the half height of Au grains, in the plane parallel to the sample surface distributions and are presented for (3×3) cell fragments of infinite periodic arrays. It is to be noted that the maximal near-field intensity can be measured beyond the aforementioned plane presented as the nearfield distribution images.

3. Plasmonic properties of non-percolated, anisotropic Au metal films

In this chapter the structural and optical properties of non-percolated ultrathin metal films on corrugated sapphire substrates are discussed, further the type of plasmons supported in these structures and their plasmonic hybridization and relaxation processes are discussed with simulated near-field spatial distributions and far-field steady state and transient absorption spectroscopy.

3.1. Formation and structure of non-percolated, anisotropic Au metal films

Ultrathin Au films of thickness $t \sim 2,4,6,7,8,9$, and 10 nm were deposited onto the fabricated corrugated templates with $P \sim 290\text{nm}$ in a low deposition rate of $10 \text{ \AA}/\text{hour}$ at normal incidence angle. (as in Table 2.2). During the electron beam deposition process for ultralow non-percolated film thickness, the fractional coverage f of the metal layer is $f < f_c$ (the film acts as isolated grains), where f_c is the percolation threshold as discussed in section 1.3b. Subsequently, the film approaches the percolation threshold ($f = f_c$) during increasing t and undergoes a transition into a semi-continuous connected state, according to the Volmer-Weber growth mechanism^{124,127}. Typically, for Au metal films with thickness $t \sim 8\text{--}10$ nm undergoes the transition from a non-conductive (localized electrons) to conductive (high mobility free electrons) with Drude metal characteristics based on the deposition conditions.



Figure 3.1. AFM topography image of ~ 7 nm thick non-percolated Au layer deposited on a corrugated template of $P \sim 290\text{nm}$ exhibiting the randomly oriented Au grains with diameter $d \sim 27$ nm. (k_x direction is along the spatial corrugation vector)²¹⁸.

On analyzing the structural properties of the $t \sim 7\text{nm}$ thick Au film in Figure 3.1. which was deposited at a very low rate of $10 \text{ \AA}/\text{hour}$ onto the corrugated template with period $P \sim 290\text{nm}$. The non-percolated layer exhibited Au grain like structures with diameter $d \sim 27\text{nm}$ due to the poor wettability of metals on the sapphire surfaces¹⁸¹. These clusters were distributed randomly onto the corrugated facets due to the high surface diffusivity on the relatively wide facets with $P \sim 290\text{nm}$ – similar to non-percolated metal films deposited on a flat surface (the surface reconstructed corrugated templates are short elevations of facets rather than high-aspect-ratio grating like structures)⁹⁷. As a result of this effect, for templates with $P \gg d$ the ordering of the nucleating Au grains was heterogeneous resembling the behavior of non-percolated films observed on flat sapphire templates (compare Figures 3.1 and 3.2a.).

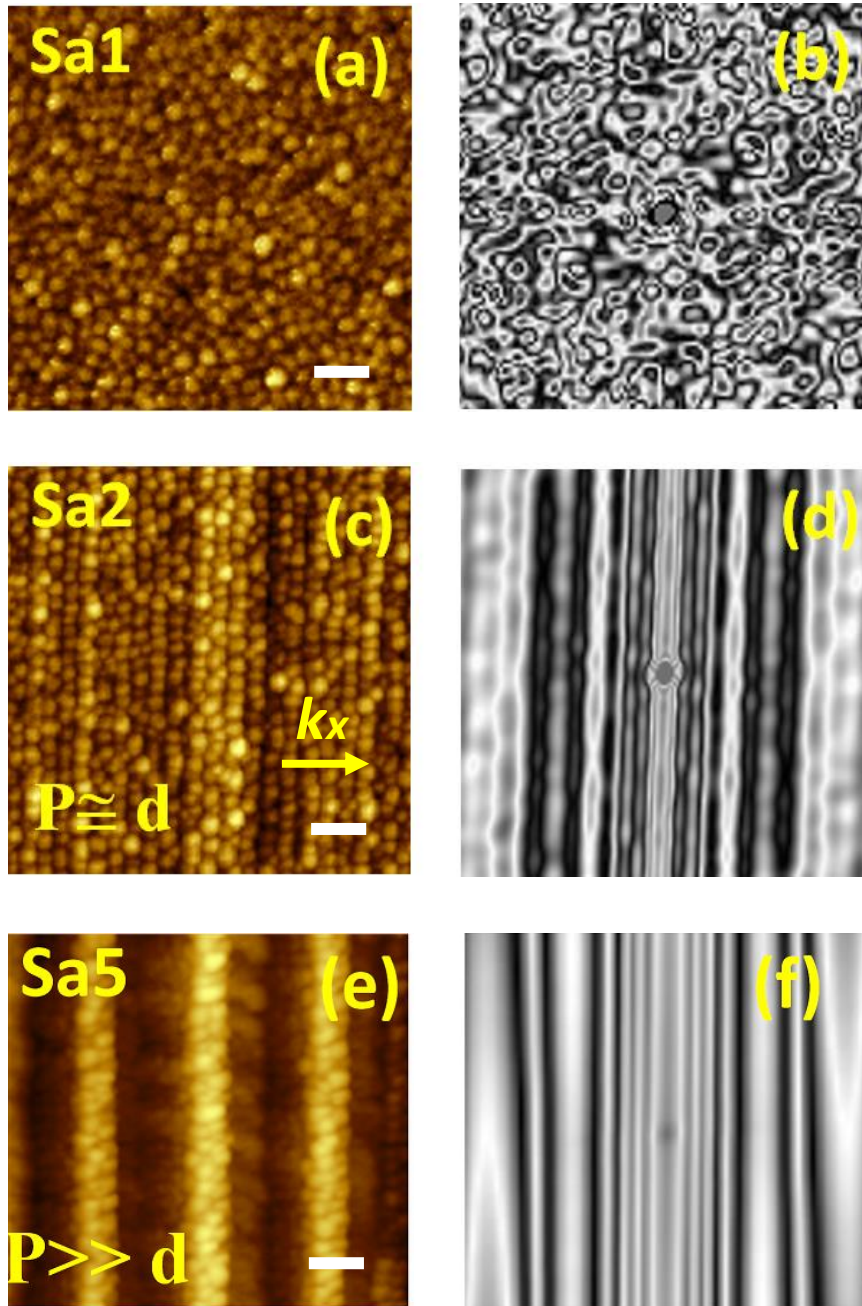


Figure 3.2 AFM topography images of Samples²¹⁸ (a), Sa1, (c), Sa2 and (e), Sa5. (The white bar represents 100 nm scale). Autocorrelation patterns from the AFM graphs of the samples (b), Sa1, (d), Sa2 and (f), Sa5.

Further in Figure 3.2c, an anisotropic in-plane ordering of nucleating Au grains was observed on templates with smaller period (P). As P decreases towards $P \cong d$ the motion of the randomly nucleating Au adatoms towards its adjacent adsorption sites is restricted along the spatial corrugation vector k_x . This is due to the surface corrugation acting as a barrier reducing the surface diffusivity along k_x . This can also be depicted as the optimum deposition condition for forming favorable Au nucleation density, where the ratio of flux of Au atoms arriving at the template surface and its adatom surface diffusivity results in formation of Au grains of $d \cong P$. Further, these thermodynamically-mediated kinetic processes of Au grains nucleation are

further favored by the excellent thermal-conductivity of the sapphire templates^{181,182} which results in oblate shaped nucleating grains with in-plane dimensions larger than its vertical dimension, making them as spheroidal Au disks during the deposition process. This facilitates in the ordering of the nucleating Au disks as chains on these short heighted periodic elevations of templates without utilizing complex glancing angle deposition techniques as used in other studies. The samples Sa2 shown in Figure 3.2c with the anisotropic in-plane array ordering exhibited nucleating Au disk diameter of $d \sim 27$ nm for an Au thickness $t \sim 6$ nm deposited at a rate of 10 \AA/hour on the corrugated sapphire with structural feature $P \cong d$ (where $P \cong 30$ nm and $d \sim 27$ nm). The anisotropic ordering of Au disks as chain-like arrays was along the corrugation long axis. In the contrary, the orientation of the Au disks was randomized for the sample Sa5 with template feature ($P \gg d$) (where $P \cong 150$ nm and $d \sim 27$ nm) as the value of P largely increased beyond d , as illustrated in Figure 3.2e. This is due to the enhanced surface-diffusivity along k_x onto the corrugated facets with large P as discussed earlier. Further, the in-plane pattern of the ordered Au disks resembling as chains of particles was confirmed from the autocorrelation function in Figure 3.2b, d and f. processed from the respective AFM images of samples Sa1, 2 and 5 in Figure 3.2a, c and e.

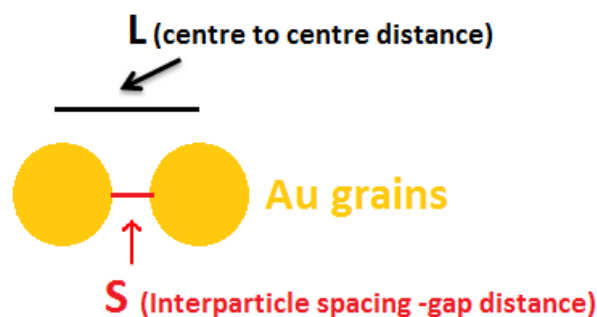


Figure 3.3, Schematics explaining the meaning of inter-particle spacing S ²¹⁸. The calculated values of inter-particle gap distance $S_1 \sim 3$ nm and $S_2 \sim 1$ nm for sample Sa2.

The Auto correlation image in (Figure 3.2d.) confirms that the disks are nucleated with an average inter-particle gap distance $S_1 \cong P$ dictated by the corrugation barriers along k_x . Whereas, in the direction perpendicular to k_x along the corrugation's long axis, the Au disks are ordered and more appear closer together with an inter-particle gap distance S_2 due to the enhanced surface diffusivity similar to a flat sample. The inter-particle gap distances S were measured from the line graphs obtained from the autocorrelation patterns. Figure 3.3. shows the schematic explaining inter-particle gap distance S and center to center distance L . Similarly, when measuring the inter-particle gap distances of the nucleating Au disks of samples Sa1 (flat) and Sa5 (with feature $P \gg d$) from their autocorrelation patterns (in Figures 3.2b. and 3.2f.) exhibited similar inter-particle distances S along k_x and the corrugation long axis. The similar values of S measured in these samples were same as the value of S_2 along k_x for sample Sa2 due to the increased surface diffusivity on these sample similar to the flat sample. Only the sample Sa2 along the direction of k_x exhibited an interparticle spacing S_1 resulting in an anisotropic ordering.

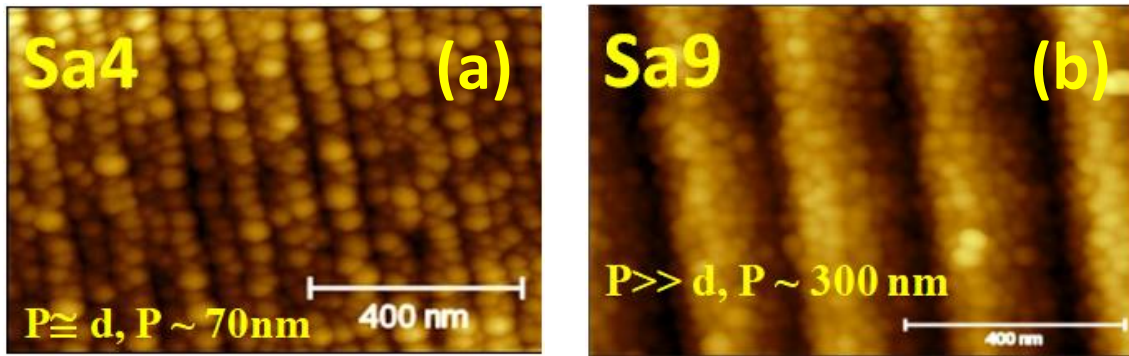


Figure 3.4a, b. AFM topography of samples Sa4 and Sa9 exhibiting Au disks with larger diameter $d \sim 60 \text{ nm}$ ²¹⁸.

This effect of the anisotropic in-plane ordering of the nucleating Au disks was studied for a similar set of samples with larger value of d . Here, the electron beam deposition rate was increased to promote the nucleation of Au disks with a larger diameter $d \sim 60 \text{ nm}$. This increase in the flux of particles reaching the surface influenced the nucleation density of the Au disks, resulting in larger disk diameters. Figures 3.4a. and 3.4b. show the AFM images of the samples Sa4 and Sa9 with the nucleated Au disk diameter of $d \sim 60 \text{ nm}$. These set of samples Sa4, Sa6 and Sa9 were fabricated as a result of depositing Au films of $t \sim 7.5 \text{ nm}$ onto the templates with varying P at an increased deposition rate of 79 \AA/hour . Similarly, the ordering of disks in the sample Sa4 with $P \sim 70 \text{ nm}$ ($P \cong d$) were aligned as a chain-like arrays along the corrugation long axis, whereas their orientation became randomized for the Au deposited on sample Sa9 ($P \sim 300 \text{ nm}$, $P \gg d$).

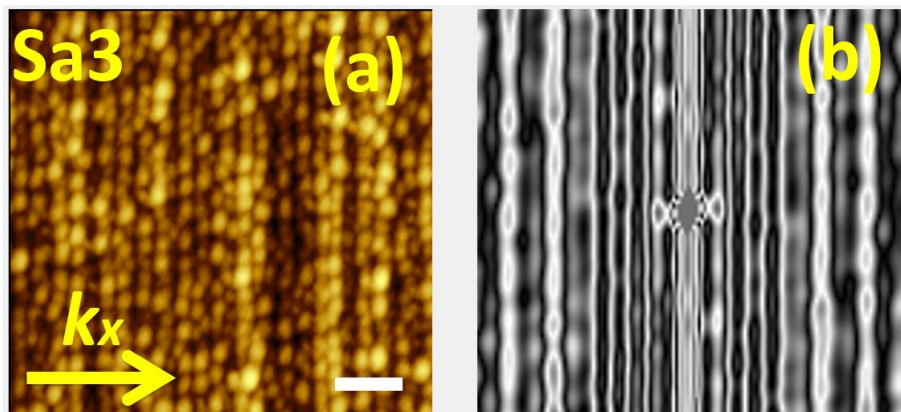


Figure 3.5(a) AFM topography images of Sample Sa3²¹⁸. The white bar represents 100 nm scale **(b)**Autocorrelation patterns from the AFM graphs of the sample Sa3.

Further, Figures 3.5a. and 3.5b. exhibits the AFM image and its corresponding autocorrelation function patterns of sample Sa3 comprising of elliptically shaped Au disks. This sample with an Au disk in-plane shape aspect ratio of about $1.6:1.25$ (32 nm along $\sigma = 90^\circ$ and 25nm along $\sigma = 0^\circ$) (azimuthal angle σ is explained in Figure 2.12c.) was fabricated when corrugated templates with features $P \cong d$ was placed at the edge of the e-beam evaporator stage and coated

with Au $t \sim 7\text{nm}$. This anisotropic shape effect was due to the slightly off-normal deposition angle (ξ) occurring along the direction of k_x for samples placed at the edge of the deposition stage due to the e-beam deposition cone¹⁸³ as in Figure 2.5.

3.2. Optical response of non-percolated, anisotropic Au metal films

Ellipsometry was used to measure the far-field polarized reflectance of the fabricated 2D-Au disk arrays. Figure 3.6b. shows the reflectance spectra measured for the samples (Sa11 - Sa17) with a constant period $P \sim 290\text{ nm}$ and deposited with varying Au thicknesses ranging from $t \sim 2\text{ nm}$ to 10nm .

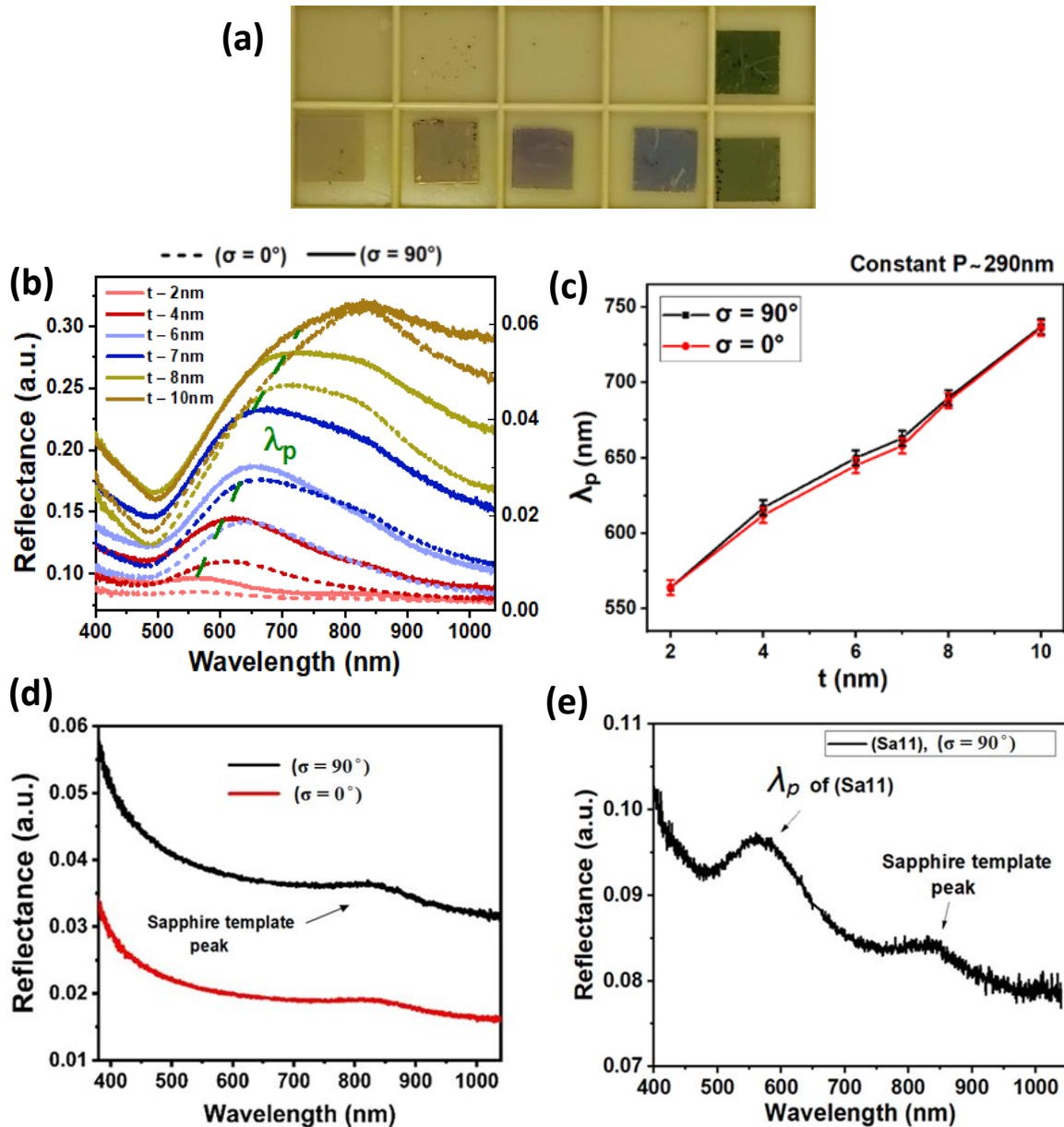


Figure 3.6(a). Photographic image showing the fabricated plasmonic samples deposited with varying incremental Au thickness from $t \sim 2\text{ nm}$ to 10 nm exhibiting a range of colours. (b). Reflectance measured for Samples (Sa11 - Sa17) with a constant template period $P \sim 290\text{ nm}$ deposited with varying Au thickness ranging from $t \sim 2\text{ nm}$ to 10 nm (c). quantitative comparison of λ_p at $\sigma = 0^\circ$ and $\sigma = 90^\circ$ showing

very low values of $\Delta\lambda_p$ for samples from the plot in Figure 3.6a. **(d)**. Reflectance measurement on a bare, non-reconstructed M-plane sapphire template with an elevated peak at 831nm. **(e)**. Reflectance measurement of Sa11 with 4nm thick Au showing sapphire template peak at 831nm and λ_p of Sa11 around 575 nm²¹⁸.

It exhibits an incremental red-shift in the plasmon wavelength position (λ_p) and an increase in peak broadening for samples with increasing Au thickness t . The broad peak observed near 830nm is not as a result the plasmon resonance but the sapphire template peak - see Figure 3.6e. The plasmon wavelength shifted from $\lambda_p \sim 565$ nm (with a FWHM ~ 100 nm) for sample with $t \sim 2$ nm to $\lambda_p \sim 737$ nm (FWHM > 450 nm) for the sample with $t \sim 10$ nm at both $\sigma = 90^\circ$ (dotted lines) and $\sigma = 0^\circ$ (continuous lines) polarization angles see Figure 3.6b. This incremental plasmon shift ($\Delta\lambda_p$) is indicated by the dotted green line. This effect of plasmon peak broadening and shifting is attributed due to the increasing interaction between *LSPR* modes of individual Au disks as they nucleate more denser and closer to each another in increasing film t according to the Volmer-Weber growth mechanism as discussed in section 3.1.

Further, the broadening of the λ_p peak in increasing Au t is specifically caused by the increase in the rate of radiative damping, as dipoles excited in these randomly ordered Au disks interacts in a collective and a coherent way, giving rise to a radiant mode^{99,153}. This plasmonic behaviour is also dependent on the number of particles N within the illuminated area. Thus, significantly influencing the observed plasmonic properties in non-percolated metal films.

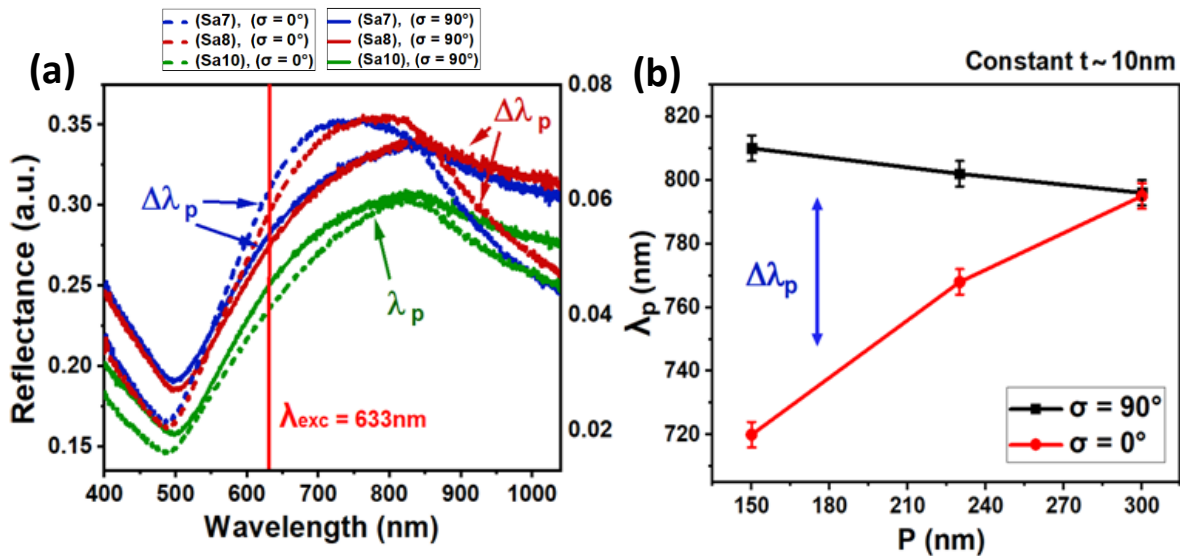


Figure 3.7 (a) Reflectance measured for the samples Sa7, Sa8 and Sa10 (with constant $t \sim 10$ nm, and varying $P \sim 150, 230$ and 290 nm) exhibiting an anisotropic response between $\sigma = 0^\circ$ and $\sigma = 90^\circ$ polarization components at decreasing corrugation P . **(b)** quantitative comparison of λ_p for the samples from the plot in Figure 3.6c. confirming the anisotropic response due the increase in value of $\Delta\lambda_p$ at decreasing value of P ²¹⁸.

Otherwise, isolated metal grains with very small diameter such as $d \sim 27$ nm absorbs most of the illuminated excitation field in its plasmon λ_p resonance regime, remaining non-radiant according to the Mie theory^{153,184}. Furthermore, the region of coupling between the confined

LSPR near-fields of two neighbouring Au disks gives rise to an enormous near-field enhancement - which are connected with the collective plasmon modes, this phenomenon will be discussed in detail in section 3.3. Similarly in Figures 3.6c, when analysing the λ_p peak positions of samples (Sa11–Sa17) obtained from Figures 3.6b. which was performed for a constant fixed period $P \sim 290$ nm and varying thickness t revealed that $\Delta\lambda_p$ – (representing the difference in plasmon resonance positions between $\sigma = 0^\circ$ and $\sigma = 90^\circ$ polarization angles) is very low and insignificant. However, in Figure 3.7a, which exhibits the reflectance spectra for the samples (Sa7, Sa8 and Sa10) with a constant value of $t \sim 10$ nm and varying period P exhibited an anisotropic plasmonic response between $\sigma = 0^\circ$ and $\sigma = 90^\circ$ for the samples Sa7 (blue spectra) and Sa8 (red spectra). The data presented in Figure 3.7b. provides a more accurate comparison of the λ_p plasmon positions at $\sigma = 0^\circ$ and $\sigma = 90^\circ$ obtained from the plot in Figure 3.7a. which exhibits the increased value of $\Delta\lambda_p$ for the samples with decreasing value of P . This optical response with larger values of $\Delta\lambda_p$ under linearly polarized excitation is due to the anisotropic in-plane ordering of the nucleating Au disks deposited on corrugated templates with smaller period ($P \cong d$) as discussed in section 3.1.

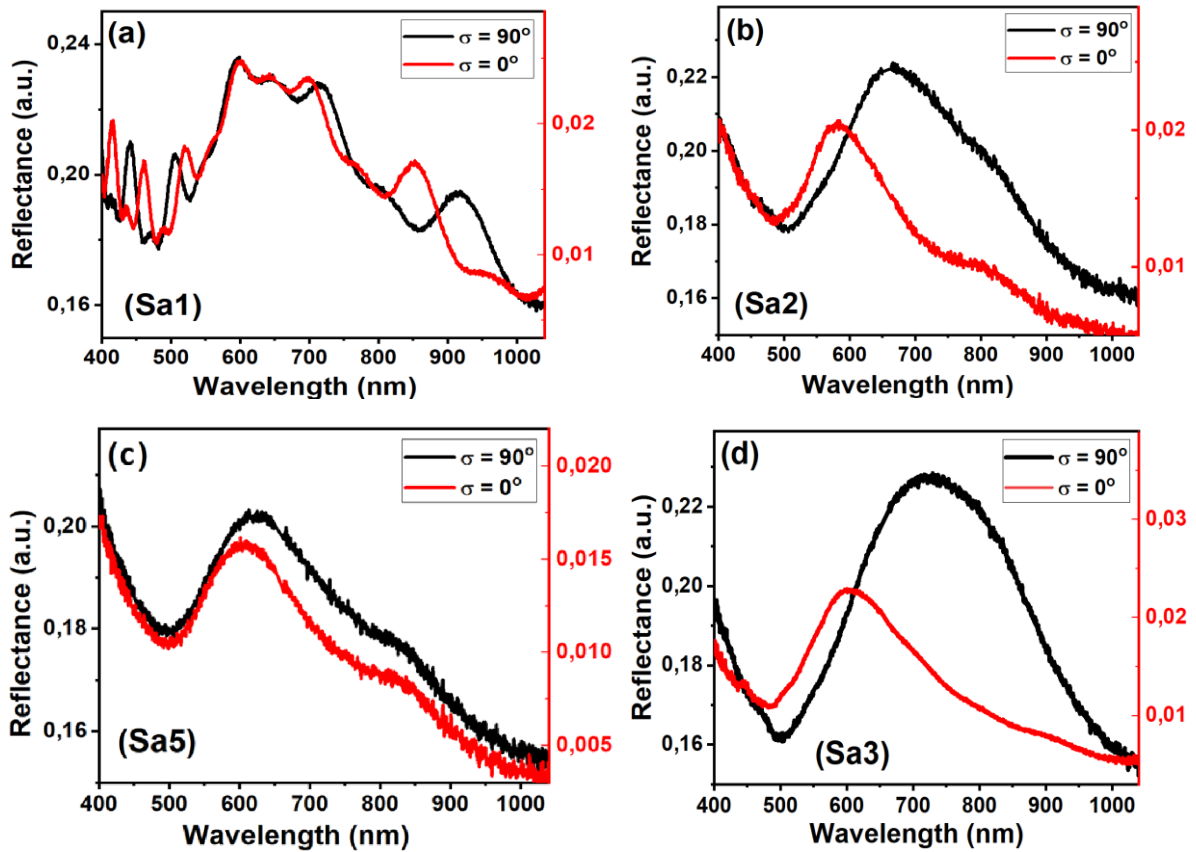


Figure 3.8. Polarized reflectance analysis of the samples²¹⁸ (a) Sa1, (b) Sa2, (c) Sa5 and (d) Sa3 performed at the incidence angle $\theta=50^\circ$.

The different inter-particle distances S along and across the corrugation vector k_x which causes different plasmon coupling strengths, restoring forces and decay rates between the Au disks along ($\sigma = 0^\circ$ and $\sigma = 90^\circ$) was the primary reason for the large anisotropy values of $\Delta\lambda_p$ for samples with $P \cong d$. Several works have also reported this effect as a result of the plasmonic

coupling between subwavelength *MNPs* under a linearly polarized excitation^{185,186}. Subsequently, samples coated with $t \sim 6$ nm Au and with similar inter-particle distances S along both $\sigma = 0^\circ$ and $\sigma = 90^\circ$ measured for Sa1 (flat template) and Sa5 (with $P \gg d$) lead to lower values of $\Delta\lambda_p$ in Figures 3.8a and c. as compared to sample Sa2 (with $P \cong d$) which exhibited larger value of $\Delta\lambda_p$ (plasmonic anisotropy) in Figure 3.8b. validating the anisotropic trend. The reflectance spectra of sample Sa1 (flat) in (Figure 3.8a.) was dominated by interference fringes, which is attributed due to the Fabry-Perot like behavior of the transparent dielectric substrate coated with very thin non-percolated Au layer¹⁸⁷, which made it difficult to analyze its value of $\Delta\lambda_p$.

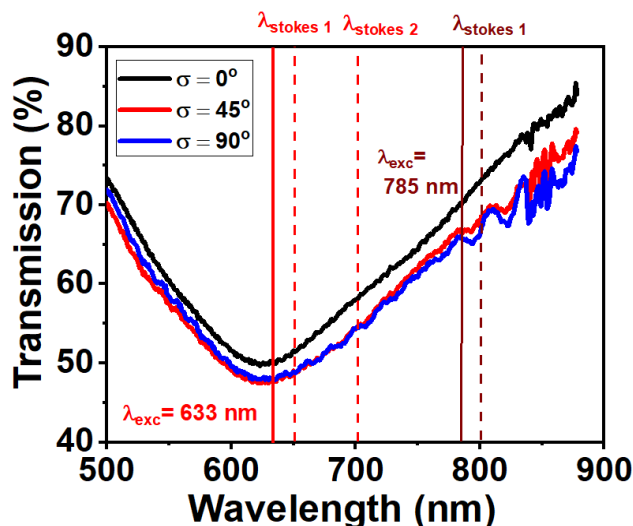


Figure 3.9. Polarized transmission spectra measured for $\sigma = 0^\circ$, 45° and 90° of the samples: **a.** Sa1 (with a flat template). The vertical lines indicate the Raman laser λ_{exc} and its corresponding λ_{Stokes} positions on the spectra²¹⁸.

As an alternative, its transmittance spectra in Figure 3.9. reveals its isotropic plasmonic response with negligible difference in λ_p positions between $\sigma = 0^\circ$ and $\sigma = 90^\circ$. The oblate shape of the nucleating Au disks did not influence the observed plasmonic anisotropy largely, due to the lack of significant $\Delta\lambda_p$ values, for both the sample with $P \gg d$ (Sa5) and the flat sample (Sa1) in Figures 3.8c and 3.9. This confirms that the different coupling rate between the nucleating disks based on S_1 and S_2 along $\sigma = 0^\circ$ and $\sigma = 90^\circ$ was the principal cause of the observed anisotropy in these samples. Similarly, Figures 3.8d. show the polarized reflectance spectra of sample Sa3 comprising elliptical disks with an in-plane shape aspect ratio of about 1.6: 1.25 (32 nm along $\sigma = 90^\circ$ and 25 nm along $\sigma = 0^\circ$) nucleated on the corrugated template with $P \cong d$. This sample exhibited slightly higher value of $\Delta\lambda_p$ when compared to the sample Sa2 with spherical disks (Figure 3.8b.). This combination of both shape anisotropy and inter-particle coupling effects is the reason for the higher value of $\Delta\lambda_p$ in this sample. To understand this anisotropic response of the Au disk chain-like arrays due to both shape anisotropy and inter-particle coupling effects *EM* simulations were performed on a corrugated Al_2O_3/Au disk array structure model. The optical constants for a 6-nm thick Au film described by Yakubovsky et al¹⁸⁰ and sapphire properties described by Paliks^{178,179} book of optical constants was used in the simulations.

When analyzing the simulated polarized reflectance spectra of the samples Sa2 and Sa3 with spherical and elliptical Au disk arrays as in Figures 3.10a, b. obtained for the angles $\sigma = 0^\circ, 45^\circ$ and 90° exhibited similar anisotropic trends at $\sigma = 0^\circ$ and 90° when compared to those collected in the experiments in Figure 3.8b and d. Although slightly red-shifted λ_p positions were observed at both $\sigma = 0^\circ$ and $\sigma = 90^\circ$ hereafter mentioned as λ_{TMp} at $\sigma = 0^\circ$ and λ_{TEp} at $\sigma = 90^\circ$ resonance positions.

This red-shifted λ_{TMp} and λ_{TEp} resonance positions is attributed to imperfections in nucleating Au disk orderings on the fabricated 2D-arrays when compared the perfectly ordered Au disk arrays modelled in simulations which results in a more uniform and stronger plasmon coupling. This explains the slightly red-shifted positions of λ_{TMp} and λ_{TEp} to longer wavelengths in the simulated spectra.

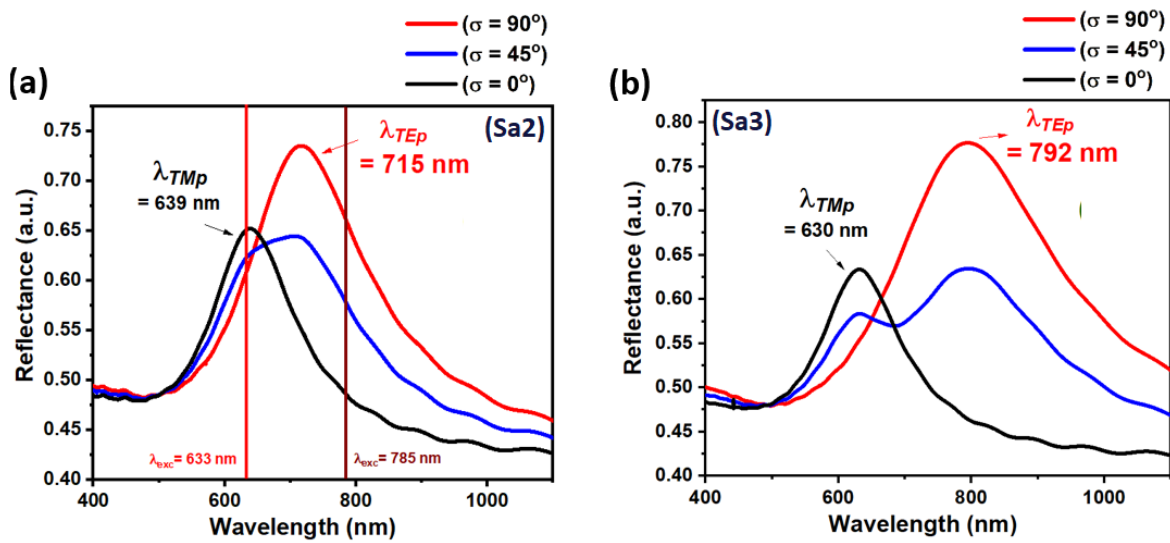


Figure 3.10. Simulated polarized reflectance spectra for angles $\theta=50^\circ$, $\sigma = 0^\circ, 45^\circ$ and 90° for samples **a.** Sa2 (spherical) and **b.** Sa3 (elliptical) Au grains. (The vertical lines represent the wavelength of the Raman laser excitation)²¹⁸.

The resulting plasmon hybridization due to these strong plasmon couplings in these fabricated ordered arrays is discussed more in detail in section 3.3. In Figure 3.10a. and b. at $\sigma = 45^\circ$ both the samples exhibit spectra's which is the linear combination of λ_p modes at $\sigma = 0^\circ$ and $\sigma = 90^\circ$ due to the contribution from both the inter-particle distances S_1 and S_2 . This effect is further confirmed by the isosbestic point at 500nm this confirms that this is not a higher order quadrupole mode as observed in nanoparticles with larger diameter due to retardation effects.

Similarly, polarized reflectance analysis performed on the samples nucleated with larger Au disk diameter $d \sim 60$ nm in Figure 3.11a. exhibited similar anisotropic plasmonic trends between $\sigma = 0^\circ$ and $\sigma = 90^\circ$. The sample Sa4 ($P \cong d$) exhibited a $\Delta\lambda_p$ value of approximately 75 nm, whereas the sample Sa9 ($P \gg d$) exhibited a smaller $\Delta\lambda_p$ value around 30 nm (in Figure 3.11b - compare plots at (x axis) $P = 75$ nm and 240nm). This further verifies the relationship of the in-plane grain ordering resulting in different inter-particle gap spacing S_1 and S_2 at $\sigma = 0^\circ$ and $\sigma = 90^\circ$ causing the observed plasmonic anisotropy. Furthermore, in Figure 3.11a. a more intense λ_p scattering intensity when compared to the spectra presented in Figures 3.8 is observed

due to the stronger scattering in the larger Au disk diameter ($d \sim 60$ nm) with larger cross-section, according to the Mie theory¹⁸⁴.

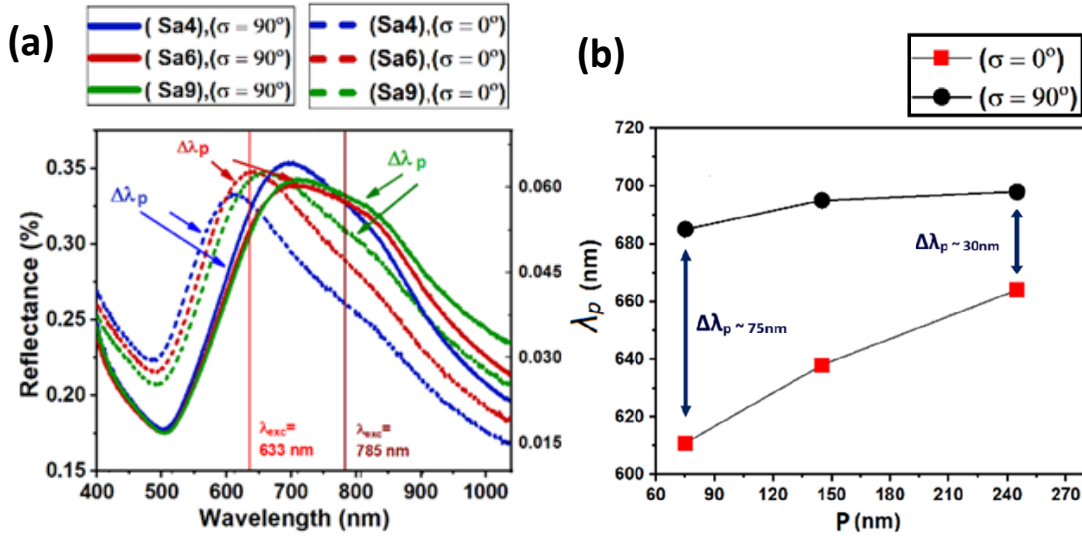


Figure 3.11a, Reflectance spectra of samples Sa4, Sa6 and Sa9. **b.** comparison of the position of λ_p of samples Sa4, Sa6 and Sa9 listed in Figure 3.10a. showing the largest value of $\Delta\lambda_p$ for the samples with the shortest corrugation period P ²¹⁸.

3.3. Plasmonic hybridization on 2D-MNP arrays

For metal nanoparticle arrays with inter-particle gaps as small as $S \leq r$, where r is the radius of the MNP, when another particle enabling the same field magnitude $E_p(\lambda_p)$ is nearby an MNP, the region of the coupling between their two confined near fields gives rise to an enormous near-field enhancement known as “plasmonic hotspot”. These hotspots related to “collective plasmonic modes” as observed in this study and its resulting plasmonic anisotropy dependent on σ , can be explained by the plasmon hybridization theory^{149,151,154}.

Both “dark-modes” exhibiting enhanced light absorption and “bright-modes” with enhanced scattering characteristics can be excited due to hybridization in these arrays with $S \leq r$. However, due to their vanishing oscillator strength in symmetric MNP dimers and chains, dark-plasmonic modes are not excited by linearly polarized free space excitation. Whereas, it is the bright-plasmonic modes with a non-zero oscillator strength due to their dipoles being aligned in-phase are excited by free-space linearly polarized excitation^{150,151}. The bright-plasmonic modes observed in the λ_p positions along TE ($\sigma = 90^\circ$) and TM ($\sigma = 0^\circ$) polarizations on dimers and *1D-MNP* arrays are described as; longitudinal (bonding) and transverse (anti-bonding) dipole mode. Due to this hybridization of plasmonic modes, depending on the inter-particle gap distance S and the number of particles N in the system, the anisotropic plasmonic effect arises in dimers and *1D-MNP* arrays^{154,156}. In the fabricated *2D-MNP* arrays discussed in this study, both $\sigma = 90^\circ$ and $\sigma = 0^\circ$ polarizations are considered to excite hybridized bonding plasmon modes assigned as λ_{TEp} and λ_{TMp} at $\sigma = 90^\circ$ and $\sigma = 0^\circ$ as in Figure 3.10a. Similarly, in these samples the plasmonic anisotropy arises due to the excitation of higher-order plasmonic modes, which are excited dependent on the different inter-particle gap distances S_1 and S_2 along

$\sigma = 0^\circ$ and $\sigma = 90^\circ$. In these arrays with $S \leq r$, hybridization induced excitation of both higher-order dark-modes described as $\lambda_{p2,4}$ (characterized by even integer fraction of the fundamental dipole mode wavelength) and higher-order bright-modes described as $\lambda_{p3,5}$ (characterized by odd integer fraction of the fundamental dipole wavelength) cannot be neglected^{154,156}. The red-shifting and broadening of λ_p modes are observed for the fabricated ordered Au arrays with $S \leq r$ as these higher-order plasmonic modes dependent on S pushes the fundamental lower-order dipole mode to longer wavelengths causing the observed plasmonic anisotropy. These, bright higher-order modes at $\lambda_{p3,5}$ can be distinguished from the lower-order dipole mode in far-field optical spectra only in MNP array system with finite N (typically $N \leq 5$). In this study, where N is assumed to be very large, this further red-shifts the higher-order bright-modes to longer wavelengths and to degenerate into the peak corresponding to the lowest-order dipole mode^{151,154} as λ_{TMp} at $\sigma = 0^\circ$ and λ_{TEp} at $\sigma = 90^\circ$ due the different inter-particle gaps S at these σ angles.

Importantly, these higher-order bright-modes at $\lambda_{p3,5}$ are sub-radiant in their nature, as the electric field induced surface charge density in these individual *MNPs* forms dipole like characteristics, whereas its charge density alternates along the *MNP* chain, thus reducing its overall dipole moment collectively as arrays¹⁵⁴. Due to this effect, these bright sub-radiant $\lambda_{p3,5}$ modes radiate less far-field scattering as compared to the super-radiant λ_p (lower-order dipole mode). The lower-order dipole mode is also a collective plasmon mode in these arrays with $S \leq r$ but radiates the coupled near-field into far-field radiation effectively and instantaneously due to its non-zero dipole moment in these frequencies collectively as arrays. As a result of this phenomenon of dynamic depolarization due to both strong coupling and instantaneous far-field radiation this mode can be described as an antenna mode. In contrast as a result of the change in the effective modal index of these particle arrays at $\lambda_{p3,5}$ to support propagating (sub-radiant SPP modes) the bright-higher order modes can be described as waveguide modes. These sub-radiant modes are advantageous to increase the excited plasmon lifetime as well as exhibiting intense nearfield.

This phenomena of both efficient light collection into the near-field and plasmon propagation induced reduced far-field radiation at these sub-radiant modes wavelengths $\lambda_{p3,5} < (\lambda_p$ lower-order dipole mode), occurs only when $S \ll r$ in ordered *MNP* array systems due to hybridization as in these experimentally studied samples. This phenomenon can be further evident when deconvoluting the obtained far-field optical spectra into separate scattering and absorption components^{189,190}. This exhibits the contributions of far-field radiative losses from the efficient light coupling occurring due to these hybridized modes. A few studies^{149,151,154} have also reported this excitation of hybridized-collective SPP mode in ordered metal array systems with $S \leq r$. Similarly, EM near-field simulations were performed, and the obtained near-field spatial distributions were corroborated with the polarized (far-field) reflectance measurements to characterize these hybridized-collective plasmon modes. Figures 3.12a-d. shows the near-field spatial distribution for the sample Sa2 with spherical Au disks excited at their resonance peak positions of $\lambda_{exc} = 639\text{nm}$ and $\lambda_{exc} = 715\text{nm}$ at ($\sigma = 0^\circ$ and $\sigma = 90^\circ$). The near-field distribution clearly exhibits that the restoring force in the collective modes is reduced along both $\sigma = 0^\circ$ and $\sigma = 90^\circ$ polarization as $S \ll r$ in both the directions on these fabricated 2D-arrays¹⁹¹. Further, they confirm the hybridization of the excited plasmonic modes with giant

near-field enhancements. These results further support the red-shifting of both the plasmon resonances at $\sigma = 0^\circ$ and $\sigma = 90^\circ$ beyond the uncoupled single-particle λ_p position of sample Sa11 deposited with Au $t \sim 2$ nm (low metal fill-factor) as in Figure 3.6d.

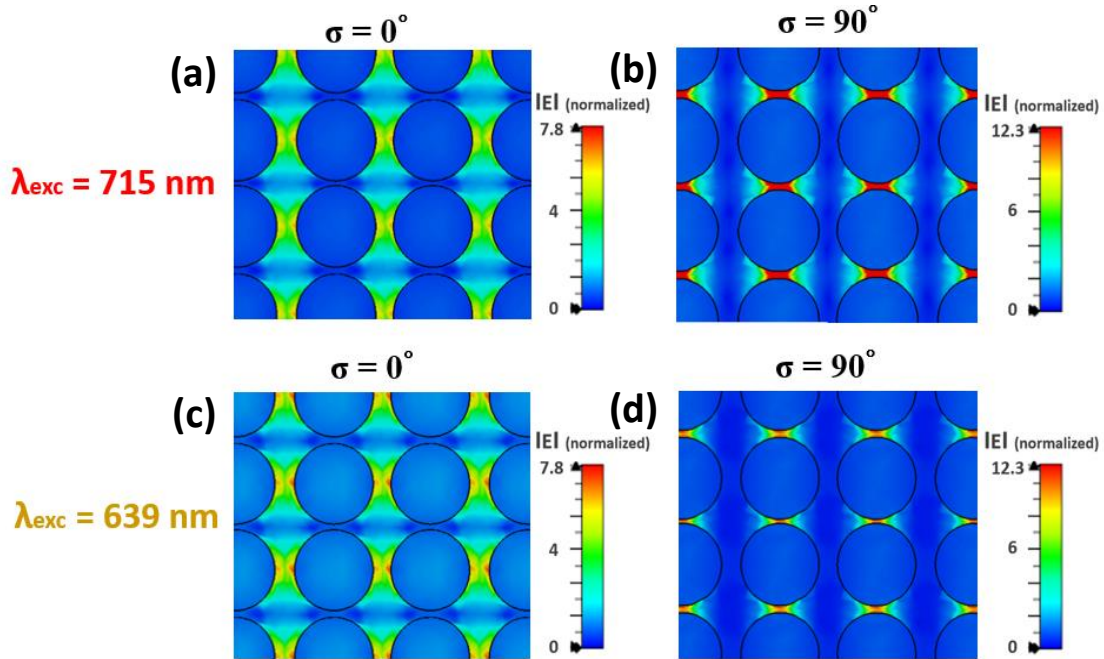


Figure 3.12a, b. Simulated EM near-field distribution images of sample Sa2 at $\lambda_{exc} = 715$ nm (for $\sigma = 0^\circ$, and 90°) and **c,d.** for sample Sa2 at $\lambda_{exc} = 639$ nm (for $\sigma = 0^\circ$, and 90°)²¹⁸.

The strongest coupling was observed at $\sigma = 90^\circ$ for both excitation wavelengths, regardless of the λ_{TMp} peak position at 639nm for $\sigma = 0^\circ$ or the λ_{TEp} peak position at 715nm for $\sigma = 90^\circ$ as in the simulated spectra in Figure 3.10a. This effect is due to the shorter inter-particle distance S_2 along $\sigma = 90^\circ$ when compared to S_1 along $\sigma = 0^\circ$. However, a moderately large spatial distribution was observed at $\lambda_{exc} = 715$ nm in Figure 3.12b. where the λ_{TEp} resonance at $\sigma = 90^\circ$ is at its maximum when compared to $\sigma = 90^\circ$ under $\lambda_{exc} = 639$ nm in Figure 3.12d. Subsequently, for $\sigma = 0^\circ$ as a result of the larger value of S_1 along this polarization angle the near-field was not as strong as it is for $\sigma = 90^\circ$ at both excitation wavelengths. The near-field at $\sigma = 0^\circ$ is weak when compared to $\sigma = 90^\circ$ even for $\lambda_{exc} = 639$ nm where the λ_{TMp} resonance peak is at its maximum in Figure 3.10a.

Further, the simulated near-field distribution of the sample Sa2 obtained at different excitation wavelengths of 600nm, 639nm, 675nm, 715nm and 785nm are presented in Figure 3.13. to compare and correlate the excitation wavelengths of the experimental SERS measurements and simulations with respective to their plasmon resonance peak positions which will be discussed in detail in Chapter 5. It further reveals that $\lambda_{exc} = 675$ nm near the wavelength of the sub radiant modes exhibit near-field amplification both in intensity and large spatial distribution along $\sigma = 0^\circ$ and $\sigma = 90^\circ$ due to the collective plasmonic hybridization on these 2D arrays.

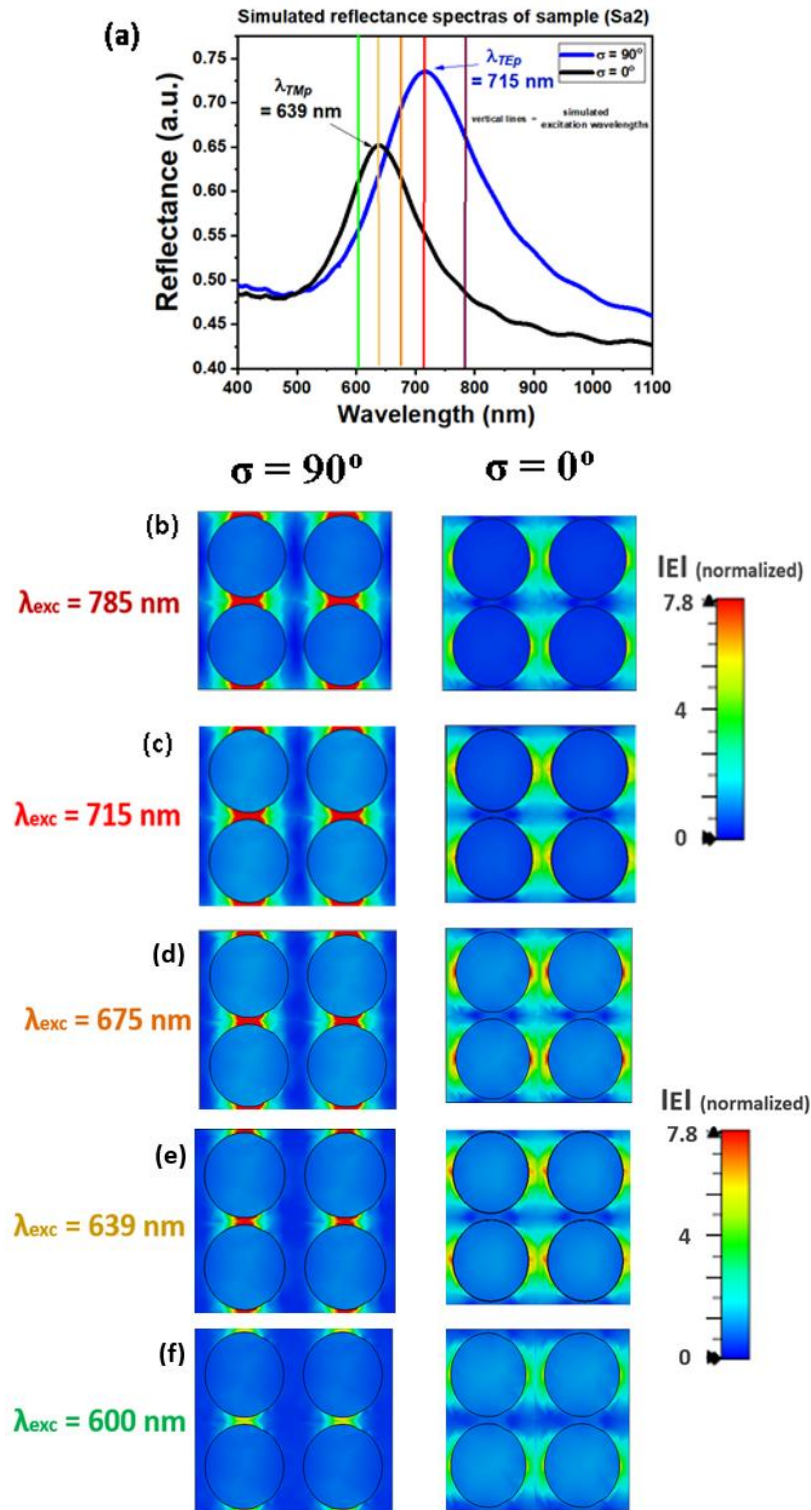


Figure 3.13. a, Simulated polarized reflectance spectra of the homogenized sample (Sa2) at ($\sigma = 0^\circ$) and ($\sigma = 90^\circ$) the vertical lines in the spectra represents the excitation wavelength positions for the simulated near-field distribution images in **b**, for $\lambda_{exc} = 785 \text{ nm}$, **c**, for $\lambda_{exc} = 715 \text{ nm}$, **d**, for $\lambda_{exc} = 675 \text{ nm}$, **e**, for $\lambda_{exc} = 639 \text{ nm}$ and **f**, for $\lambda_{exc} = 600 \text{ nm}$. (left column represent near-field distribution images at ($\sigma = 90^\circ$) and right at ($\sigma = 0^\circ$)²¹⁸.

3.4. Plasmonic anisotropy of non-percolated Au metal films on corrugated sapphire templates under steady state spectroscopy

In order to study the origin of plasmonic anisotropies due to the hybridization in these arrays with $S \ll r$ a set of anisotropic and isotropic plasmonic samples with $t \sim 8.5\text{nm}$ (near the percolating thickness at a deposition rate of $10 \text{ \AA} / \text{hour}$) were studied. Figures 3.14a and b. present the results that allows to distinguish samples that exhibit plasmonic anisotropy as a result of this hybridization, and those that do not based on incremental polarized reflectance measurements conducted at $\Delta\sigma = 20^\circ$. The sample Sa18 with $P \cong d$ (in Figure 3.12b.) exhibits an incremental shift in λ_p positions. It is evident that the plasmon modes excited in the $2D\text{-MNP}$ arrays at $\sigma = 0^\circ$ and $\sigma = 90^\circ$, are redshifted compared to the uncoupled single-particle λ_p of the sample Sa11 (with $t \sim 2 \text{ nm}$, low fill-factor) in Figure 3.6d. However, in Figure 3.14a for the sample Sa13 with $P \gg d$, (while it exhibits a redshift in λ_p when compared to the uncoupled particles λ_p of sample Sa11 as in Figure 3.6d) an isotropic plasmonic effect was observed even though the sample with $P \gg d$ exhibited short range ordering of MNPs as domains in AFM image (in Figure 3.1.) presented in section 3.1. Subsequently, here the red-shifting of λ_p for Sa13 as compared to Sa11 in Figure 3.6d. is due to the increase in interaction between the LSPR modes of the nucleating grains resulting from the increase in fill-factor for Sa13 with $t \sim 7\text{nm}$, when compared to Sa11 with $t \sim 2\text{nm}$.

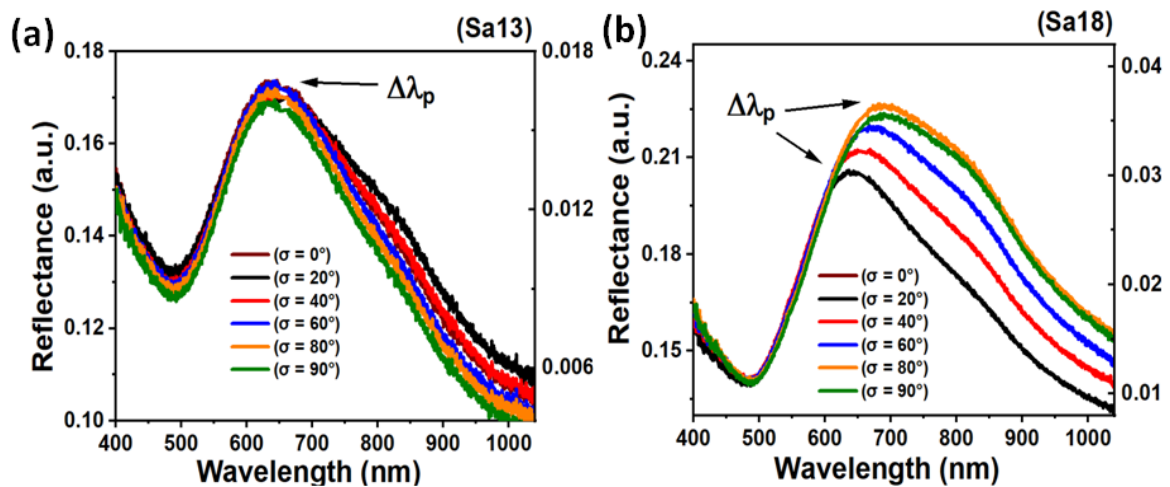


Figure 3.14 Polarized reflectance analysis performed at an angle of incidence $\theta = 50^\circ$ for the samples (a)Sa13 and (b)Sa18 at $\Delta\sigma = 20^\circ$. The sample Sa13 with $P \gg d$ shows minimal changes in λ_p but the sample Sa18 with $P \cong d$ shows large change in λ_p positions.

3.5. Plasmonic anisotropy of non-percolated Au metal films on corrugated sapphire templates under transient absorption spectroscopy.

In this section the anisotropic properties of non-percolated Au films were analyzed by the polarized-transient absorption spectroscopy. Figure 3.15a and b. shows the polarized transient absorption spectra (TAS) measured with $\lambda_{pump\ exc} = 650\text{nm}$ on a flat template with Au $t \sim 7.5\text{nm}$ exhibiting non-ordered Au grains at $\sigma = 0^\circ$ and $\sigma = 90^\circ$ polarization. The spectra's exhibit an isotropic plasmonic effect in contrast to the anisotropic plasmonic effect in Figure 3.15c and d. for the sample Sa3 with template feature $P \cong d$ exhibiting ordered Au grains with elliptically

shaped in-plane dimensions. Here the excited state's λ_p positions in the TAS spectra of sample Sa3 in Figure 3.15c and d. with ordered grains are blue shifted when compared to the λ_p positions of their respective steady state spectra in Figure 3.8d.

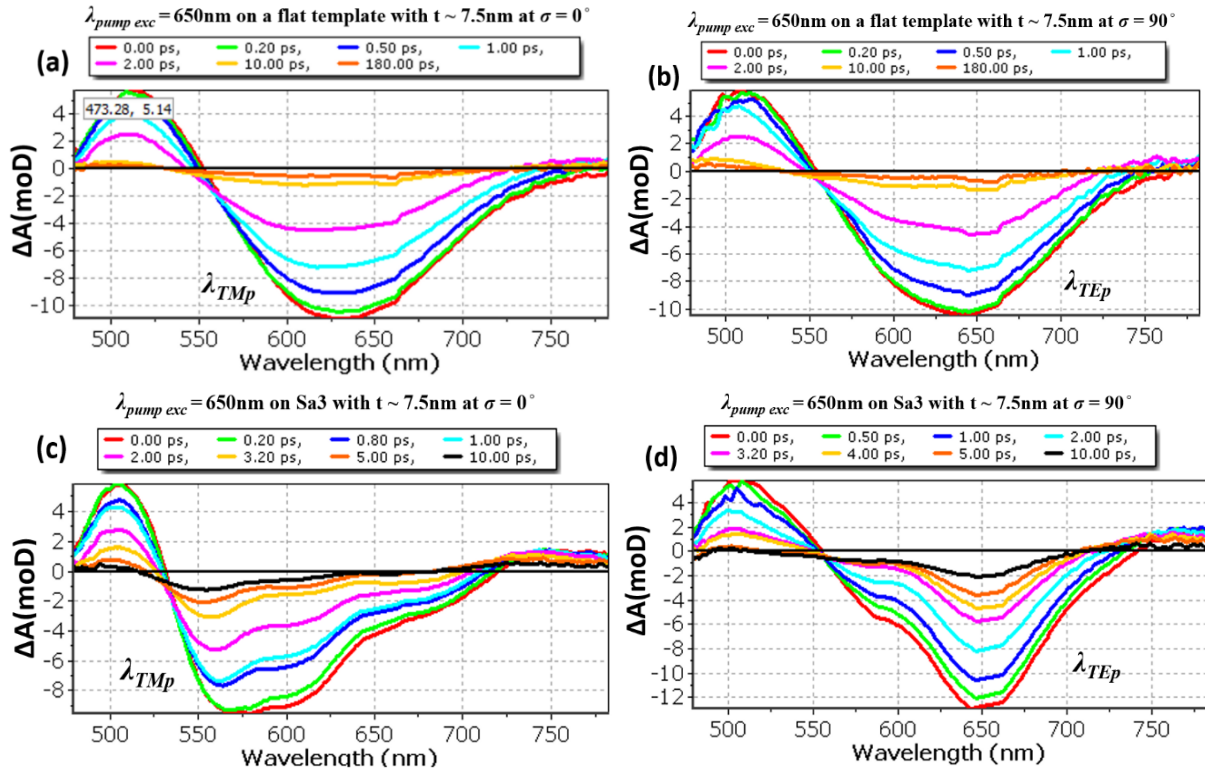


Figure 3.15. shows the TAS signal measured with $\lambda_{pump\ exc} = 650\text{nm}$ on the flat sample Sa1 at (a) $\sigma = 0^\circ$ and (b) $\sigma = 90^\circ$ polarization and the TAS signal measured with $\lambda_{pump\ exc} = 650\text{nm}$ on the flat sample Sa3 at (c) $\sigma = 0^\circ$ and (d) $\sigma = 90^\circ$ polarization.

This blue shift in the excited states both λ_{TEp} and λ_{TMp} peak positions for the sample Sa3 after $\sim 0.1\text{ps}$ is presumed due to the monochromatic ultrashort pulse excitation of plasmons onto the Au grains, resulting in photoinduced bleach of excited states to frequencies nearer to the excitation wavelength modulating its dielectric permittivity¹⁹². The incident pump pulse excites plasmon resonances which initially decays through radiation and then subsequently through Landau damping which induces the later non-radiative: electron-electron and electron-phonon scattering generating a high energetic carrier distribution of hot electrons and holes as in Figure 1.17^{158,159}. Further, when analysing the geometrical feature of the nucleating elliptical Au grain on sample Sa3 with features $P \cong d$ in Figure 3.5a, apart from its in-plane shape aspect ratio of about $1.6:1.25$ ($\sim 32\text{ nm}$ along $\sigma = 90^\circ$ and $\sim 25\text{nm}$ along $\sigma = 0^\circ$), it's out of plane diameter is presumed to be less than $\sim 7.5\text{nm}$, based on the deposited film thickness of $t \sim 7.5\text{nm}$, resulting as a triaxial ellipsoid structure in geometry.

For *MNPs* with radius $r < 10\text{nm}$ the damping factor γ becomes a function of r as electron-surface scattering increases since the diameter d of the *MNP* becomes less than the mean free path of the conduction band electrons (which is approximately in the range of tens of nanometers). This increase in the rate of plasmon decay based on the equation 53.3 is due to

elastic scattering of electrons on the surface of *MNP* with size less than the length of the mean free path of electrons^{135,71}.

$$\gamma(r) = \gamma_o + \frac{A v_F}{r} \quad (53.3)$$

where γ_o is the bulk damping constant, v_F is the Fermi velocity of the electrons and A is the theory dependent parameter incorporating details of isotropic or diffuse scattering.

This contribution of electron surface scattering due to the sub 10nm out of plane diameter of the triaxial ellipsoidal particle, further increases the rate of plasmon decay and broadens the plasmon bandwidth Γ , and resulting in enhanced generation of hot electrons on these ultrathin film-based samples. This population of energetic carriers after $\sim 0.1ps$ further facilitated by the collective nearfields (hotspot) on the surface of *MNPs*, can alter the effective dielectric environment on the surface of the *MNPs* due to the generated hot electrons temperature and influence their interparticle spacing S .

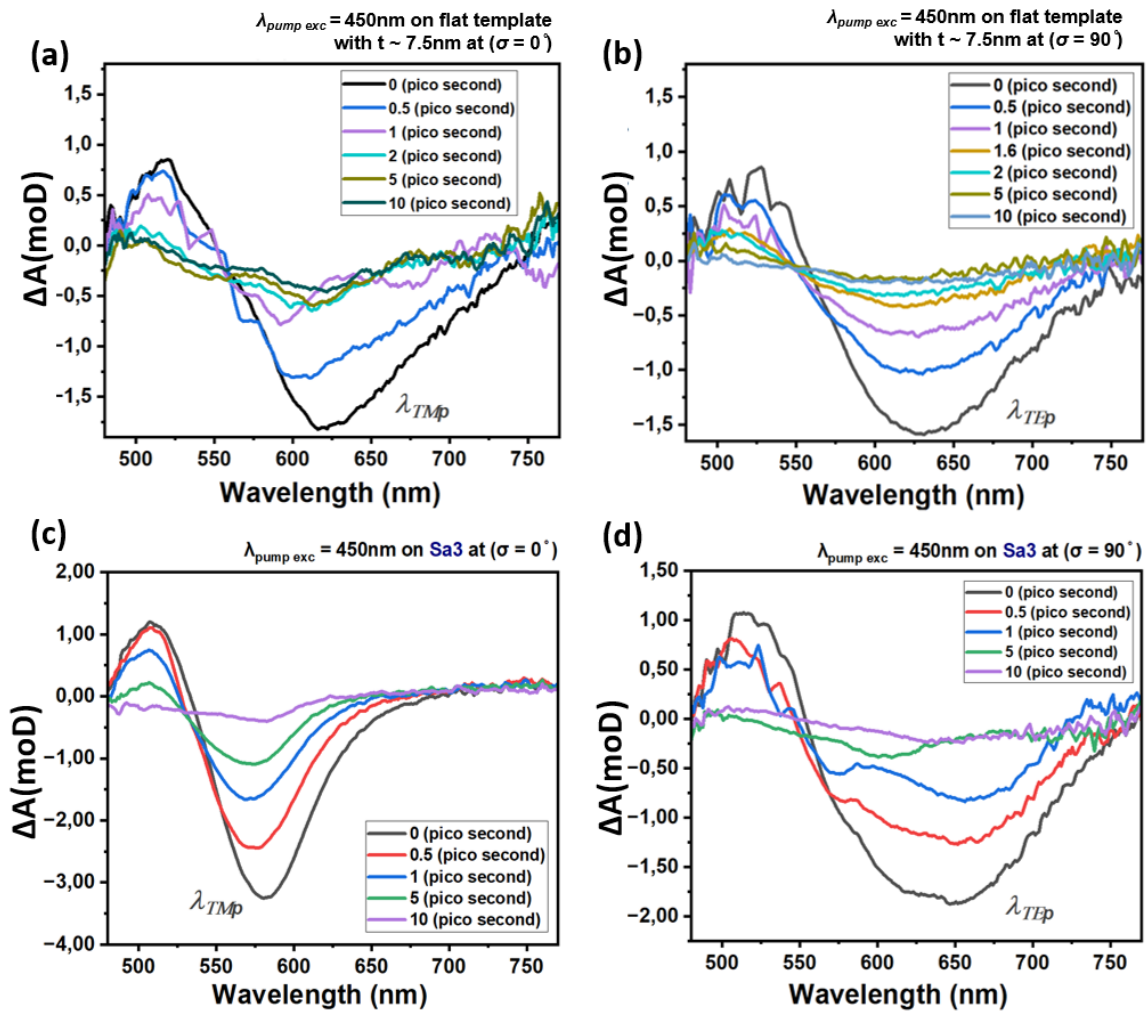


Figure 3.16 shows the TAS signal measured with $\lambda_{pump\ exc} = 450nm$ on the sample Sa3 at (a), $\sigma = 0^\circ$ and (b), $\sigma = 90^\circ$ polarization exhibiting LSPR positions at $\sim 560nm$ and $\sim 660nm$. shows the TAS signal measured with $\lambda_{pump\ exc} = 450nm$ on the sample Sa3 at (c), $\sigma = 0^\circ$ and (d), $\sigma = 90^\circ$ polarization exhibiting LSPR positions at $\sim 560nm$ and $\sim 660nm$.

Even small changes in the dielectric environment of the gaps with spacings $S \ll r$ due to these hot carriers can cause significant blueshift or redshift of the excited states λ_p positions measured in transient analysis with pump-probe delays in the picosecond temporal range¹⁹². Further, the analysis of the spectra in Figure 3.15c and d. is presumed to reveal the manifestation of additional higher-order modes which were not manifested in the steady state measurements in Figure 3.8d. The λ_{TMp} position of the excited non-radiative states in Figure 3.15c was blue shifted $\sim 30\text{nm}$, with additional peaks at $\sim 611\text{nm}$ and 680nm when compared to the single λ_{TMp} position excited on steady state measurements in Figure 3.8d. Further, the λ_{TEp} position in Figure 3.15d was blue shifted $\sim 100\text{nm}$, with additional peak at $\sim 590\text{nm}$ when compared to the λ_{TEp} position excited on steady state measurement in Figure 3.8d. Apart from the in-plane shape induced anisotropy this large blueshift of the λ_{TEp} in transient spectra is presumed due to the lower value of S_2 at $\sigma = 90^\circ$ as the generated hot electrons influence more effectively in modulating the permittivity in these smaller gaps when compared to the larger value of S_1 at $\sigma = 0^\circ$. Subsequently, the polarized TAS peaks λ_{TEp} and λ_{TMp} of the excited non-radiative states in Figure 3.16c. and d. for sample Sa3 excited under $\lambda_{pump\ exc} = 450\text{nm}$ (near the inter and intra-band transition frequencies) were similar to excited peak positions at $\lambda_{pump\ exc} = 650\text{nm}$ (near the collective plasmon frequency) in Figure 3.15c. and d. This shows that the excited charge carrier states are bleached and blue shifted independent of the excitation wavelength in these samples with $S \ll r$. However, the presumed additional peaks of the hybridized modes on Sa3 were not observed under $\lambda_{pump\ exc} = 450\text{nm}$ (near the inter and intra-band transition frequencies) in Figure 3.16c and d. The additional modes were only observed at the $\lambda_{pump\ exc}$ at 650nm (near the collective plasmon frequency) in Figure 3.15c. and d. Further, Figure 3.17b. shows the graph plotted for the λ_{TMp} at $\sigma = 0^\circ$ and λ_{TEp} at $\sigma = 90^\circ$ positions of polarized-transient absorption measurements on samples deposited with different Au thickness t on template features $P \gg d$.

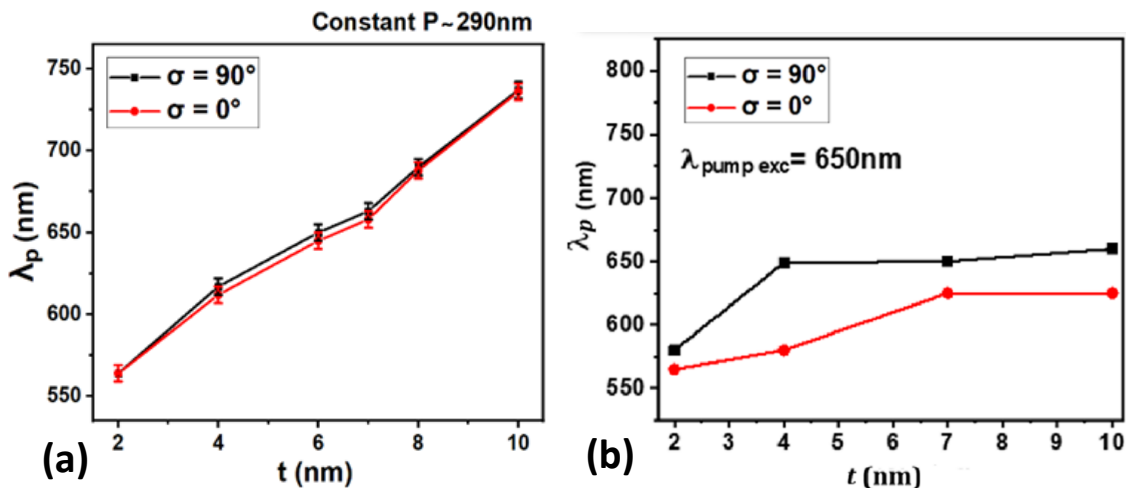


Figure 3.17. (a) shows the graph plotted with the λ_{TMp} at $\sigma = 0^\circ$ and λ_{TEp} at $\sigma = 90^\circ$ positions for polarized-steady state measurements performed on samples with features $P \gg d$ and varying Au thickness $t \sim 2,4,7,10$ exhibiting isotropic plasmonic response (b) shows the graph plotted with the λ_{TMp} at $\sigma = 0^\circ$ and λ_{TEp} at $\sigma = 90^\circ$ positions by polarized-TAS measurements performed under $\lambda_{pump\ exc}$ at 650nm on the samples with features $P \gg d$ and varying Au thickness $t \sim 2,4,7,10$ exhibiting an anisotropic plasmonic response which was invisible in steady state measurements.

The analysis revealed contrary results of anisotropic effect when compared to graph plotted for the λ_{TMp} at $\sigma = 0^\circ$ and λ_{TEp} at $\sigma = 90^\circ$ positions of polarized steady state measurements exhibiting isotropic effect between $\sigma = 0^\circ$ and $\sigma = 90^\circ$ – compare Figure 3.17a and b. Subsequently, this analysis revealed that the excited non-radiative states TAS peaks at λ_{TEp} and λ_{TMp} in Figure 3.17b. red-shifts for increasing Au film thickness t where their inter-particle spacing S decreases for increasing Au thickness t due to increasing fill factor of the metal. This shows that the bleaching of the excited non-radiative states and its influence on its λ_{TEp} and λ_{TMp} positions primarily depend on the inter-particle spacing rather than $\lambda_{pump\ exc}$ in these ultrathin metal films with short-range MNP order as in Figure 3.1. Further, the resulting anisotropic TAS effect on these samples with features $P \gg d$ is also presumed to be due to the short-range ordering of Au disks (see Figure 3.1) which were invisible in polarized steady state spectroscopy. These trends in the polarized TAS investigation confirms the possibly of utilizing polarized-transient absorption spectra as an effective qualitative way to conform short-range orderings of subwavelength nanostructures which are difficult to measure and observe in conventional steady state measurements and other microscopic techniques quickly.

4. Plasmonic properties of percolated, anisotropic Au metal films

In this chapter the structural and optical properties of percolated ultrathin metal films on corrugated sapphire substrates are discussed and presented, further the type of plasmons supported in these structures and the condition for SPP coupling are discussed with numerical calculations, simulations and far-field optical spectroscopy.

4.1. Formation and structure of percolated, anisotropic Au metal films

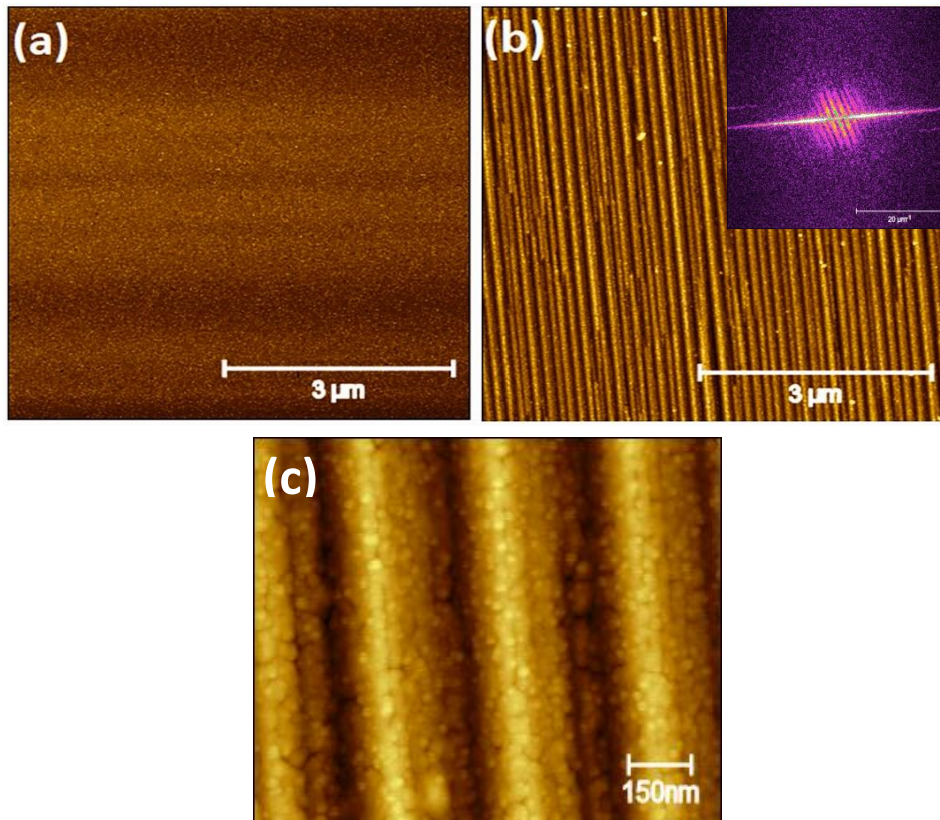


Figure 4.1. AFM images of (a) flat non-reconstructed plasmonic sample (Sa1), (b) reconstructed corrugated plasmonic sample (Sa2) and (c) Topography of percolated 10nm thick Au film deposited on corrugated sapphire substrates with larger corrugation period²¹⁷.

Figure 4.1a and b shows the AFM images of 10nm thick percolated Au on flat and onto the reconstructed corrugated template. Gold metal was chosen once again for this study due to its ability to support surface plasmons in the NIR range⁷². The Au metal layer deposited on the corrugated template follows the modulation induced by the corrugated periodic facets as in Figure 4.1b. A low- temperature post-deposition annealing step (see sample fabrication section) was performed to improve the film interconnectivity of the deposited film creating a corrugated plasmonic surface of percolated real structure as in Figure 4.1c. The performed post deposition annealing process quenched the localized plasmon resonance of the percolated 10 nm thick Au film, before any dewetting processes which usually occurs at higher annealing temperatures¹³⁰ as discussed in Figure 4.2. It shows the AFM images of the samples with 10 nm thick Au film deposited on flat sapphire template and annealed at different temperatures after deposition. It reveals that the 10nm Au thin film undergoes slight improvement in film connectivity for post

deposition annealing at a temperature of $T \ll 600^\circ\text{C}$ at a constant time of 20 mins, but dewetting processes begin to occur in higher annealing temperature of 1000°C where the diameter of the nucleating Au grains increases to $\sim 250\text{nm}$ due to film de-wetting and out of plane growth. Whereas, the performed low-temperature post deposition annealing processes is necessary for ultrathin metals films with near percolated thickness to achieve effective percolation when deposited in dielectrics with poor surface wettability by an electron beam evaporation technique. Further, a pre-annealing process was also performed on the bare sapphire templates to degas the sample surface, so that uniform metal coverage and adatom diffusion can occur at ultrathin metal film thicknesses. This is performed so as to facilitate the film to acquire percolation at the low temperature post annealing process.

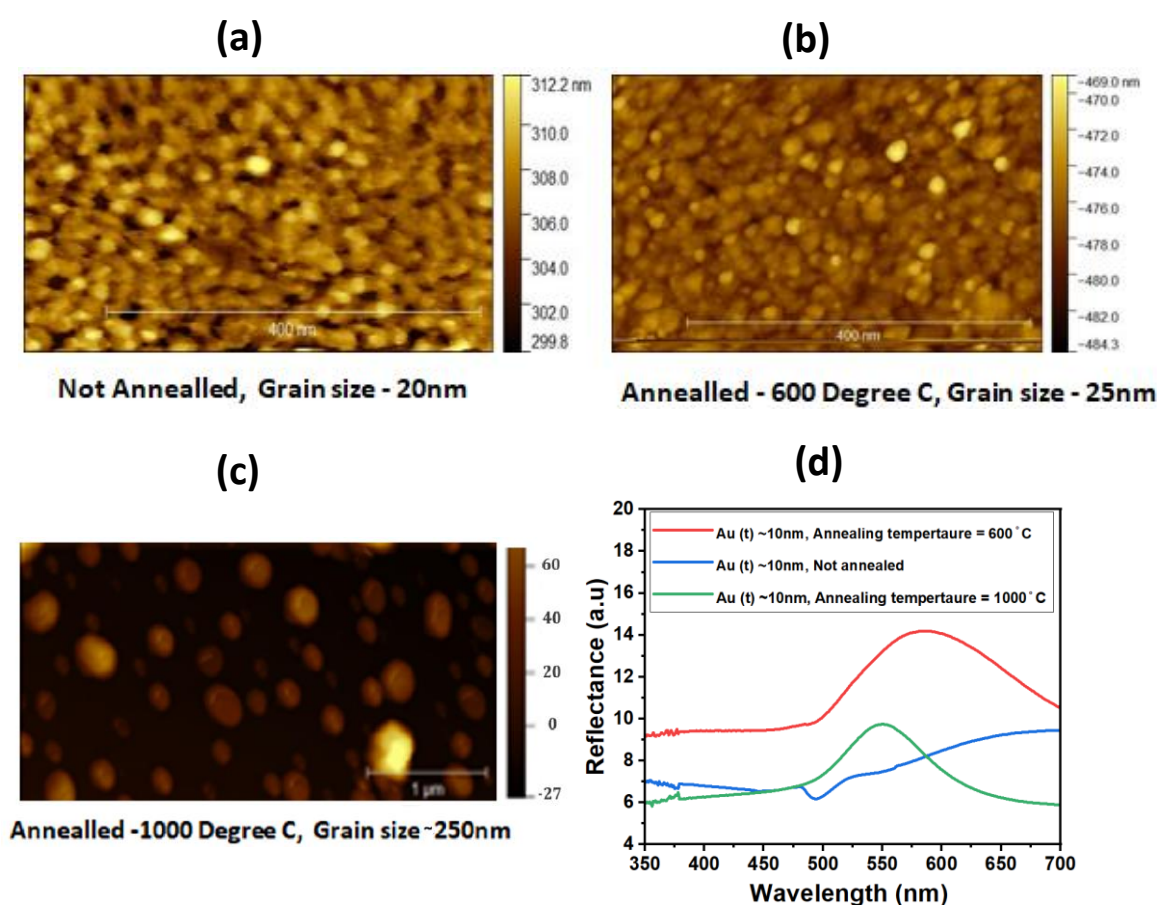


Figure 4.2. AFM images of (a) 10nm of Au deposited on flat sapphire template and not annealed (b) 10nm of Au deposited on flat sapphire template and annealed at 600°C , (c) 10nm of Au deposited on flat sapphire template and annealed at 1000°C and (d) Reflectance analysis measured with unpolarized excitation on the 10nm Au deposited on flat sapphire templates and annealed with different post deposition temperatures of 600°C and 1000°C exhibiting localized plasmon resonance due to film dewetting in higher post deposition annealing temperatures.

Thus, corrugated plasmonic films with laterally connected metal network was obtained with different surface corrugation vectors k_x , here the value of corrugation period determines the spatial corrugation vector k_x spatial corrugation.

4.2. Optical response of percolated, anisotropic Au metal films

The reflectance analysis of the flat sample Sa1P in Figure 4.3a. confirmed the percolation of the 10nm Au film after the post deposition annealing process at 300 °C due to the observance of increasing reflectance at the longer wavelengths typical for connected (percolated) metal films^{98,121} and a dip near 500 nm wavelength interpreted as the absorption due to inter-band transitions in Au metal¹⁹⁴ as in Figure 4.3a. As discussed before in chapter 3. the small peak near 831 nm in the spectra is from the α -Al₂O₃ template and not a plasmon resonance. Further a broad dip at the NIR region for TM polarization component was observed for corrugated plasmonic samples as in Figure 4.3b. indicating the coupling of a plasmon mode. Whereas, the TE polarization component exhibited similar reflectance spectra as the flat sample. The position of the broad plasmon dip redshifted beyond the NIR spectroscopic range for the fabricated plasmonic samples with increasing corrugation vectors as in Figure 4.3c.

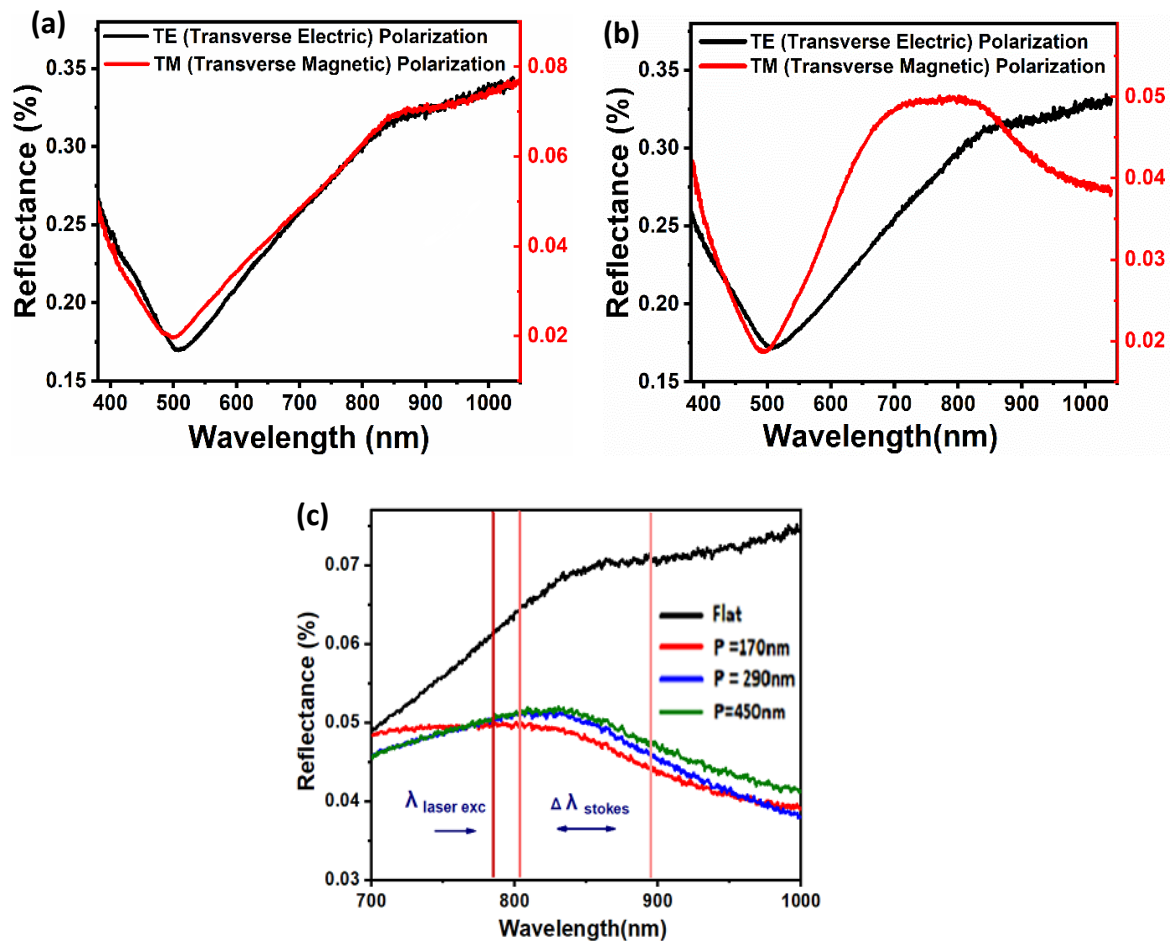


Figure 4.3. (a) Reflectance measurements of 10 nm Au film on flat template at $\theta = 50^\circ$ exhibiting percolated thin film characteristics. (b) Reflectance measurements of the percolated 10 nm Au film on the corrugated sample with period = 150nm at $\theta = 50^\circ$ showing a broad dip in the IR region for TM polarization related to the coupling of a hybrid SPP mode and (c) TM polarization components of reflectance on samples (flat (Sa1) and reconstructed corrugated with periods = 150nm, 290nm and 450nm (Sa2, Sa3, Sa4) at $\theta=50^\circ$ exhibiting red-shifting of the broad SPP resonance dip for increasing corrugation period²¹⁷.

Further, EM simulations were performed to understand the type of excited plasmon onto the corrugated plasmonic samples with percolated Au network. An $\text{Al}_2\text{O}_3/\text{Au}$ corrugated structure was modelled using the optical constants for a 11-nm thick Au film described by Rosenblatt et al¹⁴². Figure 4.4. shows the electric field intensity ($|E|^2$) distribution maps at incidence angle $\theta = 0^\circ$ and 50° for TM polarization excited at $\lambda_{exc} = 785$ nm. The simulated $|E|^2$ distribution reveals enhanced optical near field along E_x and E_z on the corrugated surface as a result of the strong plasmon coupling at $\theta = 50^\circ$ with a larger wavevector. Whereas, at $\theta = 0^\circ$ the $|E|^2$ distribution exhibited negligible enhanced optical near-field revealing no significant polariton coupling on these corrugated surface elevations with low aspect ratio of period - height. These results suggest the type of the excited plasmon mode to a propagating surface plasmon polariton (SPP) mode on these corrugated metal films.

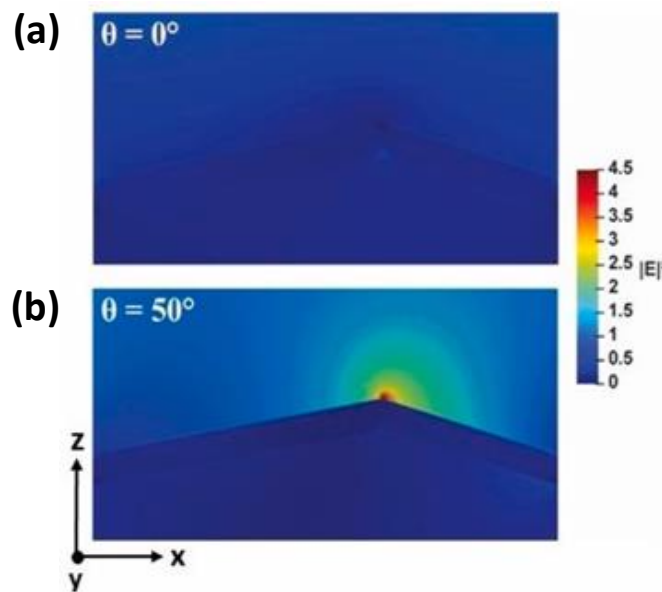


Figure 4.4. Electromagnetic near-field distribution for TM polarization at angle of incidence $\theta = 0^\circ$ and $\theta = 50^\circ$ for corrugated plasmonic sample with period =150nm under $\lambda_{exc} = 785$ nm, exhibiting the coupling of a SPP mode at $\theta = 50^\circ$ due the increased wavevector of the diffracted light²¹⁷.

However, it can be seen from the dispersion curves in Figure 1.14b. that the possible SPP modes always have a larger wavevector when compared to the wavevector of both free space photons k_o and photons in the dielectric medium $k_{dielectric}$ at similar frequencies based on the illuminated metal/dielectric interface. This constitutes a mismatch in momentum between the incident photons and possible SPP modes in the interface. Subsequently, the SPP coupling takes place at selected momentum- matching conditions between the photons and surface plasmon modes. Although, SPP modes in flat plasmonic layers can only be excited by end coupling, tapered coupling or prism which increases the wavevector of the incident light towards the SPP wavevector. Here the corrugated periodic structures can diffract light with an increased wavevector mediating plasmon-photon momentum matching conditions and thus excluding the requirement of complex optical setup¹⁹⁵.

4.3. Excitation of propagating surface plasmon polariton (SPP) mode

Corrugated surface structures with spatial corrugation vector (k_x spatial corrugation) dependent on their value of period P (see eq. 54) increases the momentum of the electromagnetic light incident on them due to diffraction¹³⁷. The momentum of these diffracted waves (k_x diffracted) is based on the eq.55.

$$k_x \text{ spatial corrugation} = n \frac{2\pi}{P} \quad (54)$$

$$k_x \text{ diffracted} = k_o \text{ inc} \sin\theta + n \frac{2\pi}{P} \quad (55)$$

$$k_{SPP} = \frac{\omega_{SPP}}{v} \sqrt{\frac{\epsilon_1 \epsilon_2}{\epsilon_1 + \epsilon_2}} \quad (56)$$

where $k_o \text{ inc}$ = wavevector of the incident light, $k_x \text{ spatial corrugation}$ = spatial wavevector of corrugation period, $k_x \text{ diffracted}$ = wavevector of diffracted light order, k_{SPP} = SPP wavevector, $n = 0; \pm 1; \pm 2$; diffraction orders, θ = incidence angle, P is the grating period, ϵ_1 and ϵ_2 are the dielectric permittivity's of metal and dielectric medium, respectively, $v = c/\mu$ is the speed of light in the dielectric medium, μ -refractive index of dielectric medium.

To understand the conditions for SPP excitation on these corrugated plasmonic samples with percolated Au films, dispersion curves of $k_o \text{ inc}$ and $k_x \text{ diffracted}$ on the corrugated samples Sa2 and Sa3 with periods $P = 150$ and 290nm were plotted in Figure 4.5a. In the dispersion curves shorter corrugation period of $P = 150$ nm with larger $k_x \text{ spatial corrugation}$ resulted in larger values of wavevector of diffracted light $k_x \text{ diffracted}$. Subsequently, the plasmon dispersion curves k_{SPP} based on eq.56. reveals that the effective SPP coupling occurs at Au/sapphire interface by transmitted diffraction wave orders¹⁹⁶⁻¹⁹⁸.

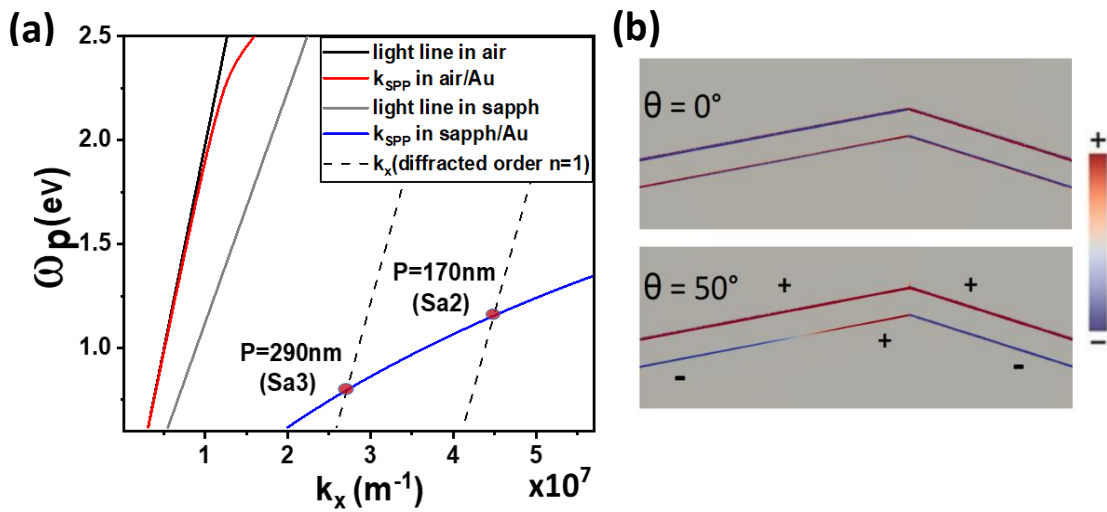


Figure 4.5. (a) Dispersion curves for SaP2 and SaP3 samples with periods $P = 150\text{nm}$ and 290nm for diffraction order $n = 1$. Incident light $k_o \text{ inc}$ (solid black line), resulting diffracted orders $k_x \text{ diffracted}$ (dashed black line), P = corrugation periods, k_{SPP} in air/Au interface = (red line), k_{SPP} in sapphire/Au interface = (blue line), SPP coupling points (red dots), (b) simulated charge density polarization on the metal

dielectric interfaces of Sa2 for TM polarization at $\lambda_{exc} = 785$ nm at $\theta = 0^\circ$ and 50° exhibiting the excited hybrid SPP mode excitation at $\theta = 50^\circ$. (Plasmon frequency $\omega_p = \hbar\omega$)²¹⁷.

The coupling region between the diffracted orders k_x diffracted and the k_{SPP} at the Au/sapphire interface is portrayed by the red dots in Figure 4.5a. where the coupling of a SPP mode at 1.17 eV due to the first-order diffracted waves is presumed to correspond to the results of reflectance measurements of sample Sa2 with period $P = 150$ nm which shows a broad dip in the near infrared range at 1040 nm (see Figure 4.3b). We find similar trends of plasmon dips for other corrugation periods in Figure 4.3c based on the coupling regions in the dispersion curves. Further, the excited SPP mode on the Au/sapphire interface with exponentially decaying electric field extends to the Au/air interface and transforms into coupled hybrid modes^{147,199}. In the discussed system (air/Au/Al₂O₃ layer) the broad plasmon reflectance dip in the NIR region is related to an anti-symmetric SPP mode^{200,201}.

When plotting the charge density polarization distribution on the (air/Au/Al₂O₃ interfaces) for TM polarization at $\theta = 0^\circ$ and 50° under $\lambda_{exc} = 785$ nm in Figure 4.5b. the charge density polarization appears to be a mixture of dipole moments at $\theta = 50^\circ$ that is typical of hybridized SPP mode on ultrathin metal films. Whereas, the propagation of high-frequency symmetric mode in the samples is damped as a result of the discontinuous percolated network, which limits charge oscillations parallel to the interface²⁰² and also by the Au inter and intra-band transitions at frequency above 500 nm^{202,203}. The nature of the broad reflectance dip here is also attributed to the enhanced scattering on percolated grains. The fabricated corrugated plasmonic surface support delocalized SPP modes in the NIR range generating large electric field components parallel and perpendicular to the surface during SPP excitation based on their k_x spatial corrugation contrary to confined LSPR mode.

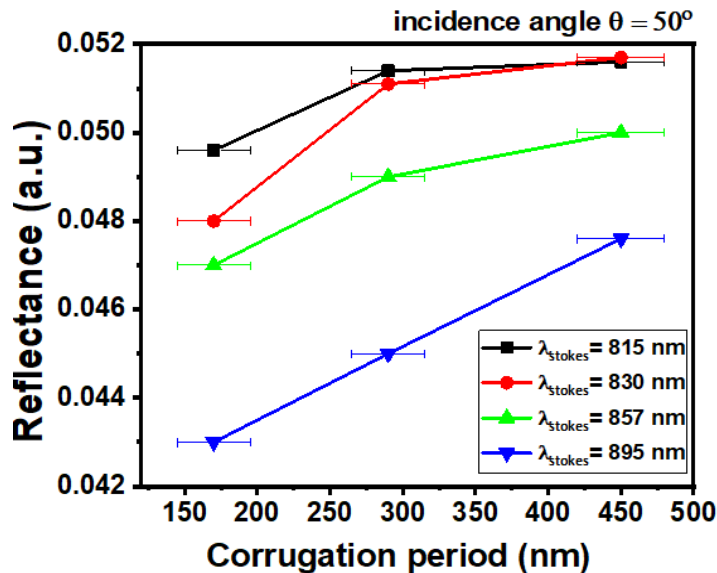


Figure 4.6. The dependency of reflectance vs. corrugation period (stronger plasmon coupling) at selected wavelengths for a shorter corrugation period²¹⁷.

Finally, Figure 4.6. shows the dependence of reflectance intensity at selected wavelengths for different sample corrugation period. It exhibits that reduced reflectance for samples with shorter corrugation period, indicating stronger plasmon coupling when compared to larger corrugation periods corroborating the plasmon coupling conditions in the dispersion curves in Figure 4.5a.

4.4. Plasmonic anisotropy of percolated, anisotropic Au metal film

Here these corrugated plasmonic samples support SPP mode only at TM polarization, along the direction of the surface corrugation vector k_x *spatial corrugation*. As a result of this the samples exhibit anisotropic plasmonic effect dependent on the excitation polarization angle σ . In contrary to the anisotropically ordered Au arrays, where the excited plasmon is LSPR mode at both $\sigma = 0^\circ$ and $\sigma = 90^\circ$. The samples here excite quenched LSPR modes at $\sigma = 90^\circ$ due to the connected percolated Au networks although with surface roughness and propagating SPP modes at $\sigma = 0^\circ$.

5. Dichroic SERS effect on anisotropic, ultrathin Au metal films

In this chapter the resulting SERS effects of a simple thio-phenol molecule chemisorbed on both the percolated and non-percolated anisotropic metal films on corrugated sapphire templates are discussed. Further, the type of SERS anisotropy resulting on these samples, its relative Raman peak intensities and enhancement factors were measured through SERS mapping, polarized and wavelength scanned Raman measurements. These measurements were performed in order to utilize a dichroic SERS response resulting on these samples, and study SERS dichroism of analyte Raman modes of different Stokes shifted frequency and analyte Raman modes of different polarizability tensors. These analyses were used to understand the non-linear Raman scattering phenomena and its surface selection rules on the fabricated samples. Substrate reproducibility and large-area sensing uniformity were also tested. Finally, the positives and drawbacks of the fabricated samples towards SERS are discussed.

5.1. Anisotropic SERS effect of non-percolated Au metal films on corrugated sapphire templates

As discussed in chapter 3. The non-percolated Au films nucleated as ordered 2D-Au arrays with giant near-field enhancements due to the hybridized-collective plasmon modes, it also exhibited an anisotropic plasmonic response with respected to the excitation polarization angle σ . Here the SERS resulting from the anisotropic non-percolated Au metal films at their super and sub-radiant plasmon frequencies were investigated.

5.1.1. Super and sub-radiant SERS

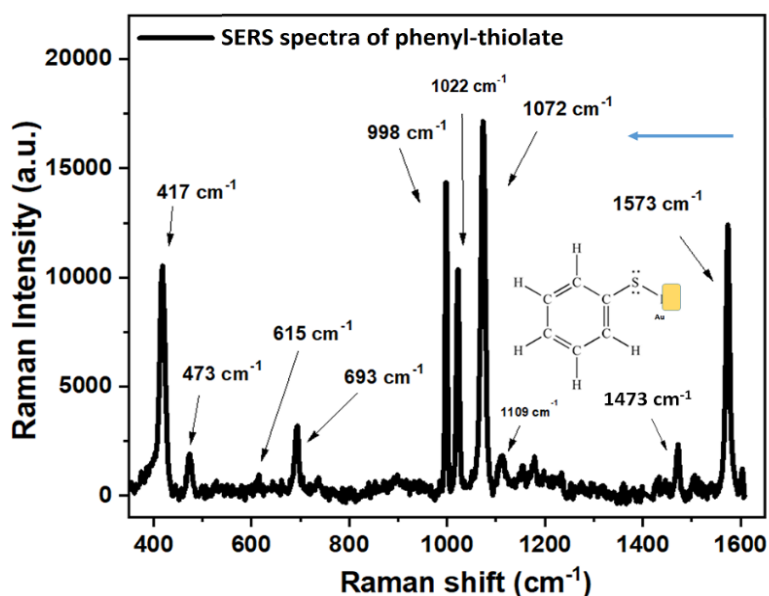


Figure 5.1 SERS spectra of phenyl-thiolate layers formed when thio-phenol molecules chemisorbed into the Au surface²¹⁸. The blue arrow indicates the down shift of the (C – C – C ring bend (ring breathing) and In- plane. C – C – C bend + C – S stretching) of bare thiophenol to 998 cm⁻¹ and 1072 cm⁻¹ confirming the chemisorption as phenyl thiolates²⁰⁴.

Polarized and wavelength scanned SERS measurements were performed for thio-phenol molecules in these samples in order to investigate the SERS enhancements due to the hybridized- super and sub-radiant collective plasmon modes. When thiophenol molecules were deposited onto the samples the phenyl ring vibration modes assigned to the (C – C – C ring bend (ring breathing) and In- plane. C – C – C bend + C – S stretching) in its SERS spectra downshifted upon the formation of phenyl thiolates (PT), to 998 cm^{-1} and 1072 cm^{-1} as in Figure 5.1, where the blue arrow indicates the downshifting. This confirms the chemisorption of thio-phenol on the Au surface to form phenyl-thiolates²⁰⁴.

Two selected Raman λ_{exc} at 633 nm and 785 nm were used in the study. The vertical lines on Figures 3.9 and 5.2a, b. indicates the Raman λ_{exc} and its corresponding λ_{Stokes} positions on the plotted polarized-reflectance spectra of the samples (Sa1- unordered grains - flat sample), (Sa2 - ordered spherical arrays - $P \cong d$), (Sa5 - un-ordered spherical arrays - $P \gg d$) and (Sa3 - ordered elliptical arrays - $P \cong d$).

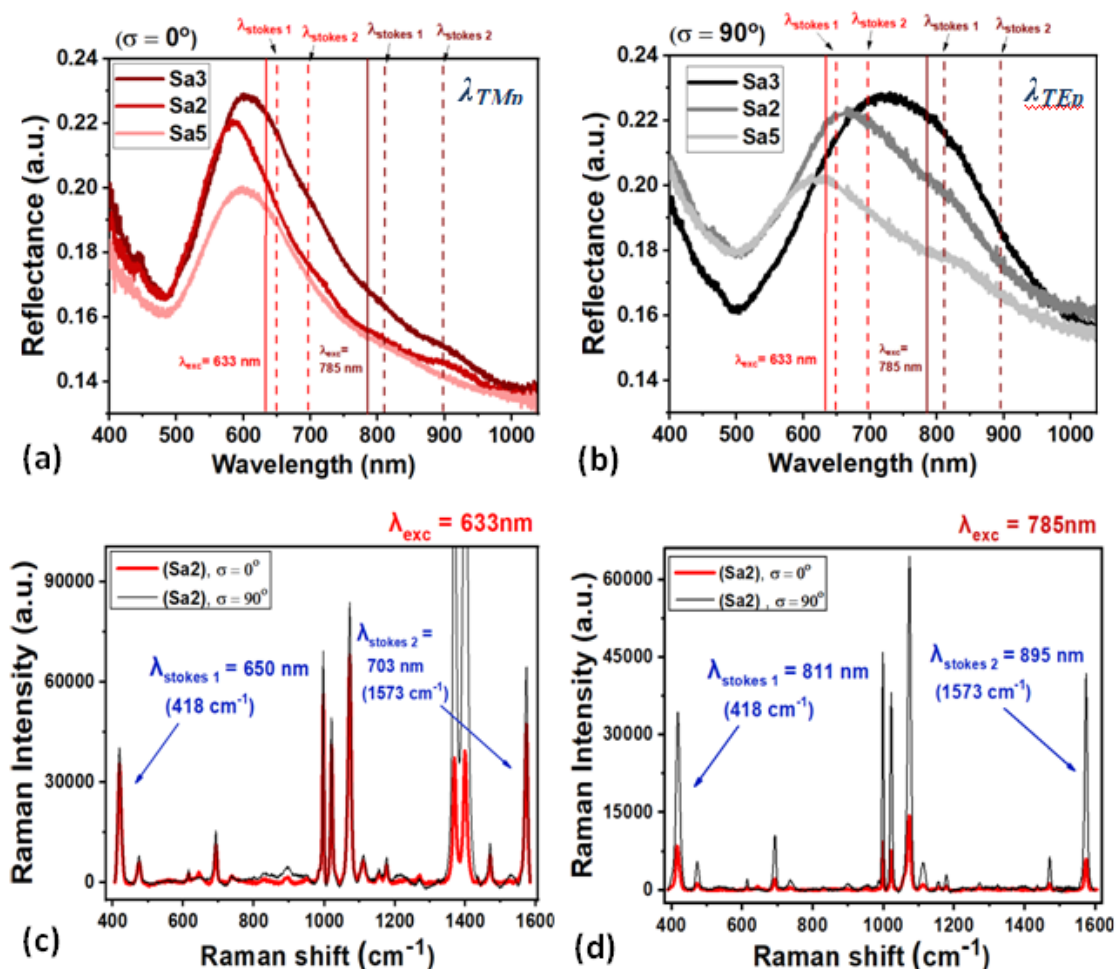


Figure 5.2 Polarized reflectance spectra²¹⁸ (a) at $\sigma = 0^\circ$ (red lines) exhibiting the excited λ_{TMp} plasmon modes and (b) at $\sigma = 90^\circ$ (black lines) exhibiting the λ_{TEp} plasmon modes for the samples Sa2, Sa3 and Sa5 (performed at an angle of incidence $\theta=50^\circ$). The vertical lines indicate the λ_{exc} and its corresponding λ_{Stokes} positions on the spectra's. (c) shows SERS spectra measured at $\lambda_{exc} = 633\text{nm}$ for the sample Sa2 at both $\sigma = 0^\circ$ and 90° polarizations. (d) presents SERS spectra measured at $\lambda_{exc} = 785\text{nm}$ for the sample Sa2 at both $\sigma = 0^\circ$ and 90° polarizations. Blue arrows indicate the $\lambda_{Stokes 1}$ and $\lambda_{Stokes 2}$ positions in (c) and (d).

Since, the SERS measurements performed in this study using a microscopic objective of high numerical aperture 0.7 *N.A.*, focusing within an aperture angle of 50° the λ_{exc} and λ_{Stokes} positions were preferred to be aligned and compared onto the reflectance spectra measured at $\theta = 50^\circ$ as in Figure 5.2a, b., rather with the transmission spectra which were obtained at normal incidence in Figure 3.9. The transmission measurements were performed to analyze the value $\Delta\lambda_p$ of the flat sample (Sa1) as its reflectance analysis in Figure 3.8. exhibited interference fringes due to the Fabry - Perot like cavity mode¹⁸⁷ of the template coupled with the *MNP* arrays λ_p resonance, which made it difficult to measure the $\Delta\lambda_p$ based on σ .

Importantly, the performed off-normal reflectance analysis at $\theta = 50^\circ$ is necessary in this study so as to account for the out-of-plane (*p*-polarized) light interaction with the plasmonic surface, in exciting both parallel and perpendicular charge oscillations²⁰⁵. This requirement is to be taken into account when studying optical properties of ultra-thin metallic films and arrays on dielectric substrates with large permittivity ($\epsilon \sim 11-9$ as for the miscut sapphire with dichroic response). In such Au metal arrays /corrugated dielectric template system, the discontinuity of ϵ due to the underlying template further breaks the symmetry of the dielectric medium surrounding the Au grains. This introduces complex phenomena such as image charges which further increase the *FWHM* of the excited λ_p peak^{206,207}. Such high permittivity dielectric substrates can efficiently concentrate the *EM* near-field at the metal/dielectric interface as confirmed by recent experimental studies¹⁷.

Further analysis of reflectance spectra in Figures 5.2a, b. and 3.9 reveals that the positions of $\lambda_{exc} = 785$ nm and its corresponding λ_{Stokes} lie in the lower frequency regime when compared to the peak maxima of the lower-order dipole antenna modes λ_{TEp} at $\sigma = 90^\circ$ and λ_{TMP} at $\sigma = 0^\circ$ for the samples Sa1, Sa2, Sa3, and Sa5. In the contrary, the $\lambda_{exc} = 633$ nm and its corresponding λ_{Stokes} lies in the higher frequency regime of λ_{TEp} at $\sigma = 90^\circ$ for samples Sa2 and Sa3 where the degenerated $\lambda_{TEp3,5}$ sub-radiant propagative (SPP mode) are excited^{151,154}. Figures 5.2c, d. show the SERS spectral measurements at both Raman $\lambda_{exc} = 633$ nm and 785nm along $\sigma = 0^\circ$ and 90° for the sample Sa2. It shows that the higher SERS intensities are acquired at $\lambda_{exc} = 633$ nm, when compared to $\lambda_{exc} = 785$ nm. Whereas, the anisotropic response in SERS intensity between $\sigma = 0^\circ$ and $\sigma = 90^\circ$ was more pronounced for $\lambda_{exc} = 785$ nm as compared to $\lambda_{exc} = 633$ nm. In order to acquire more detailed dependence, polarized SERS measurements with a precise step of $\Delta\sigma = 5^\circ$ were performed on these samples.

Figures 5.3a-d. exhibits the polarized SERS intensity plots for selected phenyl-thiolates Stokes-shifted peaks at 418 cm^{-1} and 1573 cm^{-1} designated as $\lambda_{Stokes 1}$ and $\lambda_{Stokes 2}$ based on their respective Raman emission wavelengths. Here, the $\lambda_{Stokes 1}$ peak at 418 cm^{-1} is close to the position of λ_{exc} and exhibits SERS intensity based on the enhancement factor $g \cong g^s$. The SERS intensity of this peak is approximated through the commonly used $|E|^4$ model^{65,167}. However, for the higher frequency Stokes-shifted peaks, such as the one at 1573 cm^{-1} ($\lambda_{Stokes 2}$), the factors g at λ_{exc} and g^s at λ_{Stokes} will differ and influence the SERS intensity of the peaks individually based on the position and *FWHM* of the excited λ_p plasmon mode.

The plotted polarized SERS peak intensities in Figure 5.3a-d. at both $\lambda_{exc} = 633$ nm (left column) and $\lambda_{exc} = 785$ nm (right column) provides a clearer and more precise depiction of the dichroic SERS effect in these Au arrays. Thus, allowing for a direct comparison of their SERS intensities

and anisotropies. Furthermore, the flat sample Sa1(black plots) exhibits an isotropic SERS scattering effect for both excitation wavelengths (see Figure 5.3).

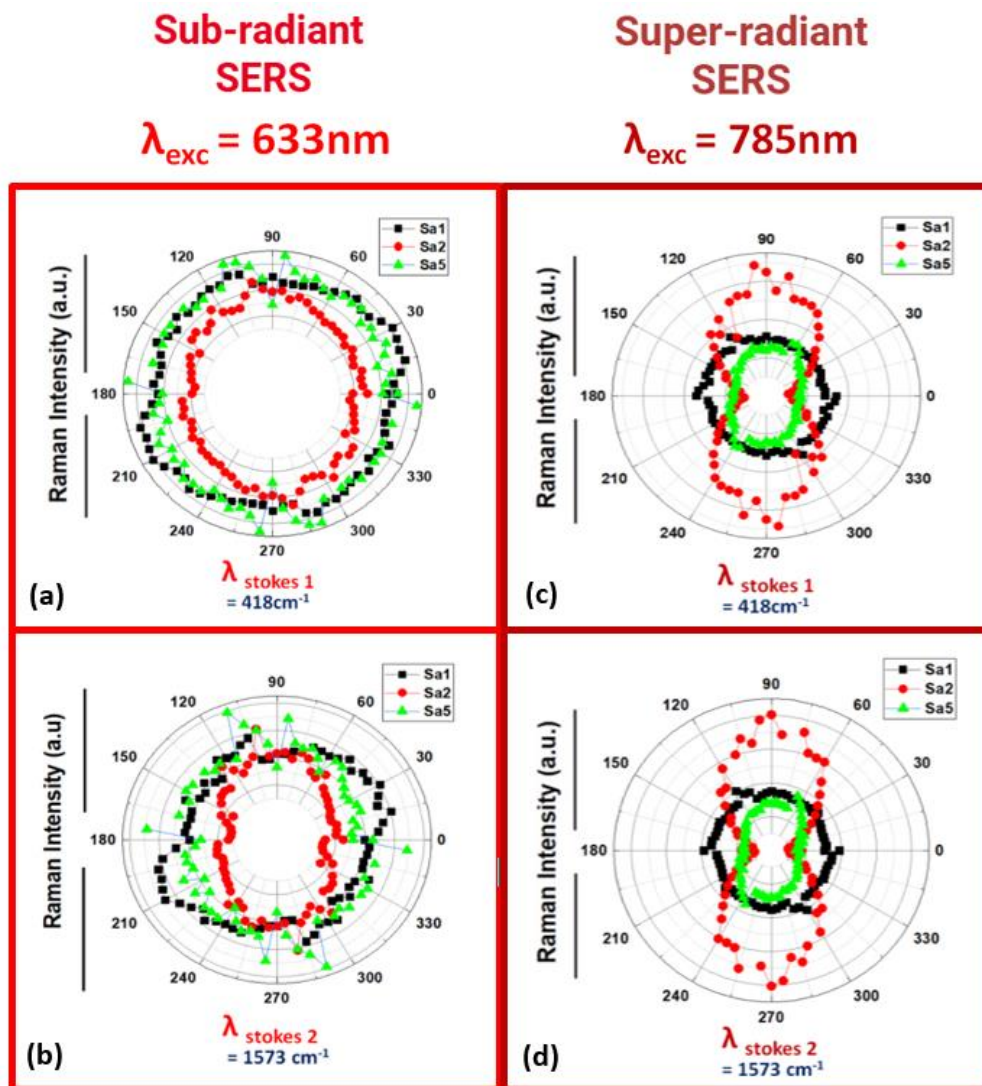


Figure 5.3.(a) and (c) show SERS intensity dichroism plots of $\lambda_{Stokes 1}$ and $\lambda_{Stokes 2}$ peaks on samples (Sa1 - unordered grains on flat template) (black plot), (Sa2 - ordered spherical arrays) (red plot) and (Sa5 - un-ordered spherical arrays) (green plot) measured for $\Delta\sigma = 5^\circ$ at $\lambda_{exc} = 633\text{nm}$. (b) and (d) present SERS intensity dichroism plots of $\lambda_{Stokes 1}$ and $\lambda_{Stokes 2}$ peaks on samples (Sa1 - unordered grains on flat template) (black plot), (Sa2 - ordered spherical arrays) (red plot) and (Sa5 - un-ordered spherical arrays) (green plot) measured for $\Delta\sigma = 5^\circ$ at $\lambda_{exc} = 785\text{nm}$ ²¹⁸.

Although, when analyzing the obtained absolute SERS intensity values at $\sigma = 90^\circ$ angle for $\lambda_{exc} = 633\text{nm} < \lambda_{TEp}$ in Figure 5.4a. and b. reveals that similar SERS intensity are observed for the samples (Sa1 - unordered grains on flat template) (black plot), (Sa2 - ordered spherical chain array along $\sigma = 90^\circ$) (red plot) and (Sa5- un-ordered spherical chain array along $\sigma = 90^\circ$) (green plot). This reveals for Raman excitation $\lambda_{exc} = 633\text{nm} < \lambda_{TEp}$ near to the frequency of the sub-radiant collective plasmon mode the resulting SERS enhancement of the analyte depends primarily on the inter-particle gap S , rather than the ordering of MNP as arrays when $S \ll r$ in

the system. This effect of similar values of absolute SERS intensities between samples Sa1, Sa2 and Sa5 along $\sigma = 90^\circ$ contradicts the far-field reflectance intensities of Sa2 and Sa5 in Figure 5.2b. as it shows a higher reflectance intensity for Sa2 when compared to Sa5 at $\lambda_{exc} = 633\text{nm}$ and its corresponding λ_{Stokes} position regions (compare the reflectance intensities of the samples Sa2 and Sa5 at light red lines position in Figure 5.2b.). This anomalous behavior in the dependency of SERS at $\lambda_{exc} = 633\text{nm}$ on the far-field reflectance intensity is due to the increase in temporal (lifetime) feature of the enhanced near-field as a result of plasmon-propagation with reduced far-field scattering loss. These sub-radiant mode at $\lambda_{exc} = 633\text{nm} < \lambda_{TEp}$ are due to hybridization of plasmonic near-fields in the Au-arrays with $S \ll r$ and cannot (couple or out-out) with far-field incident radiation. As a result of this hybridization dependent on S , only for the sample Sa2, due to the large inter-particle gap S_1 at $\sigma = 0^\circ$ polarization a slightly decreased SERS intensity was observed in Figure 5.3b. Due to this anisotropic SERS intensity along $\sigma = 0^\circ$ and $\sigma = 90^\circ$ resulted in a dichroic SERS effect dependent of the excitation polarization angle - see red plot in Figure 5.3a, b. This dichroic effect was specific to sample Sa2 ($P \cong d$) at $\sigma = 0^\circ$, where the increase in the value of S_1 is due to the corrugation barrier induced anisotropic Au array ordering. Similarly, for the flat sample Sa1 and sample Sa5 ($P \gg d$) due to the similar inter-particle gap S at both $\sigma = 0^\circ$ and $\sigma = 90^\circ$ angles resulted in an isotropic SERS effect under $\lambda_{exc} = 633\text{ nm}$ see (Sa1) black plot and (Sa5) green plot in Figure 5.3a and b. Further in contrast to $\lambda_{exc} = 633\text{ nm}$, there is a clear difference in SERS absolute intensities between the samples Sa1, Sa2 and Sa5 at $\sigma = 90^\circ$ in Figure 5.3c, d when analyzing the data for $\lambda_{exc} = 785\text{nm}$. This observation corroborates with the far-field polarized reflectance intensities at $\sigma = 90^\circ$ for $\lambda_{exc} = 785\text{ nm}$ and its respective λ_{Stokes} positions (compare Sa2 and Sa5 intensities at dark red-lines position in Figure 5.2b.).

At Raman excitation at $\lambda_{exc} = 785\text{nm} > \lambda_{TEp}$ related to the frequency of the lowest-order dipole mode the ordering of *MNPs* in the form of arrays primarily influenced the increase in its SERS signal and corroborates well with its far-field reflectance spectra for the sample Sa2 (red plot) in Figure 5.3c and d. This is as a result that the excited lowest-order dipole mode can be regarded as an (antenna mode) as it is effectively excited in the Au arrays but instantly scatters the collective plasmon near-field radiation into far-field as a result of dynamic depolarization. This dynamic depolarization is due to the non-zero dipole moment of ordered arrays collectively at $\lambda_{exc} = 785\text{nm} > \lambda_{TEp}$. As a result of this, for Raman excitation at $\lambda_{exc} = 785\text{ nm}$ the absolute SERS intensities at $\sigma = 90^\circ$ decreased for the samples Sa1 and Sa5 with un-ordered arrays (black and green plots) due to the weak excitation of the antenna mode as in Figures 5.3c. and d. In the contrary, for sample Sa2 (red plot) with ordered spherical chain array along $\sigma = 90^\circ$ the SERS intensity increased even though all the samples possessed the same inter-particle gap S_2 at this direction. As a result of this dependency on the ordering of Au arrays, the SERS dichroic effect dependent on far-field polarization angle (σ) was more prominent for sample Sa2 (red plots) at $\lambda_{exc} = 785\text{nm}$ as in Figures 5.3c, d. as its Au arrays were ordered with different inter-particle gaps S_1 and S_2 at both $\sigma = 0^\circ$ and 90° comparing to $\lambda_{exc} = 633\text{nm}$ in Figures 5.3a, b. This trend was due to the effective coupling of the dipole antenna mode at $\sigma = 90^\circ$ onto the ordered arrays with smaller value of S_2 as discussed before, whereas at $\sigma = 0^\circ$ due to the larger S_1 and the disorder in arrays resulted in weak excitation of the super radiant mode and resulted in the lowest SERS intensity observed in these samples. Subsequently, for the sample Sa5 with non-ordered arrays the dichroism becomes less pronounced and it completely

disappeared for the flat sample Sa1. Similarly, when comparing the absolute SERS intensities between these samples at $\sigma = 0^\circ$ under $\lambda_{exc} = 785 \text{ nm}$, the flat sample Sa1 with the smallest S value exhibited the highest SERS intensity and sample Sa2 with the largest gap distance S_l at $\sigma = 0^\circ$ exhibited the lowest SERS intensity, see (Sa1) black and (Sa2) red plots (in Figure 5.3c and d. (at $\sigma = 0^\circ$)). This reveals that both the factors of ordering of *MNPs* as arrays and their inter-particle gap distance S influences the SERS intensity of an analyte when excited at $\lambda_{exc} = 785 \text{ nm} > \lambda_{TEp}$ related to the frequency of the lowest-order dipole mode. The most enhanced SERS intensities in these measurements were obtained for Raman λ_{exc} at $633 \text{ nm} < \lambda_{TEp}$ near the frequency of the sub-radiant collective plasmon mode (as in Figure 5.2c.). This was due to the increase of its both the spatial and temporal near-field features as a result of the hybridized plasmon propagation, when compared to $\lambda_{exc} = 785 \text{ nm} > \lambda_{TEp}$ related to the frequency of the lowest-order (antenna) dipole mode (in Figure 5.2d.). These results were reproduced for a similar set of fabricated samples which exhibited plasmon resonance where the λ_{exc} at 633 nm was further blue shifted $\ll \lambda_{TEp}$ near the frequency of the sub-radiant collective plasmon mode when compared to the sub-radiant mode's peak maxima for both samples with flat template and $P \gg d$ feature. These reproduced results are presented as polarized SERS mapping measurements discussed in section 5.1.2. Further, the performed experimental comparison of SERS intensities and anisotropies of the samples excited at different excitations (λ_{exc}) and polarization angle (σ) summarizes, that in SERS system with $S \ll r$ the inter-particle gap distance S is the primary factor influencing higher SERS enhancements compared to the factor of ordering *MNPs* in the form of arrays at excitation frequency near the sub-radiant collective plasmon mode. Whereas, for SERS excitation related to the frequency of the lowest-order (antenna) dipole mode, the enhancements depended also on the ordering of *MNPs* as arrays resulting in a pronounced dichroism but exhibited reduced enhancement on these systems with subwavelength *MNP* diameter $d \sim 27 \text{ nm}$. This dependence becomes significant and has to be taken into account when designing large-area SERS substrates based on arrays with very small inter-particle gaps and subwavelength *MNP* diameter. As these substrates exhibit larger number of intense plasmonic SERS hot-spots in real space.

5.1.2. Non-linear Raman scattering process and verification of EM near-field mechanism of SERS.

Apart from simulated near-field spatial distributions in chapter 3, the enhanced near-field $E_p(\lambda_p)$ related to the collective plasmon modes based on equation 52. can be measured in SERS experiments. Importantly, the plasmonic modes with enhanced fields $E_p(\lambda_p)$ can influence different stages of Raman enhancement of a molecule depending on the factors g at λ_{exc} and g^s at λ_{Stokes} see equation 50. in chapter 1. The conducted experimental studies utilizing the plasmonic anisotropy allow us to retrieve the individual influence of g and g^s on the SERS signals of the investigated analyte, and to study the non-linear Raman scattering effect. Figure 5.4a. shows the polarized SERS peak intensities of sample Sa3 ($P \cong d$, ordered elliptical arrays) for $\sigma = 0^\circ$ and $\sigma = 90^\circ$.

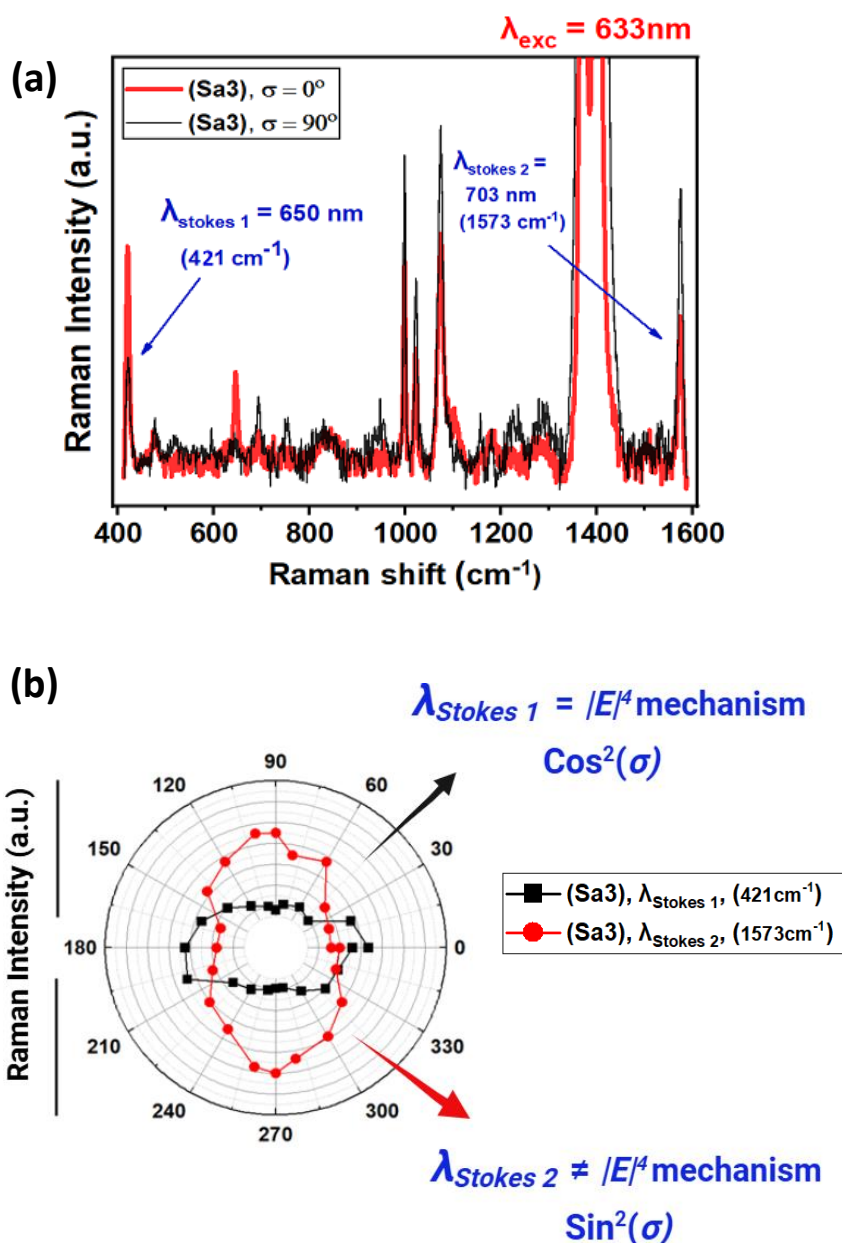


Figure 5.4(a) SERS spectra measured at $\lambda_{exc} = 633\text{nm}$ for the sample Sa3 for both $\sigma = 0^\circ$ and 90° polarizations. **(b)** polarized SERS intensities of $\lambda_{Stokes 1}$ and $\lambda_{Stokes 2}$ peaks at $\lambda_{exc} = 633\text{nm}$ for the sample Sa3, revealing that $\lambda_{Stokes 1}$ follows a $\cos^2(\sigma)$ and $\lambda_{Stokes 2}$ follows a $\sin^2(\sigma)$ dependency²¹⁸.

It revealed distinct behavior of SERS relative peak intensities between $\lambda_{Stokes 1}$ and $\lambda_{Stokes 2}$ at $\sigma = 0^\circ$ and $\sigma = 90^\circ$. At $\sigma = 90^\circ$ (black spectra) the $\lambda_{Stokes 2}$ peak is enhanced strongly as compared to $\lambda_{Stokes 1}$ peak, while the reverse is observed at $\sigma = 0^\circ$ (red spectra). This σ dependent change in the relative SERS peak intensities is only observable at $\lambda_{exc} = 633\text{nm}$, while at $\lambda_{exc} = 785\text{nm}$ the SERS anisotropy behave similarly to that observed for samples Sa2 and Sa5 (in Figure 5.4c, d.) and the distinct behavior of the SERS relative peak intensities were absent. Subsequently, when the polarized SERS intensities of $\lambda_{Stokes 1}$ and $\lambda_{Stokes 2}$ peaks under $\lambda_{exc} = 633\text{ nm}$ were plotted with a step $\Delta\sigma = 20^\circ$ as in Figure 5.4b. the analysis clearly revealed distinct dichroic response between $\lambda_{Stokes 1}$ and $\lambda_{Stokes 2}$ peaks. As specifically, $\lambda_{Stokes 1}$ exhibited a $\cos^2(\sigma)$ dependency (black plots), while $\lambda_{Stokes 2}$ exhibited a $\sin^2(\sigma)$ dependency (red plots) with respect to the polarization azimuthal angle σ . By corroborating these results with the polarized

reflectance and transmission plots (in Figures 5.2a, b.) at the $\lambda_{exc} = 633\text{nm}$ and its corresponding λ_{Stokes} positions, the λ_{exc} at 633 nm and its corresponding $\lambda_{Stokes 1}$ was closer to the λ_{TMP} resonance position at $\sigma = 0^\circ$. Due to this the $\lambda_{Stokes 1}$ peak's SERS intensity depended on the factors assumed to be $g \cong g^s$. Whereas, for the higher frequency Stokes-shifted peak $\lambda_{Stokes 2}$ due to the differing values of g and g^s at $\sigma = 0^\circ$ a reduced SERS peak intensity is observed as the λ_{TMP} resonance is blue shifted with respect to this $\lambda_{Stokes 2}$ peak.

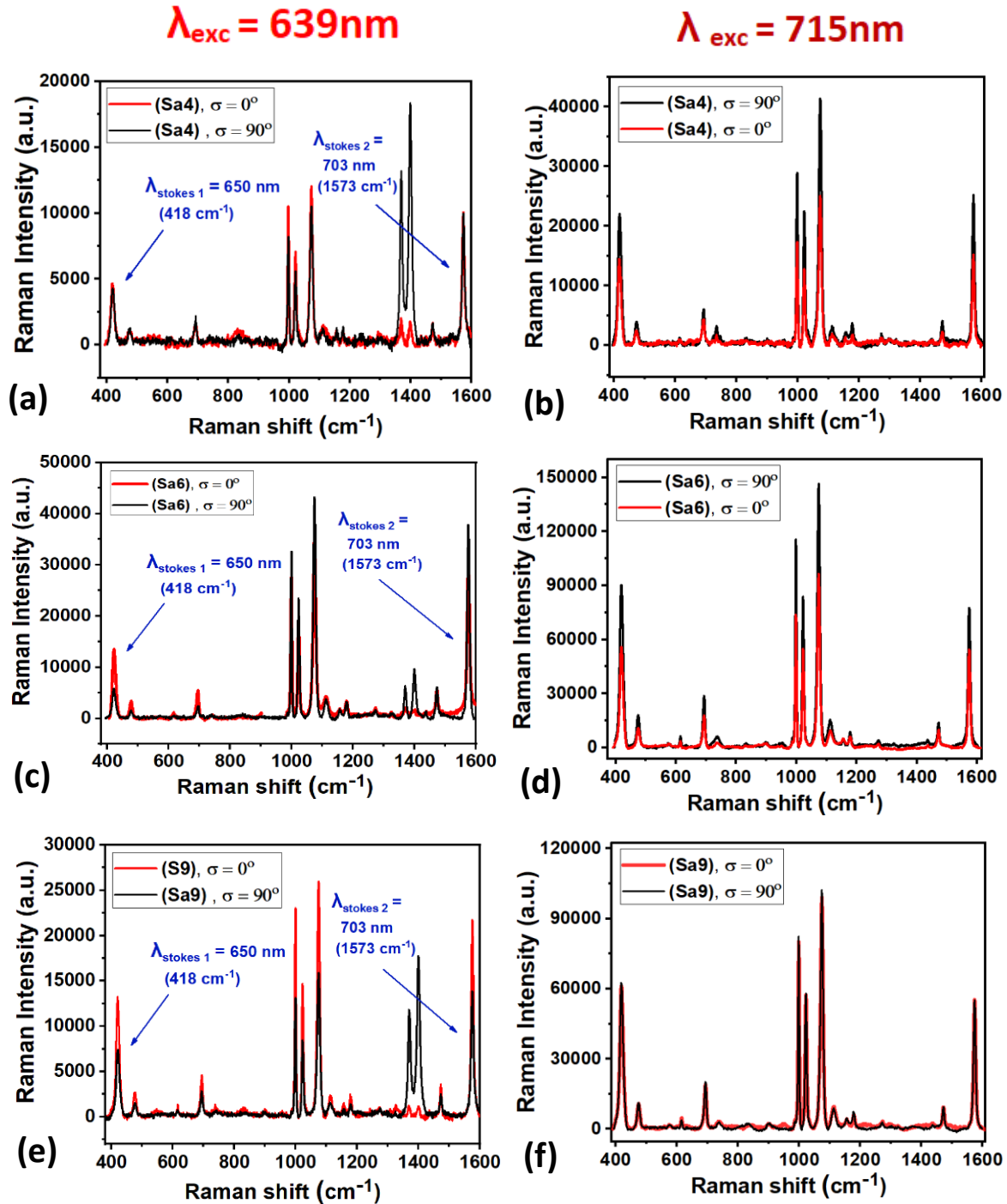


Figure 5.5a, c, e. SERS spectra measured at $\lambda_{exc} = 633\text{nm}$ for the samples Sa4, Sa6 and Sa9 at both $\sigma = 0^\circ$ and 90° polarizations. **b, d, f.** SERS spectra measured at $\lambda_{exc} = 785\text{nm}$ for the Sa4, Sa6 and Sa9 at both $\sigma = 0^\circ$ and 90° polarizations. (right column)²¹⁸.

Subsequently an increased $\lambda_{Stokes\ 2}$ peak intensity was observed at $\sigma = 90^\circ$ as the near-field E_p at λ_{TEp} is enhanced at $\lambda_{Stokes\ 2}$ position. This confirms that the intensities of λ_{Stokes} in SERS measurements depend on both the enhancement factors g and g^s . Subsequently, the factors g and g^s are determined by the λ_{exc} and its corresponding λ_{Stokes} positions relative to the excited plasmon mode and its FWHM. These experimental results emphasize the need for plasmon resonances with longer lifetime as well as a broad peaks for the efficient enhancement of both g and g^s factors in SERS sensing of a group of molecules emitting similar stokes wavelength for their vibrations. Similar experimental results were also obtained for sample Sa6 with larger nucleated Au arrays disk diameter $d \sim 60\text{nm}$ (see Figure 5.5c.). where the $\lambda_{exc} = 633\text{nm}$ position and its corresponding $\lambda_{Stokes\ 1}$ position at $\sigma = 0^\circ$ is closer to the excited resonance position λ_{TMp} at this angle when compared to its $\lambda_{Stokes\ 2}$ (in Figure 3.11a.). Thus, this sample Sa6 in Figure 5.5c (red spectra) exhibits trends similar to what was observed for the sample Sa3 in Figure 5.4a. Whereas, at $\lambda_{exc} = 785\text{nm}$ the distinct behavior of the relative SERS peak intensities in Figure 5.5d (red spectra) were absent corroborating its reflectance intensities in Figure 3.11a.

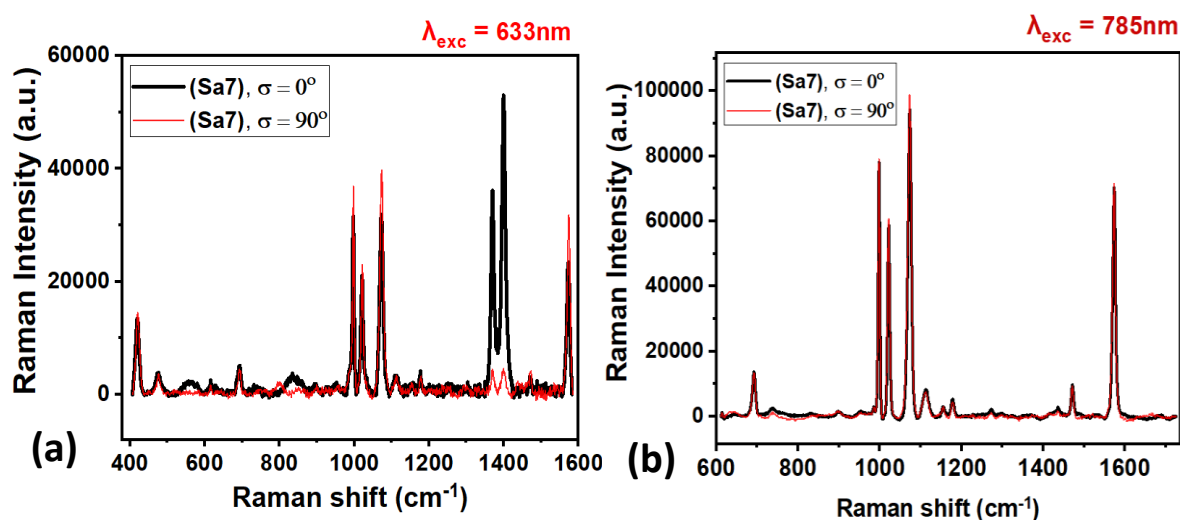


Figure 5.6. SERS spectra measured at **a.** $\lambda_{exc} = 633\text{nm}$ for the sample Sa7 at both $\sigma = 0^\circ$ and 90° polarizations. **b.** at $\lambda_{exc} = 785\text{nm}$ for the samples Sa4 at both $\sigma = 0^\circ$ and 90° polarizations. Furthermore, sample Sa7 coated with a thicker gold layer ($t \sim 10\text{nm}$) shows that its λ_{TMp} position along $\sigma = 0^\circ$ is red-shifted relative to $\lambda_{exc} = 633\text{nm}$ in Figure 1d. and thus a reversed SERS dichroism is observed (in Figure S10.) where both $\lambda_{Stokes\ 1}$ and $\lambda_{Stokes\ 2}$ peaks exhibits a $\cos^2(\sigma)$ dependency²¹⁸.

Furthermore, sample Sa7 coated with a near percolating gold layer thickness of ($t \sim 10\text{nm}$) shows that its λ_{TMp} position along $\sigma = 0^\circ$ is red-shifted relative to $\lambda_{exc} = 633\text{nm}$ in Figure 3.7a. and thus a reversed SERS dichroism is observed in Figure 5.6a. where both $\lambda_{Stokes\ 1}$ and $\lambda_{Stokes\ 2}$ peaks exhibit a $\cos^2(\sigma)$ dependency. Whereas, for $\lambda_{exc} = 785\text{nm}$ in Figure 5.6b, isotropic SERS effect was observed corroborating the reflectance spectra in Figure 3.7a. The SERS intensity and anisotropies of the samples Sa4 and Sa9 with larger Au diameter $d \sim 60\text{nm}$ in Figure 5.5a, b, e and f. corroborated with its far-field reflectance spectra in Figure 3.11a.

These findings further clearly validate the EM near-field enhancement mechanism of SERS as the SERS response is based on the anisotropic near-field enhancements. The fabricated samples exhibited capability of highly distributed hotspot ($2 \times 2\text{cm}$ arrays) and broad plasmon peaks of the collective plasmon modes for the enhancement of both g and g^s efficiently.

SERS Mapping

The SERS mapping measurements was performed in a set of reproduced Au array samples of Au $t \sim 5\text{nm}$ and nucleating grain diameter $d \sim 22\text{nm}$ exhibiting optical properties presented in Figure 5.7. under different polarization angles σ and excitation wavelengths λ_{exc} . These mapping measurements reveals the long ranged uniform sensitivity of the fabricated samples.

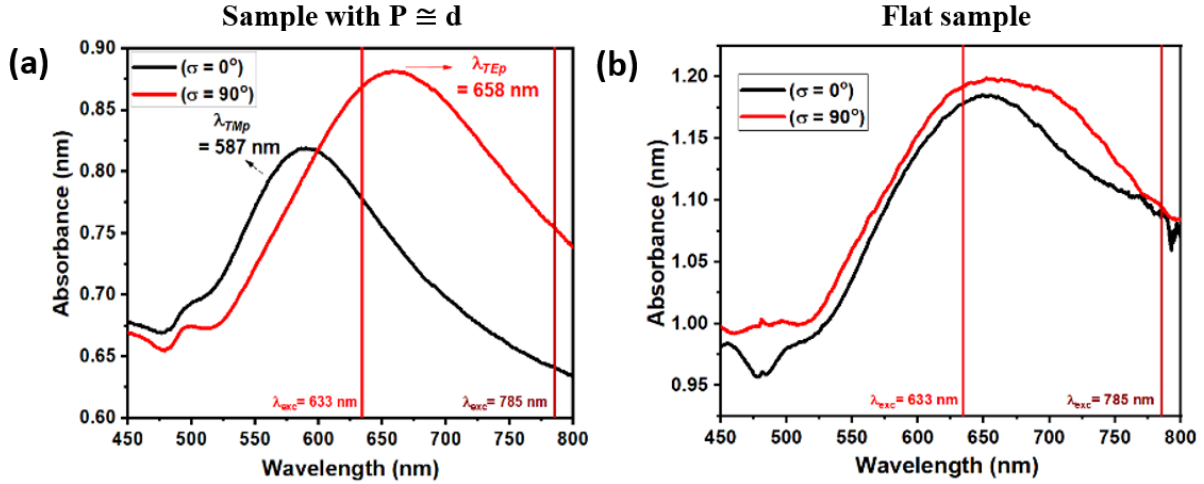


Figure 5.7. (a), Polarized reflectance spectra for sample with $P \cong d$ exhibiting anisotropic plasmon resonance peaks at $\lambda_{TMp} \sim 587\text{ nm}$ at $\sigma = 0^\circ$ and $\lambda_{TEp} \sim 658\text{ nm}$ at $\sigma = 90^\circ$ (b,) Polarized reflectance spectra for a flat sample exhibiting isotropic plasmon resonance peaks at $\lambda_{TMp} \sim 660\text{ nm}$ at $\sigma = 0^\circ$ and $\lambda_{TEp} \sim 660\text{ nm}$ at $\sigma = 90^\circ$. Vertical lines in the spectra indicate the experimental excitation wavelength (λ_{exc}) in which SERS mappings was performed for different polarizations and wavelengths²¹⁸.

The Figure 5.7 shows the absorbance spectra obtained from the reproduced samples. This confirms that the fabrication method is a reproducible technique. Further, the absolute SERS intensity and anisotropy in these samples also corroborate with values and trend observed for sample Sa3 as in Figure 5.3. For these samples the λ_{exc} at 633nm was further blue shifted from λ_{TEp} super-radiant mode more nearer the frequency of the sub-radiant collective plasmon mode when compared to the λ_{exc} positions on the reflectance spectra for the samples in Figure 5.2a and b.

This resulted in a more accurate determination of the Raman laser excitation wavelength near the sub-radiant collective plasmon modes. Figure 5.8a and b. shows the polarized SERS mapping measurements performed on the flat sample under $\lambda_{exc} = 633\text{nm} \ll \lambda_{TEp}$ near the frequency of the sub-radiant collective plasmon mode exhibiting long range isotropic uniform SERS intensity.

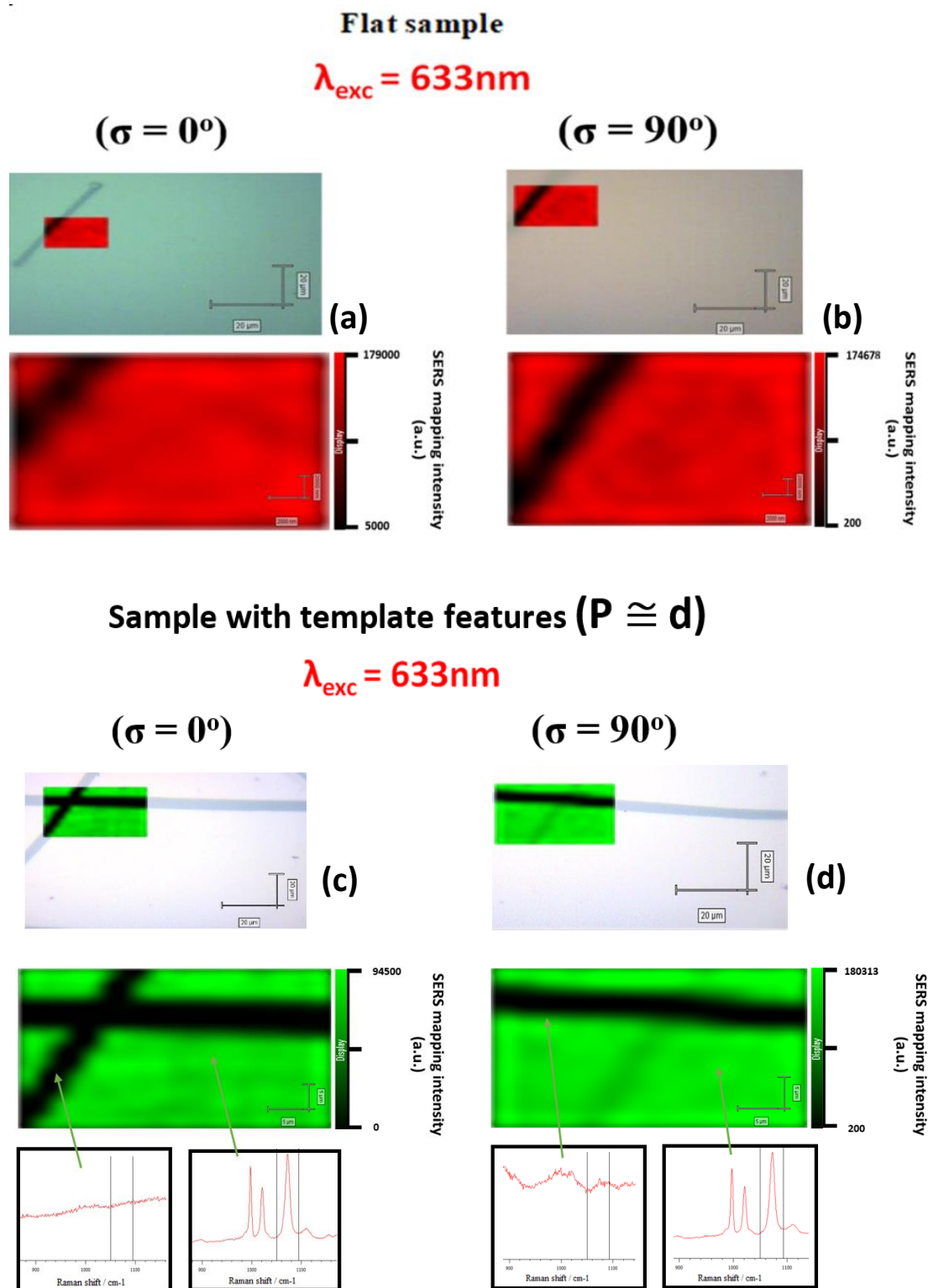


Figure 5.8. SERS Mapping measurements of phenyl thiolate peak 1081 cm^{-1} under $\lambda_{exc} = 633\text{nm}$ on flat sample at (a) $\sigma = 0^\circ$ and (b) $\sigma = 90^\circ$ exhibiting isotropic and long-ranged uniform sensing capability of the samples. (The dark black line in the SERS images represents a scratch on the Au layer). SERS Mapping measurements of phenyl thiolate peak 1081 cm^{-1} under $\lambda_{exc} = 633\text{nm}$ on sample with $P \cong d$ at (c) $\sigma = 0^\circ$ and (d) $\sigma = 90^\circ$ exhibiting anisotropic SERS and long-ranged uniform sensing capability of the samples. (The dark black line in the SERS images represents a scratch on the Au layer)²¹⁸.

Subsequently, polarized SERS mapping measurements performed on a sample with $P \approx d$ in Figure 5.8c. and d. exhibits its long-ranged anisotropic SERS on these samples under $\lambda_{exc} = 633\text{nm}$. Its SERS intensity is similar at $\sigma = 90^\circ$ where its interparticle spacing is S_2 when compared to the flat sample with interparticle spacing S_2 at both $\sigma = 0^\circ$ and $\sigma = 90^\circ$.

Whereas excitation under $\lambda_{exc} = 785\text{nm}$ near the frequency of the super-radiant mode, the SERS mapping measurement exhibited reduced but long ranged isotropic SERS intensity for the flat sample at Figure 5.9c and d. and subsequently for the sample with feature $P \approx d$ a more pronounced anisotropic response was observed in Figure 5.9 a and b. Further in Figure 5.9b, the SERS intensity at $\lambda_{exc} = 785\text{nm}$ was higher at $\sigma = 90^\circ$ where its interparticle spacing is S_2 when compared to SERS intensity of the flat sample at Figure 5.9c and d. with interparticle spacing S_2 along both $\sigma = 0^\circ$ and $\sigma = 90^\circ$. These results showcase the large area sensing ability of these samples and were similar to the SERS intensity and anisotropy trends observed for samples Sa1, Sa2 and Sa5 in Figure 5.3.

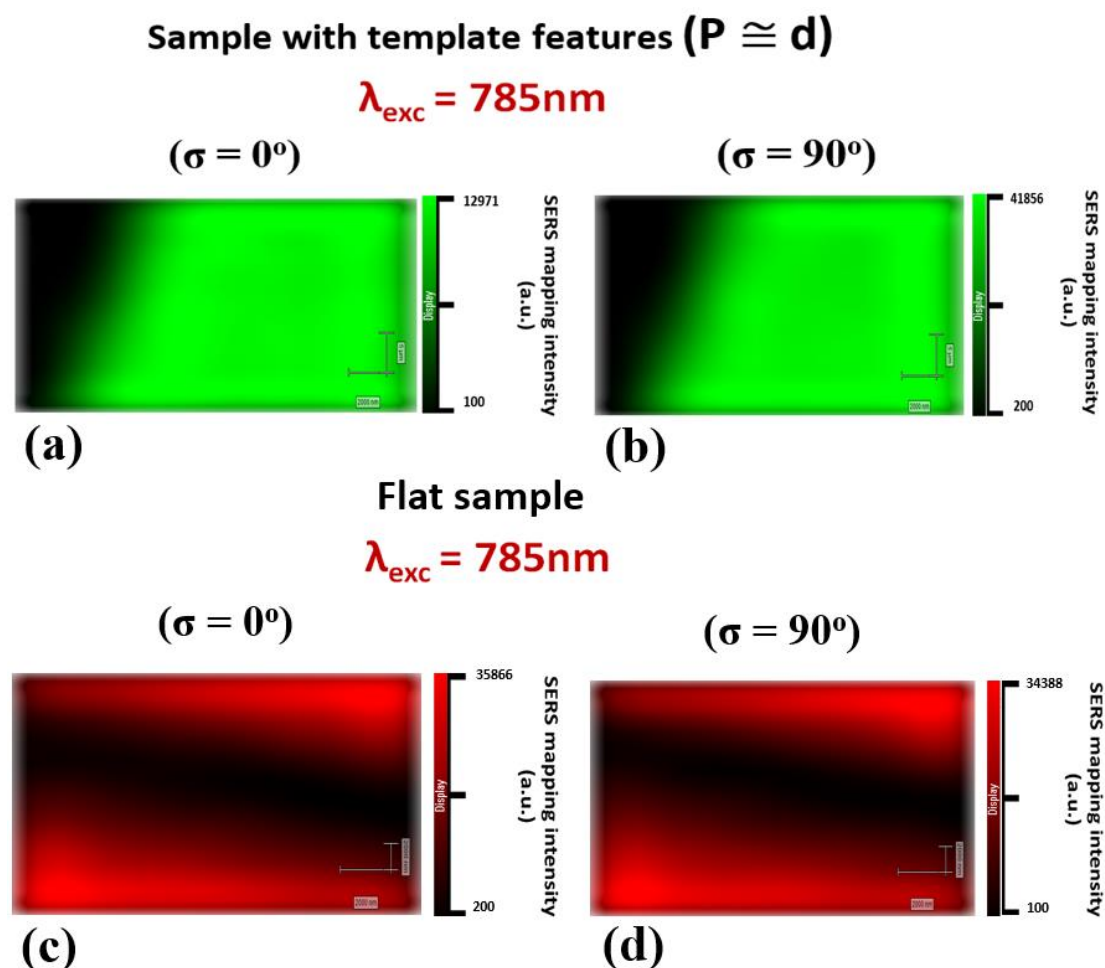


Figure 5.9 SERS Mapping measurements of phenyl thiolate peak 1081 cm^{-1} at (a) $\sigma = 0^\circ$ and (b) $\sigma = 90^\circ$ under $\lambda_{exc} = 785\text{nm}$ on sample with $P \cong d$ in the exhibiting anisotropic and long-ranged uniform sensing capability of the samples. (The dark line in the SERS images represents a scratch on the Au layer). SERS Mapping measurements of phenyl thiolate peak 1081 cm^{-1} at (c) $\sigma = 0^\circ$ and (d) $\sigma = 90^\circ$ under $\lambda_{exc} = 785\text{nm}$ on sample with flat template exhibiting isotropic and long-ranged uniform sensing capability of the samples. (The dark line in the SERS images represents a scratch on the Au layer)²¹⁸.

Further the SERS enhancement factors on these samples were calculated and reported based on the equation 57. The calculations revealed that the SERS enhancement resulting from the set of samples with larger Au grain diameter $d \sim 60\text{nm}$ exhibiting an increase in the SERS resulting from the super radiant plasmon mode when compared to the excitation on the samples with $d \sim 27\text{nm}$ corroborating the Mie theory, which states that the scattering cross section and far field radiation increases for *MNPs* with increasing diameter. This shows that the wavelength scanned SERS intensities and anisotropy trends could differ for closely spaced MNP array system with increasing MNP diameter.

SERS enhancement calculation

Calculation of enhancement Factor for the phenyl thiolate peak 1081 cm^{-1} on the samples (Sa2) and (Sa6) with template features $P \cong d$. The sample Sa2 has Au grain diameter of ($d \sim 27\text{nm}$) and Sa6 has ($d \sim 60\text{nm}$).

The enhancement factors were calculated for excitations under $\lambda_{exc} = 633$ and 785 nm excitation wavelength at both $\sigma = 90^\circ$ and $\sigma = 0^\circ$.

The enhancement factor (EF) was calculated based on the formula^{4,5}.

$$\text{Enhancement factor (EF)} = \frac{I_{SERS}}{N_{SERS}} \times \frac{N_{ref}}{I_{ref}} \dots\dots\dots 57$$

Where, I_{SERS} = Intensity of the SERS, I_{ref} = Intensity of reference Raman, N_{SERS} and N_{ref} = no of phenyl thiolate molecules in the illuminated volume.

Thio-phenol dissolved in an aqueous solution as (0.0097 M) was measured for I_{ref} value under both $\lambda_{exc} = 633$ and 785 nm excitation wavelength with a 50x, 0.7 N.A numerical aperture objective.

The minimum laser beam waist diameter ω can be calculated from the formula

$$\omega = \frac{(4 * \lambda_{exc})}{\pi * NA} \dots\dots\dots 58$$

Where, λ_{exc} is the laser wavelength and NA is the numerical aperture of the focusing objective.

$$\omega_{633nm} = 1.152\ \mu\text{m}$$

$$\omega_{785nm} = 1.42\ \mu\text{m}$$

$$\text{The depth of focus } Z = \frac{2\pi * \omega^2}{\lambda} \dots\dots\dots 59$$

$$Z_{633nm} = 13.1\ \mu\text{m}$$

$$Z_{785nm} = 16.1\ \mu\text{m}$$

The focal volume of the illumination is $V_F = \left(\frac{\pi}{2}\right)^{1.5} * \omega^2 * Z \dots\dots\dots 60$

$$V_F\ 633nm = 34.2\ \mu\text{m}^3$$

$$V_F\ 785nm = 63.8\ \mu\text{m}^3$$

The number of thio-phenol molecules N_{ref} is given by $N_{ref} = V_F * C_{Thiophenol} * N_A$

$$N_{ref\ 633nm} = 1.9 \times 10^8$$

$$N_{ref\ 785nm} = 3.7 \times 10^8$$

Where, $C_{Thiophenol}$ is the molar concentration of the thio-phenol dissolved in the aqueous solution, and N_A is the Avogadro number.

The thio-phenol molecules chemisorb as a monolayer onto the Au surface as phenyl-thiolate.

$$\text{The area of laser spot is } A_{laser} = \pi \left(\frac{\omega}{2}\right)^2 \dots\dots\dots 61$$

The Au array contained 20% less Au surface area when compared to a percolated laterally continuous flat Au surface with ($f = 1$).

$$A_{laser\ 633nm} = 1.04 \mu\text{m}^2$$

$$A_{laser\ 785nm} = 1.58 \mu\text{m}^2$$

The occupied surface area $A_{thiophenol}$ for a single thiophenol molecule²¹⁵.

$$A_{thiophenol} = 1.16 \times 10^{-16} \text{ m}^2$$

The number of thiophenol molecules in the SERS measurements is

$$N_{SERS} = A_{laser} / A_{Thiophenol} \dots\dots\dots 62$$

$$N_{SERS\ 633nm} = 7.2 \times 10^3$$

$$N_{SERS\ 785nm} = 1.08 \times 10^4$$

Table 5.1. Calculated parameters to obtain enhancement factor for sample (Sa2) with template features $P \cong d$ and Au grain diameter $d \sim 27\text{nm}$.

	$\lambda_{exc} = 633\text{nm}, \sigma = 0^\circ$	$\lambda_{exc} = 633\text{nm}, \sigma = 90^\circ$	$\lambda_{exc} = 785\text{nm}, \sigma = 0^\circ$	$\lambda_{exc} = 785\text{nm}, \sigma = 90^\circ$
I_{SERS}	65384	85004	14800	63163
N_{SERS}	7.2×10^3	7.2×10^3	1.08×10^4	1.08×10^4
I_{ref}	544	544	763	763
N_{ref}	1.9×10^8	1.9×10^8	3.7×10^8	3.7×10^8

Enhancement factor (EF) of Sample (Sa2)

$$EF_{\lambda_{exc}633nm, \sigma = 0^\circ} = 4.1 \times 10^6$$

$$EF_{\lambda_{exc}633nm, \sigma = 90^\circ} = 3.6 \times 10^6$$

$$EF \lambda_{exc785nm, \sigma = 0^\circ} = 2.8 \times 10^6$$

$$EF \lambda_{exc785nm, \sigma = 90^\circ} = 6.6 \times 10^5$$

Table 5.2. Calculated parameters to obtain enhancement factor for sample (Sa6) with template features $P \cong d$ and Au grain diameter $d \sim 60\text{nm}$.

	$\lambda_{exc} = 633\text{nm}, \sigma = 0^\circ$	$\lambda_{exc} = 633\text{nm}, \sigma = 90^\circ$	$\lambda_{exc} = 785\text{nm}, \sigma = 0^\circ$	$\lambda_{exc} = 785\text{nm}, \sigma = 90^\circ$
I_{SERS}	36787	43926	96557	148052
N_{SERS}	7.2×10^3	7.2×10^3	1.08×10^4	1.08×10^4
I_{ref}	544	544	763	763
N_{ref}	1.9×10^8	1.9×10^8	3.7×10^8	3.7×10^8

Enhancement factor (EF) of Sample (Sa6)

$$EF \lambda_{exc 633nm, \sigma = 0^\circ} = 1.7 \times 10^6$$

$$EF \lambda_{exc633nm, \sigma = 90^\circ} = 2.1 \times 10^6$$

$$EF \lambda_{exc785nm, \sigma = 0^\circ} = 4.3 \times 10^6$$

$$EF \lambda_{exc785nm, \sigma = 90^\circ} = 6.6 \times 10^6$$

The fabricated samples exhibited capability of highly distributed hotspot (2x2cm arrays), SERS enhancement of 10^6 orders and broad peaks of the collective plasmon modes for the enhancement of both g and g^s efficiently.

5.2. Anisotropic SERS effect of percolated Au metal films

As discussed in chapter 4. The percolated ultrathin Au films followed the corrugated template modulations forming laterally continuous corrugated metal films which supports “propagating” delocalized surface plasmon polariton (SPPs) in the near-infrared (NIR) region. These modes exhibited distributed EM nearfield with large electric field components parallel and perpendicular to the surface during SPP excitation based on their k_x spatial corrugation. SERS measurements were performed to investigate benefits of NIR-SERS sensing and to study the adsorbed molecules Raman vibrations – polariton interaction. This chapter further shows the dependence of SPP modes surface field orientations on corrugated surface in the enhancement of Raman modes of different polarizability tensor components. These investigations were used to determine the orientation of the adsorbed thio-phenol molecules on the Au surface and to understand the “SERS” surface selection rules on corrugated plasmonic surface.

5.2.1. Near-infrared SERS sensing on percolated anisotropic Au films

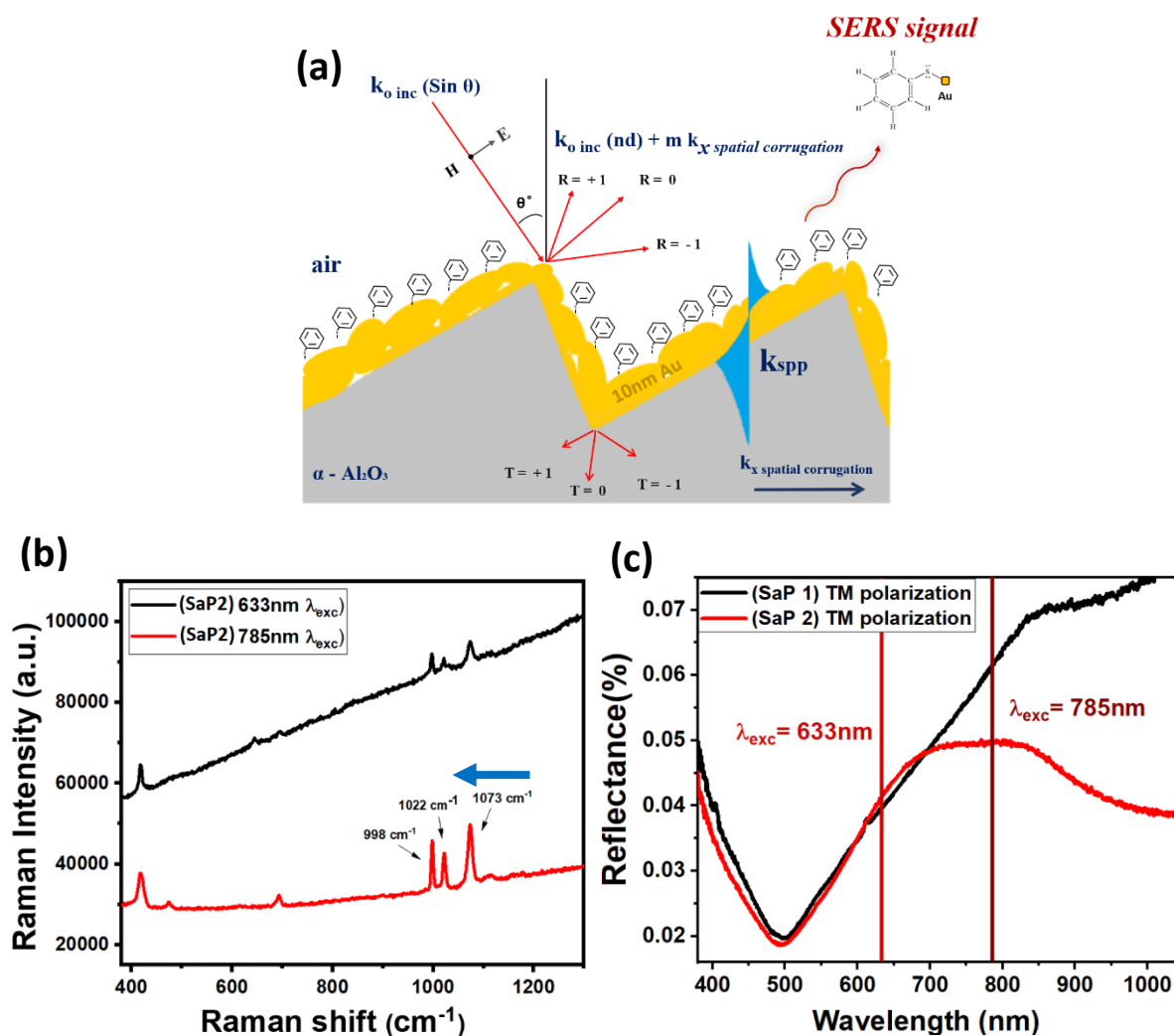


Figure 5.10 (a) Schematics depicting the excitation of hybrid SPP modes on percolated Au films deposited on corrugated sapphire templates. (b). SERS spectra of phenyl thiolate on SaP2 with $\lambda_{\text{exc}} = 633 \text{ nm}$ (black line) and $\lambda_{\text{exc}} = 785 \text{ nm}$ (red line), the blue arrow indicates the downshifting of peaks associated with phenyl ring vibrations upon chemisorption on Au (Raman spectra are presented without

fluorescence background subtraction) and (c) Reflectance measurements of sample SaP1 (black spectra) and SaP2 (red spectra) at $\theta = 50^\circ$, TM polarization, with the respective Raman laser line positions at $\lambda_{exc} = 633$ nm and $\lambda_{exc} = 785$ nm²¹⁷.

Due to the excitation of the hybrid SPP with low energy in the NIR region as discussed in chapter 4, these samples were investigated for SERS sensing of phenyl-thiolates adsorbed on the fabricated laterally continuous corrugated plasmonic surface. Similar to discussions the previous section 5.1.1. The phenyl ring vibration modes assigned to the (C – C – C ring bend (ring breathing) and In- plane. C – C – C bend + C – S stretching) downshifted to 998 cm^{-1} and 1072 cm^{-1} upon the formation as phenyl thiolates (PT), subsequently confirming the chemisorption of thio-phenol onto the Au surface²⁰⁴ see Figure. 5.10b. (where arrow indicates the downshifting).

Furthermore, in Figure. 5.10b the SERS spectra collected under $\lambda_{exc} = 785$ nm exhibited reduced interference background and more prominent SERS when compared to excitation under $\lambda_{exc} = 633$ nm. The large intensity enhancement of PT peaks under $\lambda_{exc} = 785$ nm is due to both the λ_{exc} and its related λ_{stokes} (as in Table 5.3.), are closer to the excited λ_{SPP} resonance near 1040 nm in Figure. 5.10c. Moreover, chemisorbed aromatic thiols forms S-Au bonds in the Au metal surface, thus causing charge transfer process to occur at shorter excitation wavelengths which also hybridizes their molecular orbitals²⁰⁸, changes their polarizability and increases the molecules Raman scattering cross-section²⁰⁹. As a result of these effects, intense fluorescence background and photo- reactions in thiolates is observed in SERS excitation at $\lambda_{exc} = 633$ nm.

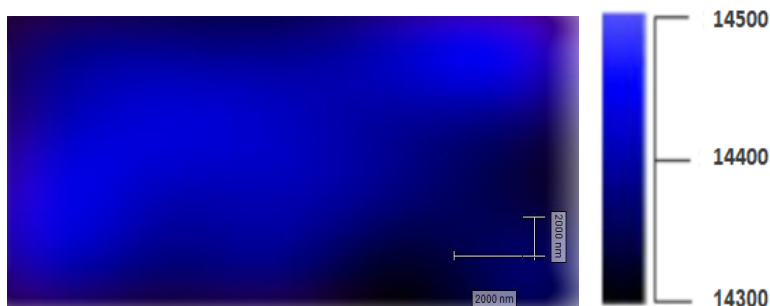


Figure 5.11. SERS intensity mapping measurements of phenyl thiolate peak 998 cm^{-1} on sample Sa2 with a step size of $3\ \mu\text{m}$ ²¹⁷.

Further, large area SERS intensity mapping measurements were performed for sample SaP2 under $\lambda_{exc} = 785$ nm which confirmed that the SERS intensity was uniform and photo-degradation of the molecule was minimal (see Figure 5.11). When comparing the SERS intensity obtained from the flat and corrugated samples in Figure. 5.12a revealed that the corrugated sample SaP2 exhibited a 46- fold SERS gain for the phenyl-thiolate Raman active mode assigned to C – C – C ring bend (ring breathing (998 cm^{-1})) when compared to the SERS intensity of the mode collected from the flat Au sample SaP1. These SERS measurements exhibiting intensity amplifications of 10^3 orders analogous to the near-field enhancement for SPP modes described in Ref²¹⁰ whereas additional enhancement from charge

transfer is also presumed to influence this value. The SERS enhancement exhibited by the fabricated samples supporting SPP in Figure 5.12a and b. are lower when compared to the non-percolated Au array substrates which exhibited collective LSPR modes in Figure 5.2c, d.

Table 5.3. Assignment of thiophenol molecules Raman vibrations and their Raman peak positions with related Stokes wavelengths and symmetry classes of vibration modes^{172,211}.

Thiophenol Raman vibration peak positions	Stokes shifted wavelength λ_{stokes} at ($\lambda_{\text{exc}} = 633 \text{ nm}$)	Stokes shifted wavelength λ_{stokes} at ($\lambda_{\text{exc}} = 785 \text{ nm}$)	Thiophenol molecular vibrations assignment	Symmetry class (C_{2v})
473 cm^{-1}	652 nm	815 nm	Out-of-plane. C-C-C bending	b_1
615 cm^{-1}	658nm	824 nm	In-plane. C-C-C ring bending + C-S stretching	b_2
693 cm^{-1}	662nm	830 nm	In-plane. C-C-C ring bending + C-S stretching	a_1
737 cm^{-1}	663nm	833 nm	Out-of-plane. C-H ring bend	b_1
998 cm^{-1}	675 nm	851 nm	C-C-C ring bend (ring breathing)	a_1
1072 cm^{-1}	679 nm	857 nm	In-plane. C-C-C bend + C-S stretching	a_1
1573 cm^{-1}	703 nm	895 nm	Symmetric in-plane. C-C ring stretching	a_1

Furthermore, Polarized Raman analysis performed between the incident polarization and the corrugation vector revealed an anisotropic SERS response for the sample SaP2. A 5-fold SERS intensity gain for the peak at 998 cm^{-1} was observed at $\sigma = 0^\circ$ where the SPP mode is excited when compared to the same peak at $\sigma = 90^\circ$ (see Figure. 5.12b). Although, the SERS intensity gain of the peak 998 cm^{-1} at $\sigma = 90^\circ$ along the corrugation long axis was higher when compared to the SERS intensity from flat sample. Subsequently, similar anisotropic SERS response dependent on the excitation polarization angle was observed for samples Sa3 and Sa4 with different k_x spatial corrugation. Further, the SERS intensity gain of phenyl-thiolate Raman modes decreased for samples with increasing corrugation period – see Figure. 5.12c. This decrease in intensity was due to the larger difference between λ_{exc} and the excited λ_{SPP} position which is dependent on the value of k_x spatial corrugation. Further, samples with larger corrugation periods fabricated by this method exhibited an increase in standard deviation δ of the average corrugation period value P , this further resulted in a weaker SPP coupling on samples with increasing corrugation period.

5.2.2. SERS “surface selection rules” for non-isotropic molecules on percolated corrugated metal film

Due to the large dipole oscillator strength of near infrared (NIR) SPP mode near-fields at $\lambda_{\text{exc}} = 785 \text{ nm}$ when compared to SPPs excited in the visible spectral range¹¹⁵, and importantly without

the disadvantages of intense interference backgrounds resulting from charge transfer hybridizations which occurs at higher excitation frequencies. These fabricated samples were suitable platforms to study molecules Raman vibrations-polariton interactions.

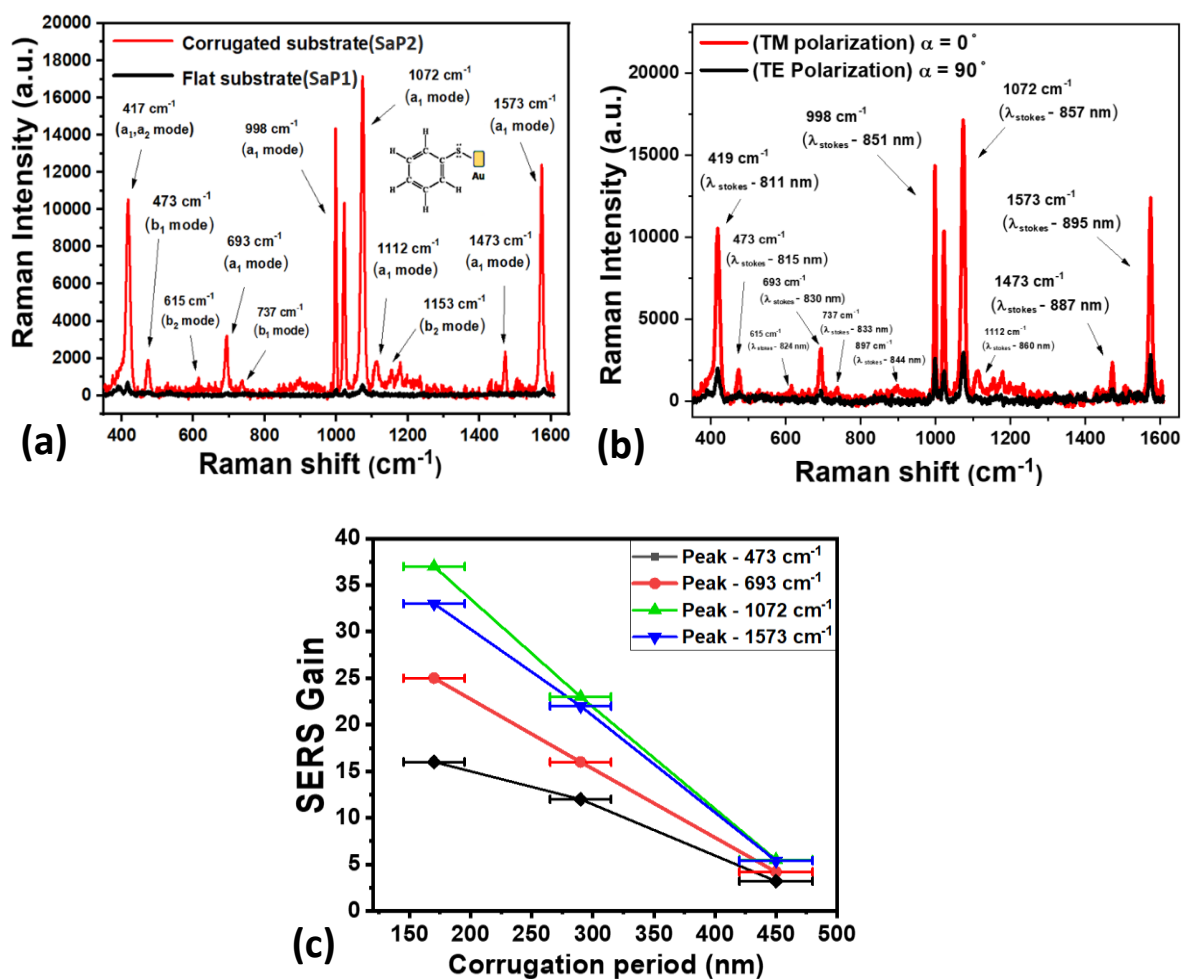


Figure 5.12. (a) SERS spectra of phenyl thiolate on flat SaP1 (black line) and corrugated sample SaP2 (red line). Vibration modes assigned to Raman peaks with their symmetry classes are listed in Table 2, (b) Schematic drawing of the polarized SERS measurement setup with indicated angle σ . (c) SERS Gain of selected phenyl thiolate Raman vibrational peaks for different grating periodicity. (SERS gain values were calculated with respect to the absolute Raman intensity of the peaks from the flat sample Sa1)

217

By analyzing the SERS anisotropies and intensities measured in polarized SERS measurements, the dependency of SERS of the adsorbed PT molecules on the excitation polarization and its resulting plasmon surface-field orientations were investigated. Polarized SERS measurements performed for $\Delta\sigma = 2.5^\circ$ in Figure 5.13. revealed a dichroic SERS anisotropy with $\cos^2(\sigma)$ dependency for PT peaks assigned in Table 5.3. This was in contrary to the $\sin^2(\sigma)$ dependency observed for PT peaks on non-percolated anisotropic arrays in Figure 5.3. Further, for anisotropic planar molecules such as the phenyl thioliates their relative Raman peaks intensities in the spectra depend on the symmetry of their Raman vibration modes⁶⁷. As a result of this dependence related to the polarizability of Raman modes, the analytes Raman modes relative

SERS intensities differ, as the orientation of the analyte's induced dipole moment can be different from incident excitation polarization¹¹³.

Here, the SERS dichroism with $\cos^2(\sigma)$ due to the plasmonic anisotropy was studied for phenyl thiolate Raman modes of different polarizability tensor components on these corrugated plasmonic samples supporting propagating SPP modes. As discussed in chapter 4. The NIR-SPP modes excited in these samples have large oscillator strength which strongly induces the dipole moment in the molecules. Further, the propagating SPP surface field orientation have an extended nearfield spatial distribution when compared to the localized confined fields of LSPR modes. Thus, these SERS on these substrates exhibit an extended SERS excitation area with reduced photo-induced effects on the probed molecule. For phenyl thiolate molecules with a C_{2v} symmetry group, the a_1 Raman modes are totally symmetric vibration with a combination of α_{xx} , α_{yy} and α_{zz} Raman tensor components on the metal surface frame of reference, whereas, the other b_1 , b_2 and a_2 are non-totally symmetric vibration modes and contains α_{xz} , α_{yz} and α_{xy} tensor components²¹¹ as in Table 5.3. The SERS dichroism due to the plasmonic anisotropy of the peak assigned to the symmetric in-plane C – C ring stretching at 1573 cm^{-1} with a_1 symmetry was more prominent in intensity and dependent on the corrugation period as in Figure 5.13a. whereas, the SERS dichroism of the peak assigned to the out-of-plane C–C–C bending at 473 cm^{-1} with non-totally symmetric vibration b_1 mode in Figure. 5.13b. exhibited less intensity compared to the a_1 modes in Figure 5.13a, c, d. and less pronounced dependence on the corrugation period.

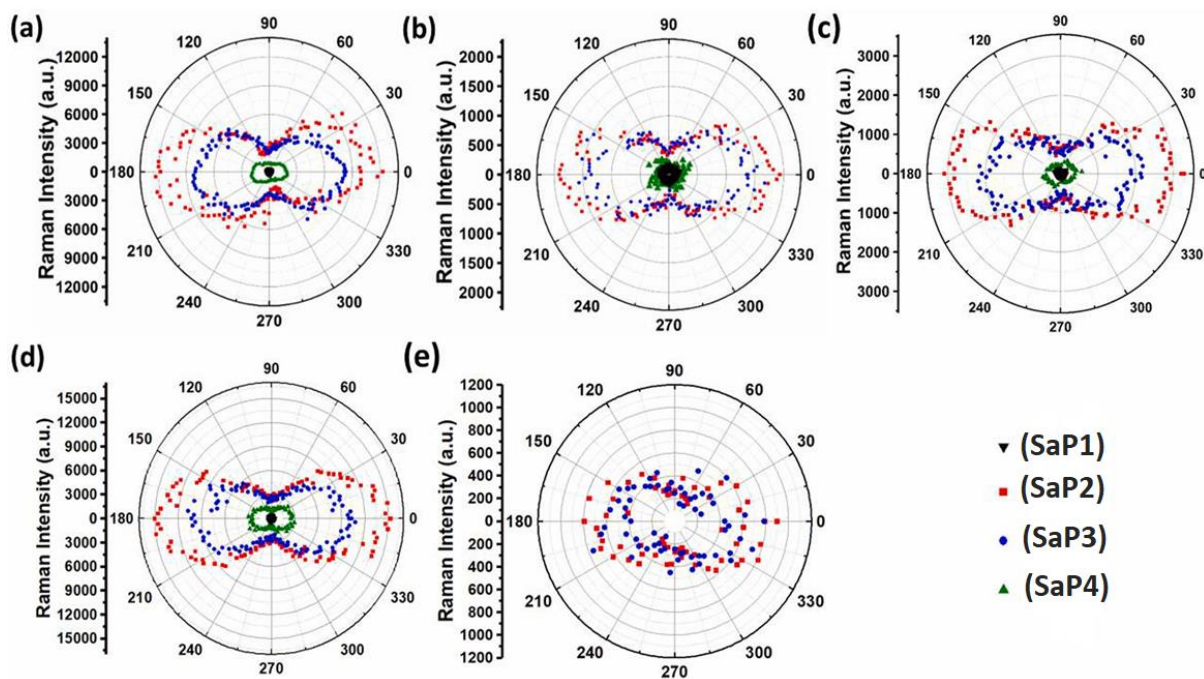


Figure 5.13. Analysis of Raman intensity of selected thio-phenol peaks in Table 2. (a) 1573 cm^{-1} , (b) 473 cm^{-1} , (c) 693 cm^{-1} , (d) 998 cm^{-1} and (e) 615 cm^{-1} as a function of the azimuthal angle ($\Delta\sigma = 2.5^\circ$) on flat and corrugated samples with different periods in polarized SERS measurements. (Table 5.3.) depicts the symmetry modes corresponding to the Raman peaks analyzed (a_1 are totally symmetric vibration), (b_1 , b_2 and a_2 non-totally symmetric vibrations)²¹⁷.

The electric field component E_x parallel to the surface becomes large only during the SPP excitation along the k_x spatial corrugation ($\sigma = 0^\circ$) - Figure. 4.4b at $\theta = 50^\circ$. This significantly excites the b_1 mode which has a α_{xz} component with vibrational motion parallel to the surface along the k_x spatial corrugation at $\sigma = 0^\circ$ as in Figure. 5.13b. resulting to cause a dichroic behavior in polarized SERS measurements due to the difference in surface fields excited at $\sigma = 0^\circ$ and 90° . Subsequently, a completely non-dichroic SERS behavior for peak 473 cm^{-1} with b_1 mode was observed on sample SaP4 (Green plots) in Figure. 5.13b. this is due to the weak SPP coupling and decrease in electric field strength along the X direction parallel to surface as δ (the standard deviation of corrugations periodicity) increases for both the height and width of the corrugated facets of this sample, which causes the dichroism to cease. Similar to the b_1 mode with a α_{xz} component, less dependency of SERS intensity on corrugation period was also observed for the peak at 615 cm^{-1} classified as the b_2 mode with α_{yz} polarizability component in Figure. 5.13e but this peak was not observed for SaP1 and SaP4. Apart from the relative intensities of Raman active modes, the dichroic SERS behavior of Raman modes in Table 5.3. were determined mostly due to the excitation of SPP along the corrugation vector rather than the orientation of the analyte on the surface for a_1 , b_1 and b_2 modes – Figure. 5.13. as these Raman modes have tensor components both parallel and perpendicular to surface. The a_2 mode with α_{xy} tensor component with both the axes in the plane of the surface was not observed on these anisotropic corrugated samples. Whereas, the peak at 834 cm^{-1} classified as a_2 mode with α_{xy} tensor component was observable in SERS spectra obtained from non-percolated Au arrays in Figure 5.2. supporting hybridized collective LSPR modes, as these modes have intense confined near-field along both E_x and E_y component on their surface due to $S \ll r$ at both $\sigma = 0^\circ$ and $\sigma = 90^\circ$. Plasmonic samples with shorter corrugation periods fabricated in this study exhibited pronounced SERS dichroism for both totally symmetric (a_1) and non-symmetric vibrations (b_1 and b_2) modes versus the substrates with larger value of corrugation periods. This was due to the effective coupling of SPP mode at $\sigma = 0^\circ$ for SaP2 when compared to the other samples SaP3 and SaP4. These experimental investigation and results show the dependence of SPPs surface field orientation excited on corrugated plasmonic surface in enhancing both diagonal and non-diagonal component of molecules polarizability tensor α . The experimental investigation using this technique can reveal information about the degree of molecular orientation as well as symmetry of highly organized samples such as *polar liquids*²¹², *crystals*, *polymers*²¹³ and *carbon materials*²¹⁴ apart from self-assembled monolayers (SAM) of molecules.

6. Summary and outlook

In this study, surface reconstruction of (α -Al₂O₃) M-plane wafers were utilized to fabricate corrugated substrates of different periods ranging from $P \sim 30\text{nm}$ (subwavelength) to $P \sim 450\text{nm}$. These corrugated substrates with high permittivity ($\varepsilon = 11-9$) were used as templates to deposit ultrathin Au films thickness $t \leq 10\text{ nm}$ to utilize and study them for surface enhanced Raman scattering applications.

The ultra-thin Au metal films with thickness below the percolation threshold nucleated into *2D-MNP* arrays with inter-particle gap $S \ll r$, where r is the radius of the *MNP*. The optimal condition for the ordering of *MNPs* as arrays was achieved at low Au deposition rate of $10 \text{ \AA} / \text{hours}$ when utilizing an e-beam evaporation method under ultra-high vacuum ($\sim 10^{-10} \text{ mbar}$). The Au disk like grains nucleated with an anisotropic in-plane ordering onto templates with feature period $P \cong d$, where d is the diameter of the nucleating grain. Subsequently, the Au disks were randomly distributed when $P \gg d$ as similar to deposition on a flat template. Further, autocorrelation functions of their respective AFM images confirmed the anisotropic ordering of nucleating 2D-MNP arrays on templates with $P \cong d$. The plasmonic properties of percolated anisotropic Au films was studied and investigated by polarized optical spectroscopy. Polarized reflectance analysis exhibited an anisotropic plasmonic response in the ordered Au arrays dependent on the angle between corrugation vector and laser polarization direction (σ). Furthermore, simulated spectra and EM near-field distributions corroborated the anisotropic plasmonic trend and revealed the excitation of hybridized collective plasmon modes as λ_{TMp} along $\sigma = 0^\circ$ and λ_{TEp} along $\sigma = 90^\circ$. This plasmonic hybridization due to the strong coupling between the *MNPs* with sub 5 nm inter-particle gap induced excitation of higher-order plasmon modes in the higher frequency region when compared to the fundamental dipole mode. Further, plasmonic hybridization and the origin of plasmonic anisotropy was studied for different sets of samples with optimized corrugation period P , Au disk diameter d , Au film thickness t and the nucleated Au grain's in-plane shape under linearly polarized excitation. These samples exhibited similar anisotropic plasmonic trends. Results further showed the range of tuneability of λ_p position for selected anisotropic samples discussed in this work from $\lambda_p \sim 550\text{nm}$ to $\lambda_p \sim 710\text{nm}$ (in the visible region). These ordered Au array structures supporting hybridized-collective plasmon modes can be used in a range of applications such as waveguides, on chip communications, and to study non-linear Raman scattering phenomena and surface selection rules. Further, transient absorption spectroscopy (TAS) measurements were performed on the samples exhibited the plasmonic anisotropy resulting from the short-ranged ordering of Au disks on samples with features $P \gg d$, this effect was invisible in polarized-steady state spectroscopic analysis. A blue shifted excited states λ_p positions in polarized-TAS measurements was observed when compared with the polarized-steady state measurement, this was presumed due to the excited non-radiative charge carriers induced effective primitivity modulation on the films with $S \ll r$ under intense pulsed laser excitation after ~ 1 picosecond. The blue shift of the λ_p positions in polarized-TAS depended on the interparticle space S rather than the pump laser excitation wavelength $\lambda_{pump \text{ excitation}}$. Here, these samples with giant EM nearfield enhancement were tested for SERS sensing. Polarized and wavelength scanned SERS measurements revealed that the SERS enhancements due to the excitation near a sub-radiant collective plasmon mode wavelength at $\lambda_{exc} = 633\text{nm} < \lambda_{TEp}$

depended primarily on the inter-particle spacing S rather than order in MNP arrays. This was concluded due to the similar absolute SERS intensities at $\lambda_{exc} = 633\text{nm}$ for $\sigma = 90^\circ$ for flat (Sa1), $P \cong d$ (Sa2) and $P \gg d$ (Sa5). In the contrary at $\lambda_{exc} = 785\text{nm} > \lambda_{TEp}$ related to the super-radiant plasmon frequency the absolute SERS intensities differed between flat (Sa1), $P \cong d$ (Sa2) and $P \gg d$ (Sa5) along both $\sigma = 90^\circ$ and $\sigma = 0^\circ$, exhibiting that the ordering of $MNPs$ as arrays influences the antenna modes scattering intensity resulting in a highly anisotropic SERS dependent on σ . Further, anomalous SERS intensity independent of the far-field optical spectra were observed at Raman excitation near the sub radiant modes wavelength. This was due to the enhanced spatial and temporal feature of the hybridized sub-radiant mode on these 2D-arrays with $S \ll r$. Subsequently, the anisotropy induced SERS dichroism of its relative Raman peak intensities depended on position of λ_{exc} when compared to the excited λ_p peak position and its $FWHM$. Due to this the lower frequency Stokes shifted peak $\lambda_{Stokes 1}$ exhibited a $\cos^2(\sigma)$ dependency as it was nearer to the excited plasmon modes λ_p and λ_{exc} . This peaks intensity was approximated by the commonly used $|E|^4$ mechanism. While, the higher Stokes shifted peak $\lambda_{Stokes 2}$ exhibited a $\sin^2(\sigma)$, as its SERS intensity depended on differing enhancement factors g at λ_{exc} and g^s at λ_{Stokes} , this observance validated the EM near field mechanism of SERS. Most of the seminal requirements for reliable, robust and reproducible SERS due to the distributed hotspot, broad resonance peak (enabling wider Stokes-shifted ranges) and near field enhancements up to 10^6 orders were achieved on the fabricated samples. Further polarized SERS mapping measurements exhibited the long-ranged SERS sensing capability of these SERS substrates based on 2D -arrays. Finally, as a suggestion for the continuation of this study, transient absorption spectroscopy with pump-probe delays in the femto-second regime can be used to experimentally investigate life time of these hybridized-collective plasmon modes in a quantitative way and corroborate it with its resulting SERS enhancements from Raman λ_{exc} at sub-radiant and super-radiant frequency, especially on arrays with number of particles $N < 10$ which would clearly manifest the sub-radiant mode wavelength distinguishing it from the super-radiant mode. This analysis of transient absorption spectroscopy in the femto-second pump-probe delays on the plasmonic samples can shed light on relaxation dynamics of both radiative decay (for applications in surface enhanced spectroscopies) as well as non-radiative plasmon decay (hot-carriers induced surface catalysis).

Secondly, Ultra-thin Au metal films of just percolated thickness $t \sim 10\text{nm}$ deposited on the corrugated templates of different periods obtained their template modulations as ultrathin corrugated plasmonic surfaces. A low temperature post deposition annealing process quenched the LSPR modes of the just percolated ultra-thin metal films and improved the film connectivity. Whereas, high temperature post deposition annealing process facilitated the dewetting of the just percolated film reducing its surface fill factor. On studying the plasmonic properties of the percolated, anisotropic sample's reflectance spectra - confirmed the improvement in percolation of the ultrathin metal film deposited at a just percolated metal thickness after the post deposition low-temperature annealing process. These periodically corrugated metal nanostructures diffracted light with an increased wavevector based on their k_x *spatial corrugation* thus mediating plasmon-photon momentum matching conditions to excite SPPs at TM polarized excitation. Numerical dispersion curve calculations and simulated near-field distributions corroborated the polarized far-field reflectance spectra in the excitation of a delocalize SPP mode. These SPP supporting structures can be used in a range of applications

such as waveguides, on chip communications, THz devices and in increasing the spatial resolution of scanning near field microscopy (SNOM). Further, field polarizations play an important role on these uniaxial corrugated thin films due to excitation of SPP only in polarization along the k_x spatial corrugation. This created an anisotropic plasmonic response dependent on the excitation polarization σ . The excited SPP mode was characterized as a hybrid SPP resonance in the NIR region. This SPP hybridization is inevitable on these ultrathin metal films with thickness of just $t \sim 10$ nm and was concluded based on analyzing the charge distribution in their metal/dielectric interfaces at SPP excitation conditions. Further, the SPP plasmons broad dip red-shifted for samples with decreasing value of k_x spatial corrugation. These samples exhibited enhanced optical near-field in the NIR range with large field oscillator strength along the E_x and E_y surface components. The surface field orientations of propagating SPP modes differs from the confined LSPR modes, thus polarized Raman measurements was utilized to study SERS “surface selection rules” due to delocalized SPP modes on these corrugated plasmonic surfaces. Further, SERS excitation at $\lambda_{exc} = 785$ nm at the NIR range exhibited reduced interference background and photoinduced disadvantages when compared to excitation at $\lambda_{exc} = 633$ nm. In polarized SERS analysis, a twofold SERS anisotropy with a $\cos^2(\sigma)$ dependency ($\sigma =$ azimuthal angle) was observed. A more pronounced SERS dependence on corrugation period P was observed for totally symmetric a_1 modes than the non-totally symmetric b_1 and b_2 modes. Further, the fabricated shorter corrugation periods exhibited pronounced SERS anisotropy of both totally symmetric (a_1) and non-symmetric vibrations (b_1 and b_2) modes when comparing the substrates with larger value of corrugation periods as the standard deviation δ of period (P) increased for increasing corrugation period value P , resulting in a weaker SPP coupling. Importantly, the behavior of SERS dichroism was determined mostly by the excitation of SPP along the k_x spatial corrugation rather than the orientation of the analyte on the laterally continuous corrugated surface for the a_1 , b_1 and b_2 modes. An edge-on orientation of the adsorbed molecule on the corrugated facets was predicted as the peak related to a_2 mode with both vibration motions along the plane of the surface was absent of these hybrid SPP supporting samples. Polarized Raman spectroscopy has the following advantages over other analytical techniques (1) determination of anisotropy, (2) both qualitative and quantitative determination of molecular orientation, and (3) exploration of both amorphicity and crystallinity in molecular system. This allows them to have a direct applicative relevance towards chemical sensing, molecular electronics, wetting and lubrication applications as in Ref [39]. These experimental results showed the dependence of SPPs surface field orientations in enhancement of Raman molecular vibrations corresponding to both diagonal and non-diagonal component of α on corrugated plasmonic surfaces. The fabricated samples supporting NIR-SPP modes were reproducible exhibiting large-area uniform SERS sensing. Further, as a continuation of this study, substrates supporting LRSPP (long range SPP modes) with millimeter scale propagation length when compared to SPP modes discussed here can be examined for increasing the intensity of Raman modes with non-totally symmetric vibrations. This hypothesis is promising foresight to improve reliable Raman sensing of non-isotropic organic molecule enhancing Raman peaks of non-totally symmetric vibrations even in trace concentrations.

Bibliography

1. Newton, I. (2014). A letter of Mr. Isaac Newton, Professor of the Mathematics in the University of Cambridge; containing his new theory about light and colors: sent by the author to the publisher from Cambridge, Febr. 6. 1671/72; in order to be communicated to the R. Society. *Philosophical transactions of the Royal Society of London*, 6(80), 3075-3087.
2. Thomas, N. C. (1991). The early history of spectroscopy. *Journal of chemical education*, 68(8), 631. DOI: 10.1021/ed068p631
3. Miller, F. A. (1983). The history of spectroscopy as illustrated on stamps. *Applied Spectroscopy*, 37(3), 219-225. <https://doi.org/10.1366/0003702834634488>
4. Sutton, M. A. SIR JOHN HERSCHEL AND THE DEVELOPMENT OF SPECTROSCOPY IN BRITAIN. <https://doi.org/10.1017/S0007087400012851>
5. Maxwell, J. C. (1865). VIII. A dynamical theory of the electromagnetic field. *Philosophical transactions of the Royal Society of London*, (155), 459-512. <https://doi.org/10.1098/rstl.1865.0008>
6. Ueber das Gesetz der Energieerteilung im Normal spectrum; von Max Planck. (In snderer Form mitgeteilt in der Deutschen Physikalischen Gesellschaft, Sitzung vom 19. October und vom 14. December 1900, Verhandlungen 2. p. 202 und p. 237. 1900. (doi:10.1002/andp.19013090310).
7. Planck, M. The Project Gutenberg EBook of The Origin and Development of the Quantum Theory, by Max Planck Title: The Origin and Development of the Quantum Theory Character Set Encoding: ASCII *** START OF THIS PROJECT GUTENBERG EBOOK QUANTUM THEORY ***. www.gutenberg.org.
8. Klassen, S. (2011). The photoelectric effect: Reconstructing the story for the physics classroom. *Science & Education*, 20(7), 719-731. <https://doi.org/10.1007/s11191-009-9214-6>
9. Broglie, L. D. (1924). XXXV. A tentative theory of light quanta. *The London, Edinburgh, and Dublin Philosophical Magazine and Journal of Science*, 47(278), 446-458. <https://doi.org/10.1080/14786442408634378>.
10. Davis, E. A. (2024). Revisiting de Broglie's famous paper of 1924. *Bulletin No 2 September 2024*, 54. DOI:10.1080/09500830600876565.
11. Dirac, P. A. M. (1927). The quantum theory of the emission and absorption of radiation. *Proceedings of the Royal Society of London. Series A, Containing Papers of a Mathematical and Physical Character*, 114(767), 243-265. <https://doi.org/10.1098/rspa.1927.0039>
12. Parker, J. E. (2016). *Chemistry: Quantum Mechanics and Spectroscopy II: Tutorial Questions and Solutions*-eBooks and textbooks from bookboon.com.
13. Pérez-Juste, I., & Nieto Faza, O. (2015). Interaction of radiation with matter. *Structure Elucidation in Organic Chemistry: The Search for the Right Tools*, 1-26.
14. Muiño, R. D., Krasovskii, E. E., Schattke, W., Lienau, C., & Petek, H. (2012). Electromagnetic Interactions with Solids. *Dynamics at Solid State Surfaces and Interfaces: Volume 2: Fundamentals*, 181-237.
15. Karg, M.; König, T. A. F.; Retsch, M.; Stelling, C.; Reichstein, P. M.; Honold, T.; Thelakkat, M.; Fery, A. Colloidal Self-Assembly Concepts for Light Management in Photovoltaics. *Materials Today*. Elsevier B.V. May 1, 2015, pp 185–205. <https://doi.org/10.1016/j.mattod.2014.10.036>.
16. Ali, A. O.; Elgohr, A. T.; El-Mahdy, M. H.; Zohir, H. M.; Emam, A. Z.; Mostafa, M. G.; Al-Razgan, M.; Kasem, H. M.; Elhadidy, M. S. *Advancements in Photovoltaic Technology: A Comprehensive Review of Recent Advances and Future Prospects. Energy Conversion and Management: X*. Elsevier Ltd April 1, 2025. <https://doi.org/10.1016/j.ecmx.2025.100952>.
17. Li, X.; Jia, C.; Ma, B.; Wang, W.; Fang, Z.; Zhang, G.; Guo, X. Substrate-Induced Interfacial Plasmonics for Photovoltaic Conversion. *Sci Rep* 2015, 5. <https://doi.org/10.1038/srep14497>.
18. Mathur, M. A Comprehensive Review of Antenna Design, Development, and Deployment for Modern Wireless Communication Systems. <https://www.researchgate.net/publication/395982179>.
19. Monticone, F.; Argyropoulos, C.; Alù, A. Optical Antennas: Controlling Electromagnetic Scattering, Radiation, and Emission at the Nanoscale. *IEEE Antennas Propag Mag* 2017, 59 (6), 43–61. <https://doi.org/10.1109/MAP.2017.2752721>.

20. Pesce, G.; Jones, P. H.; Maragò, O. M.; Volpe, G. Optical Tweezers: Theory and Practice. *European Physical Journal Plus*. Springer Science and Business Media Deutschland GmbH December 1, 2020. <https://doi.org/10.1140/epjp/s13360-020-00843-5>.
21. Huang, C. H.; Louis, B.; Rocha, S.; Liz-Marzán, L. M.; Masuhara, H.; Hofkens, J.; Bresolí-Obach, R. Plasmonic Dipole and Quadrupole Scattering Modes Determine Optical Trapping, Optical Binding, and Swarming of Gold Nanoparticles. *Journal of Physical Chemistry C* 2024, 128 (13), 5731–5740. <https://doi.org/10.1021/acs.jpcc.4c00340>.
22. Ruffato, G.; Pasqualotto, E.; Sonato, A.; Zacco, G.; Silvestri, D.; Morpurgo, M.; De Toni, A.; Romanato, F. Implementation and Testing of a Compact and High-Resolution Sensing Device Based on Grating-Coupled Surface Plasmon Resonance with Polarization Modulation. *Sens Actuators B Chem* 2013, 185, 179–187. <https://doi.org/10.1016/j.snb.2013.04.113>.
23. Chellappan, K. V., Erden, E., & Urey, H. (2010). Laser-based displays: a review. *Applied optics*, 49(25), F79-F98. DOI:10.1364/AO.49.000F79
24. Patil, U. (2008). Overview of lasers. *Indian Journal of Plastic Surgery*, 41(S 01), 101-113. DOI:10.1055/s-0039-1700481
25. Rakib, S. H. Light Emitting Diode-Theoretical Approach. <https://doi.org/10.13140/RG.2.1.1502.4726>.
26. Bourget, C. M. (2008). An introduction to light-emitting diodes. *HortScience*, 43(7), 1944-1946. DOI: 10.21273/HORTSCI.43.7.1944
27. Romaniuk, R. S., & Dorosz, J. (2020). Optical fibers and their applications 2020. In *Proc. of SPIE Vol (Vol. 11456, pp. 1145601-1)*. <https://doi.org/10.1117/12.2574574>
28. Bernatskyi, A.; Khaskin, V. The History of the Creation of Lasers and Analysis of the Impact of Their Application in the Material Processing on the Development of Certain Industries. *History of Science and Technology* 2021, 11 (1), 125–149. <https://doi.org/10.32703/2415-7422-2021-11-1-125-149>.
29. Sheppard, C. J. R. The Development of Microscopy for Super-Resolution: Confocal Microscopy, and Image Scanning Microscopy. *Applied Sciences (Switzerland)*. MDPI October 1, 2021. <https://doi.org/10.3390/app11198981>.
30. Elliott, A. D. Confocal Microscopy: Principles and Modern Practices. *Curr Protoc Cytom* 2020, 92 (1). <https://doi.org/10.1002/cpcy.68>.
31. Geoghegan, S. Lasers in Medical Diagnosis and Therapy by Stephan Wieneke and Christoph Gerhard. *Australas Phys Eng Sci Med* 2019, 42 (3), 899–900. <https://doi.org/10.1007/s13246-019-00777-y>.
32. Shi, Z.; Cheng, R.; Wei, G.; Hickman, S. A.; Shin, M. C.; Topalian, P.; Wang, L.; Coso, D.; Wang, Y.; Wang, Q.; Le, B.; Lee, L.; Lopez, D.; Wu, Y.; Braxton, S.; Koshelev, A.; Parsons, M. F.; Agarwal, R.; Silverstein, B.; Wang, Y.; Calafiore, G. Flat-Panel Laser Displays through Large-Scale Photonic Integrated Circuits. *Nature* 2025, 644 (8077), 652–659. <https://doi.org/10.1038/s41586-025-09107-7>.
33. Daukantas, P. Lasers in Communications. *Opt Photonics News* 2010, 21 (3), 28. <https://doi.org/10.1364/opn.21.3.000028>.
34. Paraíso, T. K., Woodward, R. I., Marangon, D. G., Lovic, V., Yuan, Z., & Shields, A. J. (2021). Advanced laser technology for quantum communications (tutorial review). *Advanced Quantum Technologies*, 4(10), 2100062. <https://doi.org/10.1002/qute.202100062>
35. Krasnodebski, M. Throwing Light on Photonics: The Genealogy of a Technological Paradigm. *Centaurus* 2018, 60 (1–2), 3–24. <https://doi.org/10.1111/1600-0498.12172>.
36. Kang, L.; Xu, P.; Zhang, B.; Tsai, H.; Han, X.; Wang, H. L. Laser Wavelength- and Power-Dependent Plasmon-Driven Chemical Reactions Monitored Using Single Particle Surface Enhanced Raman Spectroscopy. *Chemical Communications* 2013, 49 (33), 3389–3391. <https://doi.org/10.1039/c3cc40732b>.
37. Singh, R. (2002). CV Raman and the Discovery of the Raman Effect. *Physics in Perspective*, 4(4), 399-420. DOI:10.1007/s000160200002
38. Griffiths, P. R. Introduction to Vibrational Spectroscopy. 2006. <https://doi.org/10.1002/9780470027325.s0102>.
39. Harris, D. C.; Bertolucci, M. D. Symmetry and Spectroscopy: An Introduction to Vibrational and Electronic Spectroscopy; Dover Publications, 1989/1978.
40. Singh, R. (2008). 80 years ago-the Discovery of the Raman Effect at the Indian Association for the Cultivation of Science, Kolkata, India. *Indian Journal of Physics*, 82, 987-1001.

41. Smith, R.; Wright, K. L.; Ashton, L. Raman Spectroscopy: An Evolving Technique for Live Cell Studies. *Analyst*. Royal Society of Chemistry June 21, 2016, pp 3590–3600. <https://doi.org/10.1039/c6an00152a>.
42. Hardy, M.; Chu, H. O. M. Laser Wavelength Selection in Raman Spectroscopy. *Analyst*. Royal Society of Chemistry April 7, 2025, pp 1986–2008. <https://doi.org/10.1039/d5an00324e>.
43. Lin, Y. K.; Leong, H. Y.; Ling, T. C.; Lin, D. Q.; Yao, S. J. Raman Spectroscopy as Process Analytical Tool in Downstream Processing of Biotechnology. *Chinese Journal of Chemical Engineering*. Materials China February 1, 2021, pp 204–211. <https://doi.org/10.1016/j.cjche.2020.12.008>.
44. Jones, K. Historical Journey of the Fast Fourier Transform –From Enlightenment Europe via Bletchley Park to the Modern World. November 20, 2023. <https://doi.org/10.20944/preprints202311.1204.v1>.
45. Fosskett, C. T. Revolution and Evolution in Fourier Transform Infrared (FTIR) Software. <http://proceedings.spiedigitallibrary.org/>. doi:1117/12.932213.
46. Pasteris, J. D.; Beyssac, O. Welcome to Raman Spectroscopy: Successes, Challenges, and Pitfalls. *Elements* 2020, 16 (2), 87–92. <https://doi.org/10.2138/GSELEMENTS.16.2.87>.
47. Zhang, Y., Hong, H., & Cai, W. (2010). Imaging with Raman spectroscopy. *Current pharmaceutical biotechnology*, 11(6), 654-661. DOI:10.2174/138920110792246483.
48. Choi, S.; Kim, P.; Boutillier, R.; Kim, M. Y.; Lee, Y. J.; Lee, H. Development of a High Speed Laser Scanning Confocal Microscope with an Acquisition Rate up to 200 Frames per Second. *Opt Express* 2013, 21 (20), 23611. <https://doi.org/10.1364/oe.21.023611>.
49. Guselnikova, O.; Postnikov, P.; Pershina, A.; Svorcik, V.; Lyutakov, O. Express and Portable Label-Free DNA Detection and Recognition with SERS Platform Based on Functional Au Grating. *Appl Surf Sci* 2019, 470, 219–227. <https://doi.org/10.1016/j.apsusc.2018.11.092>.
50. Saikin, S. K.; Olivares-Amaya, R.; Rappoport, D.; Stopa, M.; Aspuru-Guzik, A. On the Chemical Bonding Effects in the Raman Response: Benzenethiol Adsorbed on Silver Clusters. *Physical Chemistry Chemical Physics* 2009, 11 (41), 9401–9411. <https://doi.org/10.1039/b906885f>.
51. Bilić, A.; Reimers, J. R.; Hush, N. S. The Structure, Energetics, and Nature of the Chemical Bonding of Phenylthiol Adsorbed on the Au (111) Surface: Implications for Density-Functional Calculations of Molecular-Electronic Conduction. *Journal of Chemical Physics* 2005, 122 (9). <https://doi.org/10.1063/1.1850455>.
52. Deluca, M.; Hu, H.; Popov, M. N.; Spitaler, J.; Dieing, T. Advantages and Developments of Raman Spectroscopy for Electroceramics. *Communications Materials*. Springer Nature December 1, 2023. <https://doi.org/10.1038/s43246-023-00400-4>.
53. Xu, Z.; He, Z.; Song, Y.; Fu, X.; Rommel, M.; Luo, X.; Hartmaier, A.; Zhang, J.; Fang, F. Topic Review: Application of Raman Spectroscopy Characterization in Micro/Nano-Machining. *Micromachines*. MDPI AG 2018. <https://doi.org/10.3390/mi9070361>.
54. Rull, F. Structural Investigation of Water and Aqueous Solutions by Raman Spectroscopy*; 2002; Vol. 74.
55. Foti, A.; D'Andrea, C.; Messina, E.; Irrera, A.; Maragò, O. M.; Fazio, B.; Gucciardi, P. G. On the SERS Depolarization Ratio. *Nanospectroscopy* 2015, 1 (1). <https://doi.org/10.1515/nansp-2015-0001>.
56. Wang, H. L.; You, E. M.; Panneerselvam, R.; Ding, S. Y.; Tian, Z. Q. Advances of Surface-Enhanced Raman and IR Spectroscopies: From Nano/Microstructures to Macro-Optical Design. *Light: Science and Applications*. Springer Nature December 1, 2021. <https://doi.org/10.1038/s41377-021-00599-2>.
57. Heuke, S.; Rigneault, H. Coherent Stokes Raman Scattering Microscopy (CSRS). *Nat Commun* 2023, 14 (1). <https://doi.org/10.1038/s41467-023-38941-4>.
58. Jahnce, C. L.; Zhang, W.; Demuyne, B. M.; Hill, A. D. Exploring Resonance Raman Scattering with 4-Nitrophenol. *J Chem Educ* 2022, 99 (9), 3233–3241. <https://doi.org/10.1021/acs.jchemed.2c00210>.
59. Labarthe, F. L.; Buffeteau, T.; Sourisseau, C. Molecular Orientations in Azopolymer Holographic Diffraction Gratings as Studied by Raman Confocal Microspectroscopy; 1998. <https://pubs.acs.org/sharingguidelines>. DOI. 10.1021/jp980859r
60. Min, W.; Cheng, J. X.; Ozeki, Y. Theory, Innovations and Applications of Stimulated Raman Scattering Microscopy. *Nature Photonics*. Nature Research August 1, 2025, pp 803–816. <https://doi.org/10.1038/s41566-025-01707-z>.
61. Guo, S.; Beleites, C.; Neugebauer, U.; Abalde-Cela, S.; Afseth, N. K.; Alsamad, F.; Anand, S.; Araujo-Andrade, C.; Aškračić, S.; Avci, E.; Baia, M.; Baranska, M.; Baria, E.; Batista De Carvalho, L. A. E.; De

- Bettignies, P.; Bonifacio, A.; Bonnier, F.; Brauchle, E. M.; Byrne, H. J.; Chourpa, I.; Cicchi, R.; Cuisinier, F.; Culha, M.; Dahms, M.; David, C.; Duponchel, L.; Duraipandian, S.; El-Mashtoly, S. F.; Ellis, D. I.; Eppe, G.; Falgayrac, G.; Gamulin, O.; Gardner, B.; Gardner, P.; Gerwert, K.; Giamarellos-Bourboulis, E. J.; Gizurarson, S.; Gnyba, M.; Goodacre, R.; Gysan, P.; Guntinas-Lichius, O.; Helgadottir, H.; Grošev, V. M.; Kendall, C.; Kiselev, R.; Kölbach, M.; Krafft, C.; Krishnamoorthy, S.; Kubryck, P.; Lendl, B.; Loza-Alvarez, P.; Lyng, F. M.; Machill, S.; Malherbe, C.; Marro, M.; Marques, M. P. M.; Matuszyk, E.; Morasso, C. F.; Moreau, M.; Muhamadali, H.; Mussi, V.; Notingher, I.; Pacia, M. Z.; Pavone, F. S.; Penel, G.; Petersen, D.; Piot, O.; Rau, J. V.; Richter, M.; Rybarczyk, M. K.; Salehi, H.; Schenke-Layland, K.; Schlücker, S.; Schosserer, M.; Schütze, K.; Sergo, V.; Sinjab, F.; Smulko, J.; Sockalingum, G. D.; Stiebing, C.; Stone, N.; Untereiner, V.; Vanna, R.; Wieland, K.; Popp, J.; Bocklitz, T. Comparability of Raman Spectroscopic Configurations: A Large Scale Cross-Laboratory Study. *Anal Chem* 2020, 92 (24), 15745–15756. <https://doi.org/10.1021/acs.analchem.0c02696>.
62. Humzah, M. D. Tyndall, Rayleigh, Mei, and Raman Scattering: Understanding Their Role in Aesthetics. *Journal of Cosmetic Dermatology*. John Wiley and Sons Inc November 1, 2024, pp 3493–3496. <https://doi.org/10.1111/jocd.16470>.
 63. Fleischmann, M., Hendra, P. J., & McQuillan, A. J. (1974). Raman spectra of pyridine adsorbed at a silver electrode. *Chemical physics letters*, 26(2), 163-166. [https://doi.org/10.1016/0009-2614\(74\)85388-1](https://doi.org/10.1016/0009-2614(74)85388-1)
 64. Cialla, D., März, A., Böhme, R., Theil, F., Weber, K., Schmitt, M., & Popp, J. (2012). Surface-enhanced Raman spectroscopy (SERS): progress and trends. *Analytical and bioanalytical chemistry*, 403(1), 27-54. DOI: 10.1007/s00216-011-5631-x
 65. Sharma, B.; Frontiera, R. R.; Henry, A.-I.; Ringe, E.; Van Duyne, R. P. SERS: Materials, Applications, and the Future Background and Mechanism; 2012; Vol. 15. [https://doi.org/10.1016/S1369-7021\(12\)70017-2](https://doi.org/10.1016/S1369-7021(12)70017-2)
 66. Langer, J.; de Aberasturi, D. J.; Aizpurua, J.; Alvarez-Puebla, R. A.; Auguie, B.; Baumberg, J. J.; Bazan, G. C.; Bell, S. E. J.; Boisen, A.; Brolo, A. G.; Choo, J.; Cialla-May, D.; Deckert, V.; Fabris, L.; Faulds, K.; Javier García de Abajo, F.; Goodacre, R.; Graham, D.; Haes, A. J.; Haynes, C. L.; Huck, C.; Itoh, T.; Käll, M.; Kneipp, J.; Kotov, N. A.; Kuang, H.; Le Ru, E. C.; Lee, H. K.; Li, J. F.; Ling, X. Y.; Maier, S. A.; Mayerhöfer, T.; Moskovits, M.; Murakoshi, K.; Nam, J. M.; Nie, S.; Ozaki, Y.; Pastoriza-Santos, I.; Perez-Juste, J.; Popp, J.; Pucci, A.; Reich, S.; Ren, B.; Schatz, G. C.; Shegai, T.; Schlücker, S.; Tay, L. L.; George Thomas, K.; Tian, Z. Q.; van Duyne, R. P.; Vo-Dinh, T.; Wang, Y.; Willets, K. A.; Xu, C.; Xu, H.; Xu, Y.; Yamamoto, Y. S.; Zhao, B.; Liz-Marzán, L. M. Present and Future of Surface-Enhanced Raman Scattering. *ACS Nano*. American Chemical Society January 28, 2020, pp 28–117. <https://doi.org/10.1021/acsnano.9b04224>.
 67. Creighton, J. A. Surface Raman Electromagnetic Enhancement Factors for Molecules at the Surface of Small Isolated Metal Spheres: The Determination of Adsorbate Orientation from Sers Relative Intensities. *Surf Sci* 1983, 124 (1), 209–219. [https://doi.org/https://doi.org/10.1016/0039-6028\(83\)90345-X](https://doi.org/https://doi.org/10.1016/0039-6028(83)90345-X).
 68. Moskovits, M. (2005). Surface-enhanced Raman spectroscopy: a brief retrospective. *Journal of Raman Spectroscopy: An International Journal for Original Work in all Aspects of Raman Spectroscopy, Including Higher Order Processes, and also Brillouin and Rayleigh Scattering*, 36(6-7), 485-496. <http://dx.doi.org/10.1002/jrs.1362>
 69. Moskovits, M. Surface Roughness and the Enhanced Intensity of Raman Scattering by Molecules Adsorbed on Metals. *J Chem Phys* 1978, 69 (9), 4159–4161. <https://doi.org/10.1063/1.437095>.
 70. Ding, S. Y.; You, E. M.; Tian, Z. Q.; Moskovits, M. Electromagnetic Theories of Surface-Enhanced Raman Spectroscopy. *Chemical Society Reviews*. Royal Society of Chemistry July 7, 2017, pp 4042–4076. <https://doi.org/10.1039/c7cs00238f>.
 71. Mortazavi, D.; Kouzani, A. Z.; Kaynak, A.; Duan, W. DEVELOPING LSPR DESIGN GUIDELINES; 2012; Vol. 126. DOI:10.2528/PIER12011810
 72. Yalcin, R. A.; Haratoka, C.; Babonneau, D.; Camelio, S.; Joulain, K.; Drévilion, J. The Effect of Size and Shape-Dependent Optical Properties on Colored Radiative Cooling in Metal Island Films. *J Quant Spectrosc Radiat Transf* 2024, 312. <https://doi.org/10.1016/j.jqsrt.2023.108797>.
 73. Cheng, L.; Zhu, G.; Liu, G.; Zhu, L. FDTD Simulation of the Optical Properties for Gold Nanoparticles. *Mater Res Express* 2020, 7 (12). <https://doi.org/10.1088/2053-1591/abd139>.

74. Chung, T.; Lee, S. Y.; Song, E. Y.; Chun, H.; Lee, B. Plasmonic Nanostructures for Nano-Scale Bio-Sensing. *Sensors* 2011, 11 (11), 10907–10929. <https://doi.org/10.3390/s111110907>.
75. Monticone, F.; Alù, A. *Metamaterials and Plasmonics: From Nanoparticles to Nanoantenna Arrays, Metasurfaces, and Metamaterials*. Chinese Physics B. Institute of Physics Publishing 2014. <https://doi.org/10.1088/1674-1056/23/4/047809>.
76. Stewart, M. E.; Anderton, C. R.; Thompson, L. B.; Maria, J.; Gray, S. K.; Rogers, J. A.; Nuzzo, R. G. Nanostructured Plasmonic Sensors. *Chemical Reviews*. February 2008, pp 494–521. <https://doi.org/10.1021/cr068126n>.
77. Singh, G. P.; Sardana, N. Smartphone-Based Surface Plasmon Resonance Sensors: A Review. *Plasmonics*. Springer October 1, 2022, pp 1869–1888. <https://doi.org/10.1007/s11468-022-01672-1>.
78. Holman, A. P.; Kurouski, D. Surface-Enhanced Raman Spectroscopy in Forensic Analysis. *Reviews in Analytical Chemistry*. Sciendo January 1, 2024. <https://doi.org/10.1515/revac-2023-0079>.
79. Huang, X.; El-Sayed, M. A. Gold Nanoparticles: Optical Properties and Implementations in Cancer Diagnosis and Photothermal Therapy. *Journal of Advanced Research*. January 2010, pp 13–28. <https://doi.org/10.1016/j.jare.2010.02.002>.
80. Yu, W.; Lv, Q.; Chen, Z.; Wang, X.; Liu, Y.; Wang, L.; Huang, Y. Spatial Tracking of Water Pollutions Based on SERS Spectra with Machine Learning. *ACS ES&T Water* 2025. <https://doi.org/10.1021/acsestwater.5c00592>.
81. Li, C.-Y.; Duan, S.; Yi, J.; Wang, C.; Radjenovic, P. M.; Tian, Z.-Q.; Li, J.-F. Real-Time Detection of Single-Molecule Reaction by Plasmon-Enhanced Spectroscopy; 2020; Vol. 6. DOI:10.1126/sciadv.aba6012:
82. Kennedy, D. C.; Hoop, K. A.; Tay, L. L.; Pezacki, J. P. Development of Nanoparticle Probes for Multiplex SERS Imaging of Cell Surface Proteins. *Nanoscale* 2010, 2 (8), 1413–1416. <https://doi.org/10.1039/c0nr00122h>.
83. Agarwal, N. R.; Lucotti, A.; Tommasini, M.; Neri, F.; Trusso, S.; Ossi, P. M. SERS Detection and DFT Calculation of 2-Naphthalene Thiol Adsorbed on Ag and Au Probes. *Sens Actuators B Chem* 2016, 237, 545–555. <https://doi.org/10.1016/j.snb.2016.06.143>.
84. Cardinal, M. F.; Vander Ende, E.; Hackler, R. A.; McAnally, M. O.; Stair, P. C.; Schatz, G. C.; Van Duyne, R. P. Expanding Applications of SERS through Versatile Nanomaterials Engineering. *Chemical Society Reviews*. Royal Society of Chemistry July 7, 2017, pp 3886–3903. <https://doi.org/10.1039/c7cs00207f>.
85. Li, X.; Yang, T.; Li, C. S.; Song, Y.; Lou, H.; Guan, D.; Jin, L. Surface Enhanced Raman Spectroscopy (SERS) for the Multiplex Detection of Braf, Kras, and Pik3ca Mutations in Plasma of Colorectal Cancer Patients. *Theranostics* 2018, 8 (6), 1678–1689. <https://doi.org/10.7150/thno.22502>.
86. Perumal, J.; Wang, Y.; Attia, A. B. E.; Dinish, U. S.; Olivo, M. Towards a Point-of-Care SERS Sensor for Biomedical and Agri-Food Analysis Applications: A Review of Recent Advancements. *Nanoscale*. Royal Society of Chemistry January 14, 2021, pp 553–580. <https://doi.org/10.1039/d0nr06832b>.
87. Burtsev, V.; Miliutina, E.; Erzina, M.; Kalachyova, Y.; Elashnikov, R.; Svorcik, V.; Lyutakov, O. Advanced Design of Microfluidic Chip Based on SPP-LSP Plasmonic Coupling for SERS Detection with High Sensitivity and Reliability. *Journal of Physical Chemistry C* 2019, 123 (50), 30492–30498. <https://doi.org/10.1021/acs.jpcc.9b06751>.
88. Bi, X.; Ai, X.; Wu, Z.; Lin, L. L.; Chen, Z.; Ye, J. Artificial Intelligence-Powered Surface-Enhanced Raman Spectroscopy for Biomedical Applications. *Analytical Chemistry*. American Chemical Society April 8, 2025, pp 6826–6846. <https://doi.org/10.1021/acs.analchem.4c06584>.
89. Malenfant-Thuot, O.; Shaaban Kabakibo, D.; Blackburn, S.; Rousseau, B.; Côté, M. Large Scale Raman Spectrum Calculations in Defective 2D Materials Using Deep Learning. *Journal of Physics Condensed Matter* 2025, 37 (11). <https://doi.org/10.1088/1361-648X/ada106>.
90. Amendola, V.; Bakr, O. M.; Stellacci, F. A Study of the Surface Plasmon Resonance of Silver Nanoparticles by the Discrete Dipole Approximation Method: Effect of Shape, Size, Structure, and Assembly. *Plasmonics* 2010, 5 (1), 85–97. <https://doi.org/10.1007/s11468-009-9120-4>.
91. Menghrajani, K. S.; Chen, M.; Dholakia, K.; Barnes, W. L. Probing Vibrational Strong Coupling of Molecules with Wavelength-Modulated Raman Spectroscopy. *Adv Opt Mater* 2022, 10 (3). <https://doi.org/10.1002/adom.202102065>.

92. McGlashen, M. L.; Guhathakurta, U.; Davis, K. L.; Morris, M. D. SERS Microscopy: Laser Illumination Effects. *Appl. Spectrosc.* 1991, 45 (4), 543–545. <https://doi.org/10.1366/00037029143369>
93. Cebeci-Maltaş, D.; Alam, M. A.; Wang, P.; Ben-Amotz, D. Photobleaching Profile of Raman Peaks and Fluorescence Background. *European Pharmaceutical Review* 2017, 22 (6), 18–21.
94. Škrabić, M.; Kosović, M.; Gotić, M.; Mikac, L.; Ivanda, M.; Gamulin, O. Near-Infrared Surface-Enhanced Raman Scattering on Silver-Coated Porous Silicon Photonic Crystals. *Nanomaterials* 2019, 9 (3). <https://doi.org/10.3390/nano9030421>.
95. Kneipp, K.; Roth, E.; Engert, C.; Kiefer, W. Near-Infrared Excited Surface-Enhanced Raman Spectroscopy of Rhodamine 6G on Colloidal Silver. *Chem Phys Lett* 1993, 207 (4), 450–454. [https://doi.org/https://doi.org/10.1016/0009-2614\(93\)89028-G](https://doi.org/https://doi.org/10.1016/0009-2614(93)89028-G).
96. Muniz-Miranda, F.; Pedone, A.; Muniz-Miranda, M. Raman and Computational Study on the Adsorption of Xanthine on Silver Nanocolloids. *ACS Omega* 2018, 3 (10), 13530–13537. <https://doi.org/10.1021/acsomega.8b02174>.
97. Gabai, R.; Ismach, A.; Joselevich, E. Nanofacet Lithography: A New Bottom-up Approach to Nanopatterning and Nanofabrication by Soft Replication of Spontaneously Faceted Crystal Surfaces. *Advanced Materials* 2007, 19 (10), 1325–1330. <https://doi.org/10.1002/adma.200601625>.
98. Wang, Y. L.; Nan, F.; Liu, X. L.; Zhou, L.; Peng, X. N.; Zhou, Z. K.; Yu, Y.; Hao, Z. H.; Wu, Y.; Zhang, W.; Wang, Q. Q.; Zhang, Z. Plasmon-Enhanced Light Harvesting of Chlorophylls on near-Percolating Silver Films via One-Photon Anti-Stokes Upconversion. *Sci Rep* 2013, 3. <https://doi.org/10.1038/srep01861>.
99. Berthelot, A.; Des Francs, G. C.; Varguet, H.; Margueritat, J.; Mascart, R.; Benoit, J. M.; Laverdant, J. From Localized to Delocalized Plasmonic Modes, First Observation of Superradiant Scattering in Disordered Semi-Continuous Metal Films. *Nanotechnology* 2019, 30 (1). <https://doi.org/10.1088/1361-6528/aae6ec>.
100. Seal, K.; Genov, D. A.; Sarychev, A. K.; Noh, H.; Shalaev, V. M.; Ying, Z. C.; Zhang, X.; Cao, H. Coexistence of Localized and Delocalized Surface Plasmon Modes in Percolating Metal Films. *Phys Rev Lett* 2006, 97 (20). <https://doi.org/10.1103/PhysRevLett.97.206103>.
101. Oates, T. W. H.; Ranjan, M.; Facsko, S.; Arwin, H. Highly Anisotropic Effective Dielectric Functions of Silver Nanoparticle Arrays. *Opt. Express* 2011, 19 (3), 2014–2028. <https://doi.org/10.1364/OE.19.002014>.
102. Camelio, S.; Babonneau, D.; Lantiat, D.; Simonot, L. Self-Organized Growth and Optical Properties of Silver Nanoparticle Chains and Stripes. *EPL* 2007, 79 (4). <https://doi.org/10.1209/0295-5075/79/47002>.
103. Babonneau, D.; Camelio, S.; Simonot, L.; Pailloux, F.; Guérin, P.; Lamongie, B.; Lyon, O. Tunable Plasmonic Dichroism of Au Nanoparticles Self-Aligned on Rippled Al₂O₃ Thin Films. *EPL* 2011, 93 (2). <https://doi.org/10.1209/0295-5075/93/26005>.
104. Barnes, W. L. Surface Plasmon-Polariton Length Scales: A Route to Sub-Wavelength Optics. *Journal of Optics A: Pure and Applied Optics*. April 1, 2006. <https://doi.org/10.1088/1464-4258/8/4/S06>.
105. Barnes, W. L., Dereux, A., & Ebbesen, T. W. (2003). Surface plasmon subwavelength optics. *nature*, 424(6950), 824-830. <https://doi.org/10.1038/nature01937>.
106. Broers, A. N. "Resolution limits for electron-beam lithography." *IBM Journal of Research and Development* 32, no. 4 (1988): 502-513.
107. Ambartsumyan, O.; Gribanyov, D.; Kukushkin, V.; Kopylov, A.; Zavyalova, E. SERS-Based Biosensors for Virus Determination with Oligonucleotides as Recognition Elements. *International Journal of Molecular Sciences*. MDPI AG May 1, 2020. <https://doi.org/10.3390/ijms21093373>.
108. Chen, L.; Mungroo, N.; Daikuara, L.; Neethirajan, S. Label-Free NIR-SERS Discrimination and Detection of Foodborne Bacteria by in Situ Synthesis of Ag Colloids. *J Nanobiotechnology* 2015, 13 (1). <https://doi.org/10.1186/s12951-015-0106-4>.
109. Sallam, M. O.; Vandenbosch, G. A. E.; Gielen, G.; Soliman, E. A. Integral Equations Formulation of Plasmonic Transmission Lines. *Opt Express* 2014, 22 (19), 22388. <https://doi.org/10.1364/oe.22.022388>.
110. Fang, Y.; Sun, M. Nanoplasmonic Waveguides: Towards Applications in Integrated Nanophotonic Circuits. *Light: Science and Applications*. Nature Publishing Group June 5, 2015. <https://doi.org/10.1038/lsa.2015.67>.

111. Anwar, R. S.; Ning, H.; Mao, L. Recent Advancements in Surface Plasmon Polaritons-Plasmonics in Subwavelength Structures in Microwave and Terahertz Regimes. *Digital Communications and Networks*. Chongqing University of Posts and Telecommunications November 1, 2018, pp 244–257. <https://doi.org/10.1016/j.dcan.2017.08.004>.
112. Sakuma, R.; Lin, K. T.; Kim, S.; Kimura, F.; Kajihara, Y. Passive Near-Field Imaging via Grating-Based Spectroscopy. *Review of Scientific Instruments* 2022, 93 (1). <https://doi.org/10.1063/5.0059498>.
113. Moskovits, M.; Suh, J. S. Surface Selection Rules for Surface-Enhanced Raman Spectroscopy: Calculations and Application to the Surface-Enhanced Raman Spectrum of Phthalazine on Silver. *J Phys Chem* 1984, 88 (23), 5526–5530.
114. Moskovits, M. Surface Selection Rules. *J Chem Phys* 1982, 77 (9), 4408–4416. <https://doi.org/10.1063/1.444442>.
115. Arul, R.; Menghrajani, K.; Rider, M. S.; Chikkaraddy, R.; Barnes, W. L.; Baumberg, J. J. Raman-Probing the Local Ultrastrong Coupling of Vibrational Plasmon-Polaritons on Metallic Gratings. <https://doi.org/10.1103/PhysRevLett.131.126902>.
116. Chan, C. Y.; Cao, Z. L.; Ong, H. C. Study of Coupling Efficiency of Molecules to Surface Plasmon Polaritons in Surface-Enhanced Raman Scattering (SERS). *Opt Express* 2013, 21 (12), 14674. <https://doi.org/10.1364/oe.21.014674>.
117. Rider, M. S.; Arul, R.; Baumberg, J. J.; Barnes, W. L. Theory of Strong Coupling between Molecules and Surface Plasmons on a Grating. *Nanophotonics* 2022, 11 (16), 3695–3708. <https://doi.org/10.1515/nanoph-2022-0301>.
118. Barnes, W. L.; Wedge, S. Surface Plasmon Polariton Mediated Emission of Light. In *Photonic Crystal Materials and Nanostructures*; SPIE, 2004; Vol. 5450, p 412. <https://doi.org/10.1117/12.555934>.
119. Winter, G.; Wedge, S.; Barnes, W. L. Can Lasing at Visible Wavelengths Be Achieved Using the Low-Loss Long-Range Surface Plasmon-Polariton Mode? *New J Phys* 2006, 8. <https://doi.org/10.1088/1367-2630/8/8/125>.
120. Kaiser, N. (2002). Review of the fundamentals of thin-film growth. *Applied optics*, 41(16), 3053-3060. <https://doi.org/10.1364/AO.41.003053>
121. Maniyara, R. A.; Rodrigo, D.; Yu, R.; Canet-Ferrer, J.; Ghosh, D. S.; Yongsunthon, R.; Baker, D. E.; Rezikyan, A.; García de Abajo, F. J.; Pruneri, V. Tunable Plasmons in Ultrathin Metal Films. *Nature Photonics*. Nature Publishing Group May 1, 2019, pp 328–333. <https://doi.org/10.1038/s41566-019-0366-x>.
122. Grimaldi, C. Theory of Percolation and Tunneling Regimes in Nanogranular Metal Films. *Phys Rev B Condens Matter Mater Phys* 2014, 89 (21). <https://doi.org/10.1103/PhysRevB.89.214201>.
123. Yu, X., Duxbury, P. M., Jeffers, G., & Dubson, M. A. (1991). Coalescence and percolation in thin metal films. *Physical Review B*, 44(23), 13163. <https://doi.org/10.1103/PhysRevB.44.13163>.
124. Maarouf, A. I., & Sutherland, D. S. (2010). Optimum plasmon hybridization at percolation threshold of silver films near metallic surfaces. *Journal of Physics D: Applied Physics*, 43(40), 405301. DOI 10.1088/0022-3727/43/40/405301.
125. Stauffer, D., & Aharony, A. (2018). *Introduction to percolation theory*. Taylor & Francis. <https://doi.org/10.1201/9781315274386>.
126. Alfonso, E.; Olaya, J.; Cubillos, G. Thin Film Growth Through Sputtering Technique and Its Applications. In *Crystallization - Science and Technology*; InTech, 2012. <https://doi.org/10.5772/35844>.
127. Abadias, G.; Simonot, L.; Colin, J. J.; Michel, A.; Camelio, S.; Babonneau, D. Volmer-Weber Growth Stages of Polycrystalline Metal Films Probed by in Situ and Real-Time Optical Diagnostics. *Appl Phys Lett* 2015, 107 (18). <https://doi.org/10.1063/1.4935034>.
128. Akolzina, D.; Kravets, V. G.; Berdyugin, A. I.; Grigorenko, A. N. Optical Constants and Optical Anisotropy of Ultrathin Gold Films. *Adv Photonics Res* 2024, 5 (1). <https://doi.org/10.1002/adpr.202300238>.
129. Tesler, A. B.; Maoz, B. M.; Feldman, Y.; Vaskevich, A.; Rubinstein, I. Solid-State Thermal Dewetting of Just-Percolated Gold Films Evaporated on Glass: Development of the Morphology and Optical Properties. *Journal of Physical Chemistry C* 2013, 117 (21), 11337–11346. <https://doi.org/10.1021/jp400895z>.

130. Hedl, E.; Bregović, V. B.; Rakić, I. Š.; Mandić, Š.; Samec, Ž.; Bergmann, A.; Sancho-Parramon, J. Optical Properties of Annealed Nearly Percolated Au Thin Films. *Opt Mater (Amst)* 2023, 135. <https://doi.org/10.1016/j.optmat.2022.113237>.
131. Seguini, G.; Llamoya Curi, J.; Spiga, S.; Tallarida, G.; Wiemer, C.; Perego, M. Solid-State Dewetting of Ultra-Thin Au Films on SiO₂ and HfO₂. *Nanotechnology* 2014, 25 (49). <https://doi.org/10.1088/0957-4484/25/49/495603>.
132. Liu, H.; Zhang, X.; Zhai, T.; Sander, T.; Chen, L.; Klar, P. J. Centimeter-Scale-Homogeneous SERS Substrates with Seven-Order Global Enhancement through Thermally Controlled Plasmonic Nanostructures. *Nanoscale* 2014, 6 (10), 5099–5105. <https://doi.org/10.1039/c4nr00161c>.
133. Gompf, B., Brandt, T., Beister, J., Dressel, M., & Drichko, N. (2006, September). Optical Properties of Ultra-thin Metal Films. In 2006 Joint 31st International Conference on Infrared Millimeter Waves and 14th International Conference on Terahertz Electronics (pp. 468-468). IEEE.
134. Griffiths, D. J., & Colleger, R. (1999). *Introduction to Electrodynamics* Prentice Hall Upper Saddle River. New Jersey, 7458.
135. Maier, S. A. (2007). *Plasmonics: fundamentals and applications* (Vol. 1, p. 245). New York: Springer.
136. Kittel, C. (1955). *Solid state physics* (Vol. 3). Emeryville: Shell Development Company.
137. Raether, H. (1988). *Plasmons on smooth and rough surfaces and on gratings*. Springer tracts in modern physics, 10.
138. Zayats, A. V.; Smolyaninov, I. I.; Maradudin, A. A. Nano-Optics of Surface Plasmon Polaritons. *Physics Reports*. March 2005, pp 131–314. <https://doi.org/10.1016/j.physrep.2004.11.001>.
139. Derkachova, A.; Kolwas, K.; Demchenko, I. Dielectric Function for Gold in Plasmonics Applications: Size Dependence of Plasmon Resonance Frequencies and Damping Rates for Nanospheres. *Plasmonics* 2016, 11 (3), 941–951. <https://doi.org/10.1007/s11468-015-0128-7>.
140. Novotny, L., & Hecht, B. (2012). *Principles of nano-optics*. Cambridge university press <https://doi.org/10.1017/CBO9780511794193>
141. Johnson, P. B., & Christy, R. W. (1972). Optical constants of the noble metals. *Physical review B*, 6(12), 4370. DOI: <https://doi.org/10.1103/PhysRevB.6.4370>.
142. Rosenblatt, G.; Simkhovich, B.; Bartal, G.; Orenstein, M. Nonmodal Plasmonics: Controlling the Forced Optical Response of Nanostructures. *Phys Rev X* 2020, 10 (1). <https://doi.org/10.1103/PhysRevX.10.011071>.
143. Bergman, D. J., Li, X., & Stockman, M. I. Localized Eigenstates of the Electromagnetic Field: Beyond the Quasi-Static Regime.
144. Gan, X.; Lei, D.; Ye, R.; Zhao, H.; Wong, K. Y. Transition Metal Dichalcogenide-Based Mixed-Dimensional Heterostructures for Visible-Light-Driven Photocatalysis: Dimensionality and Interface Engineering. *Nano Research*. Tsinghua University June 1, 2021, pp 2003–2022. <https://doi.org/10.1007/s12274-020-2955-x>.
145. Zyubin, A. Y.; Kon, I. I.; Poltorabtko, D. A.; Samusev, I. G. FDTD Simulations for Rhodium and Platinum Nanoparticles for UV Plasmonics. *Nanomaterials* 2023, 13 (5). <https://doi.org/10.3390/nano13050897>.
146. C. M. Baltar, H. T. M.; Drozdowicz-Tomsia, K.; M., E. Propagating Surface Plasmons and Dispersion Relations for Nanoscale Multilayer Metallic-Dielectric Films. In *Plasmonics - Principles and Applications*; InTech, 2012. <https://doi.org/10.5772/51218>.
147. Chen, Z.; Feng, K.; Chen, Z.; Shen, J.; Li, H. Surface-Enhanced Raman Scattering on Silver Sinusoidal Nanograting: Impact of Interactions of Grating-Coupled Surface Plasmon Polaritons. *Plasmonics* 2022, 17 (2), 757–764. <https://doi.org/10.1007/s11468-021-01587-3>.
148. Deng, T. S.; Parker, J.; Yifat, Y.; Shepherd, N.; Scherer, N. F. Dark Plasmon Modes in Symmetric Gold Nanoparticle Dimers Illuminated by Focused Cylindrical Vector Beams. *Journal of Physical Chemistry C* 2018, 122 (48), 27662–27672. <https://doi.org/10.1021/acs.jpcc.8b10415>.
149. Quillin, S. C.; Cherqui, C.; Montoni, N. P.; Li, G.; Camden, J. P.; Masiello, D. J. Imaging Plasmon Hybridization in Metal Nanoparticle Aggregates with Electron Energy-Loss Spectroscopy. *Journal of Physical Chemistry C* 2016, 120 (37), 20852–20859. <https://doi.org/10.1021/acs.jpcc.6b02170>.

150. Sheikholeslami, S.; Jun, Y. W.; Jain, P. K.; Alivisatos, A. P. Coupling of Optical Resonances in a Compositionally Asymmetric Plasmonic Nanoparticle Dimer. *Nano Lett* 2010, 10 (7), 2655–2660. <https://doi.org/10.1021/nl101380f>.
151. Hanske, C.; Tebbe, M.; Kuttner, C.; Bieber, V.; Tsukruk, V. V.; Chanana, M.; König, T. A. F.; Fery, A. Strongly Coupled Plasmonic Modes on Macroscopic Areas via Template-Assisted Colloidal Self-Assembly. *Nano Lett* 2014, 14 (12), 6863–6871. <https://doi.org/10.1021/nl502776s>.
152. Lin, B.-W.; Wang, Z.; Ho, Y.-L.; Lee, Y.-C.; Xing, D.; Lee, Y.-T.; Delaunay, J.-J. High-Q Plasmonic Surface Lattice Resonance in the Ultraviolet Region. *Appl Phys Lett* 2024, 124 (21), 211701. <https://doi.org/10.1063/5.0207829>.
153. Borah, R.; Verbruggen, S. W. Coupled Plasmon Modes in 2D Gold Nanoparticle Clusters and Their Effect on Local Temperature Control. *Journal of Physical Chemistry C* 2019, 123 (50), 30594–30603. <https://doi.org/10.1021/acs.jpcc.9b09048>.
154. Willingham, B.; Link, S.; Quinten, M.; Leitner, A.; Krenn, J. R.; Aussenegg, F. R.; Maier, S. A.; Kik, P. G.; Atwater, H. A.; Meltzer, S.; Harel, E.; Koel, B. E.; Requicha, A. A.; Brongersma, M. L.; Hartman, J. W. Energy Transport in Metal Nanoparticle Chains via Sub-Radiant Plasmon Modes. *References and Links "Electromagnetic Energy Transport via Linear Chains of Silver Nanoparticles"; 1998; Vol. 23.* https://doi.org/10.1364/OA_License_v1#VOR.
155. Chen, Z.; Hooper, I. R.; Sambles, J. R. Strongly Coupled Surface Plasmons on Thin Shallow Metallic Gratings. *Phys Rev B Condens Matter Mater Phys* 2008, 77 (16). <https://doi.org/10.1103/PhysRevB.77.161405>.
156. Mayer, M.; Potapov, P. L.; Pohl, D.; Steiner, A. M.; Schultz, J.; Rellinghaus, B.; Lubk, A.; König, T. A. F.; Fery, A. Direct Observation of Plasmon Band Formation and Delocalization in Quasi-Infinite Nanoparticle Chains. *Nano Lett* 2019, 19 (6), 3854–3862. <https://doi.org/10.1021/acs.nanolett.9b01031>.
157. Wang, X.; Gogol, P.; Cambriel, E.; Palpant, B. Near-and Far-Field Effects on the Plasmon Coupling in Gold Nanoparticle Arrays. *Journal of Physical Chemistry C* 2012, 116 (46), 24741–24747. <https://doi.org/10.1021/jp306292r>.
158. Brongersma, M. L.; Halas, N. J.; Nordlander, P. Plasmon-Induced Hot Carrier Science and Technology. *Nature Nanotechnology*. Nature Publishing Group January 1, 2015, pp 25–34. <https://doi.org/10.1038/nnano.2014.311>.
159. Staechelin, Y. U.; Hoeing, D.; Schulz, F.; Lange, H. Size-Dependent Electron-Phonon Coupling in Monocrystalline Gold Nanoparticles. *ACS Photonics* 2021, 8 (3), 752–757. <https://doi.org/10.1021/acsphotonics.1c00078>.
160. Schirato, A.; Maiuri, M.; Cerullo, G.; Della Valle, G. Ultrafast Hot Electron Dynamics in Plasmonic Nanostructures: Experiments, Modelling, Design. *Nanophotonics*. De Gruyter Open Ltd January 1, 2023, pp 1–28. <https://doi.org/10.1515/nanoph-2022-0592>.
161. Keresztury, G. Raman Spectroscopy: Theory. 2006. <https://doi.org/10.1002/9780470027325.s0109>.
162. Hahn, D. W. (2007). Raman scattering theory. Department of Mechanical and Aerospace Engineering, University of Florida, 42, 43-48.
163. Moura, C. C.; Tare, R. S.; Oreffo, R. O. C.; Mahajan, S. Raman Spectroscopy and Coherent Anti-Stokes Raman Scattering Imaging: Prospective Tools for Monitoring Skeletal Cells and Skeletal Regeneration. *Journal of the Royal Society Interface*. Royal Society of London May 1, 2016. <https://doi.org/10.1098/rsif.2016.0182>.
164. Cialla-May, D.; Schmitt, M.; Popp, J. Theoretical Principles of Raman Spectroscopy. *Physical Sciences Reviews*. De Gruyter June 1, 2019. <https://doi.org/10.1515/psr-2017-0040>.
165. Masamichi TSUBOI, B.; Benevides, A. J. M.; Thomas, G. J.; Å, J. Review Raman Tensors and Their Application in Structural Studies of Biological Systems. <https://doi.org/10.2183/pjab/85.83>.
166. Walls, D. J., & Bohn, P. W. (1990). Enhanced Raman scattering at dielectric surfaces. 2. Molecular orientations from polarized surface Raman scattering. *Journal of Physical Chemistry*, 94(5), 2039-2042.
167. Le Ru, E. C.; Grand, J.; Féridj, N.; Aubard, J.; Lévi, G.; Hohenau, A.; Krenn, J. R.; Blackie, E.; Etchegoin, P. G. Experimental Verification of the SERS Electromagnetic Model beyond the |B|⁴ Approximation: Polarization Effects. *Journal of Physical Chemistry C* 2008, 112 (22), 8117–8121. <https://doi.org/10.1021/jp802219c>.

168. Kaja, S.; Nag, A. Ag-Au-Cu Trimetallic Alloy Microflower: A Highly Sensitive SERS Substrate for Detection of Low Raman Scattering Cross-Section Thiols. *Langmuir* 2023, 39 (46), 16562–16573. <https://doi.org/10.1021/acs.langmuir.3c02528>.
169. Zhang, K.; Chen, X. J. Chain Length Effects of p -Oligophenyls with Comparison of Benzene by Raman Scattering. *AIP Adv* 2018, 8 (2). <https://doi.org/10.1063/1.5016876>.
170. Heffelfinger, J. R.; Carter, C. B. Mechanisms of Surface Faceting and Coarsening; ELSEVIER, 1997; Vol. 389. [https://doi.org/10.1016/S0039-6028\(97\)00411-1](https://doi.org/10.1016/S0039-6028(97)00411-1).
171. Erb, D. J.; Perlich, J.; Roth, S. V.; Röhlberger, R.; Schlage, K. Real-Time Observation of Temperature-Induced Surface Nanofaceting in M-Plane α -Al₂O₃. *ACS Appl Mater Interfaces* 2022, 14 (27), 31373–31384. <https://doi.org/10.1021/acsami.1c22029>.
172. Madzharova, F.; Heiner, Z.; Kneipp, J. Surface-Enhanced Hyper Raman Spectra of Aromatic Thiols on Gold and Silver Nanoparticles. *The Journal of Physical Chemistry C* 2020, 124 (11), 6233–6241. <https://doi.org/10.1021/acs.jpcc.0c00294>.
173. Gartner, M.; Stoica, M.; Nicolescu, M.; Stroescu, H. The Ellipsometry Versatility in the Study of Sol-Gel Films. *Journal of Sol-Gel Science and Technology*. Springer April 1, 2021. <https://doi.org/10.1007/s10971-021-05504-2>.
174. H Oates, T. W.; Ranjan, M.; Facsko, S.; Arwin, H.; Yao, J.; Liu, Z. W.; Liu, Y. M.; Wang, Y.; Sun, C.; Barta, G.; Stacy, A. M.; Zhang, X. Ellipsometry and Polarimetry; (160.1190) Anisotropic Optical Materials; 2011.
175. Gkogkou, D.; Shaykhutdinov, T.; Oates, T. W. H.; Gernert, U.; Schreiber, B.; Facsko, S.; Hildebrandt, P.; Weidinger, I. M.; Esser, N.; Hinrichs, K. Characterization of Anisotropically Shaped Silver Nanoparticle Arrays via Spectroscopic Ellipsometry Supported by Numerical Optical Modeling. *Appl Surf Sci* 2017, 421, 460–464. <https://doi.org/10.1016/j.apsusc.2016.10.105>.
176. Tamaki, R.; Suzuki, M.; Kusaba, S.; Takeda, J.; Katayama, I. Ultrafast Pump-Probe Spectroscopy via Chirped-Pulse up-Conversion with Dispersion Compensation. *Opt Express* 2023, 31 (24), 40142. <https://doi.org/10.1364/oe.504429>.
177. Khitrova, G., Berman, P. R., & Sargent III, M. (1988). Theory of pump-probe spectroscopy. *Journal of the Optical Society of America B*, 5(1), 160-170. <https://doi.org/10.1364/JOSAB.5.000160>.
178. Palik, E. D. Handbook of Optical Constants of Solids; Academic press, 1998; Vol. 3.
179. Palik, E. D. Aluminum Oxide Revisited. In Handbook of optical constants of solids; 1998; Vol. 3.
180. Yakubovsky, D. I.; Kirtaev, R. V.; Stebunov, Y. S.; Arsenin, A. V.; Volkov, V. S. Morphology and Effective Dielectric Functions of Ultra-Thin Gold Films. In *Journal of Physics: Conference Series*; Institute of Physics Publishing, 2018; Vol. 1092. <https://doi.org/10.1088/1742-6596/1092/1/012167>.
181. Lee, J.; Pandey, P.; Sui, M.; Li, M. Y.; Zhang, Q.; Kunwar, S. Evolution of Self-Assembled Au NPs by Controlling Annealing Temperature and Dwelling Time on Sapphire (0001). *Nanoscale Res Lett* 2015, 10 (1), 1–11. <https://doi.org/10.1186/s11671-015-1200-0>.
182. Akselrod, M. S.; Bruni, F. J. Modern Trends in Crystal Growth and New Applications of Sapphire. In *Journal of Crystal Growth*; 2012; Vol. 360, pp 134–145. <https://doi.org/10.1016/j.jcrysgro.2011.12.038>.
183. Kratz, C.; Oates, T. W. H.; Hinrichs, K. Optimization and Quantification of Surface Enhanced Infrared Absorption Using Gradient Gold Island Films. *Thin Solid Films* 2016, 617, 33–37. <https://doi.org/10.1016/j.tsf.2016.02.019>.
184. Wrigglesworth, E. G.; Johnston, J. H. Mie Theory and the Dichroic Effect for Spherical Gold Nanoparticles: An Experimental Approach. *Nanoscale Adv* 2021, 3 (12), 3530–3536. <https://doi.org/10.1039/d1na00148e>.
185. Su, K. H.; Wei, Q. H.; Zhang, X.; Mock, J. J.; Smith, D. R.; Schultz, S. Interparticle Coupling Effects on Plasmon Resonances of Nanogold Particles. *Nano Lett* 2003, 3 (8), 1087–1090. <https://doi.org/10.1021/nl034197f>.
186. Ranjan, M. Predicting Plasmonic Coupling with Mie-Gans Theory in Silver Nanoparticle Arrays. *Journal of Nanoparticle Research* 2013, 15 (9). <https://doi.org/10.1007/s11051-013-1908-7>.
187. Zhang, S.; Panikkanvalappil, S. R.; Kang, S.; Smith, M. J.; Yu, S.; El-Sayed, M.; Tsukruk, V. V. Enhancing Plasmonic-Photonic Hybrid Cavity Modes by Coupling of Individual Plasmonic Nanoparticles. *Journal of Physical Chemistry C* 2019, 123 (39), 24255–24262. <https://doi.org/10.1021/acs.jpcc.9b07027>.

188. Wrigglesworth, E. G.; Johnston, J. H. Mie Theory and the Dichroic Effect for Spherical Gold Nanoparticles: An Experimental Approach. *Nanoscale Adv* 2021, 3 (12), 3530–3536. <https://doi.org/10.1039/d1na00148e>.
189. Lombardi, A.; Demetriadou, A.; Weller, L.; Andrae, P.; Benz, F.; Chikkaraddy, R.; Aizpurua, J.; Baumberg, J. J. Anomalous Spectral Shift of Near- A Nd Far-Field Plasmonic Resonances in Nanogaps. *ACS Photonics* 2016, 3 (3), 471–477. <https://doi.org/10.1021/acsp Photonics.5b00707>.
190. Huang, Y.; Chen, Y.; Gao, W.; Yang, Z.; Wang, L. Anomalous Spectral Correlations between SERS Enhancement and Far-Field Optical Responses in Roughened Au Mesoparticles. *Appl Phys Lett* 2018, 112 (17). <https://doi.org/10.1063/1.5030373>.
191. Luo, D.; Hong, P.; Wu, C.; Wu, S.; Liu, X. Optical Properties of Ag Nanoparticle Arrays: Near-Field Enhancement and Photo-Thermal Temperature Distribution. *Nanomaterials* 2022, 12 (21). <https://doi.org/10.3390/nano12213924>.
192. Schirato, A.; Silva, M. G.; Teles-Ferreira, D. C.; Manzoni, C.; de Paula, A. M.; Cerullo, G.; Della Valle, G.; Di Vece, M. Disentangling the Ultrafast Nonlinear Optical Behavior of Plasmonic Resonances Near the Interband Transition. *Adv Photonics Res* 2023, 4 (1). <https://doi.org/10.1002/adpr.202200081>.
193. Castronovo, P.; Gonzalez, C.; Ammirati, G.; Yang, S.; Catone, D.; Paladini, A.; O’Keeffe, P.; Kagan, C. R.; Murray, C. B.; Emanuele, A.; Marino, E.; Messina, F.; Sciortino, A. Interparticle Distance Controls Ultrafast Photodynamics in Crystalline Gold Superstructures. *Adv Opt Mater* 2025. <https://doi.org/10.1002/adom.202502501>.
194. Parkins, G. R.; Lawrence, W. E.; Christy, R. W. Intraband Optical Conductivity $\sigma(\omega, T)$ of Cu, Ag, and Au: Contribution from Electron-Electron Scattering. *Phys Rev B* 1981, 23 (12), 6408.
195. Liu, Y.; Zhang, H.; Geng, Y.; Xu, S.; Xu, W.; Yu, J.; Deng, W.; Yu, B.; Wang, L. Long-Range Surface Plasmon Resonance Configuration for Enhancing SERS with an Adjustable Refractive Index Sample Buffer to Maintain the Symmetry Condition. *ACS Omega* 2020, 5 (51), 32951–32958. <https://doi.org/10.1021/acsomega.0c03923>.
196. Singh, B. K.; Hillier, A. C. Surface Plasmon Resonance Enhanced Transmission of Light through Gold-Coated Diffraction Gratings. *Anal Chem* 2008, 80 (10), 3803–3810. <https://doi.org/10.1021/ac800045a>.
197. Baba, A.; Kanda, K.; Ohno, T.; Ohdaira, Y.; Shinbo, K.; Kato, K.; Kaneko, F. Multimode Surface Plasmon Excitations on Organic Thin Film/Metallic Diffraction Grating. *Jpn J Appl Phys* 2010, 49 (1 Part 2). <https://doi.org/10.1143/JJAP.49.01AE02>.
198. Mahmood, R.; Johnson, M. B.; Hillier, A. C. Massive Enhancement of Optical Transmission across a Thin Metal Film via Wave Vector Matching in Grating-Coupled Surface Plasmon Resonance. *Anal Chem* 2019, 91 (13), 8350–8357. <https://doi.org/10.1021/acs.analchem.9b01148>.
199. Burke, J. J.; Stegeman, G. I.; Tamir, T. Surface-Polariton-like Waves Guided by Thin, Lossy Metal Films; 1986; Vol. 33. DOI: <https://doi.org/10.1103/PhysRevB.33.5186>.
200. Lenac, Z.; tomaš, M. S. Attenuation of Long-Range Surface Polaritons in a Thin Metallic Slab with a Dielectric Coating. *Surf Sci* 1985, 154 (2), 639–657. [https://doi.org/https://doi.org/10.1016/0039-6028\(85\)90055-X](https://doi.org/https://doi.org/10.1016/0039-6028(85)90055-X).
201. Fukui, M.; So, V. C. Y.; Normandin, R. Lifetimes of Surface Plasmons in Thin Silver Films. *physica status solidi (b)* 1979, 91 (1), K61–K64. <https://doi.org/https://doi.org/10.1002/pssb.2220910159>.
202. Salwen, A.; Stensland, L. SPECTRAL FILTERING POSSIBILITIES OF SURFACE PLASMA OSCILLATIONS IN THIN METAL FILMS; Vol. 2. [https://doi.org/10.1016/0030-4018\(70\)90018-0](https://doi.org/10.1016/0030-4018(70)90018-0).
203. Borelli, M.; Giordano, M. C.; Gucciardi, P. G.; Buatier De Mongeot, F. Self-Organized Nanogratings for Large-Area Surface Plasmon Polariton Excitation and Surface-Enhanced Raman Spectroscopy Sensing. *ACS Appl Nano Mater* 2020, 3 (9), 8784–8793. <https://doi.org/10.1021/acsanm.0c01569>.
204. Saikin, S. K.; Chu, Y.; Rappoport, D.; Crozier, K. B.; Aspuru-Guzik, A. Separation of Electromagnetic and Chemical Contributions to Surface-Enhanced Raman Spectra on Nanoengineered Plasmonic Substrates. *Journal of Physical Chemistry Letters* 2010, 1 (18), 2740–2746. <https://doi.org/10.1021/jz1008714>.
205. Swanglap, P.; Slaughter, L. S.; Chang, W. S.; Willingham, B.; Khanal, B. P.; Zubarev, E. R.; Link, S. Seeing Double: Coupling between Substrate Image Charges and Collective Plasmon Modes in Self-Assembled Nanoparticle Superstructures. *ACS Nano* 2011, 5 (6), 4892–4901. <https://doi.org/10.1021/nn2009694>.

206. Li, G.; Cherqui, C.; Wu, Y.; Bigelow, N. W.; Simmons, P. D.; Rack, P. D.; Masiello, D. J.; Camden, J. P. Examining Substrate-Induced Plasmon Mode Splitting and Localization in Truncated Silver Nanospheres with Electron Energy Loss Spectroscopy. *Journal of Physical Chemistry Letters* 2015, 6 (13), 2569–2576. <https://doi.org/10.1021/acs.jpcclett.5b00961>.
207. Shopa, M.; Kolwas, K.; Derkachova, A.; Derkachov, G. Dipole and Quadrupole Surface Plasmon Resonance Contributions in Formation of Near-Field Images of a Gold Nanosphere. 2010. <https://doi.org/10.2478/s11772-010-0047-2>.
208. Álvarez-Puebla, R. A. Effects of the Excitation Wavelength on the SERS Spectrum. *Journal of Physical Chemistry Letters*. April 5, 2012, pp 857–866. <https://doi.org/10.1021/jz201625j>.
209. Ye, J.; Hutchison, J. A.; Uji-i, H.; Hofkens, J.; Lagae, L.; Maes, G.; Borghs, G.; Van Dorpe, P. Excitation Wavelength Dependent Surface Enhanced Raman Scattering of 4-Aminothiophenol on Gold Nanorings. *Nanoscale* 2012, 4 (5), 1606. <https://doi.org/10.1039/c2nr11805j>.
210. Homola, J. Electromagnetic Theory of Surface Plasmons; 2006; pp 3–44. https://doi.org/10.1007/5346_013.
211. Cunningham, J. E.; Flynn, C. P. Axial and Azimuthal Angle Determination with Surface-Enhanced Raman Spectroscopy: Thiophenol on Copper, Silver, and Gold Metal Surfaces; 1991; Vol. 95. <https://pubs.acs.org/sharingguidelines>.
212. Castriota, M.; Fasanella, A.; Cazzanelli, E.; De Sio, L.; Caputo, R.; Umerton, C. In Situ Polarized Micro-Raman Investigation of Periodic Structures Realized in Liquid-Crystalline Composite Materials. *Opt Express* 2011, 19 (11), 10494. <https://doi.org/10.1364/oe.19.010494>.
213. Presser, V.; Schuster, B. E.; Casu, M. B.; Heinemeyer, U.; Schreiber, F.; Nickel, K. G.; Chassé, T. Raman Polarization Studies of Highly Oriented Organic Thin Films. *Journal of Raman Spectroscopy* 2009, 40 (12), 2015–2022. <https://doi.org/10.1002/jrs.2361>.
214. Coca-López, N.; Hartmann, N. F.; Mancabelli, T.; Kraus, J.; Günther, S.; Comin, A.; Hartschuh, A. Remote Excitation and Detection of Surface-Enhanced Raman Scattering from Graphene. *Nanoscale* 2018, 10 (22), 10498–10504. <https://doi.org/10.1039/c8nr02174k>.
215. Gui, J. Y.; Stern, D. A.; Frank, D. G.; Lu, F.; Zapien, D. C.; Hubbard, A. T. Adsorption and Surface Structural Chemistry of Thiophenol, Benzyl Mercaptan, and Alkyl Mercaptans. Comparative Studies at Ag(LII) and Pt(LII) Electrodes by Means of Auger Spectroscopy, Electron Energy Loss Spectroscopy, Low-Energy Electron Diffraction, and Electrochemistry; 1991; Vol. 7. <https://pubs.acs.org/sharingguidelines>
216. Atomic force microscope block diagram. svg. (2023, September 30). Wikimedia Commons.
217. Mathew, E., Jencyk, J., Miłosz, Z., Henzie, J., Florczak, P., Andrzejewska, W., ... & Wiesner, M. (2024). Polarized-SERS of non-isotropic molecules on thermally-induced corrugated plasmonic surface supporting a NIR-SPP mode. *Applied Surface Science*, 659, 159821. <https://doi.org/10.1016/j.apsusc.2024.159821>.
218. Mathew, E. T.; Serebryannikov, A. E.; Jencyk, J.; Iatsunskyi, I.; Murawka, S.; Lewandowski, M.; Wiesner, M. Raman Scattering Enhancements Due to Super- and Subradiant Collective Plasmon Modes on Large-Area 2D-Au Arrays. *ACS Applied Mater Interfaces* 2025. <https://doi.org/10.1021/acsami.5c04804>.

List of journal publication (related to the PhD Thesis)

1. **Mathew, E.**, Jencyk, J., Miłosz, Z., Henzie, J., Florczak, P., Andrzejewska, W., ... & Wiesner, M. (2024). Polarized-SERS of non-isotropic molecules on thermally-induced corrugated plasmonic surface supporting a NIR-SPP mode. *Applied Surface Science*, 659, 159821. <https://doi.org/10.1016/j.apsusc.2024.159821>. **Impact factor: 6.3, Ministerial points: 140**
2. **Mathew, E. T.**; Serebryannikov, A. E.; Jencyk, J.; Iatsunskyi, I.; Murawka, S.; Lewandowski, M.; Wiesner, M. Raman Scattering Enhancements Due to Super- and Subradiant Collective Plasmon Modes on Large-Area 2D-Au Arrays. *ACS Applied Mater Interfaces* 2025. <https://doi.org/10.1021/acsami.5c04804>. **Impact factor: 8.5, Ministerial points: 200**
3. **Mathew E.T**, Peckus. D, J. Jencyk, S. Murawka, T. Tamulevicius, I. Iatsunskyi, S. Tamulevicius, M. Lewandowski, M. Wiesner, Polarization and wavelength dependent transient spectroscopic analysis of anisotropic ultrathin Au films deposited on thermally induced corrugated sapphire wafers. **(Under preparation)**.
4. **Mathew E.T**, Sarkar. S, Yu. Z, Ghosh. A. K, Li. Q, Zhou, Z, Fery. A, Wavelength scanned SERS measurements of non-isotropic molecules on large area wrinkle based plasmonic gratings supporting long- ranged and short ranged surface plasmon polaritons. **(Under preparation)**.

List of conference presentations (related to the PhD Thesis)

1. **Mathew, E. T.**; Serebryannikov, A. E.; Jencyk, J.; Iatsunskyi, I.; Murawka, Florczak, P. S.; Lewandowski, M.; Wiesner. Optical properties of anisotropic sub-wavelength metal nanostructures, *NanoTech Poland 2024*, March 5-7th, *International conference Poznan, Poland*. **(Poster - Distinction award)**.
2. **Mathew, E. T.**; Serebryannikov, A. E.; Jencyk, J.; Iatsunskyi, I.; Murawka, Florczak, P. S.; Lewandowski, M.; Wiesner. Hybridized collective plasmon modes in ordered 2D-metal nanoparticle arrays and its resulting dichroic SERS enhancement. *(AES) 11th International conference on antennas and electromagnetism systems 2025*, Tangier, Morocco. **Scopus Indexed. (Invited talk)**.
3. **Mathew, E.T**, Jencyk, J., Miłosz, Z., Henzie, J., Florczak, P., Andrzejewska, W., ... & Wiesner, M. (2024). The effect of periodically corrugated substrates on SERS anisotropy of organic molecules, *Condensed Matter Division (CMD) Fismat, Milan, Italy 4-8th September 2023*. **(Oral presentation)**.
4. **Mathew, E. T.**; Femtosecond laser micromachining, *International conference on material science 2022*, Department of Physics, Loyola College (affiliated to University of Madras), Chennai, India. **(Invited talk)**.
5. **Mathew, E. T.**; Serebryannikov, A. E.; Jencyk, J.; Iatsunskyi, I.; Murawka, Florczak, P. S.; Lewandowski, M.; Wiesner. Optical properties of anisotropic sub-wavelength Au arrays. *International Conference on Materials Science & Nanotechnology (Future Materials-2024)*, October 21-25, 2024, Athens, Greece. **(Poster presentation)**.

6. **Mathew, E. T.**; Jencyk, J.; Lewandowski, M.; Wiesner. Fabrication of long range ordered plasmonic nanostructures by electron beam lithography, *NanoTech Poland 2022, International conference Poznan, Poland. (Poster presentation)*.
7. **Mathew, E. T.**; Serebryannikov, A. E.; Jencyk, J.; Iatsunskiy, I.; Murawka, Florczak, P. S.; Lewandowski, M.; Wiesner. Fabrication Anisotropy of Surface enhanced Raman scattering of organic molecules on corrugated substrates, *NanoTech Poland 2023, International conference Poznan, Poland. (Poster presentation)*.
8. **J. Jencyk, E.T. Mathew**, M. Jancelewicz, P. Florczak, M. Lewandowski, M. Wiesner, The SoftComp/EUSMI Annual Meeting, 23-25.05.2023 Ancona, Italy „Copolymeric templates for plasmonic substrates fabrication”.
9. **J. Jencyk, E.T. Mathew**, M. Jancelewicz, P. Florczak, M. Lewandowski, M. Wiesner, Nanotech Poland, 14-16th June Poznań, 2023, „Block copolymer templates for plasmonic substrates fabrication”.
10. **J. Jencyk**, M. Jancelewicz, Z. Miłosz, **E.T. Mathew** „Well-ordered gold nanostructures fabricated via block copolymer lithography” –International Soft Matter Conference 2022, Poznań 19-13 wrzesień.
11. **J. Jencyk**, M. Jancelewicz, Z. Miłosz, **E.T. Mathew** „Fabrication of well-ordered gold nanostructures via block copolymer lithography” NanoTech Poland 2022, Poznań 1-3 czerwiec.
12. **E.T. Mathew**, J. Jencyk, Z. Miłosz, W. Andrzejewska, M. Lewandowski, **M. Wiesner**, The effect of periodically corrugated substrate on SERS anisotropy of organic molecules, The 13th International Conference on Metamaterials, Photonic Crystals and Plasmonics(META2023), 18–21.07.2023, Paryż, Francja.
13. **Maciej Wiesner, E. T. Mathew**, Andriy E. Serebryannikov, Jacek Jencyk, Igor Iatsunskiy, Szymon Murawka, Mikołaj Lewandowski, Anisotropic response of hybridized collective plasmon modes of 2D-metal nanoparticle arrays assembled on periodically corrugated sapphire substrates, META 2025, Malaga, Spain 22-26th July 2025.

List of internships and foreign research visits (related to the PhD studies)

1. Scientific Internship program

Place: Leibniz Institut für Polymerforschung Dresden, Technical University Dresden, Germany.

Date: 15/06/2025 – 15/12/2025. **(6 months)**

2. Participated in scientific research collaboration.

Place: Kaunas University of Technology, Kaunas, Lithuania

Date: 05/02/2024 – 05/03/2024. **(1 month)**

List of awards in competition (during the PhD studies)

1, (Poster - Distinction award). Optical properties of anisotropic sub-wavelength metal nanostructures, Nano-Tech Poland 2024, March 5-7th, International conference Poznan, Poland.

2, IPF Institute fellowship for collaborative guest researcher, Award =2000 EUR/month, Leibnitz Institut für Polymerforschung, eV Dresden, Germany.

3, IDUB competition for mini grant 054/13/SNS/004, Award = 20000 PLN, Name of funding institution: IDUB Adam Mickiewicz University, IDUB Role in Grant: Manager.

4, IDUB Competition for international scientific visit180/13/UAM/0060, Award = 7000 PLN, Name of funding institution: IDUB Adam Mickiewicz University, IDUB Role in Grant: Manager.

5, IDUB Competition for International conference 172/06/POB4/0008 Award = 6600 PLN, Name of funding institution: IDUB Adam Mickiewicz University, IDUB Role in Grant: Manager.

Other scientific activities (during the PhD studies)

1, Assistance in the organization of the 9th Polish conference of “Graphene and other 2D materials” in Poznan, Poland, 8-10th September,2024.

Ephraim T. Mathew

Faculty of Physics

Adam Mickiewicz University in Poznan

Ul. Uniwersytetu Poznanskiego 2, 61-614 Poznan, Poland

Statement

I hereby provide the statement regarding my specific - quantitative contribution to the following full length research article related to the Thesis:

“**Mathew, E.**, Jencyk, J., Miłosz, Z., Henzie, J., Florczak, P., Andrzejewska, W., ... & Wiesner, M. (2024). Polarized-SERS of non-isotropic molecules on thermally-induced corrugated plasmonic surface supporting a NIR-SPP mode. *Applied Surface Science*, 659, 159821. <https://doi.org/10.1016/j.apsusc.2024.159821>. Impact factor: 6.3, Ministerial points: 140”

- Writing first draft, preparation of all figures and tables (except for EM simulations).
- Conceptualization of studying plasmonic anisotropy of percolated metal films for SPP based NIR-SERS sensing.
- Performed AFM and micro-Raman experimental measurements.
- Data analysis and interpretation of AFM, Raman and reflectance spectra results
- Numerical and analytical calculation – 50%
- Revision and rewriting of manuscript
- Writing supporting information for the manuscript.
- Visualization and graphical abstract – 50%

My overall contribution to the manuscript in percentage is 70%

M. Nierna

Signature of promotor



Signature of Student

Permission to use figures from my own articles

CC BY 4.0

Attribution 4.0 International Deed


You are free to:

Share — copy and redistribute the material in any medium or format for any purpose, even commercially.

Adapt — remix, transform, and build upon the material for any purpose, even commercially.

The licensor cannot revoke these freedoms as long as you follow the license terms.

Under the following terms:

 **Attribution** — You must give [appropriate credit](#), provide a link to the license, and [indicate if changes were made](#). You may do so in any reasonable manner, but not in any way that suggests the licensor endorses you or your use.

No additional restrictions — You may not apply legal terms or [technological measures](#) that legally restrict others from doing anything the license permits.

Complete contact information is available at:

<https://doi.org/10.1016/j.apsusc.2024.159821>

CRediT authorship contribution statement

Ephraim T. Mathew: Writing – original draft, Visualization, Validation, Software, Methodology, Investigation, Formal analysis, Data curation, Conceptualization, Writing – review & editing. **Jacek Jencyk:** Writing – review & editing, Methodology. **Zygmunt Miłośz:** Methodology. **Joel Henzie:** Writing – review & editing, Visualization, Software. **Igor Iatsunskiy:** Writing – review & editing, Investigation. **Patryk Florczak:** Methodology. **Weronika Andrzejewska.:** Writing – review & editing, Visualization. **Mikołaj Lewandowski:** Writing – review & editing, Resources, Project administration, Methodology, Funding acquisition. **Maciej Wiesner:** Writing – original draft, Validation, Supervision, Resources, Methodology, Conceptualization, Writing – review & editing.

Ephraim T. Mathew

Faculty of Physics

Adam Mickiewicz University in Poznan

Ul. Uniwersytetu Poznanskiego 2, 61-614 Poznan, Poland

Statement

I hereby provide the statement regarding my specific - quantitative contribution to the following full length research article related to the Thesis:

“**Mathew, E. T.**; Serebryannikov, A. E.; Jencyk, J.; Iatsunskyi, I.; Murawka, S.; Lewandowski, M.; Wiesner, M. Raman Scattering Enhancements Due to Super- and Sub-radiant Collective Plasmon Modes on Large-Area 2D-Au Arrays. ACS Applied Mater Interfaces 2025. <https://doi.org/10.1021/acsami.5c04804>. Impact factor: 8.5, Ministerial points: 200”

- Conceptualization of studying plasmonic anisotropy of ultrathin non-percolated metal films, studying sub and super radiant SERS and method for validating EM near field mechanism of SERS.
- Performed AFM, UV-vis, micro-Raman measurements
- Data analysis and interpretation of experimental results
- Writing first draft, preparing all figures and tables (except for EM simulations)
- Revision and editing of manuscript
- Writing supporting information for the manuscript.
- Visualization and Graphical abstract

My overall contribution to the manuscript in percentage is 70%

M. Werner

Signature of promotor



Signature of Student

Permission to use figures from my own articles

CC BY 4.0

Attribution 4.0 International Deed


You are free to:

Share — copy and redistribute the material in any medium or format for any purpose, even commercially.

Adapt — remix, transform, and build upon the material for any purpose, even commercially.

The licensor cannot revoke these freedoms as long as you follow the license terms.

Under the following terms:

 **Attribution** — You must give appropriate credit, provide a link to the license, and indicate if changes were made. You may do so in any reasonable manner, but not in any way that suggests the licensor endorses you or your use.

No additional restrictions — You may not apply legal terms or technological measures that legally restrict others from doing anything the license permits.

Complete contact information is available at:

<https://pubs.acs.org/10.1021/acsami.5c04804>

Author Contributions

E.T.M.: Conceptualization; sample preparation; AFM, UV–vis spectroscopy, and micro-Raman investigation; methodology; interpretation; formal analysis; writing—original draft; validation; visualization; writing—review and editing. J.J.: Corrugated template fabrication; writing—review and editing. A.E.S.: Simulations; writing—review and editing. I.I.: Ellipsometry investigation; writing—review and editing. S.M.: ultrathin metal deposition in UHV. M.L.: Sample preparation; resources; funding acquisition; project administration; writing—review and editing. M.W.: Supervision; methodology; interpretation; writing—original draft; validation; resources; writing—review and editing.

Poznan:17/12/2025

Maciej Wiesner

Faculty of Physics

Adam Mickiewicz University in Poznan

Ul. Uniwersytetu Poznanskiego 2, 61-614 Poznan, Poland

Statement

I hereby provide the statement regarding my specific - quantitative contribution to the following full length research article related to the Thesis:

“**Mathew, E.**, Jencyk, J., Miłosz, Z., Henzie, J., Florczak, P., Andrzejewska, W., ... & Wiesner, M. (2024). Polarized-SERS of non-isotropic molecules on thermally-induced corrugated plasmonic surface supporting a NIR-SPP mode. *Applied Surface Science*, 659, 159821. <https://doi.org/10.1016/j.apsusc.2024.159821>. Impact factor: 6.3, Ministerial points: 140”

- Supervision of original research methodology and experimental resources
- Conceptualization of angle based polarized Raman spectroscopy
- AFM and Raman results discussion
- Numerical and analytical calculation of SPP dispersion relation in MATLAB
- Writing first draft
- Revision and editing of Manuscript

M. Wiesner
Signature

Poznan: 17/12/2025

Maciej Wiesner

Faculty of Physics

Adam Mickiewicz University in Poznan

Ul. Uniwersytetu Poznanskiego 2, 61-614 Poznan, Poland

Statement

I hereby provide the statement regarding my specific - quantitative contribution to the following full length research article related to the Thesis:

“**Mathew, E. T.**; Serebryannikov, A. E.; Jencyk, J.; Iatsunskyi, I.; Murawka, S.; Lewandowski, M.; Wiesner, M. Raman Scattering Enhancements Due to Super- and Sub-radiant Collective Plasmon Modes on Large-Area 2D-Au Arrays. ACS Applied Mater Interfaces 2025. <https://doi.org/10.1021/acsami.5c04804>. Impact factor: 8.5, Ministerial points: 200”

- Supervision of research methodology and experimental resources of the manuscript
- AFM, SEM and Raman results interpretation and discussion
- Performed SEM measurements
- Revision, rewriting and editing of manuscript



Signature

Poznan:30/08/2025

Jacek Jencyk

Faculty of Physics

Adam Mickiewicz University in Poznan

Ul. Uniwersytetu Poznanskiego 2, 61-614 Poznan, Poland

Statement

I hereby provide the statement regarding my specific - quantitative contribution to the following full length research article related to the Thesis:

“**Mathew, E.**, Jencyk, J., Mitosz, Z., Henzie, J., Florczak, P., Andrzejewska, W., ... & Wiesner, M. (2024). Polarized-SERS of non-isotropic molecules on thermally-induced corrugated plasmonic surface supporting a NIR-SPP mode. *Applied Surface Science*, 659, 159821. <https://doi.org/10.1016/j.apsusc.2024.159821>. Impact factor: 6.3, Ministerial points: 140”

- **Sample fabrication** of corrugated sapphire templates of different periods
 - **Atomic force microscopy** measurement of corrugated templates
- **Interpretation and discussion** of results of AFM images of corrugated templates
 - **Revision and editing** of manuscript– 5%


Signature

Poznan:30/08/2025

Jacek Jencyk

Faculty of Physics

Adam Mickiewicz University in Poznan

Ul. Uniwersytetu Poznanskiego 2, 61-614 Poznan, Poland

Statement

I hereby provide the statement regarding my specific - quantitative contribution to the following full length research article related to the Thesis:

“**Mathew, E. T.**; Serebryannikov, A. E.; Jencyk, J.; Iatsunskyi, I.; Murawka, S.; Lewandowski, M.; Wiesner, M. Raman Scattering Enhancements Due to Super- and Sub-radiant Collective Plasmon Modes on Large-Area 2D-Au Arrays. ACS Applied Mater Interfaces 2025. <https://doi.org/10.1021/acsami.5c04804>. Impact factor: 8.5, Ministerial points: 200”

- **Sample fabrication** of corrugated sapphire templates of different periods, double side sapphire annealing procedures and its optimization
- **Interpretation and discussion** of results of AFM images and of the formation of double side corrugated structures on the templates
 - **Revision and editing** of manuscript– technical


Signature

25/11/2025

Dr. Joel Henzie

Principal Researcher

Research Center for Materials Nano-architectonics (MANA)

National Institute for Materials Science (NIMS)

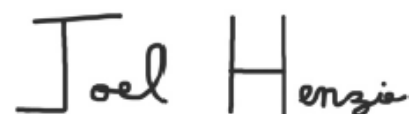
Tsukuba, Japan

Statement

I hereby provide the statement regarding my specific - quantitative contribution to the following full length research article related to the Thesis:

“**Mathew, E.**, Jencyk, J., Miłosz, Z., Henzie, J., Florczak, P., Andrzejewska, W., ... & Wiesner, M. (2024). Polarized-SERS of non-isotropic molecules on thermally-induced corrugated plasmonic surface supporting a NIR-SPP mode. *Applied Surface Science*, 659, 159821. <https://doi.org/10.1016/j.apsusc.2024.159821>. Impact factor: 6.3, Ministerial points: 140”

- Performing **EM Simulations** and acquiring near-field distributions
- **Reviewing and editing** of Manuscript - (Simulations section)

Handwritten signature of Joel Henzie in black ink.

Signature

Poznan:25/11/2025

Dr hab. Andriy Serebryannikov, prof. UAM

Faculty of Physics

Adam Mickiewicz University in Poznan

Ul. Uniwersytetu Poznanskiego 2, 61-614 Poznan, Poland

Statement

I hereby provide the statement regarding my specific - quantitative contribution to the following full length research article related to the Thesis:

“**Mathew, E. T.**; Serebryannikov, A. E.; Jencyk, J.; Iatsunskyi, I.; Murawka, S.; Lewandowski, M.; Wiesner, M. Raman Scattering Enhancements Due to Super- and Sub-radiant Collective Plasmon Modes on Large-Area 2D-Au Arrays. ACS Applied Mater Interfaces 2025. <https://doi.org/10.1021/acsami.5c04804>. Impact factor: 8.5, Ministerial points: 200”

- Performing **EM Simulation** for acquiring near field distributions
- **Discussion** on plasmon hybridization and Fabry Perot fringes
- **Editing and reviewing** of manuscript (EM simulations section and editorial corrections)


Signature

Poznań, 25.11.2025

Dr. Weronika Andrzejewska
NanoBiomedical Centre
Adam Mickiewicz University in Poznań
ul. Wszechnicy Piastowskiej 3
61-614 Poznań, Poland

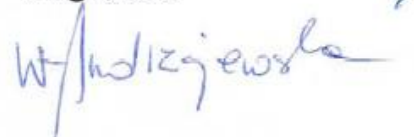
Statement

I hereby provide the statement regarding my specific - quantitative contribution to the following full length research article related to the Thesis:

“**Mathew, E.**, Jencyk, J., Miłosz, Z., Henzie, J., Florczak, P., Andrzejewska, W., ... & Wiesner, M. (2024). Polarized-SERS of non-isotropic molecules on thermally-induced corrugated plasmonic surface supporting a NIR-SPP mode. *Applied Surface Science*, 659, 159821. <https://doi.org/10.1016/j.apsusc.2024.159821>. Impact factor: 6.3, Ministerial points: 140”

- **Creating Graphical abstract** – 50%
- **Discussion** on choosing SERS analyte
- **Editing** the Manuscript (Editorial corrections)

Signature



Patryk Florczak
NanoBioMedical Centre
Adam Mickiewicz University, Poznań
Wszechniczy Piastowskiej 3 St., PL 61614 Poznań, Poland

Poznań, 25.11.2025

Statement

I hereby provide the statement regarding my specific - quantitative contribution to the following full length research article related to the Thesis:

“**Mathew, E.**, Jencyk, J., Miłosz, Z., Henzie, J., Florczak, P., Andrzejewska, W., ... & Wiesner, M. (2024). Polarized-SERS of non-isotropic molecules on thermally-induced corrugated plasmonic surface supporting a NIR-SPP mode. *Applied Surface Science*, 659, 159821. <https://doi.org/10.1016/j.apsusc.2024.159821>. Impact factor: 6.3, Ministerial points: 140”

- **Depositing** thiophenol molecules as SERS analytes


Signature

Poznan: 02/12/2025

Szymon Murawka

NanoBioMedical Centre

Adam Mickiewicz University in Poznan

Wszechnicy Piastowskiej 3 St., PL 61614 Poznań, Poland

Statement

I hereby provide the statement regarding my specific - quantitative contribution to the following full length research article related to the Thesis:

“**Mathew, E. T.**; Serebryannikov, A. E.; Jencyk, J.; Iatsunskyi, I.; Murawka, S.; Lewandowski, M.; Wiesner, M. Raman Scattering Enhancements Due to Super- and Sub-radiant Collective Plasmon Modes on Large-Area 2D-Au Arrays. ACS Applied Mater Interfaces 2025. <https://doi.org/10.1021/acсами.5c04804>. Impact factor: 8.5, Ministerial points: 200”

- **Sample fabrication:** performing metal deposition process in UHV conditions

Signature

Murawka Szymon

Poznan:25/11/2025

Zygmunt Miłosz

NanoBiomedical Centre

Adam Mickiewicz University in Poznan

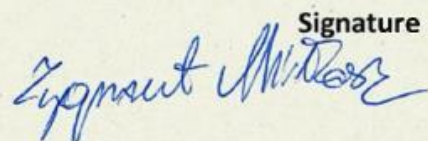
Ul. Uniwersytetu Poznanskiego 2, 61-614 Poznan, Poland

Statement

I hereby provide the statement regarding my specific - quantitative contribution to the following full length research article related to the Thesis:

“**Mathew, E.**, Jencyk, J., Miłosz, Z., Henzie, J., Florczak, P., Andrzejewska, W., ... & Wiesner, M. (2024). Polarized-SERS of non-isotropic molecules on thermally-induced corrugated plasmonic surface supporting a NIR-SPP mode. *Applied Surface Science*, 659, 159821. <https://doi.org/10.1016/j.apsusc.2024.159821>. Impact factor: 6.3, Ministerial points: 140”

- **Sample fabrication:** Au metal deposition in UHV, performing pre and post annealing of metal experimental procedures

Signature


Poznan:25/11/2025

Prof. Igor Iatsunskyi

Faculty of Physics

Adam Mickiewicz University in Poznan

Ul. Uniwersytetu Poznanskiego 2, 61-614 Poznan, Poland

Statement

I hereby provide the statement regarding my specific quantitative contribution to the following full length research article related to the Thesis:

“**Mathew, E.**, Jencyk, J., Miłosz, Z., Henzie, J., Florczak, P., Andrzejewska, W., ... & Wiesner, M. (2024). Polarized-SERS of non-isotropic molecules on thermally-induced corrugated plasmonic surface supporting a NIR-SPP mode. Applied Surface Science, 659, 159821. <https://doi.org/10.1016/j.apsusc.2024.159821>. Impact factor: 6.3, Ministerial points: 140”

- **Experimental characterization** – Performing ellipsometry
- **Review and editing** of the Manuscript (Ellipsometer section and editorial corrections)



Signature

Poznan: 25/11/2025

Prof. Igor Iatsunskyi

Faculty of Physics

Adam Mickiewicz University in Poznan

Ul. Uniwersytetu Poznanskiego 2, 61-614 Poznan, Poland

Statement

I hereby provide the statement regarding my specific - quantitative contribution to the following full length research article related to the Thesis:

“**Mathew, E. T.**; Serebryannikov, A. E.; Jencyk, J.; Iatsunskyi, I.; Murawka, S.; Lewandowski, M.; Wiesner, M. Raman Scattering Enhancements Due to Super- and Sub-radiant Collective Plasmon Modes on Large-Area 2D-Au Arrays. ACS Applied Mater Interfaces 2025. <https://doi.org/10.1021/acscami.5c04804>. Impact factor: 8.5, Ministerial points: 200”

- **Experimental characterization** – Performing ellipsometry
- **Review and editing** of the Manuscript (Ellipsometer section and editorial corrections)



Signature

Poznań, 11.12.2025

Prof. UAM dr hab. Mikołaj Lewandowski

Centrum NanoBioMedyczne
Uniwersytet im. Adama Mickiewicza
ul. Wszechnicy Piastowskiej 3
61-614 Poznań

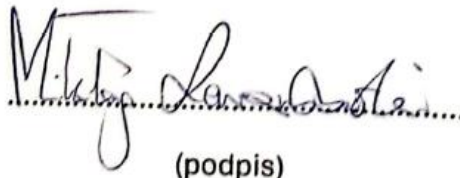
OŚWIADCZENIE

Niniejszym oświadczam, że mój wkład w pracę

E. T. Mathew, J. Jencyk, Z. Mitośz, J. Henzie, I. Iatsunskyi, P. Florczak, W. Andrzejewska, M. Lewandowski, M. Wiesner, *Polarized-SERS of non-isotropic molecules on thermally-induced corrugated plasmonic surface supporting a NIR-SPP mode*, Applied Surface Science 659 (2024) 159821 (DOI: 10.1016/j.apsusc.2024.159821)

– zawarte w której wyniki zostaną włączone w rozprawę doktorską Ephraima Thomasa Mathew, polegał na:

- kierowaniu projektem badawczym, w ramach którego były realizowane badania;
- częściowemu zapewnieniu materiałów do badań;
- opracowywaniu metodologii i nadzorowaniu eksperymentów związanych z naporowywaniem złota na podłoża szafirowe oraz jego wygrzewaniem w warunkach ultra-wysokiej próżni;
- udziale w dyskusji wyników badań;
- udziale przygotowywaniu publikacji.


(podpis)

Poznań, 11.12.2025

Prof. UAM dr hab. Mikołaj Lewandowski

Centrum NanoBioMedyczne
Uniwersytet im. Adama Mickiewicza
ul. Wszechnicy Piastowskiej 3
61-614 Poznań

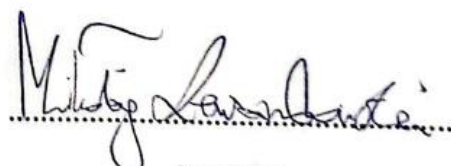
OŚWIADCZENIE

Niniejszym oświadczam, że mój wkład w pracę

E. T. Mathew, A. E. Serebryannikov, J. Jenczyk, I. Iatsunskyi, S. Murawka, M. Lewandowski, M. Wiesner, *Raman Scattering Enhancements Due to Super- and Sub-radiant Collective Plasmon Modes on Large-Area 2D-Au Arrays*, ACS Applied Materials & Interfaces 17 (2025) 33176–33190 (DOI: 10.1021/acsami.5c04804)

– zawarte w której wyniki zostaną włączone w rozprawę doktorską Ephraima Thomasa Mathew, polegał na:

- kierowaniu projektem badawczym, w ramach którego były realizowane badania;
- częściowemu zapewnieniu materiałów do badań;
- uczestniczeniu w realizacji eksperymentów związanych z naparowywaniem złota na podłoża szafirowe w warunkach ultra-wysokiej próżni;
- udziale w dyskusji wyników badań;
- udziale przygotowywaniu publikacji.


.....
(podpis)

Permission to adapt figures from articles into the theoretical section of thesis in chapter 1

CC BY 4.0

Attribution 4.0 International Deed


You are free to:

Share — copy and redistribute the material in any medium or format for any purpose, even commercially.

Adapt — remix, transform, and build upon the material for any purpose, even commercially.

The licensor cannot revoke these freedoms as long as you follow the license terms.

Under the following terms:

 **Attribution** — You must give [appropriate credit](#), provide a link to the license, and [indicate if changes were made](#). You may do so in any reasonable manner, but not in any way that suggests the licensor endorses you or your use.

No additional restrictions — You may not apply legal terms or [technological measures](#) that legally restrict others from doing anything the license permits.

Permission to adapt figures from articles into the theoretical section of thesis in chapter 1

SPRINGER NATURE LICENSE
TERMS AND CONDITIONS

Oct 21, 2025

This Agreement between Ephraim Mathew, Adam Mickiewicz University ("You") and Springer Nature ("Springer Nature") consists of your license details and the terms and conditions provided by Springer Nature and Copyright Clearance Center.

License Number 6133771120278

License date Oct 21, 2025

Licensed Content Publisher Springer Nature

Licensed Content Publication Journal of Sol-Gel Science and Technology

Licensed Content Title The ellipsometry versatility in the study of sol-gel films

Licensed Content Author Mariuca Gartner et al

Licensed Content Date Mar 8, 2021

Type of Use Thesis/Dissertation

Requestor type academic/university or research institute

Format print and electronic

Portion figures/tables/illustrations

Number of figures/tables/
illustrations 1

Permission to adapt figures from articles into the theoretical section of thesis in chapter 1

JOHN WILEY AND SONS LICENSE
TERMS AND CONDITIONS

Oct 21, 2025

This Agreement between Ephraim Mathew, Adam Mickiewicz University ("You") and John Wiley and Sons ("John Wiley and Sons") consists of your license details and the terms and conditions provided by John Wiley and Sons and Copyright Clearance Center.

License Number 6133720908450

License date Oct 21, 2025

Licensed Content Publisher John Wiley and Sons

Licensed Content Publication Advanced Materials

Licensed Content Title Nanofacet Lithography: A New Bottom-Up Approach to Nanopatterning and Nanofabrication by Soft Replication of Spontaneously Faceted Crystal Surfaces

Licensed Content Author R. Gabai, A. Ismach, E. Joselevich

Licensed Content Date Apr 18, 2007

Licensed Content Volume 19

Licensed Content Issue 10

Licensed Content Pages 6

Type of use Dissertation/Thesis

**Permission to adapt figures from articles into the theoretical section of
thesis in chapter 1**

AMERICAN CHEMICAL SOCIETY LICENSE
TERMS AND CONDITIONS

Oct 20, 2025

This Agreement between Ephraim Mathew Adam Mickiewicz University ("You") and American Chemical Society ("American Chemical Society") consists of your license details and the terms and conditions provided by American Chemical Society and Copyright Clearance Center.

License Number	6133280990083
License date	Oct 20, 2025
Licensed Content Publisher	American Chemical Society
Licensed Content Publication	The Journal of Physical Chemistry C
Licensed Content Title	Coupled Plasmon Modes in 2D Gold Nanoparticle Clusters and Their Effect on Local Temperature Control
Licensed Content Author	Rituraj Borah, Sammy W. Verbruggen
Licensed Content Date	Dec 1, 2019
Licensed Content Volume	123
Licensed Content Issue	50
Volume number	123
Issue number	50

Permission to adapt figures from articles into the theoretical section of thesis in chapter 1

SPRINGER NATURE LICENSE
TERMS AND CONDITIONS

Oct 20, 2025

This Agreement between Ephraim Mathew, Adam Mickiewicz University ("You") and Springer Nature ("Springer Nature") consists of your license details and the terms and conditions provided by Springer Nature and Copyright Clearance Center.

License Number	6133260070812
License date	Oct 20, 2025
Licensed Content Publisher	Springer Nature
Licensed Content Publication	Nano Research
Licensed Content Title	Transition metal dichalcogenide-based mixed-dimensional heterostructures for visible-light-driven photocatalysis: Dimensionality and interface engineering
Licensed Content Author	Xiaorong Gan et al
Licensed Content Date	Jul 17, 2020
Type of Use	Thesis/Dissertation
Requestor type	academic/university or research institute
Format	print and electronic
Portion	figures/tables/illustrations

**Permission to adapt figures from articles into the theoretical section of
thesis in chapter 1**

AMERICAN CHEMICAL SOCIETY LICENSE
TERMS AND CONDITIONS

Oct 20, 2025

This Agreement between Ephraim Mathew Adam Mickiewicz University ("You") and American Chemical Society ("American Chemical Society") consists of your license details and the terms and conditions provided by American Chemical Society and Copyright Clearance Center.

License Number 6133230112980

License date Oct 20, 2025

Licensed Content Publisher American Chemical Society

Licensed Content
Publication The Journal of Physical Chemistry C

Licensed Content Title Solid-State Thermal Dewetting of Just-Percolated Gold
Films Evaporated on Glass: Development of the Morphology
and Optical Properties

Licensed Content Author Alexander B. Tesler, Ben M. Maoz, Yishay Feldman, et al

Licensed Content Date May 1, 2013

Licensed Content Volume 117

Licensed Content Issue 21

Volume number 117

Issue number 21

Type of Use	Thesis/Dissertation
Requestor type	Author (original work)
Format	Print and Electronic
Portion	Table/Figure/Micrograph
Number of Table/Figure/ Micrographs	1
Title of new work	Plasmonic properties of anisotropic, ultra-thin Au films and its resulting dichroic Raman effect towards the development of surface enhanced Raman spectroscopy
Institution name	Adam Mickiewicz University
Expected presentation date	Mar 2026
Portions	Graphical Abstract
The Requesting Person / Organization to Appear on the License	Ephraim Mathew Adam Mickiewicz University
Requestor Location	Pradnicka 3 Poznan, Wielkopolski 60-401 Poland
Order reference number	147
Payment Type	Invoice
Email Address	ephream030@gmail.com

**Permission to adapt figures from articles into the theoretical section of
thesis in chapter 1**

AMERICAN CHEMICAL SOCIETY LICENSE
TERMS AND CONDITIONS

Oct 20, 2025

This Agreement between Ephraim Mathew, Adam Mickiewicz University ("You") and American Chemical Society ("American Chemical Society") consists of your license details and the terms and conditions provided by American Chemical Society and Copyright Clearance Center.

License Number	6133290212512
License date	Oct 20, 2025
Licensed Content Publisher	American Chemical Society
Licensed Content Publication	Nano Letters
Licensed Content Title	Coupling of Optical Resonances in a Compositionally Asymmetric Plasmonic Nanoparticle Dimer
Licensed Content Author	Sassan Sheikholeslami, Young-wook Jun, Prashant K. Jain, et al
Licensed Content Date	Jul 1, 2010
Licensed Content Volume	10
Licensed Content Issue	7
Volume number	10
Issue number	7

Type of Use	Thesis/Dissertation
Requestor type	Author (original work)
Format	Print and Electronic
Portion	Table/Figure/Micrograph
Number of Table/Figure/ Micrographs	2
Title of new work	Plasmonic properties of anisotropic, ultra-thin Au films and its resulting dichroic Raman effect towards the development of surface enhanced Raman spectroscopy
Institution name	Adam Mickiewicz University
Expected presentation date	Mar 2026
Portions	Figure 2b. on page no 2657 and Figure 2c. on page no 2657
The Requesting Person / Organization to Appear on the License	Ephraim Mathew, Adam Mickiewicz University
Requestor Location	Mr. Ephraim Mathew Pradnicka 3 Poznan, Wielkopolski 60-401 Poland
Order reference number	207
Payment Type	Invoice
Email Address	ephream030@gmail.com

Permission to adapt figures from articles into the theoretical section of thesis in chapter 1



PARTIES:

1. **Cambridge University Press** (Licensor); and
2. **Ephraim Mathew** (Licensee).

Thank you for your recent permission request. Some permission requests for use of material published by the Licensor, such as this one, are now being facilitated by PLSclear.

Set out in this licence cover sheet (the **Licence Cover Sheet**) are the principal terms under which Licensor has agreed to license certain Licensed Material (as defined below) to Licensee. The terms in this Licence Cover Sheet are subject to the attached General Terms and Conditions, which together with this Licence Cover Sheet constitute the licence agreement (the **Licence**) between Licensor and Licensee as regards the Licensed Material. The terms set out in this Licence Cover Sheet take precedence over any conflicting provision in the General Terms and Conditions.

Free Of Charge Licence Terms

Licence Date: 20/10/2025
PLSclear Ref No: 110753

The Licensor

Company name: Cambridge University Press
Address: University Printing House
Shaftesbury Road
Cambridge
CB2 8BS
GB

The Licensee

Licensee Contact Name: Ephraim Mathew
Licensee Address: Pradnicka 3
Poznan
60-401
Poland

Licensed Material

title: Principles of Nano-Optics
ISBN: 9780521539883
publisher: Cambridge University Press

Are you requesting permission to reuse the cover of the publication?	No
Figure number & title	Figure 12.1 Real and imaginary part of the dielectric constant for gold according to the Drude-Sommerfeld free electron model ($\omega_p = 13.8 \cdot 10^{15} \text{ s}^{-1}$, $\Gamma = 1.075 \cdot 10^{14} \text{ s}^{-1}$)
Page numbers	409
Name of illustrator	Lukas Novotny and Bert Hecht
Are you the author of the content that you are requesting to reuse?	No
Additional Information	I am requesting to use this image in my Doctoral Dissertation
Will you be changing or editing the image?	No
Are you requesting permission to reuse the cover of the publication?	No
Figure number & title	Figure 12.2: Contribution of bound electrons to the dielectric function of gold. The parameters used are $\tilde{\omega}_p = 45 \cdot 10^{14} \text{ s}^{-1}$, $\gamma = 8.35 \cdot 10^{-16} \text{ s}^{-1}$, and $\omega_0 = 2\pi c/\lambda$, with $\lambda = 450 \text{ nm}$.
Page numbers	410
Name of illustrator	Lukas Novotny and Bert Hecht
Are you the author of the content that you are requesting to reuse?	No
Additional Information	I am requesting to use this image in my Doctoral Dissertation
Will you be changing or editing the image?	No

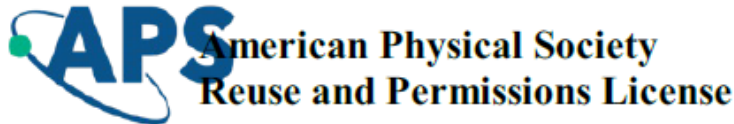
For Use In Licensee's Publication(s)

usage type	Book, Journal, Magazine or Academic Paper-Thesis or Dissertation
Will your dissertation be placed in an online repository?	Yes
Author	Ephraim Mathew
Estimated publication date	31/03/2026
Language	English
Title of dissertation/thesis	Plasmonic properties of anisotropic, ultra-thin Au films and its resulting dichroic Raman effect towards the development of surface enhanced Raman spectroscopy
University or institution	Adam Mickiewicz University
Unlimited circulation?	No

Rights Granted

Exclusivity:	Non-Exclusive
Format:	Thesis or Dissertation
Language:	English
Territory:	World
Duration:	Lifetime of Licensee's Edition

Permission to adapt figures from articles into the theoretical section of thesis in chapter 1



20-Oct-2025

This license agreement between the American Physical Society ("APS") and Ephraim Mathew ("You") consists of your license details and the terms and conditions provided by the American Physical Society and SciPris.

Licensed Content Information

License Number:	RNP/25/OCT097699
License date:	20-Oct-2025
DOI:	10.1103/PhysRevB.89.214201
Title:	Theory of percolation and tunneling regimes in nanogranular metal films
Author:	Claudio Grimaldi
Publication:	Physical Review B
Publisher:	American Physical Society
Cost:	USD \$ 0.00

Request Details

Does your reuse require significant modifications:	No
Specify intended distribution locations:	Worldwide
Reuse Category:	Reuse in a thesis/dissertation
Requestor Type:	Student
Items for Reuse:	Figures/Tables
Number of Figure/Tables:	1
Figure/Tables Details:	Figure 1a. for using in my Thesis
Format for Reuse:	Electronic

Information about New Publication:

University/Publisher:	Adam Mickiewicz University
Title of dissertation/thesis:	Plasmonic properties of anisotropic, ultra-thin Au films and its resulting dichroic Raman effect towards the development of surface enhanced Raman spectroscopy
Author(s):	Ephraim Mathew
Expected completion date:	Mar. 2026

License Requestor Information

Name:	Ephraim Mathew
Affiliation:	Individual
Email Id:	ephream030@gmail.com
Country:	Poland

1. Journal of the Royal Society interface

0,00 EUR

Article: Raman spectroscopy and coherent anti-Stokes Raman scattering imaging: prospective tools for monitoring skeletal cells and skeletal regeneration.

Order License ID	Pending	Publisher	ROYAL SOCIETY
ISSN	1742-5662	Portion	Image/photo/ illustration
Type of Use	Republish in a thesis/ dissertation		

LICENSED CONTENT

Publication Title	Journal of the Royal Society interface	Rightsholder	The Royal Society (U.K.)
Article Title	Raman spectroscopy and coherent anti-Stokes Raman scattering imaging: prospective tools for monitoring skeletal cells and skeletal regeneration.	Publication Type	e-Journal
		Start Page	20160182
		Issue	118
		Volume	13
		URL	https://royalsocietypublishing.org/journal/rsif
Author / Editor	Royal Society (Great Britain)		
Date	01/01/2004		
Language	English		

Country	United Kingdom of Great Britain and Northern Ireland
----------------	--

REQUEST DETAILS

Portion Type	Image/photo/illustration	Distribution	Worldwide
Number of Images / Photos / Illustrations	1	Translation	Original language of publication
Format (select all that apply)	Print, Electronic	Copies for the Disabled?	No
Who Will Republish the Content?	Academic institution	Minor Editing Privileges?	No
Duration of Use	Life of current edition	Incidental Promotional Use?	No
Lifetime Unit Quantity	Up to 499	Currency	EUR
Rights Requested	Main product		

NEW WORK DETAILS

Title	Plasmonic properties of anisotropic, ultra-thin Au films and its resulting dichroic Raman effect towards the development of surface enhanced Raman spectroscopy	Institution Name	Adam Mickiewicz University
		Expected Presentation Date	2026-03-31
Instructor Name	Ephraim Mathew		

ADDITIONAL DETAILS

Order Reference Number	217	The Requesting Person / Organization to Appear on the License	Ephraim Mathew, Adam Mickiewicz University
-------------------------------	-----	--	--

REQUESTED CONTENT DETAILS

Title, Description or Numeric Reference of the Portion(s)	Figure 2. Schematic diagram of the energy transitions involved in Rayleigh scattering (a) and Raman scattering (b,c). Raman scattering occurs through the interaction of an incident photon with a molecular vibration mode	Title of the Article / Chapter the Portion Is From	Raman spectroscopy and coherent anti-Stokes Raman scattering imaging: prospective tools for monitoring skeletal cells and skeletal regeneration.
Editor of Portion(s)	Moura, Catarina Costa; Tare, Rahul S; Oreffo, Richard O C; Mahajan, Sumeet	Author of Portion(s)	Moura, Catarina Costa; Tare, Rahul S; Oreffo, Richard O C; Mahajan, Sumeet
Volume / Edition	13	Issue, if Republishing an Article From a Serial	118
Page or Page Range of Portion	20160182	Publication Date of Portion	2016-05-01

RIGHTSHOLDER TERMS AND CONDITIONS

Out of Copyright - any journal requested with a Publication date older than 70 years.

Total Items: 1

Total Due: 0,00 EUR